Study of the dynamics of streamers in air at atmospheric pressure

Sébastien Celestin

École Centrale Paris

THÈSE

présentée par

Sébastien Célestin

pour l'obtention du

GRADE de DOCTEUR

Formation doctorale : **Physique**

Laboratoire d'accueil : **Laboratoire d'Energétique Moléculaire et Macroscopique, Combustion (EM2C) du CNRS et de l'ECP**

Study of the dynamics of streamers in air at atmospheric pressure

Soutenue le 8 Décembre 2008

Composition du jury :

MM.	**Boeuf**	**J.-P.**	**Reviewer**
	Bourdon	**A.**	**Advisor**
	Hassouni	**K.**	**Reviewer**
	Paillol	**J.-H.**	
	Pasko	**V.**	
	Rousseau	**A.**	**Co-advisor**
	Ségur	**P.**	
	Starikovskaia	**S.**	

École Centrale des Arts et Manufactures
Grand Etablissement sous tutelle
du Ministère de l'Education Nationale
Grande Voie des Vignes
92295 CHATENAY MALABRY Cedex
Tél. : 33 (1) 41 13 10 00 (standard)
Télex : 634 991 F EC PARIS

Laboratoire d'Énergétique Moléculaire et Macroscopique, Combustion (E.M2.C.)
UPR 288, CNRS et École Centrale Paris
Tél. : 33 (1) 41 13 10 31
Fax : 33 (1) 47 02 80 35

2008 - 53

Résumé

Dans cette thèse, nous avons étudié d'un point de vue expérimental et numérique la dynamique et la structure des décharges de type streamer dans l'air à la pression atmosphérique. Deux configurations ont été étudiées: une décharge Nanoseconde Répétitive Pulsée (NRP) entre deux pointes dans l'air préchauffé et une Décharge à Barrière Diélectrique (DBD) dans une configuration pointe-plan. Nous avons montré que les simulations de la dynamique de ces décharges sur des temps courts permettent d'obtenir des informations sur la structure et les propriétés de ces décharges observées expérimentalement, généralement sur des temps plus longs. Dans le cadre de cette thèse, du point de vue de la simulation des décharges, deux nouvelles approches ont été développées: pour le calcul de la photoionisation et pour la prise en compte d'électrodes de forme complexe dans des maillages cartésiens.

Pour le calcul de la photoionisation dans l'air, le modèle intégral de référence requiert de longs temps de calcul. Dans ce travail, afin d'éviter de lourds calculs intégraux, nous avons développé plusieurs modèles différentiels qui permettent de prendre en compte la dépendance spectrale de la photoionisation, tout en restant simples et peu coûteux en temps de calcul. Parmi les modèles développés, nous avons montré que le modèle appelé SP3 3-groupes basé sur une approximation d'ordre 3 de l'équation de transfert radiatif était plus précis pour la simulation des streamers.

Afin de prendre en compte des électrodes de forme complexe dans les simulations, nous avons adapté une méthode GFM ("Ghost Fluid Method") pour résoudre l'équation de Poisson afin de calculer précisément le potentiel et le champ électrique près de l'électrode. Cette méthode nous permet de prendre en compte l'influence de la forme exacte de l'électrode dans un maillage régulier, et ce quelque soit la forme de l'électrode.

Nous avons réalisé des simulations en géométrie pointe-pointe étroitement liées à de récents travaux expérimentaux concernant des décharges générées par NRP dans de l'air préchauffé. Nous avons étudié la dynamique de la décharge dans l'espace inter-électrode pour différentes températures de l'air et différentes tensions appliquées. Nous avons montré que la structure de la décharge dépendait fortement de la tension appliquée, ce qui est en bon accord avec les expériences.

Dans la partie expérimentale de ce travail, nous avons étudié un comportement particulier des filaments de plasma dans une DBD pendant la demi-alternance positive de la tension appliquée. La dynamique des décharges est fortement affectée par la charge de surface déposée sur le diélectrique. Nous avons simulé une configuration pointe-plan avec un diélectrique plan sur la cathode dans le but de mieux comprendre l'influence de l'accumulation de la charge de surface sur l'allumage et la propagation de décharges successives dans une DBD. Dans ce travail, nous avons simulé la propagation d'un streamer initié près de l'anode jusqu'au diélectrique, ainsi que la formation d'une décharge de surface sur celui-ci. Nous avons ainsi déterminé les échelles de temps et les processus responsables de l'écrantage d'un filament de plasma et les conditions d'allumage des décharges successives. Les résultats obtenus sont en bon accord avec l'expérience.

Abstract

In this Ph.D. thesis we contribute to several aspects of research on streamer physics in air at atmospheric pressure through both experimental and numerical studies. We show that studying transient phenomena such as streamer discharges, whose timescales are very short compared to the operating times in applications, results in useful informations concerning their underlying physical mechanisms.

The classical integral model for photoionization generated by streamers in air is very time consuming. In this work we have developed three differential approaches: a three-exponential Helmholtz model, a three-group Eddington model, and a three-group improved Eddington (SP_3) model. The Helmholtz model is based on approximating the absorption function of the gas in order to transform the integral expression of the photoionization term into a set of Helmholtz differential equations. The Eddington and SP_3 methods are based on the direct numerical solution of an approximation of the radiative transfer equation. Finally, we have derived accurate definitions of boundary conditions for these differential models.

To take into account the electrode shapes in the simulations, we have adapted the Ghost Fluid Method to solve Poisson's equation in order to calculate the electric potential and field close to the electrode accurately. This method allows us to take into account the influence of the exact shape of the electrodes in the framework of finite volume methods using a regular grid, no matter how the electrode surfaces cross the grid. We use this method in simulations of streamer discharges generated by Nanosecond Repetitively Pulses (NRP) and in Dielectric Barrier Discharges (DBD), both of which involve needle-shaped electrodes.

We have carried out simulations in a point-to-point geometry closely linked with recent experimental works in pre-heated air discharges generated by NRP. We found out that by considering the propagation timescales of streamers in these configurations, it is possible to draw some conclusions about the final discharge structure (i.e., sparks or coronas discharges) which are in good agreement with the experiments.

In the experimental part of this work, we have studied a particular behavior of plasma filaments in a DBD during the positive half-cycle of the applied voltage. The dynamics of discharges is found to be greatly affected by the surface charge deposited upon the dielectric material. We have simulated a point-to-plane configuration, with a dielectric upon the plane cathode, in order to better understand the influence of the surface charge accumulation on successive discharges in a DBD. In this work we are able to simulate the propagation of the streamer from its ignition close to the anode up to the dielectric material, as well as its splitting into surface discharges upon reaching the dielectric. This simulation provides information on the timescales and processes responsible for plasma filament screening and ignition conditions of successive discharges, which are in agreement with experiment.

Acknowledgements

Je tiens tout d'abord à remercier mes directeurs de thèses *Anne Bourdon* et *Antoine Rousseau* pour leur soutien, leur disponibilité et leur dynamisme. Ce fut un véritable plaisir de travailler avec vous et j'éspere sincèrement que nous aurons encore l'occasion de travailler ensemble pendant longtemps.

Cette thèse s'est déroulée sur deux laboratoires: EM2C (Ecole Centrale Paris) et LPP, ex-LPTP, (Ecole Polytechnique). Je voudrais remercier ici l'ensemble du personnel de ces deux laboratoires, indispensable à la réussite de toutes les thèses qui s'y tiennent.

Un très grand merci à tous les thésards des deux laboratoires pour l'entre-aide, l'accueil et l'ambiance qu'ils réussirent à apporter chaque jour. Je tiens à remercier tout particulièrement les doctorants de l'axe Plasma Froid du LPP: *Katia Allegraud*, *Lina Gatilova*, *Emilie Despiau-Pujo*, *Claudia Lazzaroni*, *Paul Ceccato*, *Xavier Aubert*, *Joseph Youssef*, *Gary Leray*, *Laurent Liard* et *Garrett Curley*. Sans oublier *Sedina Tsikata* et *Richard Cousin*. Un immense merci a *Olivier Guaitella* avec qui faire de la recherche est toujours si enthousiasmant! Coté EM2C, je tiens à remercier tout d'abord ceux qui m'ont fait l'honneur de partager mon bureau: *Yacine Babou*, *Rogerio Goncalves do Santos*, *Junhong Kim*, et *Christophe Arnold*. Je remercie très chaleureusement *Christophe Laux*, pour m'avoir accueilli dans le groupe Plasmas Hors-Équilibres, ainsi que *Deanna Lacoste* et tous les doctorants de l'équipe: *Guillaumme Pilla*, *Fara Kaddouri* et *Philippe Berard*. J'ai une pensée toute particulière pour *David Pai*, tout d'abord par amitié, mais également pour l'effort considérable qu'il a produit en parcourant le mauvais anglais de ce manuscrit et en me prodiguant ses nombreux conseils. Et les post-docs de l'équipe! Merci *Gabi Stancu*, *Thierry Magin*, *Lise Caillaults* et *Gelareh Momen* pour votre bonne humeur et vos conseils. Durant ma thèse, j'ai eu le grand plaisir de collaborer avec *Barbar Zeghondy* et *Zdenek Bonaventura*, merci à vous pour toutes les discussions passionnantes que l'on a eues et pour vos encouragements constants. Je tiens aussi à saluer la bonne humeur si communicative des doctorants des autres équipes: *Elodie Betbeder*, *Laetitia Pons*, *Séverine Barbosa*, *Jin Zhang*, *Anne-Laure Birbaud*, *Stéphane de Chaisemartin*, *Nicolas Tran*, *Romain*, *Jean-Mich*, *POC*, *Nics*, et tous les autres.

À bien des égards *Delphine Bessières*, *Julien Capeillère*, *Jean Paillol*, *Pierre Ségur*, *Sergey Pancheshnyi*, et *Emmanuel Marode* permirent la réalisation des travaux de cette thèse par notre collboration au sein du "Club Streamer". Ce fut un véritable plaisir de travailler avec vous, et j'éspere que nos chemins se recroiseront très bientot.

Je tiens également à remercier ici ma famille (et par là j'entends aussi ma "belle-famille") ainsi que ma femme, *Céline*, pour leur soutien inconditionnel.

I wish to express my sincere gratitude to all members of my committee for their thoughtful comments and questions about this work. It has certainly increased the quality of this thesis. Some of them traveled a very long distance for attending the defense, and I am grateful to them for that.

†

This work has been supported by a grant from the French Ministry of Research delivered by École Centrale Paris. It has also been partly supported by ANR grant IPER "Interaction plasma-écoulement réactif" 2005-2008 and GDR CATAPLASME.

List of publications

Here is a list of articles written in the framework of this thesis and published in international journals with peer review:

1. Bourdon, A., V. P. Pasko, N. Y. Liu, S. Célestin, P. Ségur, and E. Marode (2007), Efficient models for photoionization produced by non-thermal gas discharges in air based on radiative transfer and the Helmholtz equations, *Plasma Sources Sci. Technol.*, *16*(3), 656–678, doi: 10.1088/0963-0252/16/3/026.

2. Liu, N., S. Célestin, A. Bourdon, V. P. Pasko, P. Ségur, and E. Marode (2007), Application of photoionization models based on radiative transfer and the Helmholtz equations to studies of streamers in weak electric fields, *Appl. Phys. Lett.*, *91*(21), 211501, doi: 10.1063/1.2816906.

3. Celestin, S., G. Canes-Boussard, O. Guaitella, A. Bourdon, and A. Rousseau (2008), Influence of the charges deposition on the spatio-temporal self-organization of streamers in a DBD, *J. Phys. D: Applied Physics*, *41*(20), 205214, doi: 10.1088/0022-3727/41/20/205214.

4. Celestin, S., K. Allegraud, G. Canes-Boussard, N. Leick, O. Guaitella, and A. Rousseau (2008), Patterns of plasma filaments propagating on a dielectric surface, *IEEE Trans. Plasma Sci.*, *36*(4), 1326–1327, doi: 10.1109/TPS.2008.92451.

5. Liu, N., S. Celestin, A. Bourdon, V. P. Pasko, P. Segur, and E. Marode (2008), Photoionization and Optical Emission Effects of Positive Streamers in Air at Ground Pressure, *IEEE Trans. Plasma Sci.*, *36*, 942–943, doi: 10.1109/TPS.2008.927088.

6. Capeillère, J., P. Ségur, A. Bourdon, S. Célestin, and S. Pancheshnyi (2008), The finite volume method solution of the radiative transfer equation for photon transport in non-thermal gas discharges: application to the calculation of photoionization in streamer discharges, *J. Phys. D: Applied Physics*, *41*, 234018. doi: 10.1088/0022-3727/41/23/234018.

7. Celestin, S., Z. Bonaventura, B. Zeghondy, A. Bourdon, and P. Ségur (2009), The use of the ghost fluid method for Poisson's equation to simulate streamer propagation in point-to-plane and point-to-point geometries, *Journal of Physics D Applied Physics*, *42*(6), 065203, doi: 10.1088/0022-3727/42/6/065203.

8. Celestin, S., Z. Bonaventura, O. Guaitella, A. Rousseau, and A. Bourdon (2009), Influence of surface charges on the structure of a dielectric barrier discharge in air at atmospheric pressure: experiment and modeling, *Eur. Phys. J.: Appl. Phys.*, *47*(2), 022810, doi: 10.1051/epjap/2009078.

À mon grand-père André,
et à ma femme Céline

Contents

Introduction

Motivation and context

Cold plasmas in atmospheric pressure air have been used in many different applications in the past few years. Air pollutant removal has become a major concern due to the tightening of environmental laws. Because of its low energy cost and its high chemical reactivity, cold plasma treatment appears to be a promising solution. Surface treatment applications (such as textile or biological treatments) require nondestructive solutions that still induce strong modifications of physical properties of the surface. In cold plasmas, electrons are heated up to a few tens of thousands of degrees Kelvin, while the heavy species such as neutral species or ions remain at room temperature. Cold plasmas are therefore an appropriate solution for surface treatment [see *Kogelschatz*, 2004]. Furthermore, the necessity of reducing pollutant emissions in aircraft engines, gas turbines and internal combustion engines has also motivated studies on the stabilization of the combustion of lean mixtures by cold plasma discharges. Very promising results have been obtained so far [*Starikovskaia*, 2006; *Pilla et al.*, 2006]. Finally, plasma actuators have been extensively studied to modify the laminar-turbulent transition inside the boundary layer and therefore reduce the drag in order to avoid unsteadiness that generates unwanted vibrations and noise [see *Moreau*, 2007]. For these two last applications, atmospheric pressure plasmas present very interesting features: robustness, low power consumption and the ability to impact the flow at high-frequency.

One of the main problems in plasma discharge experiments and applications comes from the fact that, at atmospheric pressure, the cold nonequilibrium plasma discharge is a transient event. A simple way to generate cold plasmas is to use electrodes at high-voltage separated by a gaseous gap. However, at atmospheric pressure, the originally cold plasma rapidly becomes a high-conducting junction that evolves into a thermal plasma where heavy species tend to be in equilibrium with the electrons at a few tens of thousands degrees Kelvin. This is the so-called arc discharge, which is then very destructive. There are several ways to prevent this equilibrium of temperature between heavy species and electrons. Two main solutions are Dielectric Barrier Discharges (DBD) and Nanosecond Repetitively Pulsed (NRP) discharges.

Dielectric barrier discharges have been studied since the invention of the ozonizer by Siemens in 1857. DBDs at atmospheric pressure produced by applied voltage at low frequency in gaseous gaps on the order of a few millimeters are mainly constituted of unstably triggered nonequilibrium transient plasma filaments. The dielectric barrier prevents the formation of an arc because charges deposited by the plasma filament on the dielectric material are trapped. These charges are deposited such that the electric field becomes too low to produce more current and the process stops in a few tens of nanoseconds. One of the current chal-

lenges of DBDs is to gain a better understanding of interactions between plasma filaments. Recently, *Guaitella et al.* [2006] described the bimodal behavior of the statistical distribution of current peaks in a cylindrical DBD operating at low frequency and concluded that the high-current mode was due to the self-triggering of several filaments, possibly influenced by the surface charge.

Another solution is to turn off the electric field before substantial ionization occurs, and thus avoid an extremely fast increase of the gas temperature. Repetitive pulsing results in the accumulation of active species, which produces a rich chemistry. NRP are also able to generate glow discharges between two point electrodes at quite high gas temperatures (∼1000 K) [e.g., *Pai*, 2008; *Pai et al.*, 2008]. Currently, finding a range of parameters resulting in a diffuse discharge at atmospheric pressure and ambient temperature is of great interest for prospective applications.

The physical comprehension of cold nonequilibrium plasmas at atmospheric pressure, at least at small time scales, rests upon the concept of highly nonlinear space charge waves, or so-called streamers. Streamers were introduced in the 1930's to explain naturally occurring spark discharges [*Loeb and Meek*, 1940a, b]. Plasma filaments in DBDs are created along the path of streamers. Streamers are also regarded as the precursors to spark discharges. They can initiate spark discharges in relatively short (several cm) gaps near atmospheric pressure in air. In atmospheric pressure applications, the typical transverse scale of individual streamer filaments in air is a fraction of millimeter, and may be substantially wider depending on external conditions. For example, lightning is a natural phenomenon directly related to streamer discharges. A streamer zone consisting of many highly-branched streamers usually precedes leader channels, which initiate lightning discharges in large volumes at near ground pressure.

It is interesting to note that, about two decades ago, large-scale electrical discharges were discovered in the mesosphere and the lower ionosphere above large thunderstorms, which are now commonly referred to as sprites [e.g., *Franz et al.*, 1990; *Sentman et al.*, 1995; *Stanley et al.*, 1999; *Lyons*, 2006]. In fact, the filamentary structures observed in sprites are the same phenomenon as streamer discharges at atmospheric pressure scaled to the reduced air density at higher altitudes [*Pasko et al.*, 1998; *Liu and Pasko*, 2004]. An overview of the physical mechanism and aspects of the molecular physics of sprite discharges in comparison with laboratory discharges can be found in [*Pasko*, 2007].

The streamer is thus present in many applications and physical phenomena, involving numerous time scales and characteristic lengths. Unfortunately, there is no analytical model able to describe all its properties accurately. Numerical simulations are therefore required. The numerical model proposed by *Dhali and Williams* [1987] is an effective model using drift-diffusion equations for charged species coupled with Poisson's equation. This model has been widely used in simulations of streamer propagation in plane-plane and point-to-plane geometry for many purposes [e.g., *Vitello et al.*, 1994; *Babaeva and Naidis*, 1997; *Kulikovsky*, 2000a; *Pancheshnyi et al.*, 2001; *Arrayás et al.*, 2002]. It is interesting to mention that the recent work of *Chanrion and Neubert* [2008] based on the resolution of the Boltzmann equation using particle techniques validates the fluid approach for streamer simulations.

It is important to note that recent developments in experimental diagnostics and simulation tools make it possible to carry out challenging thorough comparison studies on discharge dy-

namics and structure. This enables the understanding of important properties of discharges for the application of interest.

Scope of the Ph.D. thesis

The streamer discharge is very complex and is thus a subject of study in itself. The experiments and physical phenomena involving streamers couple many different time scales and characteristic lengths. The complexity in making theoretical predictions concerning experiments arises in these multiscale problems. In this thesis we have developed accurate numerical models to simulate streamers in NRP and DBD discharges, and the results obtained have been compared to experiments. The objective of this Ph.D. thesis is to answer two main questions:

1. For the DBD studied by *Guaitella et al.* [2006]: what is the influence of surface charges deposited on the dielectric by one discharge on the subsequent discharges.
2. For the NRP studied by *Pai* [2008]: what is the dynamics at short time scales of the diffuse discharge observed in experiments between two point electrodes.

These two questions require the study of discharge dynamics at short time scales.

To answer the first question, following the work of *Guaitella et al.* [2006], we have carried out a detailed experimental study at LPTP (Laboratoire de Physique et Technologies des Plasmas at Ecole Polytechnique, France) in a simpler geometry than the wire-cylinder geometry used in [*Guaitella et al.*, 2006]. In our work we have used a metallic point-to-plane dielectric configuration, and we have carried out detailed imaging and electrical diagnostics.

To answer the first and second questions, we have developed a 2D code at the EM2C laboratory (Energetique Moleculaire et Macroscopique, Combustion, at Ecole Centrale Paris, France) to study discharge dynamics based on the classical drift-diffusion equations coupled to Poisson's equation.

Two aspects in particular have been studied in this work:

- The development of an accurate method to take into account electrodes of complex geometries (needle-shaped in both experiments considered in this work) in Cartesian grids. Indeed, in a Cartesian grid, the exact shape of the electrode is replaced by a staircase, which may be inaccurate even with a refined grid.
- The development of an accurate and efficient model to take into account the photoionization in air. The objective is to avoid the use of the classical *Zheleznyak et al.* [1982] integral model, which is very time-consuming in computations, and to replace it with a more efficient model.

In Chapter I we present the formulation of the physical model of streamer dynamics. Chapter II presents the main numerical methods used and developed in this work. In Chapter III we derive three new models of photoionization. These new models are also tested in real streamer simulations in two configurations. The influence of electrodes of complex shapes is discussed in Chapter IV. Then, this method is applied to the study of the dynamics of the discharge in the configuration of the NRP. Chapter V presents the experimental study

of the DBD discharge. VI shows the numerical simulation of the DBD and the comparison with experiment.

Chapter I

Streamer fluid model

Table of Contents

I.1 Electron avalanche

I.1.1 Electron drift velocity

Let us consider a free electron in a gas immersed in a homogeneous field. This electron is initially ($t = 0$) placed at $x = 0$. Under this field, the electron is accelerated by the electric force between two collisions with neutral molecules of the gas. A collision between an electron and a molecule changes the direction of motion of the electron, although the molecules are considered to be static since they are much heavier than the electrons. As charged particles are very rare compared to the molecules in weakly ionized plasmas, we will not consider electron-electron collisions[1] nor electron-ion collisions in this section. The inelastic collisions are much less frequent than the elastic collisions, and they can be neglected in the analysis of the general motion of the electrons we present here [*Raizer*, 1991, Sec. 2.1.1, p. 8]. The electron is then accelerated in the electric field until the next collision, when the direction of the velocity changes sharply in a random fashion. Afterwards, the electron is re-accelerated in the direction of the electric field, and so on. One of the main results of the rigorous analysis of this problem is the fact that on a mesoscopic scale of space and time [e.g., *Rax*, 2005, Sec. 2.1.1] the average velocity of the electron becomes proportional to the electric field. That is, the electric force compensates for the resistive force from the large number of collisions. This mean velocity of the electron is named *drift velocity*, and is written as:

$$\vec{v_e} = -\mu_e \vec{E} = -\frac{q}{m_e \nu} \vec{E} \tag{I.1}$$

where μ_e is the *electron mobility*, q is the elementary charge, m_e is the mass of the electron, ν is the *effective collision frequency for momentum transfer* between electrons and neutral molecules, and $\vec{E}$ is the electric field. In general, relation (I.1) is more complicated because ν depends on the electron energy. The characteristic time for the mean velocity to reach a constant value and take the form (I.1) is on the order of $1/\nu$ (which is also the characteristic time for the isotropization of microscopic velocities). From [*Raizer*, 1991, Table 2.1, p. 10] we find that $1/\nu \simeq 3 \cdot 10^{-13}$ s in air at atmospheric pressure for a typical electric field range between 3-40 kV/cm, which is much less than the time scale of propagation of the discharges we study in this report (i.e., the nanosecond time scale). Thus, in our study we can consider Equation (I.1) to be a very good approximation.

It is interesting to note that the time scale of the energy relaxation (also called the time scale of thermalization) is also linked to ν. This link is often described using a parameter δ

[1] Electron-electron collisions do not contribute to the electric resistance, as the total momentum of an electron colliding pair is conserved. However, they can indirectly affect the conductivity by changing the electron energy distribution function [see *Raizer*, 1991, Sec. 2.2.3, p. 14].

for which the energy relaxation time scale is then $(\delta\nu)^{-1}$. In the model of elastic collisions $\delta = 2m_e/M$, where M is the mass of the neutral molecule, and therefore $\delta \ll 1$. This time is much longer than that required for the mean velocity to reach a steady state.

I.1.2 Electron diffusion

Another physical quantity important for characterization of the motion of a group of electrons in a gas is the *electron diffusion*. The diffusion characterizes the speed of the spreading of the electron cloud due to the collisions with neutral molecules. It is related to the mean quadratic deviation of the electron motion [*Rax*, 2005, e.g., Sec. 2.1.1] and it is characterized by the coefficient:

$$D_e = \frac{kT_e}{m_e\nu} \tag{I.2}$$

where k is the Boltzmann constant, and T_e is the temperature of the electrons. The link between the mobility (I.1) and the diffusion (I.2) is the *Einstein relation*:

$$\frac{D_e}{\mu_e} = \frac{kT_e}{q} \tag{I.3}$$

I.1.3 Electron amplification

If the electric field is strong enough, the energy gained by the electron between collisions enables it to ionize the molecules of the gas. Then, *secondary electrons* will be created and follow the same life cycle as the first electron: acceleration, collision (maybe ionization), then acceleration again, etc. This leads to an exponential increase of the electron cloud as electrons move forward, globally in the opposite direction of the electric field. It is then natural to introduce a number that characterizes the increase of this *electron avalanche*. This number is called the *first Townsend coefficient* after John Sealy Edward Townsend and is often written as α. It represents the mean number of electrons created by electron impact on neutral molecules per unit length. The electron density in the avalanche in one dimension, and with the electric field oriented in the decreasing x direction, can then be written as:

$$\frac{\mathrm{d}N_e}{N_e} = \alpha \mathrm{d}x \tag{I.4}$$

where N_e is the number of electrons. Thus, from our single electron, we generate $N_e = \exp(\alpha x)$ electrons after propagation across a distance x. The natural link between the drift velocity and the first Townsend coefficient is the ionization frequency:

$$\nu_i = \alpha v_e \tag{I.5}$$

In electronegative gases one has to replace α by an effective ionization coefficient $\alpha_{\text{eff}} = \alpha - \beta$ where β is the attachment coefficient, which is the mean number of electrons attached by molecules per unit length. Note that β can also take into account the electron-ion recombination processes. In the same way that the characteristic distance of ionization $1/\alpha$ is linked to the characteristic time $1/\nu_i$, the characteristic distance of attachment is

linked to $1/\nu_a$ where ν_a is the attachment frequency. For low electric fields, α is less than β. However, α grows much faster with the electric field than β does, and then for high electric fields α becomes much greater than β. The equality of those two coefficients defines the conventional breakdown threshold field $E_k \simeq 30$ kV/cm in air at atmospheric pressure [e.g., see *Raizer*, 1991, Sec. 7.2.5, p. 136]. For electric fields lower than this value, one does not observe any appreciable discharge in the gas.

I.1.4 Avalanche-to-streamer transition

For an avalanche, the electron cloud is only controlled by the external electric field. In other words, the number of electrons is small enough such that the avalanche is not perturbed by its own electric field, also called the *space charge field*. However, if the electron amplification is sufficiently high, that is after a certain distance, the space charge field can considerably perturb the external field (see Fig. I.1), eventually leading to an object mainly controlled by its own field. This object is the streamer itself and will be discussed in the next section. In this section, let us focus on the transition between the electron avalanche and the streamer.

As the avalanche moves in the opposite direction of the electric field, the number of electrons increases exponentially (I.4) and spreads out because of the diffusion. One can find that the characteristic radius of the avalanche started from one single electron $n_e(x, t = 0) = \delta(0)$, where δ is the Dirac delta function [*Raizer*, 1991, Sec. 12.2.1, p. 328]:

$$r_D = \sqrt{4D_e t} = \sqrt{4\frac{D_e x_0}{\mu_e E_0}} \tag{I.6}$$

where x_0 is the position of the center of the plasma cloud, and E_0 is the external homogeneous field. The space charge forms a dipole, where electrons are at the head of the avalanche and the mean position of positive ions is behind. It is interesting to note that the characteristic length between the electron and ion clouds is a constant $1/\alpha(E_0)$ [*Raizer*, 1991; *Montijn and Ebert*, 2006]. One can clearly see in Figure I.1(a) that the resulting field in front of the avalanche is higher than E_0, and that the field between the negative cloud and the positive cloud is smaller than E_0. It is possible to approximate the space charge electric field in front of the avalanche by considering it as a spherical electron cloud of radius r_D: $E' = \frac{1}{4\pi\epsilon_0}\frac{qN_e}{r_D^2}$, where ϵ_0 is the permittivity of free space. For air at atmospheric pressure, one finds from (I.6) that E' is on the order of the conventional breakdown field E_k for $N_e \simeq 0.8 \cdot 10^7$, which corresponds to $\alpha d \simeq 18$, where d is the distance from the center of the electron cloud to the initial position of the primary electron. This is the so-called *Raether-Meek criterion* [*Raizer*, 1991, Sec. 12.2.5, p. 332]. For the original study of this criterion, see [*Meek*, 1940; *Loeb and Meek*, 1940a]. Refinement of the Raether-Meek criterion is possible by taking into account the real shape of the electron cloud (which is only influenced by the external homogeneous field), the influence of the ion field, and finding by simulation the electric field generated by the avalanche for which the deviation from an avalanche purely controlled by the external field becomes significant. This study was done by *Montijn and Ebert* [2006], who found that for air at atmospheric pressure the new criterion was really close to the classical Raether-Meek criterion $\alpha d \simeq 18$. Discrepancies are more noticeable for non-attaching gases.

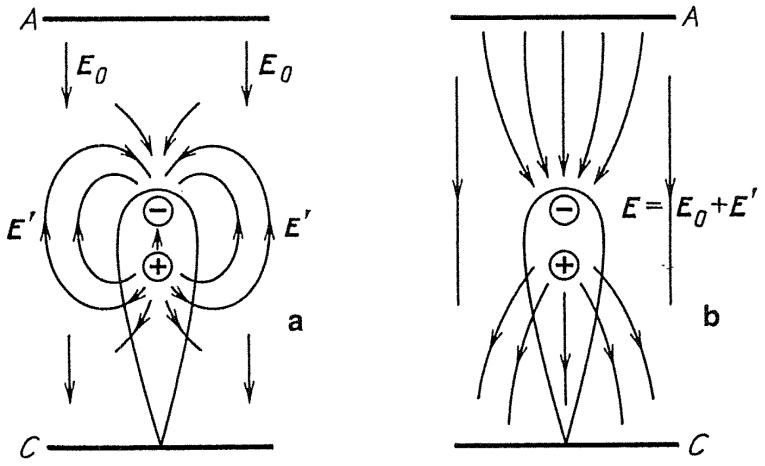

Figure I.1: Avalanche between two planar electrodes (A is the anode and C is the cathode) generating the homogeneous electric field $\vec{E}_0$. (a) Representation of the space charge electric field $\vec{E}'$. (b) Representation of the total electric field $\vec{E} = \vec{E}_0 + \vec{E}'$. Figure taken from [*Raizer*, 1991, Fig. 12. 3, p. 332].

When the density of electrons is sufficiently high in the avalanche head (i.e., when $\alpha d \gtrsim 14$), the role of repulsion between electrons becomes non-negligible compared to diffusion for the expansion of the radius of the avalanche. Furthermore, the rate of expansion due to diffusion is $\delta r_D/\delta t \sim t^{-1/2}$, but the rate of expansion due to the repulsion is given by [*Raizer*, 1991, Sec. 12.2.6, p. 334]:

$$\frac{\mathrm{d}R}{\mathrm{d}t} = \mu_e E' = \frac{q\mu_e R^{-2}\exp\left(\alpha\mu_e E_0 t\right)}{4\pi\epsilon_0} \tag{I.7}$$

Which leads to:

$$R = \left(\frac{3q}{4\pi\epsilon_0\alpha E_0}\right)^{1/3}\exp\left(\frac{\alpha x}{3}\right) = \frac{3E'}{\alpha E_0}, \qquad n_e = \frac{3N_e}{4\pi R^3} = \frac{\epsilon_0\alpha E_0}{q} \tag{I.8}$$

Equation (I.8) shows that repulsion of electrons results in an exponential increase of the avalanche radius. Furthermore, we see that the electron density is not changed by this repulsion effect.

It is interesting to note here that the time scale linked to this expansion rate is the Maxwell time, also called the dielectronic relaxation time τ_m. Indeed, $\frac{\mathrm{d}R}{\mathrm{d}t} \sim R/\tau_m$, where:

$$\tau_m = \frac{\epsilon_0}{qn_e\mu_e} \tag{I.9}$$

which is quite important in the streamer simulations, as we will see in the following. We noticed previously that the mean distance between the ion and the electron clouds is characterized by $1/\alpha$. When the radius reaches this value, the mean distance between ions and electrons is small, and the spreading of the electrons begins to slow down. The maximum radius of the avalanche is then $\sim 1/\alpha$. In air at atmospheric pressure this value is roughly 0.1 cm at the breakdown field E_k. This phenomenon takes place before the Raether-Meek criterion is reached, but we see what is taking place for this avalanche: it starts to be managed by its own charge field. Afterwards, the Raether-Meek criterion is overtaken, and

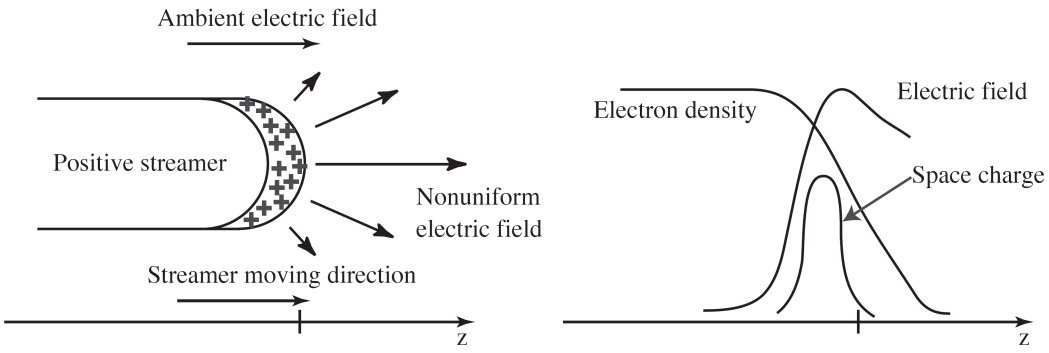

Figure I.2: Diagram of a positive streamer propagating in an ambient field [*Liu*, 2006; *Bazelyan and Raizer*, 1998].

the field in front of the avalanche is able to ionize the gas close to this head. This also occurs at the back of the avalanche where the ion density is high. These new electrons allow propagation due to drift to be replaced by a new mode based on the ionization of the neutral gas, and this new propagating object is called the *streamer discharge*.

I.2 Mechanism of streamer discharge propagation

I.2.1 Basics

The concept of streamer discharges was put forward in the 1930's by Raether and Loeb to explain spark discharges and by Cravath and Loeb to explain very fast phenomenon (i.e., close to the speed of light) in low pressure long tubes first observed by J. J. Thompson in 1893 [*Loeb*, 1965]. Meek, Loeb and Raether further developed this theory [*Loeb and Meek*, 1940a, b; *Loeb*, 1965].

The concept of streamers is based on a mode of propagation: they are filamentary plasmas driven by their own space charge field. The dynamics of the streamer is mainly controlled by a high-field region called the *streamer head*. The head of the streamer is depicted as a crescent shape in the left panel of Figure I.2. In the head the net charge is high and positive or negative for a positive streamer or negative, respectively. The principle is that the high-field region is quickly enhanced by electrons that drift and amplify on the length scale of this region, in a kind of avalanche. In the case of positive streamers, they neutralize the positive charge zone and therefore the space charge electric field, but repeat the charge pattern a bit farther down by leaving the ions behind them during their drift. If the electrons are amplified enough to compensate the positive head of the streamer, then the streamer can propagate in a stable manner. Thus, the positive streamer propagates step-by-step in the direction of the ambient field, which is why the streamer is also called a *space charge wave*. For air at atmospheric pressure, the streamers propagate very fast: typically with velocity $\sim 10^8$ cm/s, that is one hundredth of the speed of light in the vacuum. The peak of electric field in the streamer head can reach 4-7 times the breakdown field E_k [e.g., see *Dhali and Williams*, 1987; *Liu*, 2006].

Therefore, the positive streamer moves in the reverse direction of the electrons. Then, it

needs electrons upstream its head to propgate. These electrons may come from the natural electron background, essentially due to natural radioactivity and cosmic rays, from a pre-ionization of the gas, for example due to previous discharges or photoionization by external source (UV lamps, etc). Furthermore, the high-field region is the place of very intense electron impact on neutral molecules which leads to ionization, excitation, or creation of active species. The molecules excited by the electron impact can relax to lower energy states by emitting photon radiation. A certain range of photons can themselves ionize neutral molecules by photoionization, which provide seed electrons ahead of the streamer. These electrons enter the high-field region and participate in its enhancement of electron density. The photoionization has been found to be essential for the positive streamers to propagate with the observed velocities. This physical phenomenon and its modeling will be extensively discussed in Chapter III.

For negative streamers, the principle of propagation is the same but the net charge in the head is negative and it propagates in the opposite direction of positive streamers, that is in the opposite direction of the electric field. Thus, electrons behind the streamer head participate in the local electron amplification in the high-field region. Pre-ionization and photoionization are then less important in the case of negative streamers. However, as for positive streamers, pre-ionization level and photoionization play important roles in their structures and guide streamer propagation [e.g., *Vitello et al.*, 1994].

For both streamer types, the forward-moving streamer head leaves behind quasi-neutral plasma, where the field is very low ($E \lesssim E_k$). This is often called the *streamer channel*, or streamer tail, and can be described as an ambipolar zone [e.g., *Hassouni et al.*, 2004].

I.2.2 Estimation of the propagation velocity

An electron which enters the streamer head ignites the avalanche at a time t, until the electron density, due to the amplification from this electron, reaches the positive ion density at a time $t + \delta t$. Assuming this amplification behaves like an avalanche for a constant field, one can estimate that the characteristic distance between the new created electrons neutralizing the streamer head and the new created ions left behind is α^{-1}, as for the classical avalanche (see previous section). The characteristic length of the streamer head is then $\delta l \sim \alpha(E_{\max})^{-1}$, where $E_{\max}$ is the maximum field in the streamer head. The characteristic time of ionization over such a characteristic length is precisely the ionization time: $\delta t \sim \nu_i(E_{\max})^{-1}$. Then one obtains a rough estimation of the propagation velocity V_s by writing:

$$V_s \sim \alpha(E_{\max})^{-1}\nu_i(E_{\max}) = v_e(E_{\max}) \tag{I.10}$$

We can find in results provided in [*Dhali and Williams*, 1987] that this approximation is quite accurate, given the simplicity of this relation. In fact, V_s calculated here is underestimated by less than one order of magnitude.

A more complete approximation has been derived in [*Dyakonov and Kachorovskii*, 1988], which presents a clear relation between the propagation velocity and the density far beyond the streamer head. One can consider that, as for an electrode with a tip radius R, the region around the streamer head with a substantial field has a size on the order of the streamer radius R. Moreover, it is well known that the ionization frequency is a function of the

electric field and saturates above a field E_s. *Dyakonov and Kachorovskii* [1988] concluded that the size of the substantial field region ($\sim R$) around the streamer head should be on the same order as the size of the region where substantial ionization takes place, for the streamer to have a stable propagation. Then, the field at the streamer head would be on the order of E_s, and then one has $\nu_i \sim \nu_i(E_s) \equiv \nu_{i,s}$ in this region. The increase of the electron density in the high field region stops when the repulsion of electrons is faster than the ionization, that is when the Maxwell time is on the order of the ionization time: $\tau_m \sim \nu_{i,s}^{-1}$ (see Section I.1.4). For the exponential growth of the electron density $n(t) = n_0 \exp(\nu_{i,s} t)$, where n_0 is the electron density far beyond the streamer head (e.g., due to photoionization), one finds that the characteristic time of the electron density growth is:

$$\tau \sim \nu_{i,s}^{-1} \log\left(\frac{\nu_{i,s}\epsilon_0}{q n_0 \mu_e}\right) \tag{I.11}$$

One sees that in these conditions the density in the streamer channel is:

$$n_c \sim n(t=\tau) = \frac{\nu_{i,s}\epsilon_0}{q\mu_e} \tag{I.12}$$

Thus, one obtains the streamer velocity:

$$V_s \sim \frac{R}{\tau} = \frac{R\nu_{i,s}}{\log(n_c/n_0)} \tag{I.13}$$

As a qualitative result, one sees that the smaller n_c/n_0 (keeping the other parameters as constants), the faster the streamer. In [*Dyakonov and Kachorovskii*, 1989] authors showed that their model (not restricted to Equation (I.13)) was in good agreement with [*Dhali and Williams*, 1987]. Note that a similar equation of the streamer propagation velocity was already provided by *Loeb* [1965], and that two other analytical models are provided in [*Kulikovsky*, 1998]. *Kulikovsky* [2000b] also proposed to replace R in (I.13) by the characteristic length of the absorption of photoionizing radiation. However, these models all contain at least one arbitrary parameter which is a priori not known (e.g., n_0 in (I.13)).

As for the calculation of the streamer velocity, a full and accurate investigation of the streamer properties is only possible by a more complete description than the existing analytical models, and due to the high non-linearity of the source terms and the transport coefficients, the numerical simulation is required.

I.3 Model formulation

I.3.1 Elements of kinetic theory

Kinetic theory aims at describing the motion of particles by one distribution function $f(\vec{r}, \vec{v}, t)$. The statistical meaning of the number $f(\vec{r}, \vec{v}, t)\mathrm{d}^3r\mathrm{d}^3v$ is the number of particles (electrons in our case) inside the phase-space volume $\mathrm{d}^3r\mathrm{d}^3v$ at $(\vec{r}, \vec{v})$ and at time t. On this basis one can define the density of particles:

$$n(\vec{r}, t) = \int f(\vec{r}, \vec{v}, t)\mathrm{d}^3v \tag{I.14}$$

and the mean velocity of the group of particles, also named the *fluid velocity*:

$$\vec{V}(\vec{r},t) = \langle\vec{v}\rangle_v \equiv \frac{1}{n(\vec{r},t)}\int \vec{v} f(\vec{r},\vec{v},t)\mathrm{d}^3v \tag{I.15}$$

In the same way, we can obtain the characteristic frequencies of collision from their cross sections, for example:

$$\nu(\vec{r},t) = N\langle\sigma\vec{v}\rangle_v = \frac{N}{n(\vec{r},t)}\int \sigma\vec{v} f(\vec{r},\vec{v},t)\mathrm{d}^3v \tag{I.16}$$

where N is the neutral molecule density and σ is the momentum transfer cross section.

The evolution of the distribution function is governed by the Boltzmann equation:

$$\frac{\partial f}{\partial t} + \vec{v}\cdot\vec{\nabla}_{\vec{r}} f + \frac{\vec{F}}{m}\cdot\vec{\nabla}_{\vec{v}} f = \left(\frac{\partial f}{\partial t}\right)_c \tag{I.17}$$

where $\vec{F}$ is the force exerted on the particles and $\left(\frac{\partial f}{\partial t}\right)_c$ accounts for the change in f due to collisions.

I.3.2 Fluid reduction

It is possible to obtain a very good description of the dynamics of particles by taking the first moments of Equation (I.17). However, the dynamics of moment v^k is coupled to the dynamics of moment v^{k+1}. It is then necessary to truncate the moment series at a finite stage. We will take the first two moments of (I.17). The first moment ($k = 0$) of the electron Boltzmann equation gives the *continuity equation*:

$$\frac{\partial n_e}{\partial t} + \vec{\nabla}\cdot(n_e\vec{V_e}) = G - L \tag{I.18}$$

where subscript "e" stands for "electrons". The functions G and L describe the creation rate and the loss rate for electrons, respectively. The second moment of the Boltzmann equation gives the conservation of momentum flux, also called the *Euler equation*:

$$\frac{\partial\vec{V_e}}{\partial t} + (\vec{V_e}\cdot\vec{\nabla})\vec{V_e} = -\frac{\vec{\nabla}P_e}{n_e m_e} + \frac{\langle\vec{F_e}\rangle_v}{m_e} - \nu\vec{V_e} \tag{I.19}$$

for a weakly ionized plasma where only electron-neutral collisions are taken into account. The quantity P_e in (I.19) is the electron pressure.

It is very interesting to see how we can simplify the Euler equation. First, the first term of the left-hand side of Equation (I.19) falls very quickly to zero, since the electron flow velocity $\vec{V_e}$ we consider here becomes stationnary on a time scale on the order of at most ν^{-1}, which is short compared to the propagation time scale of the streamer:

$$\frac{\partial V_e}{\partial t} \sim 0$$

Second, since the streamer proceeds as a fast ionization wave, one has in principle $V_s \gtrsim V_e$. The quantity $\delta l \sim \alpha^{-1}$ is the characteristic length of the flow. Therefore, $\nu \simeq 3\cdot10^{12}$ s^{-1} (see

Section I.1.1) is much greater than $V_e/\delta l \lesssim V_s\alpha \simeq 10^9$ s^{-1}, for $V_s \simeq 10^8$ cm/s and $\alpha \geq 10$ cm^{-1} (see previous discussion), and one gets:

$$\nu V_e = \frac{v_{th} V_e}{\lambda} \gg \frac{V_e^2}{\delta l} \sim |(\vec{V_e}\cdot\vec{\nabla})\vec{V_e}|$$

where λ is the mean free path of momentum transfer, and v_{th} is the usual thermal velocity of electrons. In fact, one has: $\frac{V_e^2}{\delta l} = \frac{V_e^2}{\lambda} K_n$, where $K_n = \lambda/\delta l$ is called the Knudsen number and characterizes whether the fluid is in molecular or continuous flow. In our case $\lambda \ll \delta l \Rightarrow K_n \ll 1$ and therefore the regime is continuous and the inertial term is neglected comparing to the friction force [*Rax*, 2005, Sec. 6.2.1]. Thus, from this short analysis one can neglect the left-hand side of Equation (I.19) and one obtains:

$$\vec{V_e} = -\frac{\vec{\nabla} P_e}{m_e n_e \nu} + \frac{\langle \vec{F_e}\rangle_v}{m_e \nu} \tag{I.20}$$

On time scale of electron flow larger than $(\delta\nu)^{-1}$, one can consider the electrons as a locally isothermal fluid, and thus assume $P_e = n_e k T_e$. This leads to the relation for the fluid velocity:

$$\vec{V_e} = -\frac{kT_e}{m_e\nu}\frac{\vec{\nabla} n_e}{n_e} + \frac{\langle \vec{F_e}\rangle_v}{m_e\nu} = -D_e\frac{\vec{\nabla} n_e}{n_e} + \mu_e\frac{\langle \vec{F_e}\rangle_v}{q} \tag{I.21}$$

This equation closes the system of moments of the Boltzmann equation. Note that although we focused on the motion of electrons, positive ions can be treated in a similar fashion.

I.3.3 Lorentz force and magnetic field

As the electric field due to the streamer head varies very quickly in the reference frame of the experimentalist, one can ask if the induced magnetic field has a role in governing streamer propagation in an external constant Laplacian electric field. The magnetic field is governed by the Maxwell-Ampère Equation:

$$\vec{\nabla}\times\vec{B} = \mu_0 q n_e \vec{V_e} + \mu_0\epsilon_0\frac{\partial\vec{E}}{\partial t} \tag{I.22}$$

where $\vec{B}$ is the magnetic field, and μ_0 is the permeability of free space. Now, let us make an approximate analysis to see under what conditions one can neglect the magnetic field.

We consider the characteristic length scale δl to be on the order of the size of the streamer head radius. We saw in Section I.2.2 that in the streamer dynamics this length scale can be linked to the time scale $\delta t \simeq \nu_{i,max}^{-1}\log(n_c/n_0)$. Thus, one can approximate the terms of left and right sides of Equation (I.22) as:

$$|\vec{\nabla}\times\vec{B}| \sim \frac{B}{\delta l} \qquad \text{and} \qquad \mu_0 q n_e |\vec{V_e}| + \mu_0\epsilon_0\left|\frac{\partial\vec{E}}{\partial t}\right| \sim \frac{q n_e \mu_e E}{\epsilon_0 c^2} + \frac{1}{c^2}\frac{E}{\delta t}$$

where we used the relation $\epsilon_0\mu_0 c^2 = 1$, with c being the speed of light in free space. We therefore obtain the approximation[2] for B:

$$B \sim \frac{q n_e \mu_e E \delta l}{\epsilon_0 c^2} + \frac{1}{c^2}\frac{E\delta l}{\delta t} \tag{I.23}$$

[2]Because of the triangle inequality, B is actually overestimated in the Equation (I.23).

We see that the Maxwell time (I.9) appears in Equation (I.23):

$$B \sim \left(\frac{1}{\tau_m} + \frac{1}{\delta t}\right)\frac{\delta l}{c^2}E \tag{I.24}$$

Besides, we saw in Section I.1.4 and I.2.2 that the Maxwell time becomes comparable to the ionization time $\tau_m \sim \nu_{i,max}^{-1}$ in the streamer head. The electron density in the streamer channel is much greater than that ahead of the streamer. Therefore $n_c/n_0 \gg 1$, and even if this factor is in the logarithm ($\log(n_c/n_0) \simeq 10$ typically in our studies), one can consider that $\delta t^{-1} \simeq \nu_{i,max}/\log(n_c/n_0)$ is negligible compared to τ_m^{-1}. Moreover, according to (I.13) one has the streamer velocity $V_s \sim \delta l/\delta t$. Therefore, one obtains:

$$B \sim \frac{\delta l}{c^2\tau_m}E = \frac{\delta l}{\delta t}\frac{\log(n_c/n_0)}{c^2}E = \frac{V_s}{c^2}\log(n_c/n_0) \tag{I.25}$$

The electron fluid is subject to the *mean* Lorentz force:

$$\langle\vec{F}\rangle_v = q(\vec{E} + \vec{V_e}\times\vec{B}) \sim q\vec{E} + q\frac{V_e V_s}{c^2}\log(n_c/n_0)E\vec{u}_m \tag{I.26}$$

where $\vec{u}_m = \frac{\vec{V_e}\times\vec{B}}{|\vec{V_e}\times\vec{B}|}$. We know that at most, the mean velocity of the electron fluid is $V_e \lesssim V_s$ in the streamer head:

$$q|\vec{V_e}\times\vec{B}| \lesssim q\frac{V_s^2}{c^2}\log(n_c/n_0)E$$

And since $V_s \ll c$ (in air at atmospheric pressure $V_s/c \simeq 1/100$), one has:

$$\langle\vec{F}\rangle_v \sim q\vec{E} \tag{I.27}$$

Thus, the motion of the electron fluid is only subjected to the electrostatic force, and this is the approximation we will employ in the rest of this work. Note that the streamer model we present in Section I.4 does not prevent the streamer velocities from reaching and exceeding the speed of light [see *Liu and Pasko*, 2004, Sec. 4.3]. However, the streamers we will study have a much lower velocity than light in vacuum.

I.3.4 Diffusion coefficient

The analysis made in section I.3.2 to obtain Equation (I.21) is not general. Indeed, we assumed that the problem was perfectly isotropic and that D_e was a scalar. Generally, this is not true in the presence of high density gradients and if the collision frequency for momentum transfer depends on electron energy [*Parker and Lowke*, 1969]. Typically for electrons, ν increases with energy which leads to a slowing down of these electrons. In the presence of high density gradients, the mean energy of electrons going down through the gradient in the opposite direction of the field is not compensated by the less numerous electrons passing in the other direction. These energetic electrons encounter a greater friction force due to the increase in collision frequency. On a mesoscopic scale, this behavior is equivalent to a reduction of the coefficient of diffusion in the direction of the field $D_\parallel$ compared to that of diffusion in the transverse direction $D_\perp$. At most, $D_\parallel$ and $D_\perp$ differ by a factor of 2 [*Raizer*, 1991, Sec 2.4.4, p. 23]. In the streamers we study here, the gradients of electron density are not high enough for electron diffusion to significantly affect the streamer dynamics, which is principally governed by the electron drift and source terms. Thus, these differences in the diffusion coefficients are considered to be negligible, and we take $D_\parallel = D_\perp = D_e$.

I.3.5 Local field approximation

As is very often the case in the literature, we will assume that the *local field approximation* is valid in our study. This approximation implies that local equilibrium of electrons is achieved instantaneously in time in response to the electric field $\vec{E}$. This allows us to express all the transport coefficients and source terms as explicit functions of the norm of the local reduced electric field E/N. This is the case when the time scales of variations of the electric field and electron density are long compared to the time scale of energy relaxation, and this approximation is not always valid in the streamer head. Several approaches have been taken to examine the differences due to the nonlocality in streamers. The first one consists of taking nonequilibrium into account by adding additional moments of the Boltzmann equation to increase the accuracy of the fluid description [*Kunhardt et al.*, 1988]. In [*Guo and Wu*, 1993] an equation of the energy balance appears naturally, and therefore the mean energy of electrons is used in the ionization coefficient as part of streamer simulations (positive and negative) for nitrogen at atmospheric pressure. The effects of nonlocality on positive streamers in air at atmospheric pressure were studied by *Naidis* [1997], who corrected the electron source term rates calculated with the local field approximation following the work of [*Aleksandrov and Kochetov*, 1996]. Deviations from the local field approximation were studied for negative streamers in nitrogen at atmospheric pressure by [*Li et al.*, 2007] by means of a comparison between 1D fluid and particle models. By taking into account the nonlocal effects, all of these authors found an increase of the ionization in the streamer head, a resulting increase of the electric field and a small increase of the streamer velocity.

However, these discrepancies are far smaller than an order of magnitude. For example, *Li et al.* [2007] found a relative difference between the fluid and the particle models of $\sim$10% and $\sim$20% in the ionization level behind the streamer front for homogeneous applied electric fields of 50 kV/cm and 100 kV/cm, respectively. For practical accuracy, one can obtain the main streamer characteristics by a fluid model [*Naidis*, 1997]. Furthermore, recently *Chanrion and Neubert* [2008] used a PIC code to solve the Boltzmann equation and a Monte Carlo simulation to simulate collisions, in the framework of streamer simulations in the Earth's atmosphere as applicable to sprite discharges. These authors found an excellent agreement with results obtained by a fluid model by *Liu and Pasko* [2004] (a comparison of our results with this work will be presented in Chapter III) both for positive and negative streamers. This agreement is surprisingly good, as noted by the authors themselves, especially given the discrepancies in the modeling of the photoionization and of course in the local field approximation used in [*Liu and Pasko*, 2004] but not in [*Chanrion and Neubert*, 2008]. We will thus also assume that the local field approximation is valid in the following section.

I.4 Streamer equations

From the previous sections of this chapter, one can derive the most common and effective model to study the dynamics of streamers based on the following drift-diffusion equations for electrons and ions coupled with Poisson's equation [e.g., *Kulikovsky*, 1997b]:

$$\frac{\partial n_e}{\partial t} + \vec{\nabla}\cdot(n_e\vec{v_e}) - \vec{\nabla}\cdot(D_e\vec{\nabla}n_e) = S_{\text{ph}} + S_e^+ - S_e^- \tag{I.28}$$

$$\frac{\partial n_p}{\partial t} + \vec{\nabla}\cdot(n_p \vec{v_p}) = S_{\text{ph}} + S_p^+ - S_p^- \tag{I.29}$$

$$\frac{\partial n_n}{\partial t} + \vec{\nabla}\cdot(n_n \vec{v_n}) = S_n^+ - S_n^- \tag{I.30}$$

$$\vec{\nabla}^2 V = -\frac{q}{\epsilon_0}(n_p - n_n - n_e) \tag{I.31}$$

where subscripts "e", "p" and "n", respectively, refer to electrons, positive and negative ions, n_i is the number density of species i, V is the potential, $\vec{v_e}$ is the drift velocity of electrons, D_i and μ_i are respectively the diffusion coefficient and the absolute value of mobility of species i, q is the absolute value of electron charge, and ϵ_0 is permittivity of free space. The S^+ and S^- terms stand for the rates of production and loss of charged particles. They will be taken with the following general form:

$$S_e^+ = S_p^+ = n_e \alpha v_e \tag{I.32}$$
$$S_n^+ = n_e \beta_{\text{att}} v_e \tag{I.33}$$
$$S_e^- = n_e \beta_{\text{att}} v_e + n_e n_p \beta_{ep} \tag{I.34}$$
$$S_p^- = n_e n_p \beta_{ep} + n_n n_p \beta_{np} \tag{I.35}$$
$$S_n^- = n_n n_p \beta_{np} \tag{I.36}$$

where β_{att} accounts for the electron attachment on neutral molecules, β_{ep} accounts for the electron-positive ion recombination, and β_{np} accounts for the negative-positive ion recombination. In the present study, the S_e^+ and S_p^+ production rates are the ionization rate due to the electron impact ionization of air molecules. The origin of the coefficient sets we use will be indicated each time, as needed.

The S_{ph} term is the rate of electron-ion pair production due to photoionization in a gas volume. For photoionization calculations in the streamer model, we employed techniques discussed in Chapter III. Specifically, for the present study we have implemented the three-group Eddington and SP_3, the three-exponential Helmholtz, and the Zheleznyak classical integral models [*Ségur et al.*, 2006; *Bourdon et al.*, 2007; *Zheleznyak et al.*, 1982].

The coefficients of the model are assumed to be explicit functions of the local reduced electric field E/N, where E is the electric field magnitude and N is the neutral density of air (see Section I.3.5).

As a rough approximation, one can consider that the characteristic length of the variation of electron and ion densities in the streamer head is on the order of α^{-1} (see Section I.2.2). One notes $\vec{v}_{\text{diff}_i} = -D_i \vec{\nabla} n_i / n_i$ the "diffusion velocity" of ions (positive or negative). Using the Einstein relation (I.3) it then follows that $v_{\text{diff}_i}/v_i = D_i |\vec{\nabla} n_i| / (n_i v_i) \sim D_i \alpha / (\mu_i E_{\max}) = kT_i \alpha / (q E_{\max}) \simeq 10^{-2}$, since the ion temperature is roughly the ambient temperature, using $E_{\max} \simeq 150$ kV/cm and by taking α from [*Morrow and Lowke*, 1997] (e.g., see Section II.3). The density gradients are even weaker in the streamer channel and before the streamer head. Thus, in all cases we present in this Ph.D. thesis, the diffusion of ions will be neglected. A similar analysis for an electron thermal energy of $\sim$1 eV shows that the electron diffusion is mostly negligible compared to the drift velocity of the electrons.

In this report, axisymmetric streamers are studied and thus cylindrical coordinates are used.

The computational models used for solving the drift-diffusion equations as well as for Poisson's equation are described in Chapter II.

Chapter II

Numerical models

Table of Contents

II.1 Poisson's equation

For streamer simulations, the electric field is a key parameter for two reasons. First, the transport parameters and source terms have a non-linear dependence on it. Second, the electric field is directly related to charged species densities (I.31). In streamer simulations, the electric field is derived from the electric potential given by Poisson's equation. A small error in the calculation of the electric potential leads to large fluctuations in the electric field, which may lead to considerable errors in the simulation results. Thus, it is important to solve Poisson's equation accurately. Moreover, we show in Chapter III that techniques similar to those we use for solution of Poisson's equation are also used for the modeling of the photoionization source term.

Three important points have to be considered for the numerical solution of Poisson's equation:

- The discretization scheme: it defines the numerical accuracy of the resolution of Poisson's equation. The discretization we use is derived in Section II.1.1.
- The boundary conditions: as an elliptic equation, the resolution of Poisson's equation requires the boundary conditions to be set. It is especially important in the case of Laplace's equation where the solution is entirely governed by the boundary conditions. We discuss this point in Section II.1.2, and we present in detail the calculation of boundary conditions for two configurations studied in this work.
- The numerical method used: the resolution of Poisson's equation can be very time consuming. For this reason, one has to find the most efficient solver for each new configuration under study. Some solvers are iterative, and some are direct. In the present work, both are used and we will briefly present them and compare them in Section II.1.3.

II.1.1 Discretization

In cylindrical coordinates, Equation (I.31) can be written as:

$$\frac{\partial}{\partial x}\left(\frac{\partial V}{\partial x}\right)+\frac{1}{r}\frac{\partial}{\partial r}\left(r\frac{\partial V}{\partial r}\right)=-\frac{\rho(x,r)}{\epsilon_0} \tag{II.1}$$

where x and r are axial and radial coordinates, respectively, and $\rho = q(n_p - n_n - n_e)$. In this work, we consider that the computational domain is discretized on a rectilinear grid. The nodes of the grid are indexed with i and j in the axial and radial directions respectively,

such that $V_{i,j} = V(x_i, r_j)$. The edges of the cell indexed (i, j) are located by $x_{i\pm1/2}$ and $r_{j\pm1/2}$, in the axial and radial direction, respectively (see Figure II.6).

In the volume of the computational domain (i.e., far from the boundaries) the second order discretization of Eq. (II.1) in cylindrical coordinates gives the classical five diagonal linear system:

$$V^{\mathrm{e}}_{i,j}V_{i+1,j} + V^{\mathrm{w}}_{i,j}V_{i-1,j} + V^{\mathrm{s}}_{i,j}V_{i,j-1} + V^{\mathrm{n}}_{i,j}V_{i,j+1} + V^{\mathrm{c}}_{i,j}V_{i,j} = -\frac{\rho_{i,j}}{\epsilon_0} \tag{II.2}$$

with:

$$\begin{cases} V^{\mathrm{e}}_{i,j} &= \dfrac{1}{\Delta x_i(x_{i+1/2} - x_{i-1/2})} \\ V^{\mathrm{w}}_{i,j} &= \dfrac{1}{\Delta x_{i-1}(x_{i+1/2} - x_{i-1/2})} \\ V^{\mathrm{n}}_{i,j} &= \dfrac{r_{j+1/2}}{\Delta r_j \left(\frac{r^2_{j+1/2} - r^2_{j-1/2}}{2}\right)} \\ V^{\mathrm{s}}_{i,j} &= \dfrac{r_{j-1/2}}{\Delta r_{j-1} \left(\frac{r^2_{j+1/2} - r^2_{j-1/2}}{2}\right)} \\ V^{\mathrm{c}}_{i,j} &= -(V^{\mathrm{w}}_{i,j} + V^{\mathrm{e}}_{i,j} + V^{\mathrm{s}}_{i,j} + V^{\mathrm{n}}_{i,j}) \end{cases} \tag{II.3}$$

where $\Delta x_i = x_{i+1} - x_i$ and $\Delta r_j = r_{j+1} - r_j$. In this work, we have used this second order discretization of Poisson's equation because it is sufficiently accurate and robust for the cases we have considered.

II.1.2 Boundary conditions

Different sets of boundary conditions are used for Poisson's equation, depending on the problem studied. In this work, we have considered discharges propagating between two electrodes (plane-to-plane, point-to-plane and point-to-point). For metallic electrodes, the potential is fixed on the electrodes, and in Chapter IV we will present how to impose this boundary condition for an electrode of complex shape in a rectilinear mesh. The case of boundary conditions in presence of a dielectric material will be addressed in Chapter VI. In this work, we have only considered axisymmetric geometries, and thus a symmetry condition is used on the axis of symmetry.

In this section, we present the calculation of boundary conditions for two different cases that we have extensively studied for streamer simulations. In the first one, shown in Figure II.1, a strong homogeneous electric field (i.e., greater than E_k everywhere in the simulation domain) is applied externaly. In order to simulate streamer propagation in a weak electric field (i.e., less than E_k), the second case shown in Figure II.2 consists of a narrow high-field region generated by a spherical electrode placed in a weak and originally homogeneous electric field. In this test case the spherical electrode is considered to be outside of the simulation domain.

In streamer simulations, computational domains are usually large in the radial directions and therefore, the electric potential at the boundary $r = R$ is specified by neglecting contributions from the charges inside the domain since they occupy a relatively small space. Two different types of boundary conditions can be used at the boundary $r = R$. The homogeneous Neumann boundary condition ($\vec{\nabla}V \cdot \vec{n} = 0$, $\vec{n}$ being the normal vector of the surface boundary), and the Dirichlet boundary condition based on the solution of Laplace's equation (i.e., $\rho = 0$ in Equations (I.31) and (II.1)).

If one wants to use a computational domain with a smaller radial extension, the influence of charges inside the domain has to be considered. In this case, It is possible to compute directly the Dirichlet boundary conditions from a Laplacian potential and to add the influence of the charges on the boundaries from the integral solution of Equation (II.1). This approach is very time-consuming as each node of the boundary requires an integration of the charge densities over the whole simulation domain. Therefore, we have carried out some tests to try to find a compromise on the size of the computational domain between:

- a computational domain with a large radial extension, for which the resolution of equations in the volume of the computational domain (e.g., drift-diffusion equations) is very time consuming,
- a computational domain with a small radial extension, for which the computation of boundary conditions for Poisson's equation is very time consuming.

We have observed that the least time-consuming way for a given accuracy and for configurations presented in this Chapter is to work with a computational domain with a small radial extension and the integral solution of Poisson's equation for boundary conditions. We present the detailed calculation of these boundary conditions for the cases presented in Figures II.1 and II.2.

External homogeneous electric field

Figure II.1 shows the computational domain immersed in a homogeneous electric field virtually generated by two infinite planar electrodes. The general solution of Equation (I.31) can be written as:

$$V(\vec{r}) = V_L(\vec{r}) + \frac{1}{4\pi\epsilon_0} \iiint_{\Omega'} \frac{\rho(\vec{r}\,')}{|\vec{r} - \vec{r}\,'|} \mathrm{d}\Omega' \tag{II.4}$$

where $\vec{r}$ is the position vector (x, r) (from the origin point $(0, 0)$ in Figures II.1 and II.2), Ω' is the volume of the computational domain, and V_L is the Laplacian part of the electric potential, that is $\vec{\nabla}^2 V_L = 0$. In the case of an external homogeneous field E_0 in the axial direction Ox, one has:

$$V_L(x, r) = -E_0 x + C \tag{II.5}$$

where C is an arbitrary constant. Equation (II.4) is used to calculate the potential at the boundaries of the domain. Inside the simulation domain, the electric potential is calculated based on the numerical solution of the discretized form of Poisson's equation (Equation (II.2)). The different numerical methods used will be discussed in Section II.1.3.

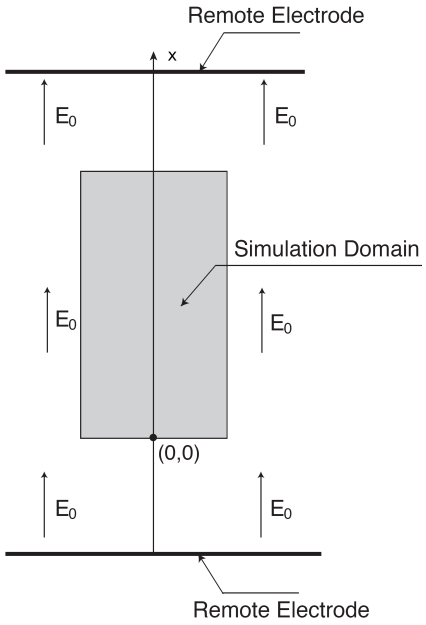

Figure II.1: Representation of the simulation domain in a homogeneous electric field generated by two infinite planar electrodes [*Liu and Pasko*, 2004].

Field generated by a spherical electrode placed in an weak external homogeneous electric field

Figure II.2 shows a representation of the computational domain and the virtual electrodes used. A potential V_0 is applied to the conducting sphere, which is put into an originally homogeneous electric field virtually established by two remote plane electrodes placed very far from the sphere.

This test case was initially proposed for streamer simulations by [*Babaeva and Naidis*, 1996]. It enables the study of the ignition of a streamer in the high field region close to the sphere and the propagation of the streamer in a homogeneous weak electric field. The interest of this test case is its geometric simplicity, since the spherical electrode is not included in the computational domain. In Figure II.2, we note that there is only one point of contact between the sphere and the computational domain.

Because of the layout of charges on the spherical electrode under application of a homogeneous field, the Laplacian component of the electric potential becomes [*Durand*, 1966b, p. 202]:

$$V_L(x,r) = \frac{V_0 b}{d_s} - E_0 \left[1 - \left(\frac{b}{d_s}\right)^3\right](x+b) \tag{II.6}$$

where $d_s = \sqrt{(b+z)^2 + r^2}$ is the distance between the sphere center and the observation point (x,r), V_0 is the potential of the spherical electrode, and b is the sphere radius (see Figure II.2). Furthermore, if one considers each cell of the simulation grid as a point charge, it becomes possible to take into account the influence of the corresponding *image charge* in the sphere on the electric potential in the simulation domain[1]. In this case Equation (II.4)

[1]The image method introduces point charges inside the spherical electrode in order to keep the electric

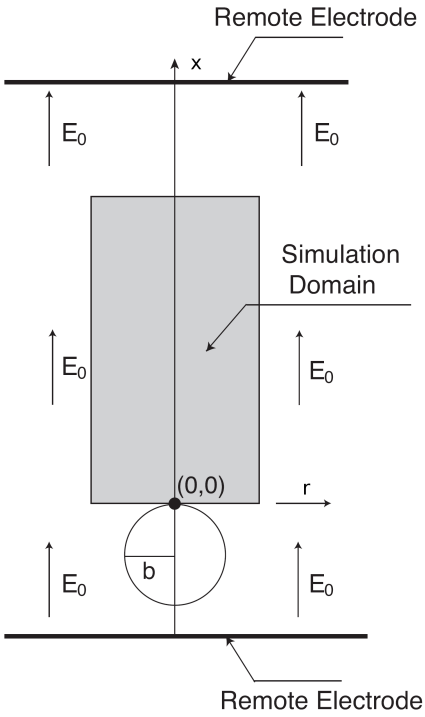

Figure II.2: Representation of the simulation domain where the electrical field is generated by a spherical electrode in a homogeneous electric field [*Liu and Pasko*, 2006].

becomes:

$$V(\vec{r}) = V_L(\vec{r}) + \frac{1}{4\pi\epsilon_0}\iiint_{\Omega'}\frac{\rho(\vec{r}\,')}{|\vec{r}-\vec{r}\,'|}\mathrm{d}\Omega' + \frac{1}{4\pi\epsilon_0}\iiint_{\Omega'}\frac{\rho_i(\rho(\vec{r}\,'))}{|\vec{r}-\vec{r}_i(\vec{r}\,')|}\mathrm{d}\Omega' \tag{II.7}$$

where $V_L(\vec{r})$ is defined by Equation (II.6) and ρ_i is a virtual charge density accounting for the influence of the image charges. One has [*Durand*, 1966b; *Liu*, 2006]:

$$\rho_i(\rho(\vec{r}\,')) = -\frac{b}{d_s}\rho(\vec{r}\,') \tag{II.8}$$

$$\vec{r}_i(\vec{r}\,') = \frac{b^2}{d_s^2}(\vec{r}\,' + b\vec{u_x}) - b\vec{u_x} \tag{II.9}$$

where $\vec{u}_x$ is the unit vector of the x-axis. As for Equation (II.4), the integrals in Equation (II.7) are only computed on the boundaries of the simulation domain.

Elliptic integral approach

The calculation of the integrals in Equations (II.4) and (II.7) is very time-consuming. Therefore, we have carried out some tests to compare different numerical methods for computing them, namely, by Gaussian quadrature, Romberg's method and an elliptic integral approach [these methods were taken from *Press et al.*, 1992]. For studies presented in this work, the most efficient numerical method is the elliptic integral approach [*Liu and Pasko*, 2006].

potential as a constant V_0 on its surface.

As the model is cylindrically symmetric, one can integrate over the volume of the simulation domain using elementary rings of radius r' at axial position x', corresponding to an individual grid node, around the axis of symmetry. Thus, the elementary potential at the observation point $\vec{r}$ due to this infinitesimal ring is:

$$dV(x,r;x',r') = \frac{1}{4\pi\epsilon_0}\rho(x',r')r'\mathrm{d}r'\mathrm{d}x' \int_0^{2\pi} \frac{\mathrm{d}\phi}{\sqrt{r^2+r'^2+(x-x')^2-2rr'\cos\phi}} \tag{II.10}$$

where ϕ is the azimuthal angle (see Fig. III.1(a)). By making the substitution $\phi = \pi + 2\beta$, one obtains:

$$dV(x,r;x',r') = \frac{\rho(x',r')r'\mathrm{d}r'\mathrm{d}x'}{\pi\epsilon_0\sqrt{(r+r')^2+(x-x')^2}}\,\mathcal{K}(k(x,r;x',r')) \tag{II.11}$$

where $\mathcal{K}(k) = \int_0^{2\pi}(1-k^2\sin^2\beta)^{1/2}\mathrm{d}\beta$ is the complete elliptic integral of the first kind, and $k(x,r;x',r') = \frac{4rr'}{(r+r')^2+(x-x')^2}$. Note that the denominator in Equation (II.11) is always non-zero, since we used a simulation grid with cell interfaces at $r = 0$ or $z = 0$ instead of grid nodes (see Section II.2.1).

The above method can also be applied to the image part of Equation (II.7). The numerical method we used to compute $\mathcal{K}(k)$ is taken from [*Press et al.*, 1992] and based on the Carlson's function R_F [*Carlson*, 1977]. The integration over x' and r' is performed using the trapezoidal integration.

II.1.3 Numerical methods for solving Poisson's equation

In streamer simulations, the discretized form of Poisson's equation (II.2) inside the computational domain is usually solved using the symmetrical successive overrelaxation (SOR) method. This method has been widely used because it is simple to implement and robust. However, the SOR method is well-known to converge rather slowly. To reduce computation times, we have used the D03EBF module of the NAG Fortran library (`http://www.nag.co.uk`) in this work, which is based on the iterative Strongly Implicit Procedure [*Stone*, 1968]. This method converges more rapidly than the SOR method for the same accuracy.

Recently, different efficient direct solvers (e.g., MUMPS [*Amestoy et al.*, 2000, 2001, 2006] and the SuperLU solver [*Demmel et al.*, 1999a, b] (`http://crd.lbl.gov/~xiaoye/SuperLU/`)) have been developed for large systems of linear equations and can be applied to solve Poisson's equation. As part of the preparatory work for the studies presented in this thesis, we have conducted several test runs to compare the results obtained using the iterative NAG module and the direct SuperLU solver. Both solvers have very good performances. The main asset of SuperLU is its accuracy, but its main drawback is the consumption of memory and the speed of the *LU* factorization. On the other hand, the main asset of the NAG routine is that, as an iterative solver, it is faster to converge from previous solutions than through a direct matrix inversion, even when using a moving mesh. However, its main drawback is that it takes a few iterations to converge at each timestep, and moreover, it is difficult to estimate *a priori* its accuracy for a given set of convergence criteria in each studied configuration.

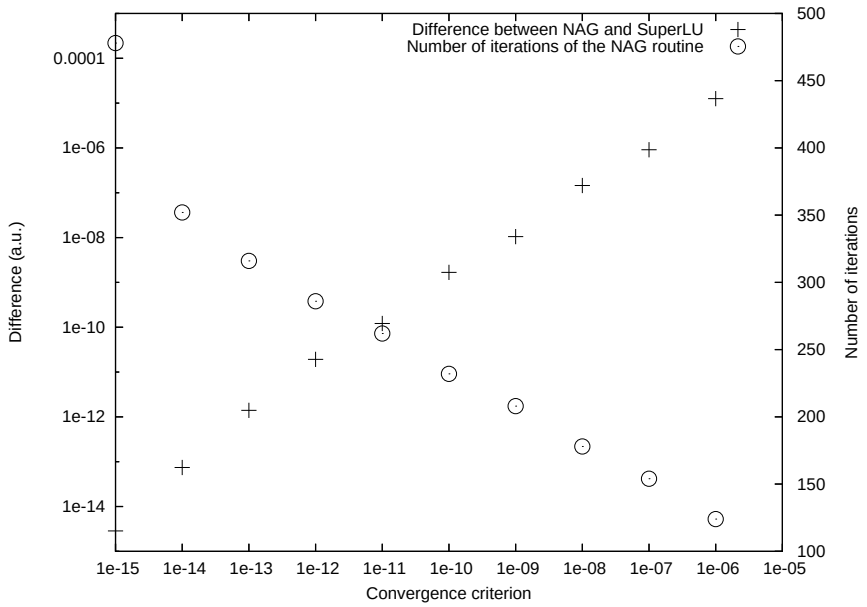

Figure II.3: Maximum difference between results given by the iterative NAG solver and by SuperLU, as well as the number of iterations of the NAG solver, both as a function of one convergence criterion.

For the sake of brevity, we present here only one example among all the different comparison tests done. In this example, the simulation domain is $[0,1] \times [0,1]$ (arbitrary units), discretized on a 41×41 Cartesian grid. We take a source term on the right hand side of Poisson's equation, such that the corresponding solution of Poisson's equation is a Lorentzian function centered in the middle of the domain. The maximum of the Lorentzian function is 10 (a.u.) with a half width at half maximum of $10^{-3/2}$ (a.u.). The iterative NAG solver is initialized with zero potential in the overall domain. Figure II.3 shows the maximum difference between results obtained using the iterative NAG solver and the direct SuperLU solver, and the number of iterations of the NAG solver, as a function of one convergence criterion of the NAG routine. This convergence criterion is defined as the maximum absolute value of the change made to the elements of the matrix at each iteration. Details on the convergence criterion can be found in the D03EBF - NAG Fortran Library Routine Document.

We have noted that the maximum difference between the result given by SuperLU and the analytical solution (the Lorentzian function used) is $2 \cdot 10^{-15}$ (a.u.). Figure II.3 clearly shows that the precision of the iterative solver is always less than that of SuperLU. However, one notes that the results of the iterative solver become closer to those obtained with SuperLU when the convergence criterion is reduced. However, this involves an increase in the number of iterations. Note that the number of iterations obtained for a convergence criterion of 10^{-15} seems to deviate from the general trend. At this point, the required precision is close to the accuracy of representation of double precision numbers. This means that any

arithmetic operation suffers a large rounding error and causes poor convergence[2]. We note that for a convergence criterion of 10^{-16}, the iterative solver never converges.

Thus, as part of the preparatory work for further simulations, we have conducted several test runs in streamer simulations to compare the results obtained using the iterative NAG module and the direct SuperLU solver. It turned out that there are only minor changes in the streamer dynamics computed using these two solvers. Direct solvers are inherently very accurate and robust. Furthermore, for the case of a fixed grid, the most time-consuming step in the calculation of the solution (i.e., the factorization) needs to be done only once at the beginning of the discharge simulation. Then, at each timestep of the discharge simulation, the calculation of the solution for different source terms (i.e., term on the right hand side of Equation (II.1)) is fast.

In the following sections and chapters, we use either the SuperLU or the NAG routine, depending on the context and their time consumption in a given configuration. Using two different solvers is useful for demonstrating the accuracy of the results for each new external configuration (e.g., electrode geometry). Furthermore, we can cross-check the two solvers to ensure that a particular streamer effect does not results from an inaccurate computation of the electric potential.

II.2 Numerical resolution of the drift-diffusion equations

Many problems arise in connection with solution of drift-diffusion equations (I.28)–(I.30) applied to streamer simulations. It is important to note that most of these problems are related to the great spatial variations of densities of charged species. For example, Figures II.4 and II.5 show the evolution of the densities of electrons, positive ions and net charge densities for negative and positive streamer heads. Thus, to solve the drift-diffusion equations applied to streamer simulations, a suitable numerical method has to comply with two requirements: a sufficient accuracy for exact description of the density gradients and positivity of densities. As discussed for example in [*Godunov*, 1959], it is difficult to satisfy both constraints.

In this section, first, we present the finite volume method applied to the drift-diffusion equations, and then we discuss the advantages and limitations of three numerical schemes used in the literature for streamer simulations. Finally, in Section II.3 we compare the performance of these three schemes on the simulation of a positive streamer.

II.2.1 Finite volume methods

Finite volume methods are based on the integral formulation of the partial differential equations to be solved. By construction, these methods guarantee the conservation of the transported physical quantity [*Ferziger and Peric*, 2002]. For streamer simulations, this property is essential because it is particularly important to conserve the charge during the whole streamer simulation. In finite volume (or control volume) methods, the domain is

[2]Private communications with Zdenek Bonaventura.

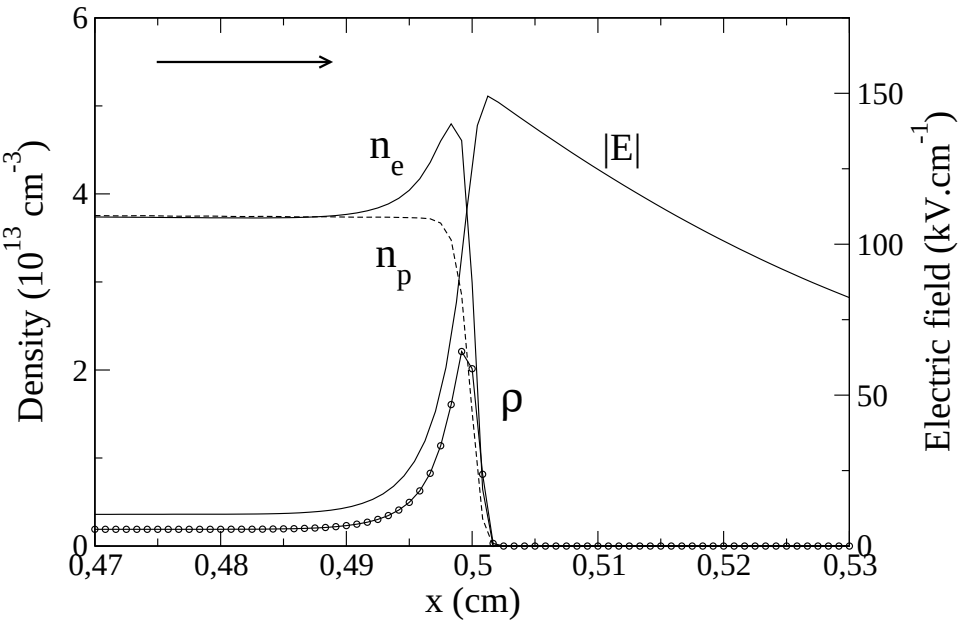

Figure II.4: Structure of a negative streamer front: absolute value of the electric field $|E|$, electron density n_e, positive ion density n_p and absolute net charge density $\rho = |n_p - n_e|$. The arrow points in the propagation direction. Simulations are performed for a 1 cm gap in nitrogen at atmospheric pressure [*Bessières*, 2006].

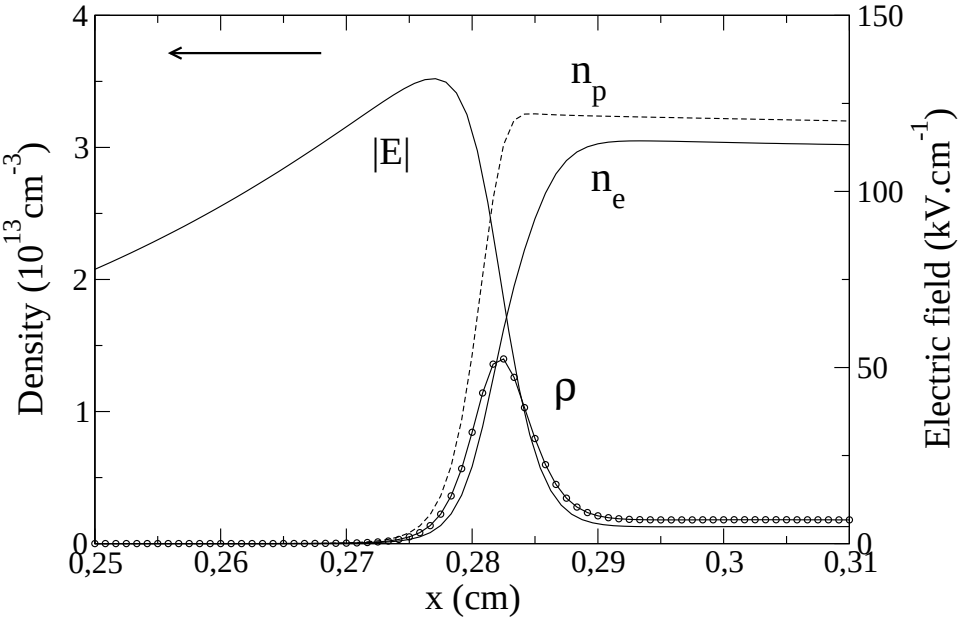

Figure II.5: Same caption as figure II.4 for a positive streamer front [*Bessières*, 2006].

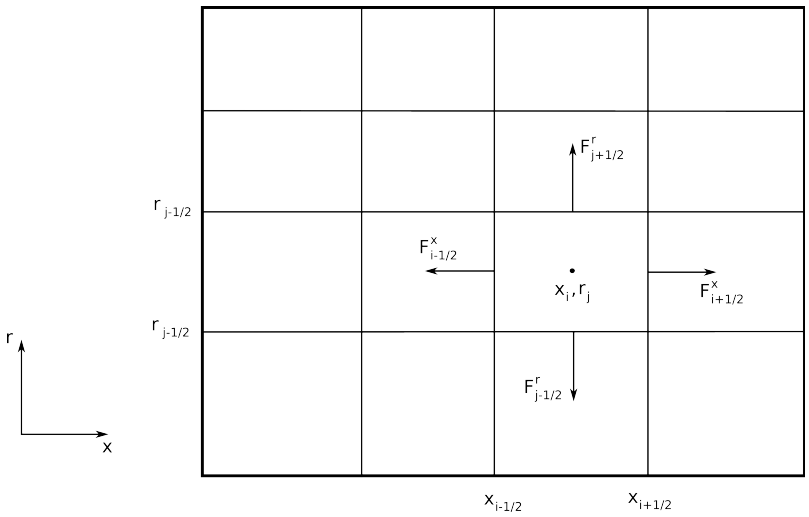

Figure II.6: Representation of the numerical grid. Control volumes are referenced by their centers and are defined by their edges between $x_{i-1/2}$ and $x_{i+1/2}$, and between $r_{j-1/2}$ and $r_{j+1/2}$. The arrows represent the outward unit normal vectors of the boundaries of the cell (i, j).

subdivided into a finite number of small control volumes by a grid. In this work we use only structured grids. For this type of grid one can work either with the *nodes centered* in control volumes (see Figure II.6) or with the *faces centered* between nodes [*Ferziger and Peric*, 2002]. Both approaches have their own advantages, and in the present work we have used node-centered grids, as they are used more frequently in the literature [*Ferziger and Peric*, 2002].

We present now the finite volume method for the case of Equation (I.28). As stated by Equation (I.18), the conservation law for electron is:

$$\frac{\partial n_e}{\partial t} + \vec{\nabla} \cdot n_e \vec{V_e} = G - L \tag{II.12}$$

The basic principle of the finite volume method is to maintain the conservative property of Equation (II.12) in every volume element. Therefore Equation (II.12) is integrated over the volume element $\Omega_{i,j}$ of the cell (i, j) (see Figure II.6) and becomes:

$$\frac{\partial}{\partial t}\bar{n}_{i,j} + \frac{1}{\Omega_{i,j}} \int_{\Omega_{i,j}} \vec{\nabla} \cdot n_e \vec{V_e} \, \mathrm{d}\Omega = \frac{1}{\Omega_{i,j}} \int_{\Omega_{i,j}} (G - L) \mathrm{d}\Omega \tag{II.13}$$

where we define $\bar{n}_{i,j}$ as the average of $n_e(x, r, t)$ over $\Omega_{i,j}$:

$$\bar{n}_{i,j} = \frac{1}{\Omega_{i,j}} \int_{\Omega_{i,j}} n_e(x, r, t) \mathrm{d}\Omega \tag{II.14}$$

Using the Gauss-Ostrogradsky theorem one obtains:

$$\frac{\partial}{\partial t}\bar{n}_{i,j} + \frac{1}{\Omega_{i,j}} \int_{\partial\Omega_{i,j}} n_e \vec{V_e} \cdot \vec{n} \, \mathrm{d}\Sigma = \frac{1}{\Omega_{i,j}} \int_{\Omega_{i,j}} (G - L) \mathrm{d}\Omega \tag{II.15}$$

where $\mathrm{d}\Sigma$ measures the infinitesimal surface of the cell boundaries, and $\vec{n}$ is the outward unit normal vector. Decomposing the surface integral on the edges of the cell shown in

Figure II.6, one obtains:

$$\frac{\partial}{\partial t}\bar{n}_{i,j} + \frac{1}{\Omega_{i,j}}(F^x_{i+1/2} + F^x_{i-1/2} + F^r_{j+1/2} + F^r_{j-1/2}) = \bar{S}_{i,j} \tag{II.16}$$

where we define the fluxes as

$$F^x_{i+1/2} = \int_{\Sigma_{i+1/2,j}} n_e \vec{V_e} \cdot \vec{n} \mathrm{d}\Sigma \simeq n_{i+1/2,j} V^x_{e_{i+1/2,j}} \Sigma_{i+1/2,j} \tag{II.17}$$

where the surface of the cell boundary $\Sigma_{i+1/2,j}$ is located at $(i+1/2, j)$, and $\bar{S}_{i,j}$ is the average of source and loss terms over the volume $\Omega_{i,j}$.

To calculate the exact change of the density $\bar{n}_{i,j}$ over an elementary time step $\Delta t = t^{k+1} - t^k$, we integrate the equation (II.16) from t^k to t^{k+1}:

$$\bar{n}^{k+1}_{i,j} = \bar{n}^k_{i,j} - \frac{1}{\Omega_{i,j}} \int_{t^k}^{t^{k+1}} (F^x_{i+1/2} + F^x_{i-1/2} + F^r_{j+1/2} + F^r_{j+1/2}) \mathrm{d}t + \int_{t^k}^{t^{k+1}} \bar{S}_{i,j} \mathrm{d}t \tag{II.18}$$

where $\bar{n}^{k+1}_{i,j}$ is the value of the mean density inside the control volume $\Omega_{i,j}$ at the end of a time step. This equation is the conservative form of Equation (II.16). Indeed, if all the fluxes are equal to zero in a control volume, Equation (II.18) shows that the change of density inside the control volume is only due to volume source and loss terms.

It is important to note that no approximation has been made in deriving Equation (II.18). In order to solve this equation numerically, it is necessary to express the different fluxes and source terms on the right-hand side part of the equation. It is interesting to point out that the fluxes in Equation (II.18) account for both drift and diffusion fluxes. We will first consider the fluxes are constant during time step Δt and simplify Equation (II.18):

$$\bar{n}^{k+1}_{i,j} = \bar{n}^k_{i,j} - \frac{\Delta t}{\Omega_{i,j}} (F^{x,k}_{i+1/2} + F^{x,k}_{i-1/2} + F^{r,k}_{j+1/2} + F^{r,k}_{j+1/2}) + \int_{t^k}^{t^{k+1}} \bar{S}_{i,j} \mathrm{d}t \tag{II.19}$$

The main problem in solving Equation (II.19) concerns the determination of fluxes at the interfaces of the control volume. Indeed, as shown by Equation (II.17), these fluxes only strictly depend on the (unknown) values of the densities at the interfaces and not on the (known) mean value of the density $\bar{n}_{i,j}$ inside the control volume. Thus, the difficulty is to express the different fluxes as approximate functions of $\bar{n}_{i,j}$. In the following section, we will present the approximate expressions of drift fluxes for the three different schemes used in this work:

- The upwind scheme.
- A Flux-Corrected Transport method.
- The modified Scharfetter-Gummel scheme.

It is interesting to note that diffusion fluxes are calculated simultaneously with drift fluxes in the modified Scharfetter-Gummel scheme. For other schemes, diffusion and drift fluxes are calculated separately, and we present the method used to calculate diffusion fluxes in these cases. Finally, in the following section, we will present and discuss different methods for the time integration and the integration of the source term on the right-hand side of Equation (II.16).

II.2.2 Numerical schemes for drift-diffusion fluxes

In this section, the source term in Equation (II.19) is assumed to be equal to zero:

$$\bar{n}_{i,j}^{k+1} = \bar{n}_{i,j}^{k} - \frac{\Delta t}{\Omega_{i,j}}(F_{i+1/2}^{x,k} + F_{i-1/2}^{x,k} + F_{j+1/2}^{r,k} + F_{j+1/2}^{r,k}) \tag{II.20}$$

In cylindrical coordinates, the volumes $\Omega_{i,j}$ and the surfaces $\Sigma_{i+1/2,j}$ and $\Sigma_{i,j+1/2}$ are given by:

$$\Sigma_{i+1/2,j} = \pi(r_{i,j+1/2}^2 - r_{i,j-1/2}^2) \tag{II.21}$$

$$\Sigma_{i,j+1/2} = 2\pi r_{i,j+1/2}(z_{i+1/2,j} - z_{i-1/2,j}) \tag{II.22}$$

$$\Omega_{i,j} = \pi(r_{i,j+1/2}^2 - r_{i,j-1/2}^2)(z_{i+1/2,j} - z_{i-1/2,j}) \tag{II.23}$$

Upwind scheme for drift fluxes

The upwind scheme is the simplest numerical scheme. The basic idea of this scheme is to use the direction of the drift velocity to approximate the drift fluxes. The drift velocity field for charged particles can be easily derived at each time step from the calculation of the electric field. Then, for example in the axial direction, the drift fluxes are approximated as:

- $F_{i+1/2}^{x,k} = \bar{n}_{i,j}^{k} v_{e_{i+1/2,j}}^{x,k} \Sigma_{i+1/2,j}$, if $\vec{v}_{e_{i+1/2,j}}^{k} \cdot \vec{n}_i > 0$,
- $F_{i+1/2}^{x,k} = -\bar{n}_{i+1,j}^{k} v_{e_{i+1/2,j}}^{x,k} \Sigma_{i+1/2,j}$, if $\vec{v}_{e_{i+1/2,j}}^{k} \cdot \vec{n}_i < 0$.

where $v_e^{x,k}$ is the axial component of the drift velocity $\vec{v}_e$. A similar approximation is used in the radial direction.The upwind scheme is therefore very simple to implement and has the great advantage of being strictly positive. However, this first-order scheme is numerically diffusive [e.g., *Ferziger and Peric*, 2002].

This scheme has been used for streamer simulations, in particular in the work of the MIPT group in Russia [e.g., *Pancheshnyi et al.*, 2001, 2005].

Flux Corrected Transport method

To reduce the numerical diffusion and thereby increase the accuracy of the solution, different high order interpolation methods can be used to determine the drift fluxes at the cell interfaces. However, solutions by schemes of second order and higher, are not positive and these schemes generally present dispersion with spurious oscillations close to high gradient zones [e.g., *Ferziger and Peric*, 2002]. Different types of methods have been developed in the literature to reduce the spurious oscillations as much as possible and guarantee the positivity of the solution. The method of Flux Corrected Transport was developed in the 1970s [*Boris and Book*, 1973, 1976]. The basic idea of this method is to combine two numerical schemes. The first is strictly positive but diffusive (for example the upwind scheme), and the second

is a higher order, but dispersive scheme which is more accurate. In the FCT method, the solution obtained with the low-order diffusive scheme is corrected by antidiffusive fluxes calculated using the high-order scheme. However, as this scheme is dispersive, this may lead to oscillations in high gradient regions. Thus, the antidiffusive fluxes are limited in order to preserve the monotonicity of the solution. Different limiters have been developed in the literature for the FCT method [*Boris and Book*, 1973; *Zalesak*, 1979; *DeVore*, 1998]. In this work, we have used the 2D limiter proposed by *Zalesak* [1979], which appears to be a good compromise between efficiency and complexity of implementation.

The FCT method proposed by Boris and Book has been widely used in 1D and 2D discharge simulations ever since its first use by *Morrow* [1981]. In this work, we have used a slightly modified FCT method. We have developed an FCT method based on the first-order upwind scheme as the diffusive scheme, and for the high-order scheme we have used the third order QUICKEST scheme (Quadratic Upstream Interpolation for Convective Kinematics with Estimated Streaming Terms). The 1D third order QUICKEST scheme (also called QUICKEST3) was introduced by *Leonard* [1979]. It is based on a third order polynomial interpolation of the density at the interface of the cell. It is interesting to note that in the third order QUICKEST scheme, the time integration of the fluxes in equation (II.18) is carried out accurately [*Potin*, 2001; *Bessières*, 2006]. Usually, for other schemes, the simple approximation of Equation (II.19) is used. All the details on the third order QUICKEST scheme can be found in [*Leonard*, 1979] and are not repeated here for the sake of brevity. This scheme, associated with the universal limiter developed also by *Leonard* [1991], has been extensively compared with other schemes in [*Bessières*, 2006] on academic test cases and applied to different streamer simulations [*Bessières*, 2006; *Bessières et al.*, 2007].

It is important to note that the QUICKEST3 scheme with the universal limiter has been developed in 1D. The extension to 2D of the QUICKEST3 scheme with the universal limiter can be done easily by splitting the numerical treatment into two one-dimensional problems in the x and r directions, respectively. Leonard has developed a 2D numerical scheme called ENIGMATIC (Extended Numerical Integration for Genuinely Multidimensional Advective Transport Insuring Conservation) [*Leonard et al.*, 1995], although the implementation of the scheme and its 2D limiter for the purposes of streamer simulations is not straightforward.

In this work, we have used the QUICKEST3 in 1D, and we have combined it with a 1D upwind scheme to build a 2D FCT scheme based on the 2D limiter of *Zalesak* [1979].

Modified Scharfetter-Gummel scheme

The original Scharfetter-Gummel method was introduced in 1969 to obtain self-consistent numerical solutions for equations describing carrier transport, carrier generation, and space-charge balance in semiconductor devices [*Scharfetter and Gummel*, 1969]. This method is essentially a discretization scheme for variables in convection-dominated problems that employs an exponential fitting technique. One main advantage of this scheme is that it calculates drift and diffusion fluxes at the same time. The Scharfetter-Gummel method has the very important property of monotonicity, but it has been shown that this method is accurate only if the potential drop between to adjacent nodes is much less than the electron temperature [*Kulikovsky*, 1995a]. For problems in gas discharges, it is necessary to use fine grids to satisfy this condition, and therefore the computational cost becomes very

expensive. Therefore, to apply this scheme to gas discharges with reasonable computational times, *Boeuf and Pitchford* have developed an implicit variant of this sheme [*Boeuf and Pitchford*, 1991; *Fiala et al.*, 1994].

In 1995, *Kulikovsky* [1995a] proposed a modified version of the original explicit Scharfetter-Gummel method that improves the accuracy of the original scheme significantly without requiring the use of a fine grid. All the details on the scheme can be found in [*Kulikovsky*, 1995a] and are not repeated here for the sake of brevity. In this section, we present the main characteristics of the modified Scharfetter-Gummel, method and we discuss the different parameters we have made to implement it.

Kulikovsky's basic idea is to put a pair of virtual nodes, one on each side of the cell interface where the flux has to be calculated. The distance between these virtual nodes is chosen to be small enough to satisfy the condition for which the Scharfetter-Gummel method is accurate. Densities at virtual nodes are obtained using an interpolation of the density between two grid nodes. Then, based on the densities at the virtual nodes, the flux at the cell edge can be calculated accurately using the Scharfetter-Gummel scheme. It is interesting to note that in the original Scharfetter-Gummel method the electric field is assumed to be constant between the virtual nodes. Kulikovsky has proposed a more accurate approximation of the flux, in which the field is assumed to vary linearly between the virtual nodes. In [*Kulikovsky*, 1995a], it was shown that accounting for the linear field profile has a minor influence on the results obtained on a simplified test case. We have also observed this minor influence in streamer simulations, and used the constant electric field approximation (also called ISG0 in [*Kulikovsky*, 1995a]) in the streamer simulations presented in this work.

In the modified Scharfetter-Gummel scheme, the determination of the location of the virtual nodes is essential, and Kulikovsky has proposed a criterion with a constant factor ϵ which has to be selected. When ϵ changes from 0 to 1, the scheme transforms from a very accurate but dispersive one to a less accurate, diffuse but monotonic Scharfetter-Gummel algorithm. The actual value of this parameter should be chosen experimentally, and Kulikovsky suggests that a value of ϵ in the range $[0.01, 0.04]$ gives good results in most cases.

For the interpolation of the densities at the virtual nodes, *Kulikovsky* [1995a] has proposed two interpolation schemes: exponential and local cubic spline piecewise interpolation. After having checked both interpolations, and we have chosen to use the local cubic spline interpolation in this work.

It is important to note that the modified Scharfetter-Gummel scheme was developed in 1D. We have adapted it to 2D by splitting the numerical treatment into two one-dimensional problems in the x and r directions, respectively. To improve the accuracy of the splitting method, an alternation of the order between the x and r axes is used in two successive time steps.

The modified Scharfetter-Gummel scheme has been successfully applied to different 2D streamer simulations by *Kulikovsky* [e.g., 1995b, 1997a, b, 2000b, 2001] and also other authors [e.g., *Liu and Pasko*, 2004, 2006; *Liu*, 2006].

Diffusion fluxes

In the modified Scharfetter-Gummel scheme, diffusion and drift fluxes are calculated simultaneously. However, diffusion fluxes are usually calculated separately from drift fluxes and Equation (II.20) is thus splitted into two equations: one with drift fluxes and a second one with diffusion fluxes. This is for example the case for the upwind scheme or the FCT method. In this case, we have used a classical second-order central-difference scheme, representing the diffusion fluxes in the form:

$$F^{x,k}_{i+1/2} = D^k_{i+1/2,j} \frac{\bar{n}^k_{i,j} - \bar{n}^k_{i+1,j}}{x_{i+1,j} - x_{i,j}} \Sigma_{i+1/2,j} \tag{II.24}$$

$$F^{r,k}_{j+1/2} = D^k_{i,j+1/2} \frac{\bar{n}^k_{i,j} - \bar{n}^k_{i,j+1}}{r_{i,j+1} - r_{i,j}} \Sigma_{i,j+1/2} \tag{II.25}$$

II.2.3 Time integration

In this work, we have tested two different time integration methods for Equation (II.18).

- First approach: to obtain a second order scheme in time, we have developed a predictor-corrector scheme [*Ferziger and Peric*, 2002]. However, this approach is very time-consuming.
- Second approach: we have used a simple first-order Euler time integration for fluxes (Equation (II.19)) and the photoionization source term, and a fourth-order Runge-Kutta method [*Ferziger and Peric*, 2002] for the time integration of other source terms.

We have compared the results of both approaches and we found that to obtain the same accuracy of the results, it was less time consuming to use the second approach with a slightly smaller timestep than to use the predictor-corrector scheme. Therefore in this work, we have used this second approach.

Time step

We follow the approach discussed in [*Vitello et al.*, 1994] to define the time step for model execution. The time scales of relevance for selection of the time step providing model stability and accuracy are the Courant δt_c, effective ionization δt_I and dielectronic relaxation δt_D time scales (Maxwell time). The explicit expressions for δt_c, δt_I and δt_D can be found in [*Vitello et al.*, 1994]. The model time step is calculated as δt=min($A_c \delta t_c, A_I \delta t_I, A_D \delta t_D$) with A_c=0.5, A_I=0.05 and A_D=0.5. In practical streamer calculations the time step during the initial stage of streamer formation is almost always defined by the minimum value of the ionization time scale corresponding to the maximum field and the maximum ionization frequency $\nu_{i_{\max}}$ in the streamer head (δt_I=1/$\nu_{i_{\max}}$). We note that in our modeling, we adopt a small A_I value, which is a factor of two less than that used in [*Vitello et al.*, 1994]. It is interesting to note that during the stable streamer propagation phase the timestep is mostly controlled by the Maxwell time.

II.3 Numerical results

In this section, we compare the results obtained using the FCT method based on the upwind and QUICKEST3 schemes and Zalesak's limiter to the modified Scharfetter-Gummel and upwind schemes.

We consider the configuration described in Section II.1.2: a conducting sphere at a potential V_0 is placed in an originally homogeneous field. The simulation domain is discretized on a Cartesian grid with a cell size of $\Delta x = \Delta r = 6.2$ μm. The size of the domain is 1×0.125 cm^2. The electrode potential is set at $V_0 = 6500$ V, and the weak homogeneous external electric field throughout the domain is $E_0 = 10$ kV/cm.

As described in Figure II.2, the sphere is tangential to the computational domain at $x = 0$. At $t = 0$ a Gaussian spot of neutral plasma is placed initially in the high-field region, in the vicinity of the sphere. The initial electron and positive ion densities have a Gaussian shape:

$$n_e(x,r)|_{t=0} = n_p(x,r)|_{t=0} = n_0 \exp\left[-\frac{(x-2\sigma_x)^2}{\sigma_x^2} - \frac{r^2}{\sigma_r^2}\right] + n_{\text{back}} \tag{II.26}$$

where we have chosen $\sigma_x = \sigma_r = 0.01$ cm, and $n_0 = 10^{12}$ cm^{-3}. The negative ion density is initially taken to be zero. The transport coefficients and source terms are taken from formulations presented in [*Morrow and Lowke*, 1997].

For the simulation results presented in this section, the photoionization source term has been omitted and replaced with a fixed pre-ionized neutral background. The level of this pre-ionized background is fixed to $n_{\text{back}} = 10^9$ cm^{-3} to give results consistent with the ones obtained when the photoionization source term is included (see Appendix C for further details).

In the figures presented in this section, the spherical electrode is placed on the left (outside the simulation domain), and the positive streamer propagates in the $+x$ direction. As an example of the results obtained, Figures II.7 and II.8 show the cross-sectional views of the distributions of the electron density and the electric field at three moments in time, using the upwind scheme. Figure II.7 shows the evolution of the filamentary shape of the electron density in a neutral medium. Figure II.8 presents two main regions of the streamer: a crescent-shaped high-field region produced by the streamer head and a low field region behind the streamer head where the field is lower than the breakdown field, and which corresponds to the high electron density region (see Figure II.7) caused by streamer propagation.

Figures II.9 and II.10 present cross-sectional views of the distributions of the electron density and of the magnitude of the electric field, respectively, for the three different schemes at $t = 11.5$ ns. Figures II.11 and II.12 compare the corresponding profiles of the electron density and the magnitude of the electric field on the axis of symmetry of the computational domain (shown by white horizontal line in the cross-sectional figures).

We note that the results obtained by the FCT method and the modified Scharfetter-Gummel are very close. The streamer velocity is the same, as well as the electric field and the electron density profiles (see also Figures II.13 and II.14). Conversely, with the upwind scheme, the streamer velocity is much higher, with a higher electron density in the streamer head and

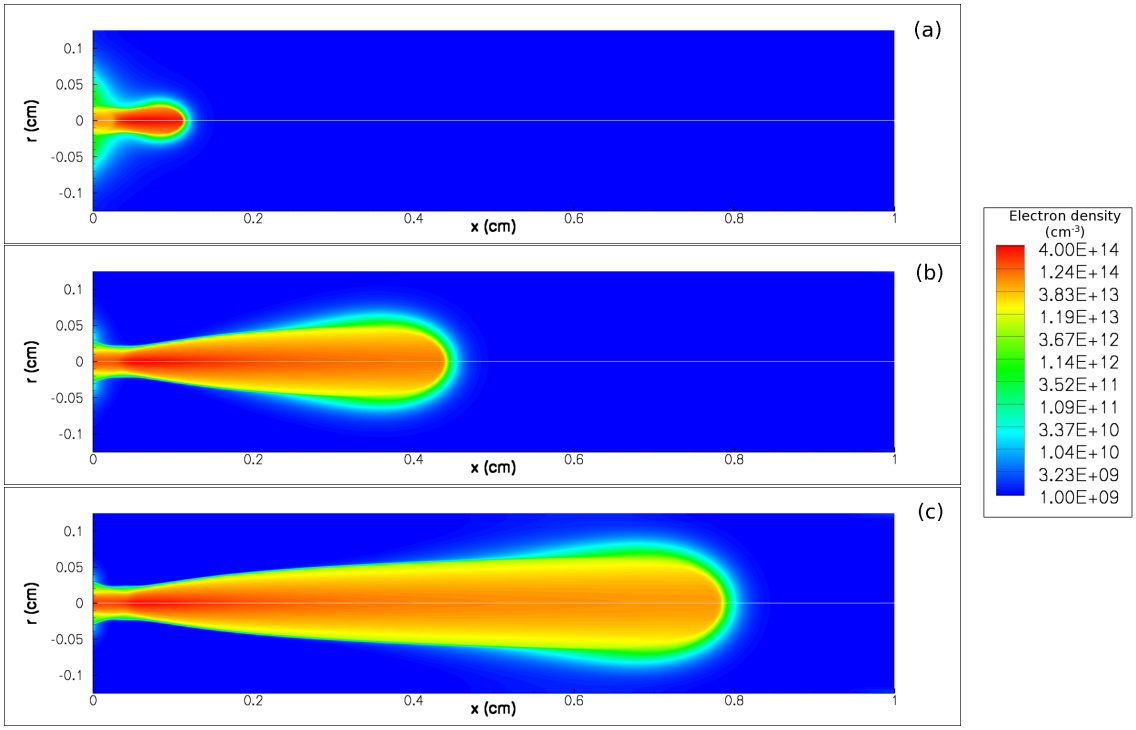

Figure II.7: Cross-sectional views of the distribution of the electron density at different times, computed using the upwind scheme. (a) $t = 2.5$ ns. (b) $t = 8.5$ ns. (c) $t = 14.5$ ns.

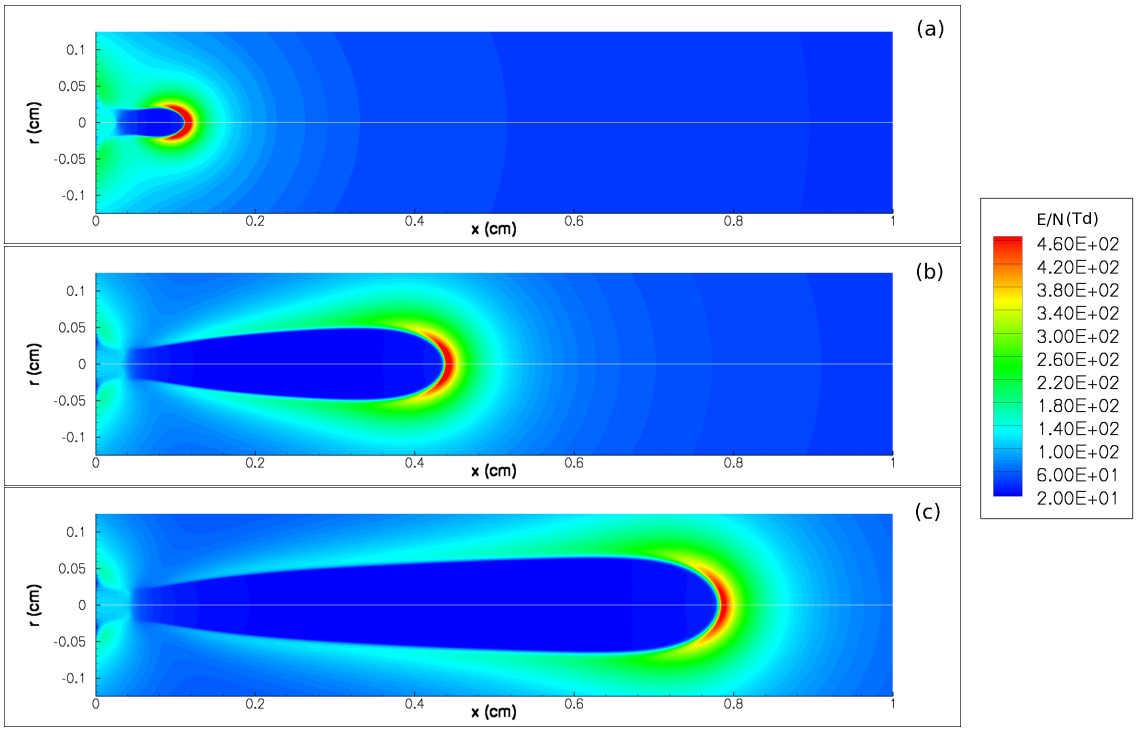

Figure II.8: Cross-sectional view of the distribution of the electric field at different times, computed using the upwind scheme. (a) $t = 2.5$ ns. (b) $t = 8.5$ ns. (c) $t = 14.5$ ns. (1 Td=10^{-17} V cm^2).

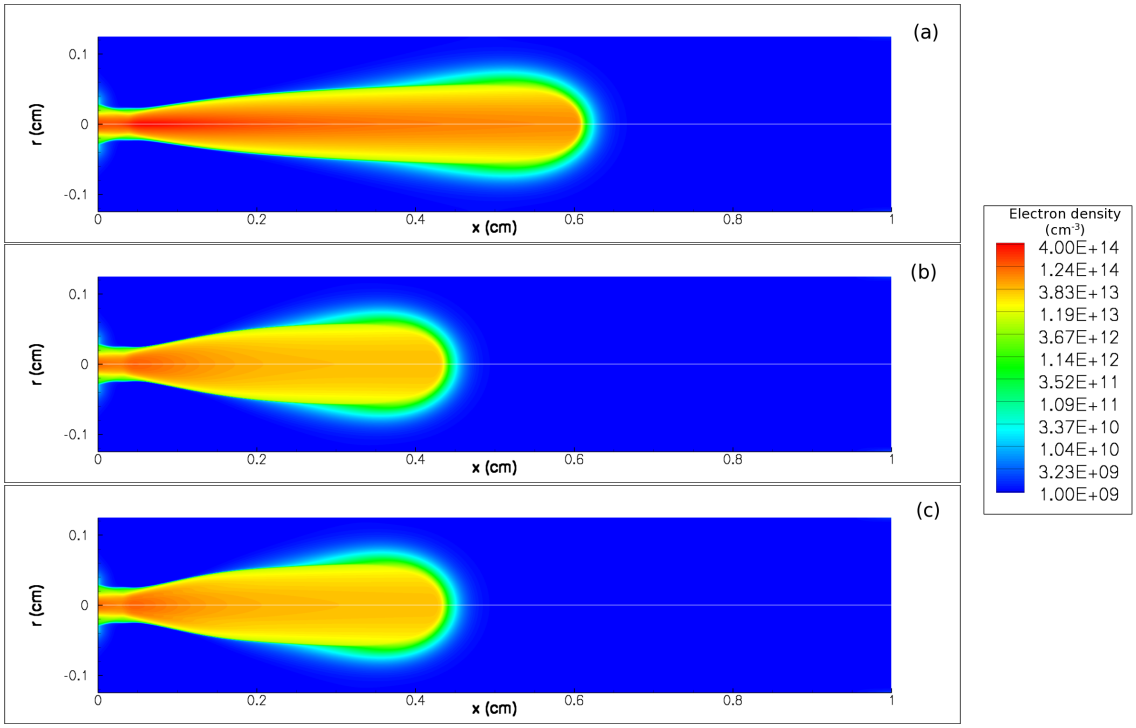

Figure II.9: Cross-sectional views of the distribution of the electron density at $t = 11.5$ ns: (a) computed using the upwind scheme; (b) computed using the FCT method based on the upwind and QUICKEST3 schemes and Zalesak's limiter; and (c) computed using the modified Scharfetter-Gummel scheme.

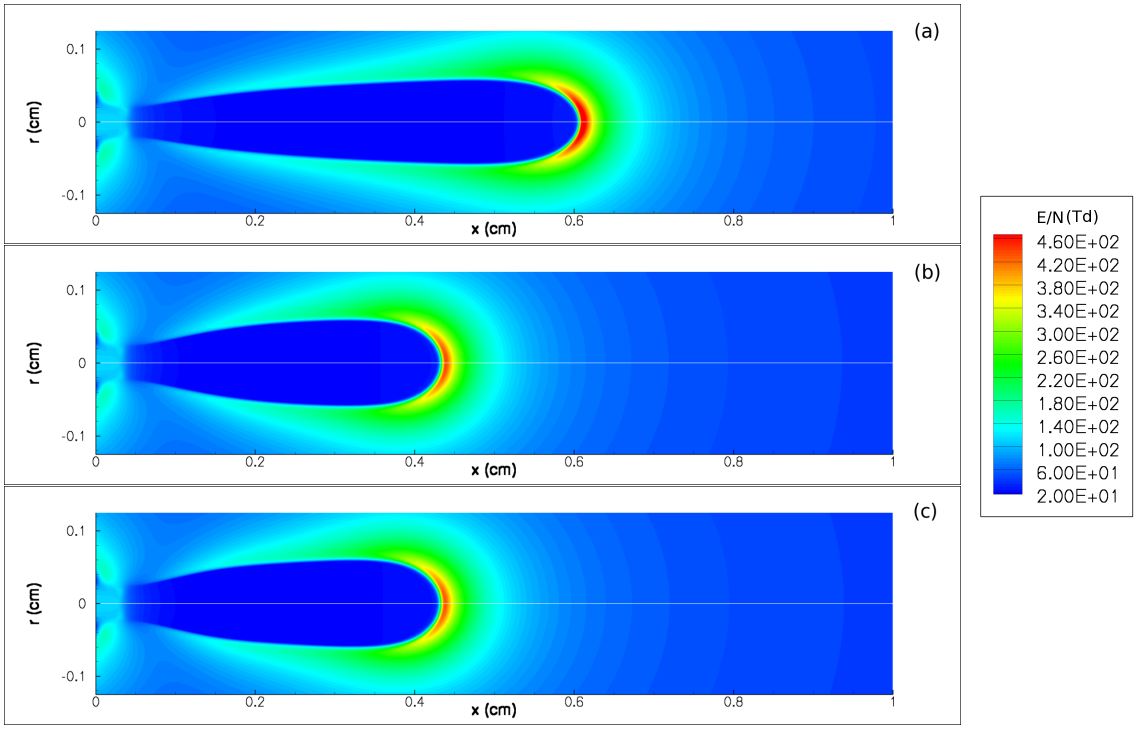

Figure II.10: Cross-sectional views of the distribution of the electric field at time $t = 11.5$ ns: (a) computed using the upwind scheme; (b) computed using the FCT method based on the upwind and QUICKEST3 schemes and Zalesak's limiter; and (c) is computed using the modified Scharfetter-Gummel scheme. (1 Td=10^{-17} V cm^2).

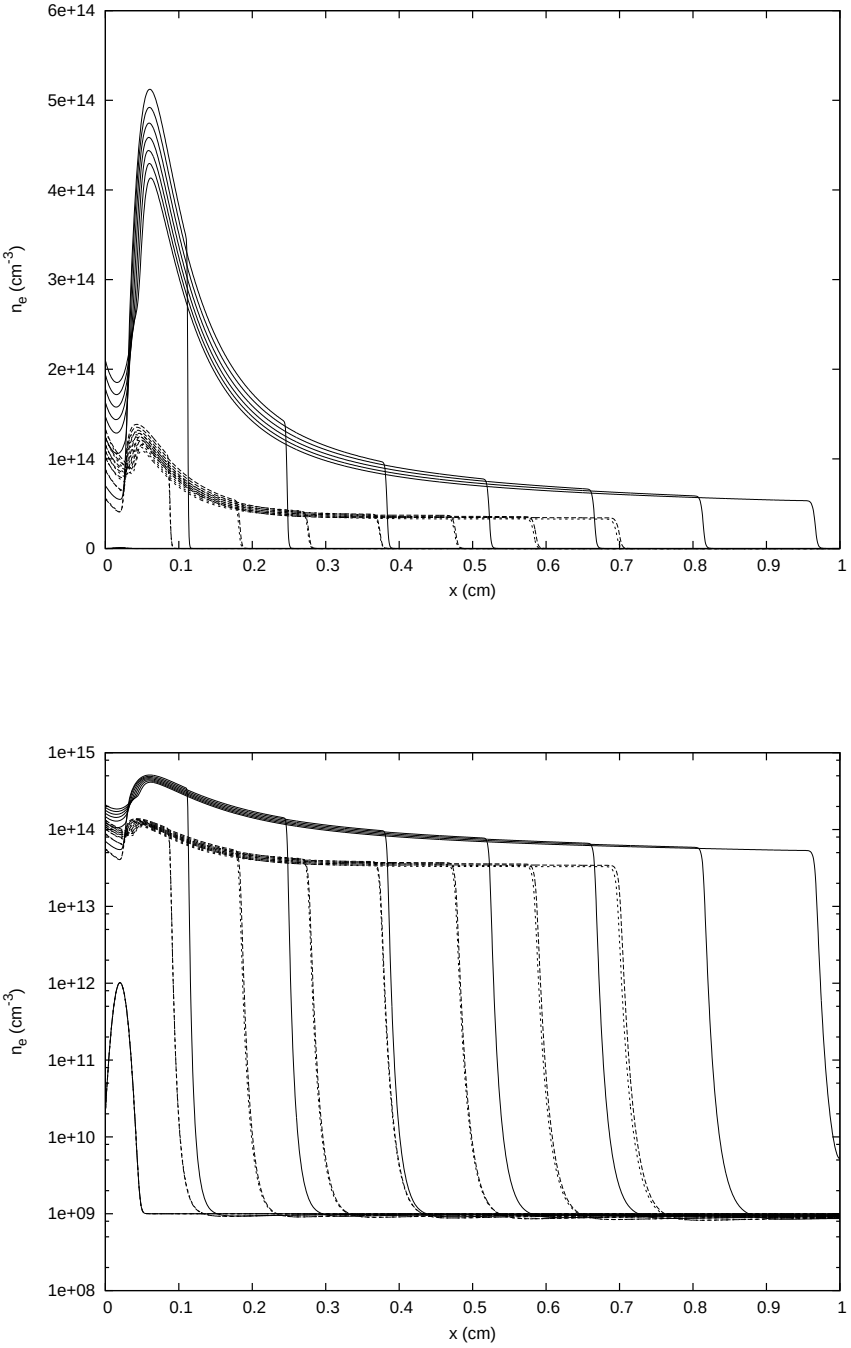

Figure II.11: Profiles of electron density on the axis of symmetry. The upper graph uses linear scale, and lower graph log scale. Solid line: results obtained with the upwind scheme. Dashed line: results obtained with the FCT method based on the upwind and QUICKEST3 schemes and Zalesak's limiter. Dotted line: results obtained with the modified Scharfetter-Gummel scheme. Results are shown from $t = 0$ to $t = 17.5$ ns, with a time step of 2.5 ns.

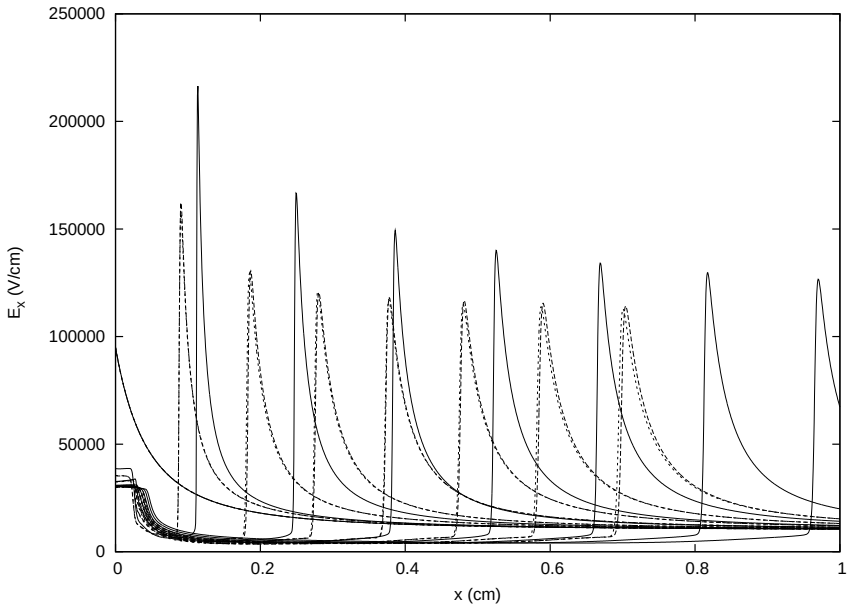

Figure II.12: Profiles of electric field on the axis of symmetry. Solid line: results obtained with the upwind scheme. Dashed line: results obtained with the FCT method based on the upwind and QUICKEST3 schemes and Zalesak's limiter. Dotted line: results obtained with the modified Scharfetter-Gummel scheme. Results are shown from $t = 0$ to $t = 17.5$ ns, with a time step of 2.5 ns.

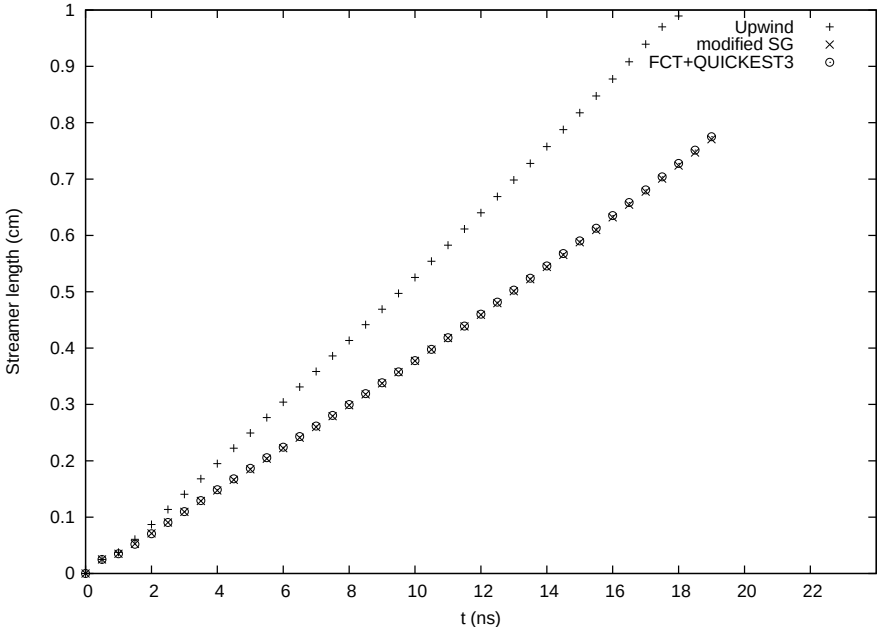

Figure II.13: Streamer length as a function of time.

in the channel (by a factor of 2 to 5 compared to the other schemes) and a higher maximum electric field (between 10% to 35% higher in comparison to other schemes).

Figure II.13 presents the streamer length as a function of the electric field. The streamer length is estimated using the maximum electric field in the streamer head as a reference. One observes that for the chosen parameters the streamer propagation is stable for the three schemes, that is the streamer velocity is almost constant.

From results presented in Figure II.11 we note that the characteristic length of variation of the electron density, as well as the charge layer size of the streamer head and the size of the zone where substantial ionization takes place is ∼0.007 cm. This is on the order of magnitude of $\alpha^{-1}(E_{\max}) \simeq 0.001$ cm [e.g., given by *Morrow and Lowke*, 1997], with $E_{\max} \simeq 114$ kV/cm taken from Figures II.10 and II.12 (for high-order schemes). This confirms the physical mechanisms considered in Chapter I.

The streamer radii calculated using the different schemes are in a good agreement at $t = 11.5$ ns. It is interesting to note that the radius of these simulated streamers is roughly 0.1 cm. In fact, this value corresponds quite well to the maximum radius of the avalanche $\alpha^{-1}(E_k)$ derived in Section I.1.4.

Furthermore, if we consider the electron density in the streamer channel given by Equation (I.12), we obtain $n_c \sim \epsilon_0 E_{\max} \alpha(E_{\max})/q \simeq 6 \cdot 10^{13}$ cm^{-3}. This value is in good agreement with the electron density value of $3 \cdot 10^{13}$ cm^{-3} found just behind the streamer head in the simulation results at $t = 17.5$ ns for high order schemes.

The accuracy of the results obtained with the upwind scheme can be increased by decreasing the cell-size of the grid. However, refining the numerical grid considerably increases the time required for the simulation. Furthermore, in this work, we have used fixed grids, and for the final studies presented in Chapters IV and VI we have to carry out simulations on computational domains of a few cm^2. The typical cell-size used in this work is on the order of $\Delta x = \Delta r = 5$ μm. Thus, to obtain results with good accuracy on such grids

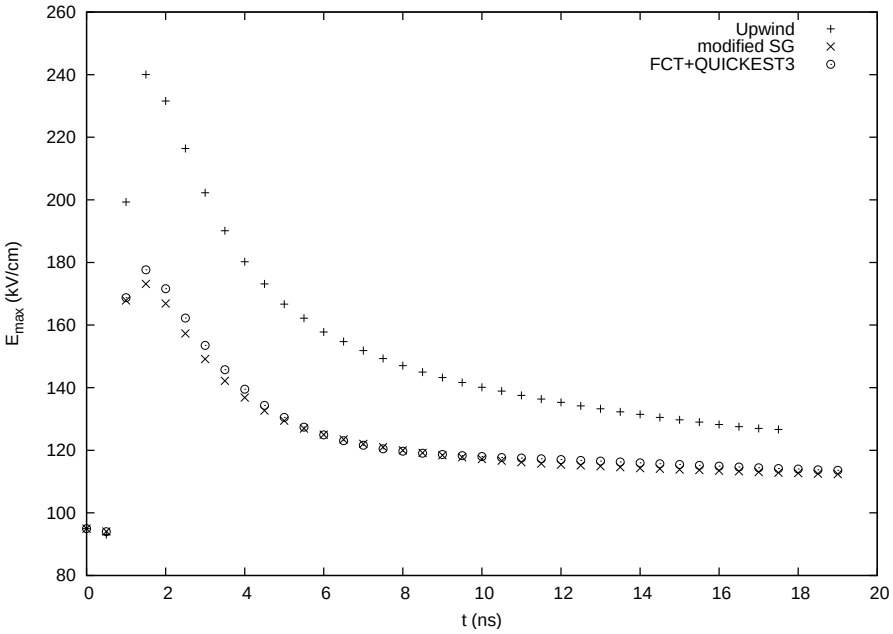

Figure II.14: Maximum electric field as a function of time.

in a reasonable time, all final results presented in this work have been obtained using the FCT method or the modified Scharfetter-Gummel scheme. As calculations with the upwind scheme are easy to perform, and as this scheme is strictly positive, we have nevertheless used this scheme as a development tool for preliminary simulations in each new configuration.

II.4 Conclusions

In this chapter we have presented the different numerical methods used in the present work. As the electric field is a key parameter in streamer simulations, it has to be calculated accurately, and therefore we have tested two different solvers for Poisson's equation. The first is an iterative solver based on a NAG library routine and the second, is a direct solver called SuperLU. Both provide very accurate solutions in all the configurations we tested and we have adopted both of them for the streamer simulations presented in this work. Note that these solvers are also used in the computation of the photoionization processes since the differential methods introduced for this purpose in Chapter III lead to sets of Helmholtz equations, which can be solved by essentially the same techniques as for Poisson's equation.

We have also discussed the calculation of boundary conditions for Laplace's and Poisson's equations, and we have presented them in detail for two configurations studied this work. The first produces a homogeneous Laplacian electric field permitting the study of the propagation of streamers of both polarities for strong applied electric fields greater than E_k. The second produces a strong electric field close to a spherical electrode in order to ignite a positive streamer but also generates a weak (less than E_k) homogeneous electric field allowing studies of streamer propagation in low fields.

We have also described in this chapter the numerical methods and schemes used to solve the drift-diffusion equations for charged species numerically. In this work, we have mainly used three different schemes: the first-order upwind scheme, the FCT method based on the

the upwind and QUICKEST3 schemes and Zalesak's limiter, and the modified Scharfetter-Gummel scheme. In the last section, we have compared the results obtained for a representative model case of propagation of a positive streamer with these three schemes, and we have demonstrated that the upwind scheme could significantly overestimate the streamer velocity, the electron density and the maximum electric field on grids with typical cell sizes on the order of 5 μm. We demonstrated that to calculate streamer propagation on such grids accurately, higher order schemes such as the FCT method and the modified Scharfetter-Gummel scheme are required. In this section we also demonstrated that some properties of the simulated positive streamer are in good agreement with simple physical models presented in Chapter I.

Chapter III

Photoionization model

Table of Contents

Some results of this chapter have been published in [*Bourdon et al.*, 2007] and in [*Liu et al.*, 2007].

III.1 Introduction

As stated in Chapter I, the presence of seed electrons in front of the propagating streamer head is believed to play a critical role for the propagation of streamers of both polarities. In some conditions these seed electrons are present in the gas, e.g., in repetitive discharges with a sufficiently high repetition rate, the gas can be efficiently pre-ionized by the previous discharge [e.g., *Pancheshnyi*, 2005; *Naidis*, 2006]. However, when the preionization of the gas is too low, the photoionization mechanism has been found to be essential to accurately model the streamer propagation, especially for positive streamers. According to *Kulikovsky* [2000a] the photoionization is responsible for the main dynamics of streamer propagation in low external field ($E < E_k$, with E_k the conventional breakdown field, see Section I.1.3). During early attempts of numerical simulations of streamers, the photoionization term was ignored and the pre-ionization needed for stable advancement of streamers of both polarities was provided by introducing a uniform neutral background ionization of the gas [e.g., *Dhali and Williams*, 1987; *Vitello et al.*, 1994]. *Pancheshnyi et al.* [2001] have compared the streamer discharge characteristics obtained using spatially uniform background pre-ionization level with those obtained with the full photoionization model in air. They found that although it is possible to obtain an agreement of some characteristics by varying the preionization level, the agreement cannot be reached for all the characteristics at a given pre-ionization level. In Appendix C, we present a method of determination of the preionization level based on the dynamics of the streamer head which gives the same propagation of a positive streamer in air in a weak field as the one obtained in taking into account the full photoionization model in air. However, it is important to note that for each new studied configuration, the *a priori* determination of the level of the background density is not obvious and therefore, it is necessary to take into account the photoionization source term in the simulations.

In a drift-diffusion approach to streamer modeling, the motion of electrons, ions and excited molecules is governed by continuity equations (I.28)-(I.30) coupled to Poisson's equation (I.31). The photoionization process is taken into account through a source term which is added to the continuity equations of electrons and ions. In the current literature, the photoionization term is usually calculated using integral models with coefficients based either on the classical experiments of *Penney and Hummert* [1970] and *Teich* [1967] [e.g., *Wu and Kunhardt*, 1988; *Kunhardt and Tzeng*, 1988; *Morrow and Lowke*, 1997], or on the description proposed by *Zheleznyak et al.* [1982] for air [e.g., *Babaeva and Naidis*, 1997; *Kulikovsky*, 2000a; *Pancheshnyi et al.*, 2001; *Liu and Pasko*, 2004, 2006]. The Zheleznyak photoionization model, discussed in the following section, has been formulated using classic

experimental data obtained at low pressure [*Penney and Hummert*, 1970; *Teich*, 1967]. However, this model agrees well with results of more recent experiments at atmospheric pressure [*Aints et al.*, 2008; *Naidis*, 2006, and references cited therein].

For the integral approach mentioned above, the calculation of the photoionization source term at a given point of the volume studied requires a quadrature over the complete volume of the discharge. Therefore, the calculation of the photoionization source term in streamer discharges is computationally expensive. To accelerate the simulation of streamers, different approximations have been proposed in the literature to reduce the computation time spent on calculation of the photoionization source term [*Kulikovsky*, 2000a; *Hallac et al.*, 2003; *Pancheshnyi et al.*, 2001]. *Kulikovsky* [2000a] proposed to confine the emitting volume of the photoionizing radiation to a small cylinder around the main axis of the discharge and to divide it into small rings. For a two-dimensional modeling of streamers assuming cylindrical symmetry, the effects of an emitting ring at a point of interest can be effectively characterized by their relative locations (described by a geometric factor in [*Kulikovsky*, 2000a]). This geometric factor only needs to be calculated once before the simulation for a specific computational geometry and can be repeatedly reused in the simulations. In [*Kulikovsky*, 2000a] and [*Hallac et al.*, 2003] photoionization is calculated on a coarse grid and interpolation is used to obtain needed values on the main grid. Finally, in [*Pancheshnyi et al.*, 2001] calculations are carried out in a small area around the streamer head. We note that all the approximate models reviewed above reduce the computation time to a certain degree but the accuracy of these models has not yet been rigorously evaluated and demonstrated in the existing literature.

Recently, two different approaches to calculate the photoionization term have been proposed to avoid the calculation of the global quadrature over the simulation domain. The first approach was tested a few years ago [*Djermoune et al.*, 1995a, b] and improved recently [*Ségur et al.*, 2006]. This method is based on the direct numerical solution of an improved Eddington approximation of the radiative transfer equation. The second approach has been proposed recently by *Luque et al.* [2007]. These authors proposed to approximate the absorption function of the gas in order to transform the integral expression of the photoionization term into a set of Helmholtz differential equations. In this chapter, we present and discuss these two approaches for the calculation of the photoionization term, and develop improved models based on the same principles by more accurately accounting for the spectral dependence of the photoionization. We also discuss the importance of accurate calculation of boundary conditions for the photoionization term and we introduce boundary conditions based on the integral Zheleznyak model and boundary conditions based on radiative transfer theory. The validity and range of applicability of the developed models for the photoionization term is demonstrated by performing direct comparisons of the results from these models and results obtained from the classic integral model of *Zheleznyak et al.* [1982]. First, specific validation comparisons are presented for a set of artificial sources of photoionizing radiation with different Gaussian dimensions. Then, we present validation comparisons for the development of a double-headed streamer in a high electric field ($>E_k$) at ground pressure and for the positive streamer propagation in weak external electric fields ($<E_k$) at ground pressure, i.e., conditions which are of great interest for practical applications.

III.2 Classical integral model for photoionization in air

In the widely used model derived by Zheleznyak *et al.* [*Zheleznyak et al.*, 1982; *Liu and Pasko*, 2004; *Naidis*, 2006] for photoionization in air, the photoionization rate at point of observation $\vec{r}$ due to source points emitting photoionizing UV photons at $\vec{r}\,'$ is

$$S_{\rm ph}(\vec{r}) = \iiint_{V'} \frac{I(\vec{r}\,')g(R)}{4\pi R^2} {\rm d}V' \tag{III.1}$$

where $R{=}|\vec{r}-\vec{r}\,'|$. In this model, to simplify calculations, the production of photons is assumed to be proportional to the ionization production rate S_i, and then $I(\vec{r})$ is given by:

$$I(\vec{r}) = \xi \frac{n_u(\vec{r})}{\tau_u} = \frac{p_q}{p+p_q}\, \xi \frac{\nu_u}{\nu_i} S_i(\vec{r}) \tag{III.2}$$

where ξ is the photoionization efficiency, $n_u(\vec{r})$ is the density of the radiative excited species u, the ratio $\frac{p_q}{p+p_q}$ is a quenching factor, τ_u is the lifetime of the excited state u only accounting for the effects of spontaneous emission (i.e., $\tau_u{=}\frac{1}{A_u}$, where A_u is the Einstein coefficient), ν_u is the electron impact excitation frequency for level u, and $S_i = \nu_i n_e$, where n_e is the electron density and ν_i is the ionization frequency. The function $g(R)$ in (III.1) is defined by

$$\frac{g(R)}{p_{\rm O_2}} = \frac{\exp(-\chi_{\rm min} p_{\rm O_2} R) - \exp(-\chi_{\rm max} p_{\rm O_2} R)}{p_{\rm O_2} R \, \ln(\chi_{\rm max}/\chi_{\rm min})} \tag{III.3}$$

where $\chi_{min} = 0.035$ Torr^{-1} cm^{-1}, $\chi_{max} = 2$ Torr^{-1} cm^{-1} and where p_{O_2} is the partial pressure of molecular oxygen (= 150 Torr at atmospheric pressure). We note that in equation (III.3) we divided $g(R)$ by $p_{\rm O_2}$ to make the result conveniently dependent on the product $p_{\rm O_2}R$, which is an important parameter for photoionization in $N_2 - O_2$ mixtures as shown by *Zheleznyak et al.* [1982]. The dependence of the right hand side of equation (III.3) on the $p_{\rm O_2}R$ product makes it easily scalable to different pressures.

The above described model has typically been employed in a cylindrical coordinate system to model the dynamics of two-dimensional azimuthally symmetric streamers. Following the approach proposed by *Kulikovsky* [2000a], the emitting volume in this kind of coordinate system (r, ϕ, z) is divided into small rings centered at the symmetry axis (Figure III.1(a)), and the photoionization rate at point of observation (r,z) due to all source rings $(r_s,\, z_s)$ in cm^{-3}s^{-1} is

$$S_{\rm ph}(r,z) = \int {\rm d}r_s \int {\rm d}z_s I(r_s, z_s) M_{\rm ph}(r, r_s, |z - z_s|) \tag{III.4}$$

In equation (III.4) the integration is performed over all source regions with significant production of photoionizing radiation and the function $M_{\rm ph}$ is defined as

$$M_{\rm ph}(r, r_s, |z - z_s|) = \frac{r_s}{4\pi} \int_0^{2\pi} \frac{g[R(\phi_s)]}{R(\phi_s)^2} {\rm d}\phi_s \tag{III.5}$$

where $R(\phi_s){=}|\vec{r}-\vec{r}\,'|{=}[r_s^2 + r^2 + (z-z_s)^2 - 2rr_s\cos(\phi_s)]^{\frac{1}{2}}$.

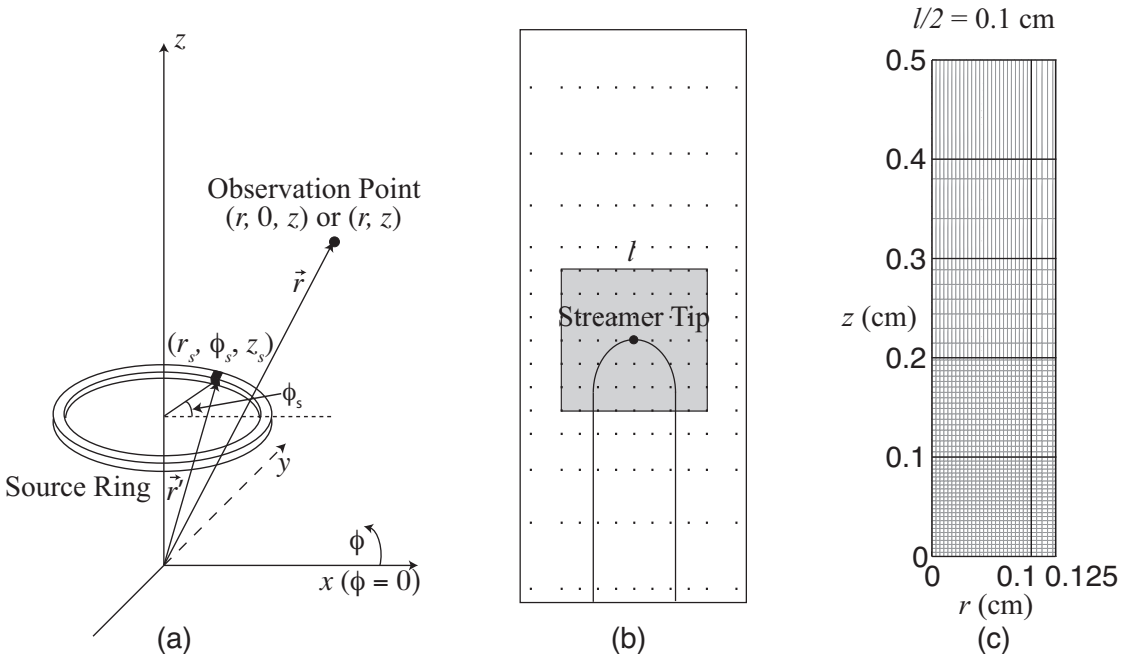

Figure III.1: (a) Elementary emitting volume (ring) for photoionization calculations; (b) Schematic illustration of the inhomogeneous grid for efficient photoionization calculations using the integral model; (c) Illustration of an inhomogeneous grid system for acceleration of photoionization calculations using the integral model.

The geometric factor $M_{\rm ph}$ depends on r, r_s, and $|z - z_s|$, and it is possible to calculate $M_{\rm ph}$ once and store it as a three-dimensional array, which can be repeatedly reused for computation of $S_{\rm ph}$ at each time step in the simulation. Even with this simplification the integral model for photoionization is computationally very expensive because a two-dimensional integration (equation (III.4)) has to be carried out for each observation point (r, z). To further improve the computation efficiency, a straightforward technique of using a coarse grid for photoionization calculation instead of the main grid can be employed, and then, interpolation is carried out to obtain the photoionization rate on the fine grid. A homogeneous coarse grid is utilized for this purpose in [*Kulikovsky*, 2000a; *Hallac et al.*, 2003].

A more accurate and efficient grid system is an inhomogeneous one with fine resolution around the streamer head and coarse resolution in the region away from the head as shown schematically in Figure III.1(b). In this approach every time when the photoionization is calculated, a new grid is generated with the origin at the streamer tip, where the electric field is maximum. The photoionizing emission source is assumed to be confined in the shaded region shown in Figure III.1(b). The value of $S_{\rm ph}$ at each point of the new grid is calculated using equation (III.4) by accounting for the sources in the shaded region only. A linear or exponential interpolation is used to obtain $S_{\rm ph}$ at the main grid points. The $M_{\rm ph}$ required for integration (III.4) still needs to be calculated only once and stored in a three-dimensional array for a repeated use.

Figure III.1(c) provides an example of practical implementation of the above discussed ideas. If the size of the simulation domain is 0.5×0.125 cm^2, a grid for the calculation of $M_{\rm ph}$ can be set up as shown in Figure III.1(c), where the effective diameter of the shaded region

shown in Figure III.1(b) is assumed to be $l = 0.2$ cm. In the z direction the simulation domain is divided in equal intervals with length $l/2$=0.1 cm. The grid size in each of these intervals is constant, and increases exponentially with the distance from the origin from one interval to the next. If the grid size in a particular interval becomes greater than the interval itself ($l/2$), then $l/2$ is used as the grid size instead, as shown, for example for the interval from z=0.4 to 0.5 cm in Figure III.1(c). The grid in r direction is generated following the same procedure. $M_{\rm ph}$ can then be calculated on this grid using equation (III.5). The grid for the problem geometry shown in Figure III.1(b) can be generated by following the same ideas with the origin placed at the streamer tip and with the $l/2$ intervals with reduced grid resolution extending in both positive and negative z directions from the shaded region. The calculation of the contribution to $S_{\rm ph}(r, z)$ due to a source ring at (r_s, z_s) is significantly accelerated by a simple call of the corresponding pre-calculated element of the three-dimensional matrix $M_{\rm ph}(r, r_s, |z - z_s|)$. Finally, the contributions from all the rings constituting the shaded source shown in Figure III.1(b) are summed up to obtain the total $S_{\rm ph}(r, z)$.

The integral approach with variable size grids based on *Zheleznyak et al.* [1982] model outlined above is used for streamer calculations reported in Section III.6.2 of the present chapter. It should be noted that for the double-headed streamer presented in Section III.6.2, there are two grid systems generated with the origin of each grid system positioned at the tip of the corresponding streamer head. However, the same precalculated $M_{\rm ph}$ matrix is used for both heads.

III.3 Two and three-exponential Helmholtz models for photoionization in air

Luque et al. [2007] have recently proposed a novel approach allowing to effectively replace the calculation of integral (III.1) of the classic photoionization model with a solution of a set of Helmholtz differential equations, which can be very efficiently solved using well developed techniques available for solution of the elliptic partial differential equations. In terms of notations adopted in the present chapter the approach proposed by *Luque et al.* [2007] involves fitting of the $g(R)/R$ ratio in (III.1) with a sum of exponential functions leading to a set of integrals, each of which can effectively be interpreted as an integral solution of a separate Helmholtz differential equation. After this equivalent representation is established the problem can be solved by solving the set of Helmholtz differential equations, instead of direct evaluation of integrals. However, the two-exponential fit provided in [*Luque et al.*, 2007] has been applied to low pressure experimental data of *Penney and Hummert* [1970] effectively corresponding to the function $g(R)$, rather than to $g(R)/R$ required for the correct solution of the problem. In this section we present correct solution of this problem using two and three-exponential fits. In Section III.6.1 we demonstrate that the two-exponential fit is generally not sufficient and the three-exponential fit is needed for obtaining the accurate solution of the problem for a full range of $p_{O_2}R$ values in which the *Zheleznyak et al.* [1982] photoionization model remains valid.

We note that the *Zheleznyak et al.* [1982] photoionization model, discussed in the previous section, has been formulated using experimental data obtained at low pressure [*Penney and Hummert*, 1970; *Teich*, 1967] and agrees well with results of more recent experiments

Table III.1: Parameters of the two-exponential fit of $g(R)/p_{O_2}/(p_{O_2}R)$ as a function of $p_{O_2}R$.

j	A_j [cm^{-2} Torr^{-2}]	λ_j [cm^{-1} Torr^{-1}]
1	0.0021	0.0974
2	0.1775	0.5877

Table III.2: Parameters of the three-exponential fit of $g(R)/p_{O_2}/(p_{O_2}R)$ as a function $p_{O_2}R$.

j	A_j [cm^{-2} Torr^{-2}]	λ_j [cm^{-1} Torr^{-1}]
1	1.986×10^{-4}	0.0553
2	0.0051	0.1460
3	0.4886	0.89

at atmospheric pressure [*Aints et al.*, 2008; *Naidis*, 2006, and references cited therein]. Therefore, in contrast to [*Luque et al.*, 2007] in our derivation below we do not employ the low pressure data of *Penney and Hummert* [1970], but rather formulate the two and three-exponential Helmholtz models using the $g(R)$ function (III.3) appearing in the classic integral model for photoionization in air [*Zheleznyak et al.*, 1982].

The function $S_{\rm ph}(\vec{r})$ given by (III.1) can be represented in the form

$$S_{\rm ph}(\vec{r}) = \sum_j S^j_{\rm ph}(\vec{r}) \tag{III.6}$$

with terms

$$S^j_{\rm ph}(\vec{r}) = \iiint_{V'} \frac{I(\vec{r}\,')A_j p^2_{O_2} e^{-\lambda_j p_{O_2} R}}{4\pi R} {\rm d}V' \tag{III.7}$$

satisfying Helmholtz differential equations

$$\nabla^2 S^j_{\rm ph}(\vec{r}) - (\lambda_j p_{O_2})^2 S^j_{\rm ph}(\vec{r}) = -A_j p^2_{O_2} I(\vec{r}) \tag{III.8}$$

Having compared equations (III.1) and (III.7) it can be easily verified that

$$\frac{g(R)}{p_{O_2}} = (p_{O_2}R) \sum_j A_j e^{-\lambda_j p_{O_2} R} \tag{III.9}$$

The solution of the problem requires fitting of the function $g(R)/p_{O_2}$ by series of exponents multiplied by $(p_{O_2}R)$. After the fitting, the photoionization problem can be solved by solving differential equations (III.8) and performing summation (III.6). In practice, it appears to be easier to fit function $g(R)/p_{O_2}/(p_{O_2}R)$ with a sum of exponents $\sum_j A_j e^{-\lambda_j p_{O_2} R}$ and then multiply the result by $(p_{O_2}R)$ to obtain the desired representation of $g(R)/p_{O_2}$ given by (III.9).

The function $g(R)/p_{O_2}$ is shown in Figure III.2 by solid line and a two-exponential fit performed by MATLAB function fminsearch (based on Nelder-Mead simplex direct search method) is shown by the dashed line. The two-exponential fit was performed for the range

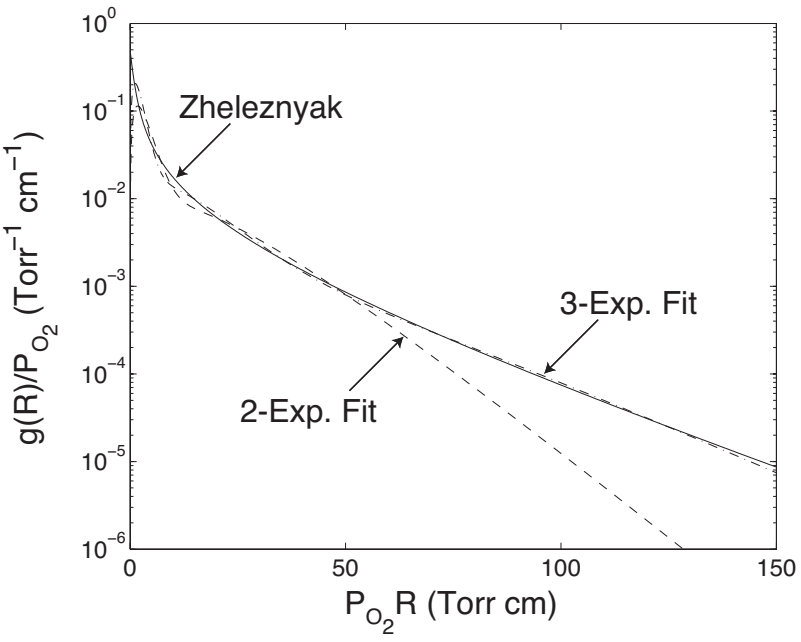

Figure III.2: Solid line: The $g(R)/p_{O_2}$ function given by equation (III.3) from the model of *Zheleznyak et al.* [1982]. Dashed line: Two-exponential fit of the form specified by equation (III.9), performed for the range $1<p_{O_2}R<60$ Torr cm and with the parameters of Table III.1. Dot-dashed line: Three-exponential fit with the parameters of Table III.2 performed for the range $1<p_{O_2}R<150$ Torr cm.

$1<p_{O_2}R<60$ Torr cm, which directly corresponds to the $p_{O_2}R$ range shown in Figure 3 of [*Zheleznyak et al.*, 1982]. The two-exponential fit parameters are shown in Table III.1. We emphasize that the fit shown in Figure III.2 by the dashed line is a product of $(p_{O_2}R)$ and $\sum_j A_j e^{-\lambda_j p_{O_2} R}$ as required for solution of the problem and represented by the right hand side in equation (III.9). It is also noted that it is very difficult to fit $g(R)/p_{O_2}$ function with two exponents multiplied by $p_{O_2}R$ and the fit given by parameters in Table III.1 and in Figure III.2 becomes invalid for $p_{O_2}R<1$ Torr cm and $p_{O_2}R>60$ Torr cm. Implications of this will be discussed in Section III.6.1.

Djakov et al. [1998] have applied a three-exponential fit in the context of *Zheleznyak et al.* [1982] photoionization model to obtain a fast recursive algorithm for solution of the photoionization problem in a quasi-two-dimensional (the 1.5D or "disk" based) streamer model. Although the fit proposed in [*Djakov et al.*, 1998] is not directly applicable in the context of the Helmholtz equations based photoionization model discussed in this section, we note that the employment of three-exponential fits represents a natural and logical step to remove the above discussed limitations of the two-exponential model for the range $1<p_{O_2}R<60$ Torr cm.

As part of this work we also performed a three-exponential fit of $g(R)/p_{O_2}$ using three exponents multiplied by $(p_{O_2}R)$. The related fit is shown in Figure III.2 by dot-dashed line. The parameters of the three-exponential fit are summarized in Table III.2. The three exponential fit is valid in the range of $p_{O_2}R$ from 1 to 150 Torr cm. We note that this range translates into 1/150=0.0067 to 1 cm at ground pressure. The fit for $p_{O_2}R>1$ Torr cm is generally improved in comparison with the two-exponential case, but it is very difficult to fit this function even with three exponents at $p_{O_2}R<1$ Torr cm. We note that the upper

limit of validity of the developed three-exponential fit ($p_{O_2}R$=150 Torr cm) exceeds the $p_{O_2}R\simeq$100 Torr cm (i.e., $pR\simeq$500 Torr cm, where p is air pressure) validity threshold of the *Zheleznyak et al.* [1982] model for photoionization in air, as discussed recently in [*Naidis*, 2006].

The accurate numerical solution of Helmholtz equations (III.8) requires knowledge about values of $S^j_{\rm ph}(\vec{r})$ functions at the boundaries of the simulation domain. The determination of boundary conditions will be presented and discussed in Section III.5.

III.4 Three-group Eddington and SP_3 approximations for photoionization in air

III.4.1 Three-group approach

In [*Ségur et al.*, 2006], the photoionization source term $S_{\rm ph}(\vec{r})$ is calculated using direct numerical solutions of the first (also called Eddington approximation) and the third order (also called SP_3) approximations of the radiative transfer equation. *Ségur et al.* [2006] introduce a simple monochromatic approach (also called one-group method) and derive the physical parameters required for applying this method to calculate $S_{\rm ph}(\vec{r})$ for non-thermal gas discharges in air at atmospheric pressure by making the model results as consistent as possible with the classical Zheleznyak model.

In order to achieve a better agreement with the Zheleznyak model for the Eddington and SP_3 approximations, we propose to consider $j = 1, N_g$ effective monochromatic radiative transfer equations. We consider that there is no photon scattering and as the timescale of photon propagation is much less than the timescale of streamer propagation, we neglect the transient term of the radiative transfer equation. For each frequency, the effective monochromatic radiative transfer equation can be written as [*Ségur et al.*, 2006]:

$$\vec{\Omega}\cdot\vec{\nabla}\Psi_j(\vec{r},\vec{\Omega}) + \lambda_j p_{O_2}\Psi_j(\vec{r},\vec{\Omega}) = \frac{n_u(\vec{r})}{4\pi c\tau_u} \tag{III.10}$$

where to simplify the notation, first, the time dependent functions $\Psi_j(\vec{r},\vec{\Omega},t)$ and $n_u(\vec{r},t)$ are noted as $\Psi_j(\vec{r},\vec{\Omega})$ and $n_u(\vec{r})$ and second, only one radiative excited state u is considered. The quantity $\lambda_j p_{O_2}$ is the absorption coefficient. It is important to mention that all monochromatic equations for $j = 1, N_g$ have the same source term but different absorption coefficients. The equation (III.10) can be simply integrated to derive $\Psi_{0,j}(\vec{r})$, the isotropic part of the photon distribution function $\Psi_j(\vec{r},\vec{\Omega})$ as:

$$\Psi_{0,j}(\vec{r}) = \iiint_{V'} \frac{n_u(\vec{r'})}{c\tau_u}\frac{\exp(-\lambda_j p_{O_2}R)}{4\pi R^2}{\rm d}V' \tag{III.11}$$

Then we assume that the isotropic part of the total distribution function $\Psi_0(\vec{r})$ can be written as:

$$\Psi_0(\vec{r}) = \sum_j \alpha_j\Psi_{0,j}(\vec{r}) \tag{III.12}$$

Table III.3: Parameters of the three-exponential fit of $g(R)/p_{O_2}$ as a function $p_{O_2}R$.

j	A_j [cm^{-1} Torr^{-1}]	λ_j [cm^{-1} Torr^{-1}]
1	0.0067	0.0447
2	0.0346	0.1121
3	0.3059	0.5994

where α_j are constants. This approach is similar to the Gaussian-type quadratures generally used in the correlated-k method [*Taine and Soufiani*, 1999]. As already mentioned in [*Ségur et al.*, 2006], to calculate the photoionization source term it is only necessary to know $\Psi_0(\vec{r})$ the isotropic part of the distribution function. Then, using equations (III.11) and (III.12), the photoionization source term can be written as:

$$S_{\text{ph}}(\vec{r}) = \sum_j A_j \xi p_{O_2} \iiint_{V'} \frac{n_u(\vec{r'})}{\tau_u} \frac{\exp(-\lambda_j p_{O_2} R)}{4\pi R^2} \mathrm{d}V' = \sum_j S^j_{\text{ph}}(\vec{r}) \tag{III.13}$$

where $A_j \xi p_{O_2}$ are coefficients, which will be defined below, with the photoionization efficiency ξ introduced in equation (III.2). To use this approach in air, the photoionization source term given by equation (III.13) has to be compared with the Zheleznyak integral expression (III.1). Both equations are identical if

$$\frac{g(R)}{p_{O_2}} = \sum_j A_j e^{-\lambda_j p_{O_2} R} \tag{III.14}$$

where A_j and λ_j are the unknowns. To obtain their values, we use the same approach as in Section III.3 and we fit the function $g(R)/p_{O_2}$ by a three-exponential fit (i.e., $N_g = 3$). The corresponding parameters A_j and λ_j are given in Table III.3. In the following, this approach is called the three-group method.

To avoid any possible confusion we emphasize the difference between the equation (III.14) and equation (III.9) of the Helmholtz model. The Helmholtz model employs series of exponents multiplied by $(p_{O_2}R)$, while equation (III.14) provides direct fit by exponents without multiplication by $(p_{O_2}R)$. We also bring to the attention of the readers the related difference in units between A_j coefficients shown in Tables III.1 and III.2 for the Helmholtz model [cm^{-2}Torr^{-2}] and those corresponding to equation (III.14) and shown in Table III.3 [cm^{-1}Torr^{-1}].

Figure III.3 shows the original function $g(R)/p_{O_2}$, the three-exponential fit (III.14) derived in this section, and the one-exponential fit proposed in [*Ségur et al.*, 2006]. The three-exponential fit was performed for the range $0.1<p_{O_2}R<150$ Torr cm. It appears that the three-exponential fit allows to have an excellent agreement with the function $g(R)/p_{O_2}$, which is much better than the one-exponential fit, in particular for large $p_{O_2}R$ values. It is interesting to note that in the $p_{O_2}R$ range $0.1<p_{O_2}R<150$ Torr cm the fit obtained using a three-group method (Figure III.3) is generally more accurate than the one obtained using a three-exponential Helmholtz model (Figure III.2).

The above analysis indicates that in order to calculate the photoionization source term $S_{\text{ph}}(\vec{r})$, the set of radiative transfer equations (III.10) has to be solved. However, the direct solution of the radiative transfer equation is not straightforward and usually in the literature

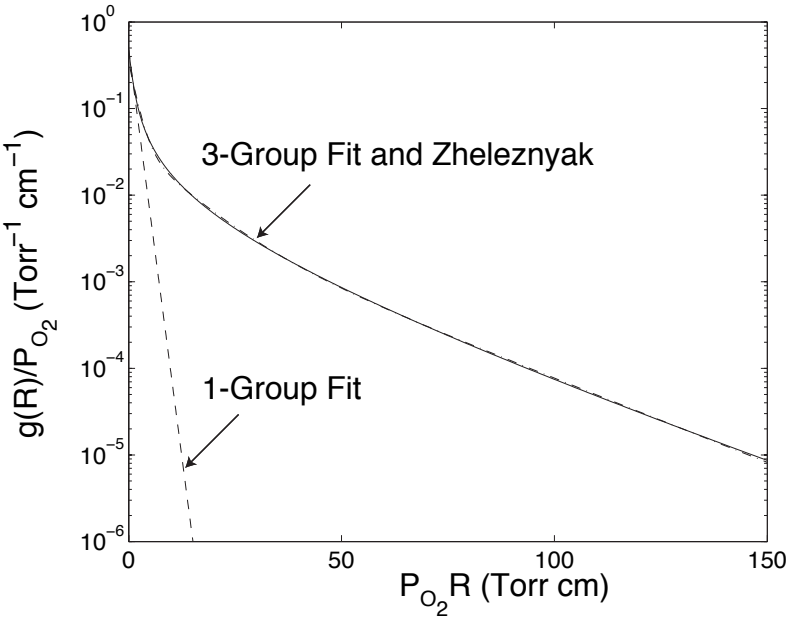

Figure III.3: Solid line: The $g(R)/p_{O_2}$ function given by equation (III.3) from the model of *Zheleznyak et al.* [1982]. Dashed line: one-exponential fit given in [*Ségur et al.*, 2006]. Dot-dashed line: Three-exponential fit of the form specified by equation (III.14), performed for the range $0.1<p_{O_2}R<150$ Torr cm, and with the parameters of Table III.3.

approximate differential models are used [*Ségur et al.*, 2006]. In this work we propose to extend to the three-group approach the Eddington and SP$_3$ methods used in [*Ségur et al.*, 2006] for a one-group approach.

III.4.2 Eddington and SP$_3$ models

Approximate differential methods are based on the assumption that the distribution function $\Psi_j(\vec{r},\vec{\Omega})$ varies only weakly with the unitary vector $\vec{\Omega}$. Using this assumption, Equation (III.10) is transformed into a partial differential equation of second order which gives directly the isotropic part $\Psi_{0,j}(\vec{r},\vec{\Omega})$. This is the so-called Eddington approximation [*Pomraning*, 1973]. Unfortunately, this approximation is valid only if the absorption coefficient $\lambda_j p_{O_2}$ is sufficiently high (i.e., in a strongly absorbing medium). To obtain higher order approximations, *Larsen et al.* [2002] proposed to introduce a small parameter in Equation (III.10) in order to expand this equation in a series of powers of this small parameter. We present here the derivation of the first order (Eddington) and the third order (SP$_3$) approximations.

We divide Equation (III.10) by $\lambda_j p_{O_2}$ and to define the vector $\vec{\mathfrak{R}} = \vec{\nabla}/(\lambda_j p_{O_2})$. Then, Equation (III.10) can be written as:

$$\left(1+\vec{\Omega}\cdot\vec{\mathfrak{R}}\right)\Psi_j(\vec{r},\vec{\Omega}) = \frac{n_u(\vec{r})}{4\pi c\tau_u\lambda_j p_{O_2}} \tag{III.15}$$

Then the photon distribution function is given by:

$$\Psi_j(\vec{r},\vec{\Omega}) = \left(1+\vec{\Omega}\cdot\vec{\mathfrak{R}}\right)^{-1}\frac{n_u(\vec{r})}{4\pi c\tau_u\lambda_j p_{O_2}} \tag{III.16}$$

and by developping into Neumann series, one obtains:

$$\Psi_j(\vec{r},\vec{\Omega}) = \left[1 - \vec{\Omega}\cdot\vec{\mathfrak{K}} + (\vec{\Omega}\cdot\vec{\mathfrak{K}})^2 - (\vec{\Omega}\cdot\vec{\mathfrak{K}})^3 + \cdots\right] \frac{n_u(\vec{r})}{4\pi c\tau_u \lambda_j p_{O_2}} \tag{III.17}$$

Thus, the isotropic part of the photon distribution function is given by:

$$\Psi_{0,j}(\vec{r}) = \int_\Omega \Psi_j(\vec{r},\vec{\Omega})\mathrm{d}\Omega = \left(1 + \frac{1}{3}\vec{\mathfrak{K}}^2 + \frac{1}{5}\vec{\mathfrak{K}}^4 + \cdots\right) \frac{n_u(\vec{r})}{c\tau_u \lambda_j p_{O_2}} \tag{III.18}$$

and then, finally, Equation (III.10) becomes :

$$\left(1 - \frac{1}{3}\vec{\mathfrak{K}}^2 - \frac{4}{45}\vec{\mathfrak{K}}^4 - \frac{44}{945}\vec{\mathfrak{K}}^6 - \cdots\right) \Psi_{0,j}(\vec{r}) = \frac{n_u(\vec{r})}{c\tau_u \lambda_j p_{O_2}} \tag{III.19}$$

Equation (III.19) shows that when the parameter

$$\frac{|\vec{\mathfrak{K}}^2 \Psi_{0,j}(\vec{r})|}{\Psi_{0,j}(\vec{r})} \ll 1,$$

that is under a weak anisotropy assumption, one can truncate the operator series.

For $j = 1, N_g$, the Eddington approximation of (III.10) to derive $\Psi_{0,j}$ is given by the truncation to the second term of operator factors in Equation III.19 [*Ségur et al.*, 2006]:

$$[\nabla^2 - 3(\lambda_j p_{O_2})^2]\Psi_{\mathrm{ED},0,j}(\vec{r}) = -3\lambda_j p_{O_2} \frac{n_u(\vec{r})}{c\tau_u} \tag{III.20}$$

where $\Psi_{\mathrm{ED},0,j}(\vec{r})$ represents the first order Eddington approximation of $\Psi_{0,j}(\vec{r})$. It is interesting to note that equation (III.20) is an elliptic equation, which has a structure very similar to Poisson's equation. Therefore, as noted in Section II.4, both Poisson's equation and the Eddington approximation can be solved with the same numerical routine.

In [*Larsen et al.*, 2002], a significant improvement of the accuracy of the solution was obtained by keeping the terms in the left hand side of equation (III.19) up to the third order Laplacian. In this case, the equation is a partial differential equation of sixth order which can be written as a set of two equations of second order verified by the functions $\phi_{1,j}$ and $\phi_{2,j}$ given by:

$$\nabla^2\phi_{1,j}(\vec{r}) - \frac{(\lambda_j p_{O_2})^2}{\kappa_1^2}\phi_{1,j}(\vec{r}) = -\frac{\lambda_j p_{O_2}}{\kappa_1^2}\frac{n_u(\vec{r})}{c\tau_u} \tag{III.21}$$

$$\nabla^2\phi_{2,j}(\vec{r}) - \frac{(\lambda_j p_{O_2})^2}{\kappa_2^2}\phi_{2,j}(\vec{r}) = -\frac{\lambda_j p_{O_2}}{\kappa_2^2}\frac{n_u(\vec{r})}{c\tau_u} \tag{III.22}$$

where $\kappa_1^2 = \frac{3}{7} - \frac{2}{7}\sqrt{\frac{6}{5}}$ and $\kappa_2^2 = \frac{3}{7} + \frac{2}{7}\sqrt{\frac{6}{5}}$. Then, for j=1, N_g, the third order SP_3 approximation of $\Psi_{0,j}$ is denoted as $\Psi_{\mathrm{SP}_3,0,j}$ and is given by [*Larsen et al.*, 2002]:

$$\Psi_{\mathrm{SP}_3,0,j}(\vec{r}) = \frac{\gamma_2\phi_{1,j} - \gamma_1\phi_{2,j}}{\gamma_2 - \gamma_1} \tag{III.23}$$

where

$$\gamma_n = \frac{5}{7}\left[1 + (-1)^n 3\sqrt{\frac{6}{5}}\right] \tag{III.24}$$

Equations (III.21) and (III.22) again have the same structure as Poisson's equation and can be solved using the same numerical methods.

After obtaining the solution for $\Psi_{\mathrm{ED},0,j}$ or $\Psi_{\mathrm{SP}_3,0,j}$, the photoionization source term can be calculated using

$$S_{\mathrm{ph}}(\vec{r}) = \sum_j A_j \xi p_{O_2} c \Psi_{0,j}(\vec{r}) = \sum_j S^j_{\mathrm{ph}}(\vec{r}) \tag{III.25}$$

by replacing $\Psi_{0,j}$ with $\Psi_{\mathrm{ED},0,j}$ or $\Psi_{\mathrm{SP}_3,0,j}$.

It is important to note that equation (III.20) of the Eddington model, and equations (III.21) and (III.22) of the SP$_3$ model are Helmholtz equations of the same structure as equations (III.8). Then the accurate numerical solution of all these equations requires knowledge about values of $S^j_{\mathrm{ph}}(\vec{r})$ functions at the boundaries of the simulation domain. The determination of boundary conditions for the different models will be presented and discussed in Section III.5.

Finally, as equations of the Eddington, SP$_3$ and Helmholtz models have the same structure, in Appendix B we show that all solutions of these models can be written in essentially same mathematical form, with differences between these models only arising from different numerical values of the model coefficients. Then we demonstrate that the three-exponential Helmholtz model is more accurate than the three-group Eddington model. In Appendix B we also demonstrate that the SP$_3$ model can be effectively represented in a mathematical form equivalent to six-exponential Helmholtz model. This analysis clearly demonstrates that the three-group SP$_3$ model is more accurate than the three-group Eddington model and the three-exponential Helmholtz model.

III.4.3 Determination of parameters of the three-group models

The formulation of the above Eddington and SP$_3$ models require separate evaluations of ξ in equation (III.25), and $\frac{n_u(\vec{r})}{\tau_u}$ in equation (III.20) for the first order approximation, or in equations (III.21) and (III.22) for the third one. For Zheleznyak and Helmholtz models, the product $\xi\frac{n_u(\vec{r})}{\tau_u}$ is computed using equation (III.2) to give the photoionization radiation source utilizing the known term $\xi\frac{\nu_u}{\nu_i}$ given by *Zheleznyak et al.* [1982]. To effectively use the same term in the Eddington approximations, we can slightly change the above formulation by multiplying both sides of the equation (III.20) or equations (III.21) and (III.22) by a constant ξ. For example, the following equation is obtained for the first order Eddington approximation:

$$[\nabla^2 - 3(\lambda_j p_{O_2})^2][\xi\Psi_{\mathrm{ED},0,j}(\vec{r})] = -3\lambda_j p_{O_2}\xi\frac{n_u(\vec{r})}{c\tau_u} \tag{III.26}$$

where we could define $\Psi^*_{\mathrm{ED},0,j}(\vec{r}) = \xi\Psi_{\mathrm{ED},0,j}(\vec{r})$. This equation is solved for $\Psi^*_{\mathrm{ED},0,j}(\vec{r})$ and, finally, we have

$$S_{\mathrm{ph}}(\vec{r}) = \sum_j A_j p_{O_2} c \Psi^*_{\mathrm{ED},0,j}(\vec{r}) = \sum_j S^j_{\mathrm{ph}}(\vec{r}) \tag{III.27}$$

By using this formulation, the factor $\xi\frac{n_u(\vec{r},t)}{\tau_u}$ in the source term of the equation (III.26) can be directly evaluated by $\frac{p_q}{p+p_q}\left(\xi\frac{\nu_u}{\nu_i}\right)\nu_i n_e$ as used by Zheleznyak and Helmholtz models (see equation (III.2)).

The same idea can be applied to equations (III.21) and (III.22) of the SP_3 model. In this way, it is also demonstrated that we could use different combinations of ξ and ν_u/ν_i as long as their product is consistent with that given by *Zheleznyak et al.* [1982].

III.5 Boundary conditions

III.5.1 Two and three-exponential Helmholtz models

The accurate numerical solution of Helmholtz equations (III.8) requires knowledge about values of $S^j_{\mathrm{ph}}(\vec{r})$ functions at the boundaries of the simulation domain. In [*Luque et al.*, 2007] these values are assumed to be zero. In Section III.6.1 we demonstrate that the definition of the boundary conditions for different components $S^j_{\mathrm{ph}}(\vec{r})$ represents an important part of accurate solution of the photoionization problem. A practical solution of this problem, is

- to define the $S^j_{\mathrm{ph}}(\vec{r})$ component with the smallest λ_j (i.e., the longest photoionization range) using the classic integral model of *Zheleznyak et al.* [1982], and
- to assume zero boundary conditions for the rest of the $S^j_{\mathrm{ph}}(\vec{r})$ components.

For both two and three-exponential models presented in this section the smallest λ_j are associated with the first terms in the corresponding series (i.e., with the $j = 1$ term), as can be directly seen from Tables III.1 and III.2.

It is expected that this approach may lead to inaccurate results for situations when the photoionization source is positioned very close to the boundary (i.e., for a streamer head approaching an electrode or a dust particle [*Babaeva et al.*, 2006]). However, the enhancement of the electric field due to the conducting surface (i.e., image charges) effects in this kind of simulation geometry may result in a relatively small contribution of the photoionization rate in comparison with the electron-ion pair production rate due to the direct electron impact ionization.

III.5.2 Three-group Eddington and SP_3 models

Boundary conditions using the integral Zheleznyak model

As for Helmholtz models, boundary conditions play an important role in the accurate evaluation of the S_{ph} term using the three-group Eddington and SP_3 models. It is interesting

to note that the approach proposed for Helmholtz models can be also used for the boundary conditions of the three-group Eddington and SP_3 models. For the three-group Eddington model, the boundary condition is set on the $\Psi^*_{ED,0,1}$ function as the component with j=1 is corresponding to the smallest λ_j value (i.e., the longest photoionization range) in Table III.3. According to equation (III.27), the boundary condition for $\Psi^*_{ED,0,1}$ is written as:

$$\Psi^*_{ED,0,1}(\vec{r}) = \frac{S_{ph}(\vec{r})}{p_{O_2} A_1 c} \tag{III.28}$$

where $S_{ph}(\vec{r})$ is calculated using the Zheleznyak integral model. Zero boundary conditions are assumed for the remaining $\Psi^*_{ED,0,j}$ components corresponding to j=2 and 3. This approach is subject to the same limitations as discussed at the end of Section III.5.1.

For the three-group SP_3 model, the same boundary condition is set on the functions defined as $\phi^*_{1,1}(\vec{r}) = \xi\phi_{1,1}(\vec{r})$ and $\phi^*_{2,1}(\vec{r}) = \xi\phi_{2,1}(\vec{r})$ according to equations (III.25) and (III.23):

$$\phi^*_{1,1}(\vec{r}) = \phi^*_{2,1}(\vec{r}) = \frac{S_{ph}(\vec{r})}{p_{O_2} A_1 c} \tag{III.29}$$

Marshak's boundary conditions for the Eddington model

For the first order Eddington model, we have also used the classical boundary conditions derived by Marshak [*Pomraning*, 1973, p. 55] for various configurations. For example, for the case of a boundary surface with no reflection or emission (i.e., the boundary surface is transparent for the radiative flux emitted in the medium), the value of $\Psi^*_{ED,0,j}$ at the boundary is given by:

$$\vec{\nabla}\Psi^*_{ED,0,j}(\vec{r}) \cdot \vec{n}_S = -\frac{3}{2}\lambda_j p_{O_2} \Psi^*_{ED,0,j}(\vec{r}) \tag{III.30}$$

where $\vec{n}_S$ is the unit outward boundary surface normal.

It is interesting to note that equations (III.26) and (III.30) form a consistent set of closed equations where the unknowns are the $\Psi^*_{ED,0,j}(\vec{r})$ functions. Furthermore, boundary conditions given by equation (III.30) are very simple to implement and very fast to calculate.

Larsen's boundary conditions for the SP_3 model

The third order Eddington approximation (SP_3) results in elliptic equations for functions $\phi^*_{1,j}(\vec{r})$ and $\phi^*_{2,j}(\vec{r})$ (see Equations (III.21) and (III.22)) and a linear combination of $\phi^*_{1,j}(\vec{r})$ and $\phi^*_{2,j}(\vec{r})$ gives the isotropic part of the photon distribution function. *Larsen et al.* [2002] derived the corresponding boundary conditions for a boundary surface without reflection and without emission:

$$\begin{cases} \vec{\nabla}\phi^*_{1,j}(\vec{r}) \cdot \vec{n_s} &= -\lambda_j p_{O_2} \alpha_1 \phi^*_{1,j}(\vec{r}) - \lambda_j p_{O_2} \beta_2 \phi^*_{2,j}(\vec{r}) \\ \vec{\nabla}\phi^*_{2,j}(\vec{r}) \cdot \vec{n_s} &= -\lambda_j p_{O_2} \alpha_2 \phi^*_{2,j}(\vec{r}) - \lambda_j p_{O_2} \beta_1 \phi^*_{1,j}(\vec{r}) \end{cases} \tag{III.31}$$

where $\vec{n}_s$ is the unit outward boundary surface normal and $\alpha_{\frac{1}{2}} = \frac{5}{96}\left(34 \pm 11\sqrt{\frac{6}{5}}\right)$ and $\beta_{\frac{1}{2}} = \frac{5}{96}\left(2 \mp \sqrt{\frac{6}{5}}\right)$.

As the coefficients $\alpha_{\frac{1}{2}} \gg \beta_{\frac{1}{2}}$ the coupling between both equations is weak. Then, to solve this problem, as recommended by Larsen, the two equations are first solved independently (considering $\beta = 0$) and iterations are carried out afterwards with the β coefficients. The convergence is very rapid and obtained in only a few iterations.

It is interesting to note that the equations (III.21–III.22) and (III.31) form a consistent set of closed equations.

III.6 Results and Discussion

III.6.1 Gaussian photoionization source

In this subsection, a simple model source of photoionizing radiation is used to compare the two and three-exponential Helmholtz, the three-group Eddington and SP_3 models introduced in Sections III.3 and III.4 with the integral model proposed by *Zheleznyak et al.* [1982] reviewed in Section III.2. We calculate the photoionization production rate S_{ph} in a two-dimensional axisymmetric computational domain of length L_d and radius R_d for a Gaussian source centered on the symmetry axis. The Gaussian ionization production rate S_i is defined by:

$$S_i(r_s, z_s) = \nu_i(r_s, z_s) n_e(r_s, z_s) = S_{i0} \exp(-(z_s - z_0)^2/\sigma^2 - r_s^2/\sigma^2) \tag{III.32}$$

where z_0 is the axial position of the source term, σ is the parameter controlling effective spatial width of the source, and S_{i0}=1.53×10^{25} cm^{-3}s^{-1}. We note that the particular S_{i0} value is chosen to be consistent with similar study presented in [*Ségur et al.*, 2006] and has no implications for test results and related conclusions presented in this section. Assuming $p_q/(p + p_q)$=0.038 (i.e., ground pressure) and $\xi\nu_u/\nu_i$=0.06 as in [*Ségur et al.*, 2006] and using (III.2) we can write

$$I(r_s, z_s) = I_0 \exp(-(z_s - z_0)^2/\sigma^2 - r_s^2/\sigma^2) \tag{III.33}$$

where $I_0 = \frac{p_q}{p+p_q}\,\xi\frac{\nu_u}{\nu_i} S_{i0}$=3.5×10^{22} cm^{-3}s^{-1} as in [*Ségur et al.*, 2006].

The finite difference forms of the differential equations involved in the Helmholtz, Eddington and SP_3 models are solved using the module D03EBF of the NAG Fortran library (see Section II.1.3). The numerical calculation of (III.4) was carried out using standard Gaussian quadratures. All calculations were carried out with a uniform grid in both directions and with $n_z = n_r = 251$, where n_z and n_r are the number of cells along the longitudinal and radial directions, respectively.

To demonstrate importance of different ranges of $p_{O_2}R$ in solution of the photoionization problems we have performed calculations for simulation domain sizes (i.e., L_d×R_d) 0.02×0.02 cm^2, 0.2×0.2 cm^2 and 2×2 cm^2, at ground pressure (p_{O_2}=150 Torr). We have

also used respective values of source sizes σ=0.001, 0.01 and 0.1 cm. It is assumed that the source is positioned in the center of the simulation domain at z_0=0.01, 0.1 and 1 cm, respectively. It is noted that σ=0.001 cm is generally smaller than the dimension of streamer head at ground pressure after it has just been born from an avalanche. The σ=0.01 cm is comparable to the size of the streamer head (e.g., see Section II.3). The streamer head can reach dimension comparable and much greater than σ=0.1 cm in large applied electric field, when the streamer expands quickly [e.g., *Briels et al.*, 2006; *Liu and Pasko*, 2004]. Therefore, all source sizes σ studied can be attributed to practical stages of propagation of real streamers. In the present chapter, we only show the results for σ=0.01 cm; results for σ=0.001 cm and σ=0.1 cm are presented in the Appendix A.

We note that the artificial source of photoionizing radiation formulated for studies in this subsection is spherically symmetric and is expected to produce identical distributions of the photoionization production rate $S_{\rm ph}$ in both, the radial and axial directions with respect to the center of the simulation domain. Therefore for the chosen domain sizes with L_d=R_d, the distance from the center to the radial boundary is two times longer than to the axial boundary. This aspect is very useful for demonstration of effects of boundaries and boundary conditions on obtained solutions as well as for direct comparison of performance of the models on different spatial scales.

Figures III.4(a) and III.4(b) show the axial and radial profiles of the photoionization source term $S_{\rm ph}$ calculated by the Zheleznyak integral model and the Helmholtz differential model based on the two-exponential fit, for the domain dimension 0.2×0.2 cm^2. The two components $S^1_{\rm ph}$ and $S^2_{\rm ph}$ of the two-exponential Helmholtz model are also shown. The solutions of Helmholtz equations are obtained using zero boundary conditions. We note that the two-exponential Helmholtz profiles deviate significantly from the Zheleznyak solution, especially near the boundaries. The importance of the boundaries in the context of differential photoionization models has not been discussed in [*Ségur et al.*, 2006] and [*Luque et al.*, 2007].

As already mentioned in Section III.5.1, the Zheleznyak integral model can be used to improve the solution of the Helmholtz model. Using (III.4), the boundary condition is defined for the $S^1_{\rm ph}$ component (i.e., for the one with the smallest λ_j). For the another component $S^2_{\rm ph}$, zero boundary conditions are used. Figures III.4(c) and III.4(d) show axial and radial profiles for the two-exponential model with thus corrected boundary conditions. The solutions are obviously improved. For the Eddington and SP_3 models, the effects of the use of boundary conditions defined for the $S^1_{\rm ph}$ component by the Zheleznyak integral model instead of zero boundary conditions for all components are very similar to those presented in Figure III.4. Then, the related results are not shown here for the sake of brevity. In the remainder of this chapter, except when stated, all Helmholtz, Eddington and SP_3 model results are obtained using the boundary conditions based on the integral Zheleznyak model.

Figures III.5(a) and III.5(b) compare the two and three-exponential Helmholtz model solutions, for the domain dimension 0.2×0.2 cm^2. The ionization term S_i (III.32) is also included for reference, as for streamer simulations, photoionization is important only in regions where S_i<$S_{\rm ph}$. The results obtained with the three-exponential fit appear to match better with the Zheleznyak integral solution. In particular, the solutions near the center of the simulation domain are significantly improved. This directly relates to a better three-exponential fit at small $p_{O_2}R$ values as can be seen in Figure III.2.

Figures III.5(c) and III.5(d) compare the Zheleznyak model with results obtained using

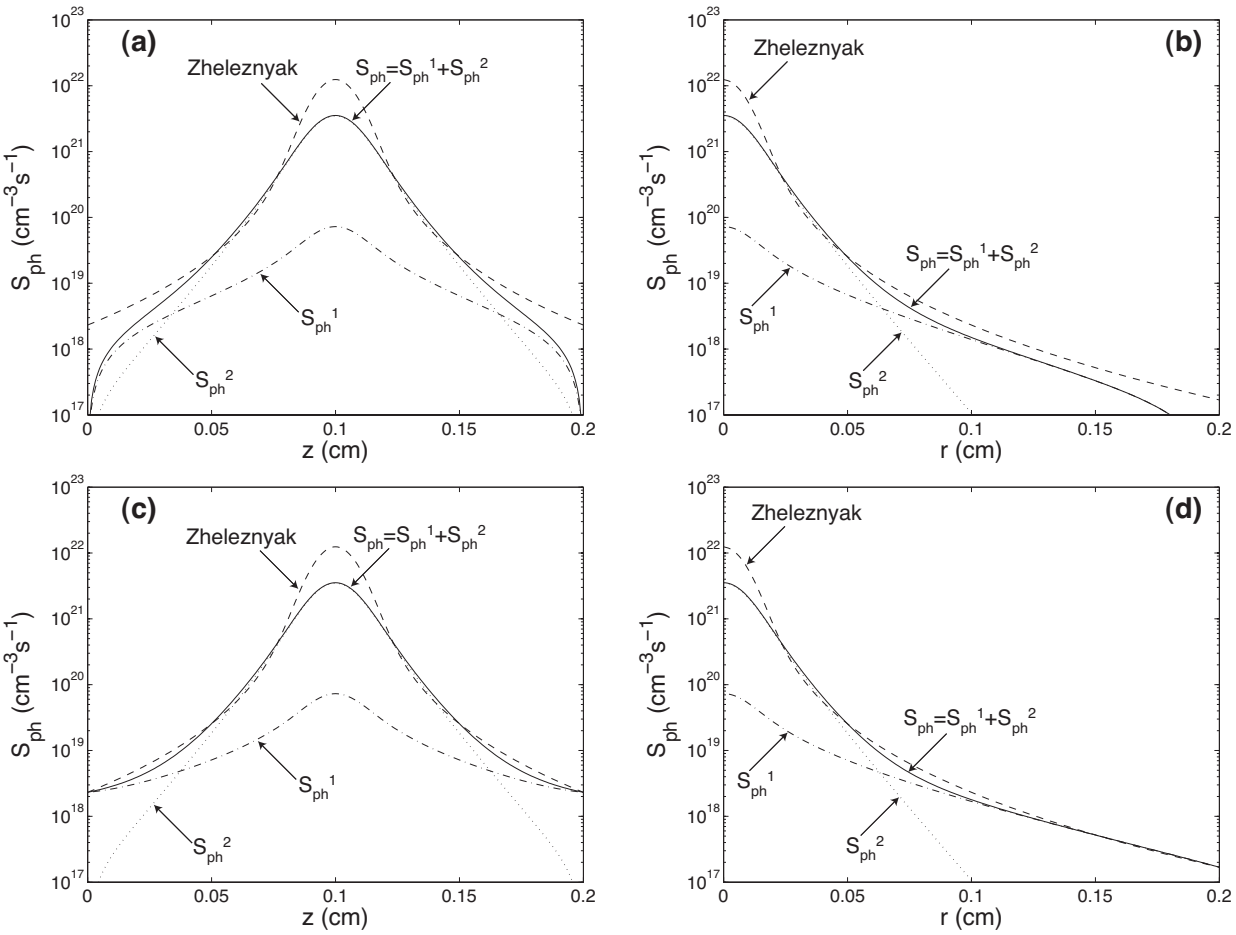

Figure III.4: Axial ((a) and (c)) and radial ((b) and (d)) profiles of the photoionization source term $S_{\rm ph}$ for the case of domain dimension 0.2×0.2 cm^2 and σ=0.01 cm. Dashed line: Results obtained with integral model of *Zheleznyak et al.* [1982]. Solid line: The photoionization source term $S_{\rm ph}$=$S^1_{\rm ph}$+$S^2_{\rm ph}$ calculated using the two-exponential Helmholtz model with zero boundary conditions ((a) and (b)), and with boundary conditions based on Zheleznyak model ((c) and (d)). Dot-dahed line: The $S^1_{\rm ph}$ component. Dotted line: The $S^2_{\rm ph}$ component.

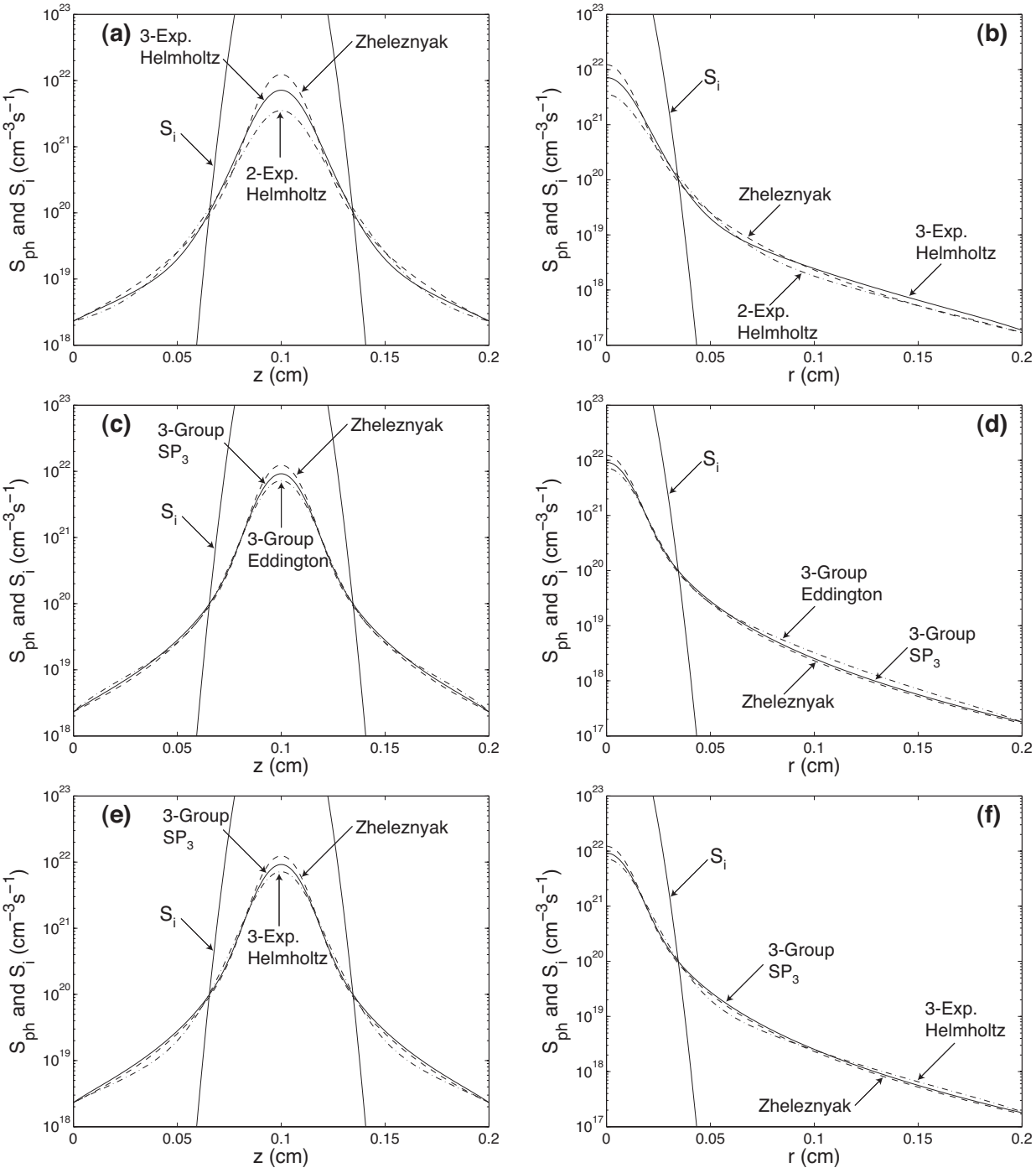

Figure III.5: Axial ((a), (c) and (e)) and radial ((b), (d) and (f)) profiles of the ionization source term S_i and the photoionization source term $S_{\rm ph}$. Dashed line: Results obtained with integral model of *Zheleznyak et al.* [1982]. (a) and (b) Dot-dashed line: $S_{\rm ph}$ using the two-exponential Helmholtz model; Solid line: $S_{\rm ph}$ using three-exponential Helmholtz model. (c) and (d) Dot-dashed line: $S_{\rm ph}$ using 3-group Eddington approximation; Solid line: $S_{\rm ph}$ using 3-group SP_3. (e) and (f) Solid line: $S_{\rm ph}$ using 3-group SP_3 approximation; Dot-dashed line: $S_{\rm ph}$ using 3-exponential Helmholtz model.

the 3-group Eddington approximation and the 3-group SP_3 model, for the same domain dimension. The results shown in these two figures demonstrate that the 3-group Eddington approximation and the 3-group SP_3 model give very similar results in the region where $S_{\text{ph}}>S_i$, and these two solutions also appear to be in good agreement with the Zheleznyak integral model. At atmospheric pressure (p_{O_2}=150 Torr), the three absorption coefficients of the three-group Eddington and SP_3 models given in Table III.3 are $\lambda_1 p_{O_2}$=6 cm^{-1}, $\lambda_2 p_{O_2}$=16 cm^{-1} and $\lambda_3 p_{O_2}$=89 cm^{-1}. It is interesting to note that even if the Eddington and SP_3 are in principle only very well suited to situations in which photon absorption is sufficiently high [*Ségur et al.*, 2006], Figure III.5 shows that these approximations can be used to calculate accurately the photoionization source term using a three-group approach for streamer propagation.

Finally, in Figures III.5(e) and III.5(f), we compare the 3-group SP_3 and the 3-exponential Helmholtz model with the Zheleznyak model. The SP_3 model appears to be slightly more accurate in the region where $S_{\text{ph}}>S_i$.

We note that the direct application to the streamer modeling of the Zheleznyak integral model given by equation (III.1), without optimizations specified in Section III.2, is prohibitively computationally expensive. In particular, results obtained in Figure III.5 using the non-optimized Zheleznyak model generally required a factor of 1000 longer computational times than those obtained with the Eddington and Helmholtz models.

Figure III.6 demonstrates comparative performance of the boundary conditions based on the Zheleznyak integral model for the three-group Eddington and SP_3 models (equations (III.28) and (III.29), respectively) and Marshak's boundary conditions for the three-group Eddington (equations (III.30)) and Larsen's boundary conditions for the three-group SP_3 (equations (III.31)). We note that whatever the boundary conditions used, the results are very close to the photoionization source term calculated with the Zheleznyak integral model in the whole computational domain. Nevertheless, the use of Larsen's boundary conditions for the SP_3 model and Marshak's boundary condition for the Eddington model slightly overestimates the exact value of the photoionization source term at the boundaries in the axial direction, but the agreement is good in the radial direction. As already mentioned in Section III.5, equations (III.26) and (III.30) for the Eddington approach and the equations (III.21–III.22) and (III.31) for the SP_3 approach, respectively, form a coherent set of closed equations. Furthermore, these differential boundary conditions are simple to implement and very fast to calculate.

Finally, in Figure III.7 we compare the profiles of each component S_{ph}^j for $j = 1, 3$ of the three-group SP_3 approach, calculated with boundary conditions based on the Zheleznyak integral model for the S_{ph}^1 component and with the Larsen's boundary conditions for all components. We note significant discrepancies in the evolutions of the different components of S_{ph} close to the boundaries. As expected, the profiles obtained with Larsen's boundary conditions appear to have more physical evolutions close to boundaries than those with boundary conditions based on the Zheleznyak model.

In conclusion, all the results obtained in this section show that the use of non-zero boundary conditions improves significantly the agreement between the Zheleznyak integral and the approximate differential models. In this work, we have used boundary conditions specified on the basis of the classic integral model of Zheleznyak and for the Eddington and SP_3 models, we have shown that a coherent set of approximate boundary conditions derived

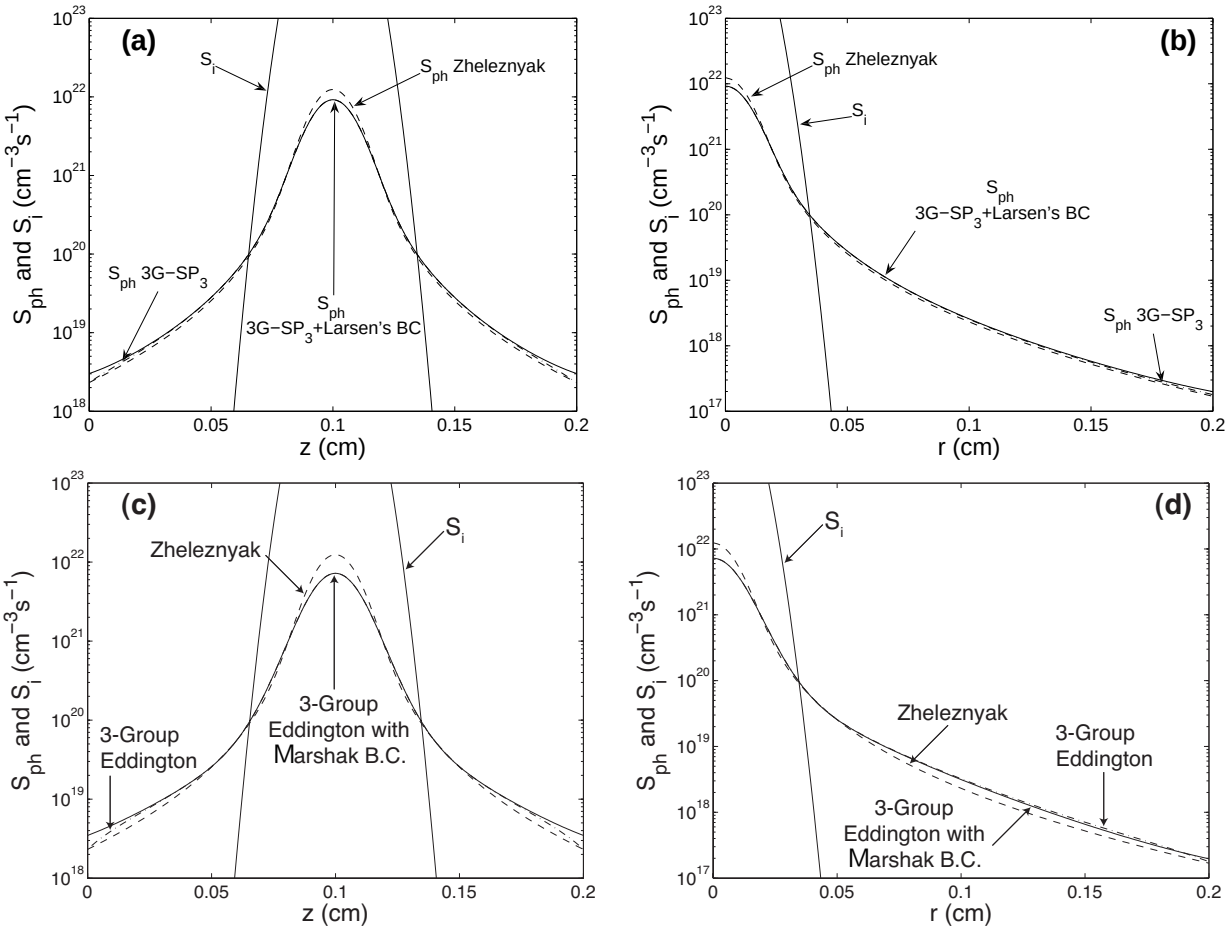

Figure III.6: Axial ((a) and (c)) and radial ((b) and (d)) profiles of the ionization source term S_i and the photoionization source term $S_{\rm ph}$. (a) and (b) present results computed using the the three-group SP_3 approximation, and (c) and (d) present results computed using the three-group Eddington approximation. Dashed line: $S_{\rm ph}$ using the integral model of *Zheleznyak et al.* [1982]. Solid line: $S_{\rm ph}$ computed using the Larsen's boundary conditions (III.31) ((a) and (b)) or using the Marshak's boundary conditions (III.30) ((c) and (d)); Dot-dashed line: $S_{\rm ph}$ computed using boundary conditions given by equation (III.29) ((a) and (b)) or using boundary conditions given by equation (III.28) ((c) and (d));

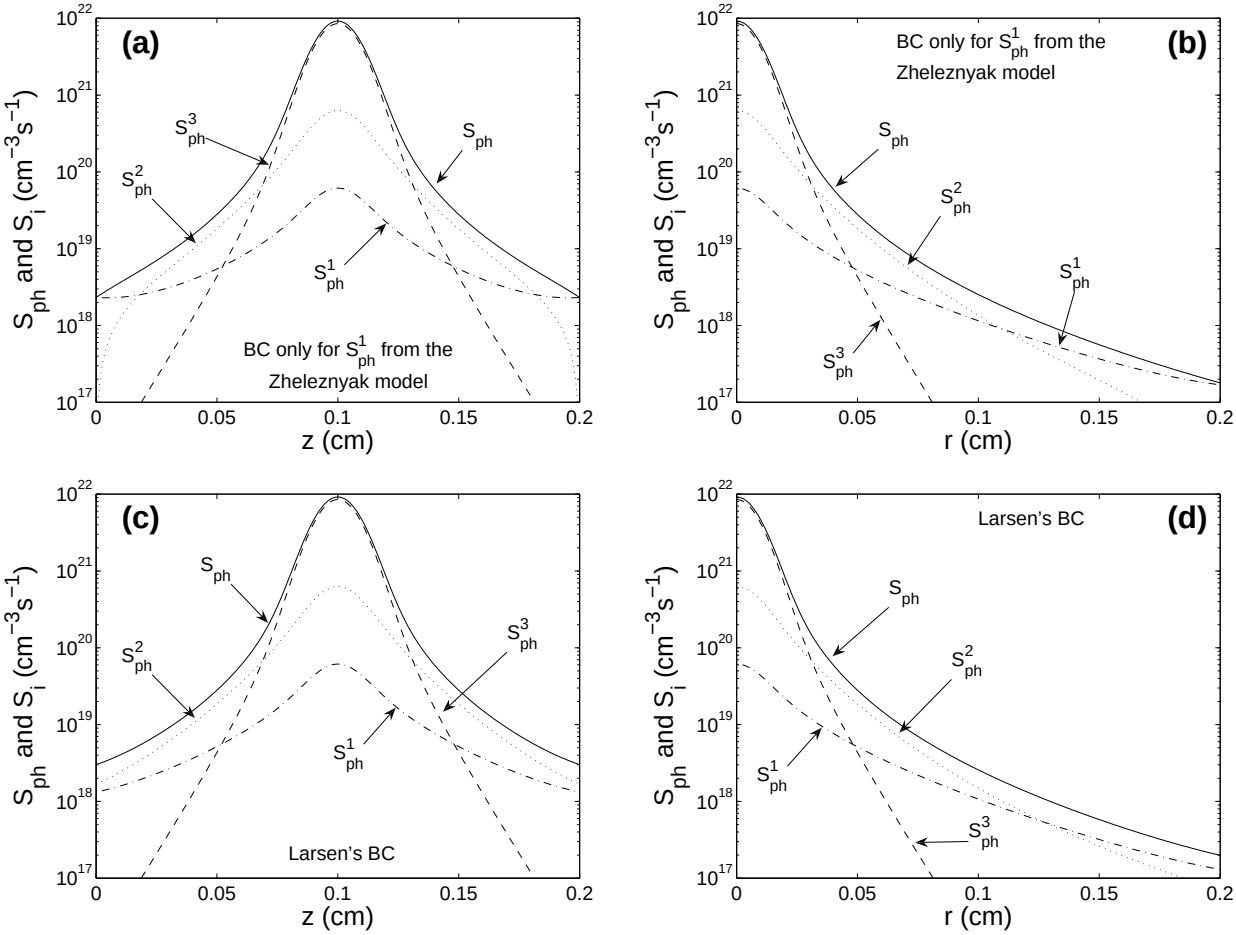

Figure III.7: Axial ((a) and (c)) and radial ((b) and (d)) profiles of the photoionization source term $S_{\rm ph}$ from the three-group SP_3 model and its three components $S^1_{\rm ph}$, $S^2_{\rm ph}$ and $S^3_{\rm ph}$ computed using the boundary conditions given by the *Zheleznyak et al.* [1982] model on the first component (III.29) ((a) and (b)), and given by *Larsen et al.* [2002] (III.31) ((b) and (c)). Solid line: The photoionization source term $S_{\rm ph}$; Dot-dashed line: The $S^1_{\rm ph}$ component; Dotted line: The $S^2_{\rm ph}$ component; Dashed line: The $S^3_{\rm ph}$ component.

from radiation transfer theory can be successfully used. We have also shown that the use of a three-exponential fit either with the SP_3 model or with the Helmholtz model allows to obtain a good agreement with the Zheleznyak integral model, and that the two-exponential fit is generally not sufficient to reproduce the Zheleznyak model accurately for the full range of validity of this model (i.e., up to $p_{O_2}R \simeq 100$ Torr cm, or $R \simeq 0.7$ cm at ground pressure [*Naidis*, 2006]; see Appendix A). It is interesting to note also that although the Eddington and SP_3 are in principle only very well suited to situations in which photon absorption is sufficiently high, these approximations can be used to calculate accurately the photoionization source term using a three-group approach for streamer propagation. The models derived in this chapter are only slightly more complicated than the one-group model proposed in [*Ségur et al.*, 2006], but remain simple to implement in streamer codes. Results of the practical application of these models to streamer problems are presented in the next section, in which we also discuss computational expenses involved in different types of photoionization models.

III.6.2 Streamer simulations

In this section, the three-exponential Helmholtz, and the three-group Eddington and SP_3 differential photoionization models are used for two realistic problems:

- the development of a double-headed streamer in a high electric field ($>E_k$) at ground pressure,
- the streamer propagation in weak external electric fields ($<E_k$) at ground pressure.

The validity and range of applicability of the developed models for the photoionization term is demonstrated by performing direct comparisons of the results from these models and results obtained from the classic integral model of *Zheleznyak et al.* [1982].

In this work we use the drift-diffusion equations of the streamer fluid model (I.28)-(I.30) coupled to Poisson's equation (I.31). On timescales of interest for studies presented in this chapter, ions are assumed to be motionless. For test studies presented in this chapter all transport parameters and reaction rates in air are taken from [*Morrow and Lowke*, 1997]. Axisymmetric streamers are studied and thus cylindrical coordinates introduced in Section III.2 are used.

In this section, two sets of numerical techniques are used for solving the streamer model equations:

1. The charged species transport equations are solved using a flux-corrected transport (FCT) method (see paragraph "FCT method" in Section II.2.2). The 3rd order QUICKEST scheme is used as the high order scheme and an upwind scheme for the low order scheme. The flux limiter derived by *Zalesak* [1979] is adopted for this FCT method. The finite difference form of the Poisson's equation is solved using the D03EBF module of the NAG Fortran library (`http://www.nag.co.uk`).
2. The charged species transport equations are solved using a modified Scharfetter-Gummel (SG) algorithm (see paragraph "Modified SG scheme" in Section II.2.2), and the finite difference form of Poisson's equation is solved by successive overrelaxation (SOR) method [see *Liu and Pasko*, 2004, and references cited therein].

It is interesting to note that we have also carried out some streamer simulations using the direct solver SuperLU [*Demmel et al.*, 1999a, b] (http://crd.lbl.gov/~xiaoye/SuperLU/) to solve the Poisson's equation. The results obtained have been found to be very close to those given by iterative solvers.

The boundary conditions for the potential required for the solution of the Poisson's equation are obtained using integral solutions of the Poisson's equation, which accounts for the known charge distribution inside of the simulation domain (see Section II.1.2). As stated in Section II.1.2, the applied technique allows to use a relatively small simulation domain in transverse (i.e., radial) direction to obtain an accurate solution for the electric potential.

The calculation of the boundary conditions in streamer simulations can be significantly accelerated since only a small number of grids inside of the simulation domain (usually around streamer body and streamer head(s)) possesses charge density values significantly contributing to the potential values at the boundary. In practical calculations the simulation domain is scanned to find the maximum magnitude of the charge density value $|\rho_{\max}|$, and it has been verified by separate tests that accounting only for grids with charge density magnitudes, which exceed 0.1% of this value (i.e., $|\rho|$>0.001 $|\rho_{\max}|$) leads to fast, accurate and robust evaluation of boundary conditions for potential, allowing effective use of simulation domains with very small size in radial direction. Further improvements in terms of execution speed can be achieved due to a relatively smooth spatial variation of the potential at the boundaries. The potential can be evaluated at a selected set of points and interpolation can be used to obtain the values at all grid points constituting the boundary. Due to a very small time step used in streamer modeling (usually defined by the ionization time scale associated with the large electric field in the streamer head as already mentioned above) it is also possible, especially for preliminary test runs, to evaluate boundary conditions only once during several steps of the model execution. However, for all streamer results presented in this section the update of potential boundary conditions has been performed at every time step for maximum accuracy of results.

For photoionization calculations in the streamer model we employ techniques discussed in Sections III.2, III.3 and III.4. Specifically, for the present study we have implemented the three-group Eddington and SP_3, the three-exponential Helmholtz, and the classical integral models. The quenching pressure is assumed to be $p_q = 30$ Torr, and the ratio $\xi\nu_u/\nu_i$, appearing in (III.2), is assumed to depend on the reduced electric field as specified in [*Liu and Pasko*, 2004]. The finite difference forms of the Eddington, SP_3 and Helmholtz photoionization model equations are solved using the same module of the NAG Fortran library used for the solution of the Poisson's equation. It is interesting to note that we have also carried out tests using the direct solver SuperLU (see Section II.1.3) for the computation of the photoionization source term based on the Eddington and SP_3 models. The results have been found to be very close to those obtained using the iterative solvers. The three differential models for photoionization are implemented within the context of the first set of numerical techniques described above (i.e., the FCT based). Within the context of the second set of numerical techniques (i.e., the SG based), we implemented the classical integral and the Helmholtz models. The finite difference equations of the Helmholtz photoionization model are solved by the SOR method for this case. The modeling results obtained by using different numerical techniques to solve the Helmholtz model equations are very similar and we will not differentiate them in the following sections of this chapter.

Double-headed streamers in air

In this section, we report and compare modeling results on a double-headed streamer developing in air at ground pressure (760 Torr) obtained with the different photoionization models discussed in this chapter. The simulation domain is the same as in [*Liu and Pasko*, 2004, Figure 4a]. Two remote electrodes with a certain potential difference establish a uniform Laplacian field E_0=4.8×10^6 V/m. All results are obtained assuming air neutral density N_0=2.688×10^{25} m^{-3}, and therefore E_0/N_0=178.6 Td (1 Td=10^{-17} V cm^2). Under the influence of this applied field, a double-headed streamer is launched by placing a neutral plasma cloud in the simulation domain. The initial plasma cloud has a Gaussian distribution in space:

$$n_e(r,z)|_{t=0} = n_p(r,z)|_{t=0} = n_0 \exp\left[-\left(\frac{r}{\sigma_r}\right)^2 - \left(\frac{z-z_0}{\sigma_z}\right)^2\right]. \tag{III.34}$$

The center of the Gaussian distribution is located in the middle of the simulation domain, at z_0=0.7 cm, and it is assumed that σ_r=σ_z=0.02 cm and n_0=10^{20} m^{-3}. The size of the computational domain is 1.4 × 0.125 cm^2. The computational grid is uniform in both radial and axial directions. The total number of cells is n_z×n_r=1681×151, where n_z and n_r represent number of cells in the axial and radial directions, respectively. As part of preparatory work for the model studies presented in this chapter we have conducted several test runs with 2400×100 grid points with a refined mesh in the radial direction and uniform mesh in the axial direction. Results appeared to be identical to those obtained with the 1681×151 uniform mesh, which therefore was adopted for all runs presented in this section.

Concerning the photoionization source term, it has been verified by practical tests that very accurate results for the photoionization production rate can be obtained even if the photoionization is calculated once during every ten steps of the execution of the streamer model. This approach is justified due to the very small time step used in the streamer modeling. Additionally, for photoionization calculations the S_{ph} term is usually negligible in the immediate vicinity of the streamer head due to the domination of the ionization term S_i, and electrons created by photoionization well ahead of the streamer head go through a relatively long (in comparison with the model time step) evolution and avalanche multiplication before they affect the dynamics of the streamer head.

Before the incorporation of different photoionization models, we tested the performance of the two sets of numerical techniques described in Sections II.2.2 and II.2.2 (i.e., the FCT and SG based) using a double-headed streamer test case for which photoionization effects are not included and the pre-ionization level is only supplied by a uniform neutral background plasma with initial density of 10^{14} m^{-3}. This approach is similar to the one applied in a classic paper of *Dhali and Williams* [1987]. Only very small differences are observed in results obtained with the two models for the modeled double-headed streamer. Specifically, by the time moment 3.5 ns from the beginning of the model execution the differences between the peak electron number densities and peak electric fields between two model streamers do not exceed 7.8% and 2.6%, respectively. It is noted that these differences do not exceed those arising from known limitations of the local field approximation in streamer modeling [*Naidis*, 1997; *Li et al.*, 2007] (see Section I.3.5). The test results concerning the double-headed streamer are not shown in this thesis for the sake of brevity, but essentially the same agreement between the two numerical techniques can be observed

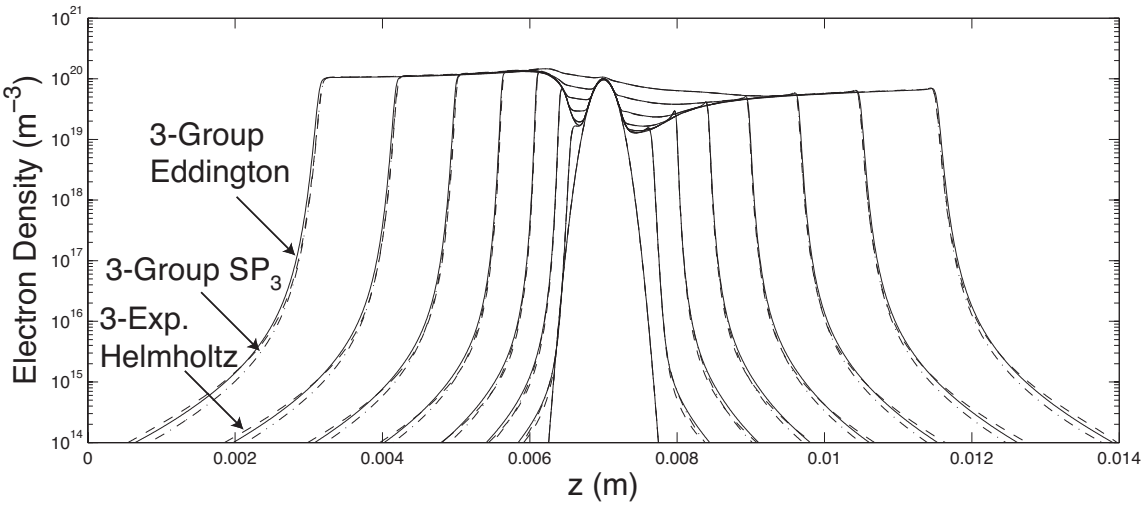

Figure III.8: Electron density profiles on the symmetry axis of the computational domain at various moments of time calculated using different photoionization models. The results are obtained by the FCT based numerical technique described in Section III.6.2. Dashed line: Three-exponential Helmholtz model; Solid line: Three-group Eddington; Dot-dashed line: Three-group SP_3. Results are shown for the moments of time from $t = 0$ to $t = 3.5$ ns, with a timestep of 0.5 ns.

by comparing results obtained with the three-exponential Helmholtz photoionization model shown in Figures III.8 and III.9(a).

Figure III.8 compares the electron number density distribution on the symmetry axis of the computational domain calculated using the three-group Eddington and SP_3, and the three-exponential Helmholtz models for the photoionization term. The results are shown for the moments of time from $t = 0$ to $t = 3.5$ ns, with a timestep of 0.5 ns. We note that there is an excellent agreement between the results obtained with these three models for both streamer heads. Small differences are observed in the region well ahead of the streamer head, and the differences increase as the streamer advances.

Figure III.9 compares the profiles of electron density and the magnitude of the electric field on the symmetry axis of the computational domain calculated using the three-exponential Helmholtz model for the photoionization term and the classical integral model of *Zheleznyak et al.* [1982] optimized as described in Section III.2. The results are also shown for the moments of time from t=0 to t=3.5 ns, with a timestep of 0.5 ns. An excellent agreement between the results is observed for the double-headed streamer. For the electron density, only small differences exist in the region well ahead of the streamer head. For electric field, the difference is almost impossible to notice before 3.0 ns and extremely small deviations between results obtained with the two models are present at 3.0 and 3.5 ns. The differences for both electron density and electric field increase as the streamer advances.

Figure III.10 shows a cross-sectional view of the distributions of the electron density, electric field and photoionization production rate at t=3.5 ns obtained using the three-exponential Helmholtz model. This cross-sectional view represents an example of two-dimensional views of simulation results obtained by using different differential equation based photoionization models. As expected, the photoionization source term is maximized in the head regions, but we also note that this term is significant in the body of the streamer in the region between

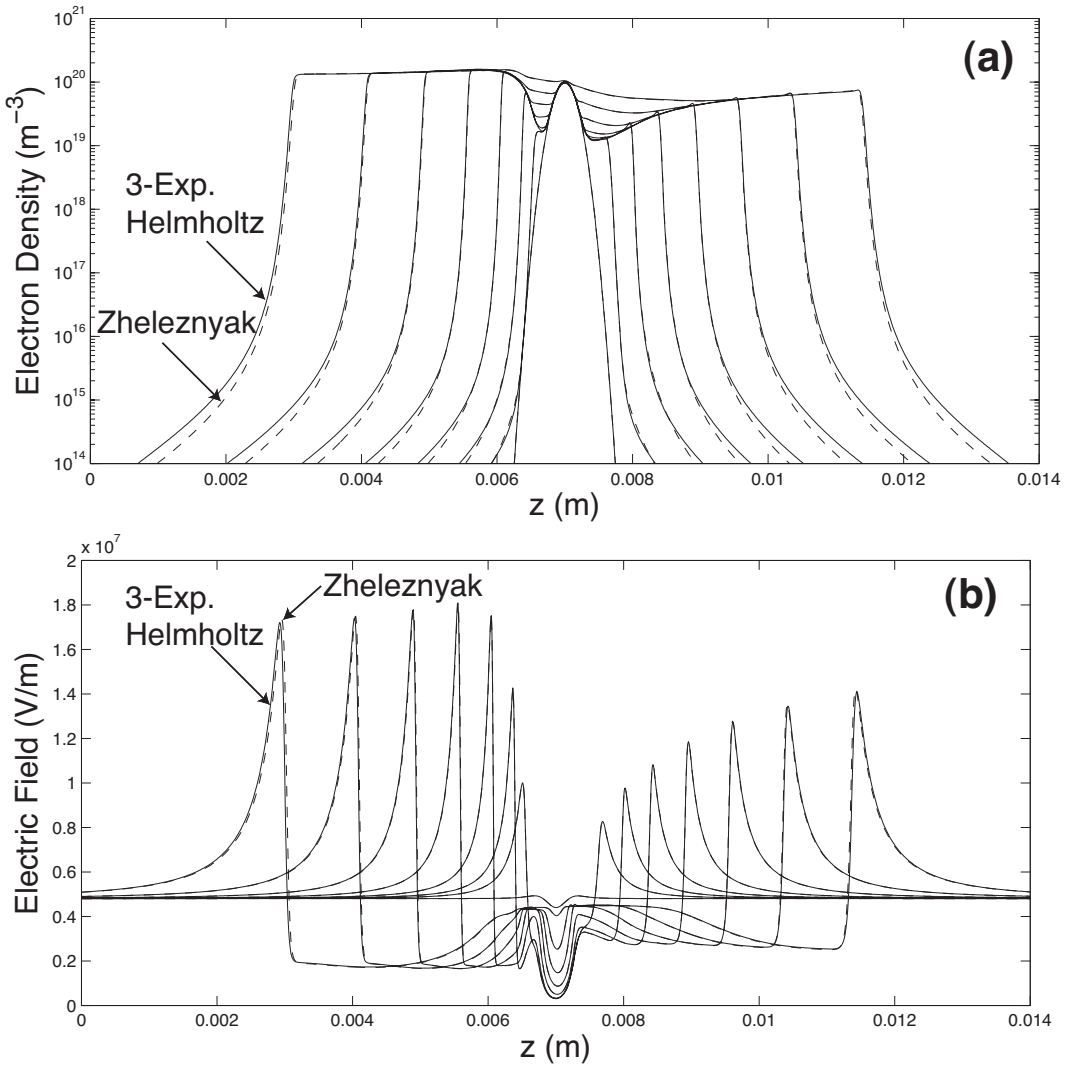

Figure III.9: Profiles of streamer characteristics along the symmetry axis of the computational domain at various moments of time calculated using different photoionization models. The results are obtained by the SG based numerical technique described in Section III.6.2. (a) Electron density. (b) Electric field. Dashed line: Optimized integral Zheleznyak model; Solid line: Three-exponential Helmholtz model. Results are shown for the moments of time from $t = 0$ to $t = 3.5$ ns, with a timestep of 0.5 ns.

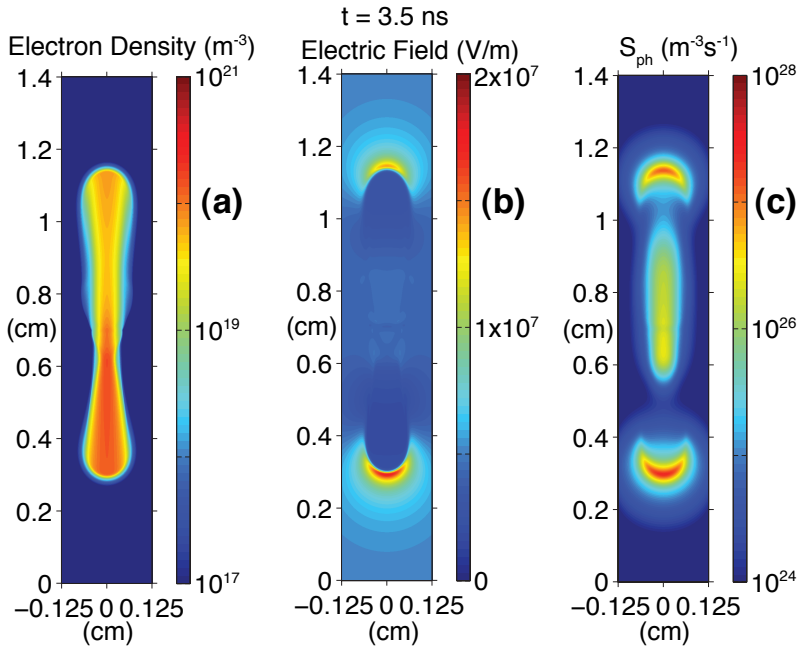

Figure III.10: A cross-sectional view of distributions of (a) electron density, (b) electric field and (c) photoionization source term at $t = 3.5$ ns calculated using the three-exponential Helmholtz model.

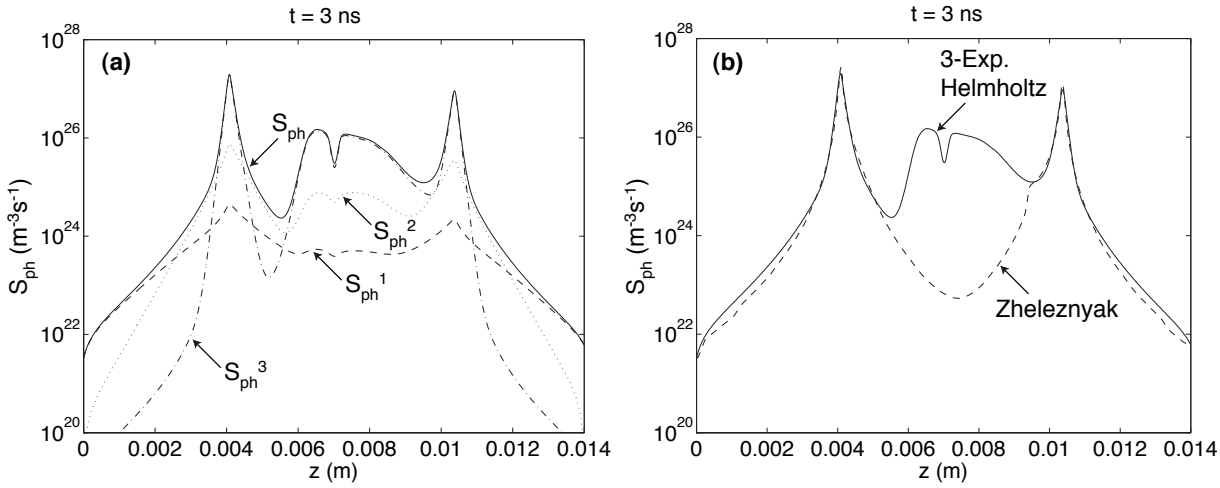

Figure III.11: Photoionization source term S_{ph} at t=3 ns along the symmetry axis of the computational domain. (a) S_{ph} and the three components S^1_{ph}, S^2_{ph} and S^3_{ph} of the three-exponential Helmholtz model. (b) S_{ph} calculated using the three-exponential Helmholtz and the optimized integral Zheleznyak models.

the two heads. As expected on physical grounds and as apparent from Figure III.10(c) the photoionization production rate appears to exhibit a high degree of spherical symmetry around both streamer heads. The direct inspection of Figure III.10(c) also emphasizes the importance of accurate definition of boundary conditions for S_{ph}, as simple zero boundary conditions on radial boundaries would clearly produce an unphysical distortion of the photoionization production rate.

Figure III.11(a) shows the S_{ph} term and the relative distributions of the three components of the three-exponential Helmholtz model on the symmetry axis of the simulation domain at $t = 3.0$ ns. The regions dominated by each component can clearly be identified in the figure. The S^1_{ph} term, associated with the smallest λ_1 and therefore with the longest photoionization range (which from the general structure of equation (III.7) is expected to approximately follow $1/\lambda_1$ dependence) dominates in the region ahead of the streamer head. The S^2_{ph} term ranks after S^1_{ph} demonstrating intermediate λ_2 value and the photoionization range (see Table III.2), while S^3_{ph} term is clearly confined and dominates inside of the streamer head (this term has the largest λ_3 as can be seen from Table III.2 and therefore is associated with the shortest photoionization range).

Figure III.11(b) compares the photoionization source term calculated by the three-exponential Helmholtz model described in Section III.3 and the optimized integral Zheleznyak model described in Section III.2. Results from both models are in a very good agreement in the regions of, and ahead of both positive (left) and negative (right) streamer heads. A significant difference is observed in the region between the streamer heads. We recall that the optimized integral solution described in Section III.2 does not include contributions from the emission sources outside of the square around each of the streamer heads (see Figure III.1(b), and discussion in at the end of Section III.2), but the Helmholtz solution does. A relatively strong ionization appears in the streamer body (Figure III.12(b)) implying strong photon emission source in this region. The Helmholtz model automatically accounts for this source by the right-hand-side term in equation (III.8). However, the photoionization source in the streamer body does not affect the dynamics of the streamer, because the electron impact ionization rate S_i is much stronger than the photoionization rate S_{ph} in the streamer body, as illustrated in Figure III.12(b).

As a follow up from discussion presented in the previous paragraph it is worthwhile to reiterate that photoionization plays a role in the streamer dynamics only when it dominates over ionization in certain regions. Figures III.12(a) and III.12(b) compare the photoionization source term S_{ph} calculated with the three-group SP_3 model and the ionization source term S_i at two different moments of time: $t = 0.2$ ns and $t = 3$ ns. At $t = 0.2$ ns, we note that in the streamer head regions the ionization term S_i exceeds the photoionization term S_{ph}. In front of the streamer heads, the photoionization source term dominates. Very rapidly as streamer starts to propagate, the ionization term becomes stronger than the photoionization term everywhere in the simulation domain as shown, for example, by Figure III.12(b) at $t = 3$ ns. These results support the conclusion made in [*Kulikovsky*, 2000a] that "In high field the streamer behaves as a flash lamp; it produces very intensive radiation when it arises and then the initial photoelectrons provide its propagation." This conclusion is only valid for streamers propagating in a high applied electric field E exceeding the conventional breakdown threshold field E_k defined by the equality of the electron impact ionization and electron dissociative attachment coefficients in air [*Raizer*, 1991, p. 135]. It is expected that the photoionization term would dominate over the ionization term

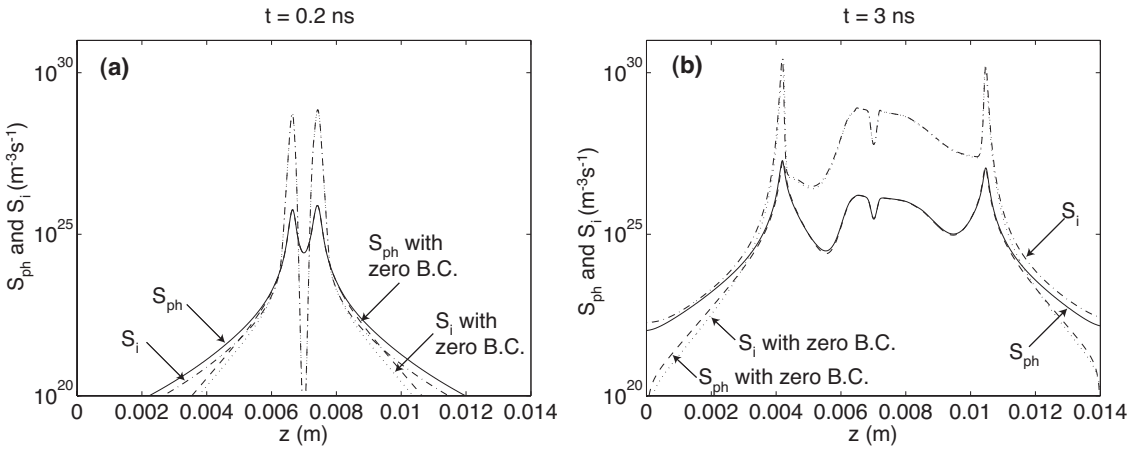

Figure III.12: Photoionization source term $S_{\rm ph}$ and ionization source term S_i along the symmetry axis of the computational domain at (a) $t = 0.2$ ns and (b) $t = 3$ ns. Solid line: the three-group SP_3 with boundary conditions based on Zheleznyak model. Dot-dashed line: ionization term with boundary conditions based on Zheleznyak model for photoionization. Dashed line: the three-group SP_3 with zero boundary conditions. Dotted line: ionization term with zero boundary conditions for photoionization.

in most of the region ahead of a streamer propagating in a low ambient field ($E<E_k$) in a point-to-plane discharge geometry where the dissociative and three-body attachment of electrons is dominant over the ionization. This case is studied in the next section.

Figures III.12(a) and III.12(b) also show the photoionization source term $S_{\rm ph}$ and the ionization term calculated for a case when zero boundary conditions for the photoionization term $S_{\rm ph}$ in SP_3 model are used. In this case, we note that in the regions of the streamer heads the ionization term dominates over photoionization term, however, the photoionization term is at all moments of time stronger than the ionization term in the region ahead of both streamer heads. This observation reiterates that the boundary conditions for the photoionization calculation have a significant impact on the ionization term as photoionization provides the initial photoelectrons for ionization in high fields. Figures III.12(a) and III.12(b) indicate that in the regions ahead of streamer heads, both photoionization and ionization terms significantly deviate from those calculated using boundary conditions based on the Zheleznyak model for $S_{\rm ph}$. We emphasize that even with these noticeable differences in ionization and photoionization, the characteristics (e.g., distributions of the electron density and electric field, speed, and radius) of the modeled streamer are still very close to the case with boundary conditions based on the Zheleznyak model for photoionization. Therefore, for this high field test-case to speed up calculation, it is possible to use zero boundary conditions for photoionization calculation if the goals of the study do not include detailed studies of properties of the ionization or photoionization in the region ahead of the streamer heads. However, as we already mentioned above, for other situations such as the propagation of streamers in low fields in point-to-plane discharge geometry when two and three-body attachment dominates over ionization in the most of the simulation domain ahead of the streamer [i.e., *Babaeva and Naidis*, 1997; *Liu and Pasko*, 2006, and references therein], it is essential to correctly take into account boundary conditions for calculation of the photoionization term.

It is instructive to compare the total execution times of the models based on differential

equation approach in comparison with the optimized integral Zheleznyak model. We have noticed that the simulation time of the three-group Eddington approach with boundary conditions given by equation (III.28) is similar to the one of the three-exponential Helmholtz model with boundary conditions based on Zheleznyak model given in Section III.3, whereas the simulation time of the three-group SP_3 with boundary conditions given by equation (III.29) is slightly longer. As an example of such comparisons we conducted accurate measurements of computation times involved in two model cases shown in Figure III.9. We reiterate that both models are executed on the same hardware (2 GHz Power Mac G5 running Mac OS X 10.4) with identical grids and algorithms to define time steps and boundary conditions. As already mentioned, the photoionization production rate has been updated after every ten steps of the model execution and the boundary conditions for the electric potential have been updated every time step. The measured total execution time of the code based on the optimized implementation of the *Zheleznyak et al.* [1982] integral photoionization model as described in Section III.2 was 53 hours and 20 minutes. The measured execution time of the code based on the three-exponential Helmholtz model with boundary conditions based on Zheleznyak model described in Section III.3 was 63 hours and 14 minutes. The time profiling indicates that about 80% of the model execution time is spent in both cases on updates of the boundary conditions for the potential and the solution of the Poisson equation for the electric field. It is noted that even if the photoionization production rate is updated at every time step, the execution times of both models will be of the same order.

The difference in the computation time presented above may seem in favor to the integral photoionization model, however, it is important to point out that the optimization (introduction of moving meshes with variable cell sizes and employment of effective windowing and interpolation techniques) of the integral model is rather involved and complex, and requires a separate adaptation effort to extend it to every new configuration studied. At the same time, the implementation of the photoionization models based on differential equation approach is straightforward and simple. Furthermore, in the optimized integral approach the photoionization source term is calculated accurately only close the the streamer heads. For example, in the double-headed test-case, we have shown that due to the optimization, in the region between the streamer heads, the photoionization source term is not calculated accurately using the integral model. Conversely with the differential approaches the photoionization term is calculated accurately in the whole computation domain.

Propagation of streamer in a weak external field

In the present section, we apply the three-exponential Helmholtz and three-group SP_3 models to the simulation of streamers propagating in weak external electric fields ($<E_k$, see I.1.3), which is a configuration where photoionization has a much more significant impact on the streamer dynamics than in the high-field case studied previously. Moreover this weak field condition is of great interest for many practical applications of streamers. We propose to validate the three-exponential Helmholtz and three-group SP_3 models by comparing the corresponding results with those obtained with the Zheleznyak model. The objective of this work is to demonstrate the validity and accuracy of the three-exponential Helmholtz and three-group SP_3 models for studies of streamer discharges in air for a wide range of applied electric fields.

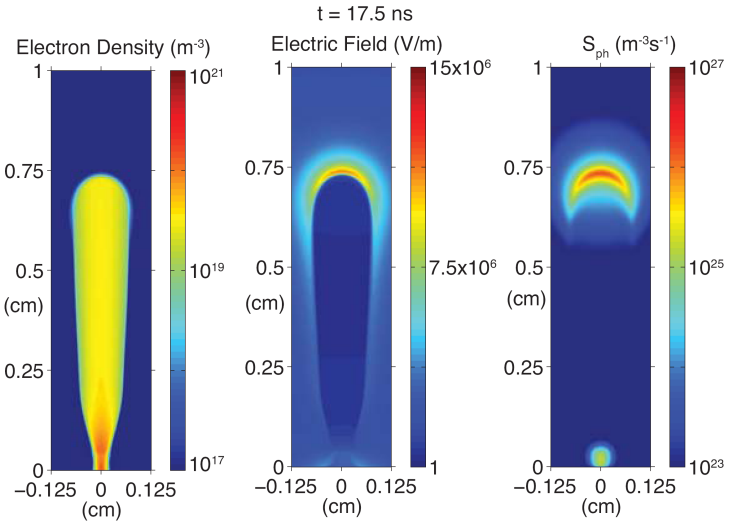

Figure III.13: A cross-sectional view of distributions of (a) electron density, (b) electric field and (c) photoionization rate at $t = 17.5$ ns calculated using the three-exponential Helmholtz model.

Except where noted, in this section we use the efficient Larsen's boundary conditions (III.31) based on radiative transfer theory in the case of three-group SP_3. The boundary conditions for the Helmholtz model are provided by the Zheleznyak integral solution. When the Zheleznyak model is used to calculate the photoionization source term, to optimize the computation of the 3D integral, an inhomogeneous grid with fine resolution around the streamer head and coarse resolution in the region away from the head is employed, and the emission source is assumed to be confined in the streamer head region.

The geometry of the simulation domain is identical to the one employed by *Liu and Pasko* [2006] in which a small conducting sphere is placed in a weak uniform electric field E_0, and is described in Section II.1.2. The air pressure is fixed at a value of 760 Torr. The external homogeneous field E_0 is 10^6 V/m. The radius b and the potential applied to the conducting sphere 0 are 0.1 cm and 6500 V, respectively. To initiate the development of a streamer, as a common practice, we place a cloud of plasma with spherically symmetric Gaussian spatial distribution on the axis of symmetry in the vicinity of the sphere, i.e.,

$$n_e = n_p = n_0 \exp\left(-(r/\sigma_r)^2 - ((z - z_0)/\sigma_z)^2\right) \tag{III.35}$$

where n_e and n_p are densities of electrons and positive ions, respectively, $n_0 = 10^{18}$ m^{-3}, $\sigma_r = \sigma_z = 0.01$ cm, and $z_0 = 0.02$ cm. The size of the computational domain is 1.0×0.125 cm^2. The computational grid is uniform in both radial and axial directions. The numbers of grid points in axial and radial directions are 1601 and 201, respectively.

Figure III.13 shows a cross-sectional view of the distributions of the electron density, electric field, and photoionization production rate at $t = 17.5$ ns obtained using the three-exponential Helmholtz model. This cross-sectional view represents an example of two-dimensional views of simulation results obtained by using different photoionization models. The streamer expands as it propagates (Fig. III.13(a)). The photoionization production rate is maximized in the head region, and there is no significant contribution in the body of the streamer (Fig. III.13(c)). These results are notably different from those obtained for

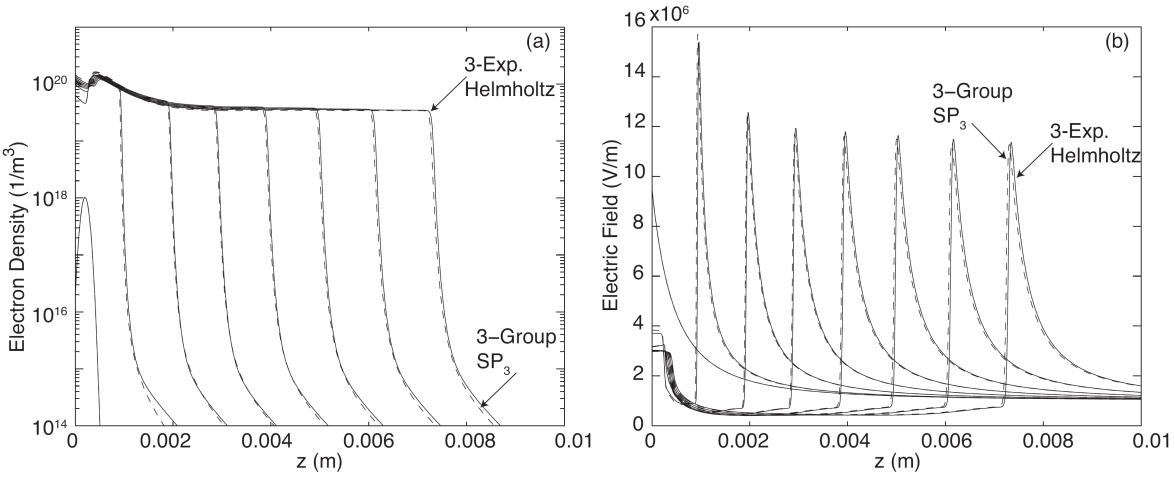

Figure III.14: Profiles of streamer characteristics along the symmetry axis of the computational domain at various moments of time calculated using different photoionization models. The results are obtained by the FCT based numerical technique. (a) Electron density. (b) Electric field. Dashed line: three-group SP_3 with boundary conditions defined by the equation (III.31); Solid line: three-exponential Helmholtz model. Results are shown for the moments of time from $t = 0$ to $t = 17.5$ ns with a timestep of 2.5 ns.

a streamer in strong electric field (see Fig. III.10), for which significant photoionization is present in the streamer body.

Figure III.14 compares the profiles of electron density and the magnitude of the electric field on the symmetry axis of the computational domain calculated using the three-group SP_3 and three-exponential Helmholtz models. The results are shown for the moments of time from $t = 0$ to $t = 17.5$ ns, with a timestep of 2.5 ns. The results obtained with these two models agree very well in terms of the shape of the profiles, and the magnitudes of the channel density and the peak electric field. For the electron density, only small differences exist in the region well ahead of the streamer head. For the electric field, the difference is almost impossible to notice before 15.0 ns, and relatively small deviations are present at 15.0 and 17.5 ns. Figure III.15 compares the profiles of electron density and the magnitude of the electric field on the symmetry axis of the computational domain calculated using the three-group SP_3 (boundary conditions provided by Zheleznyak integral solution), the three-exponential Helmholtz, and the reference Zheleznyak integral models. An excellent agreement between the results obtained with these three models is observed. Results presented in Figs. III.14 and III.15 demonstrate that for practical accuracy calculations all three photoionization models (i.e., Zheleznyak, three-group SP_3, and three-exponential Helmholtz) provide adequate and consistent solutions to the streamer problem. Careful inspection of results presented in Figs. III.14 and III.15 indicates that the modeling results obtained using the SP_3 model are closer to the reference Zheleznyak model results than those obtained with the three-exponential Helmholtz model. The observed better performance of the SP_3 model in comparison with the three-exponential Helmholtz model is consistent with the analysis reported in the appendix B. Furthermore, the possibility of formulating a consistent set of equations and boundary conditions based on radiative transfer physics is a significant advantage of the SP_3 model in comparison with the Helmholtz model.

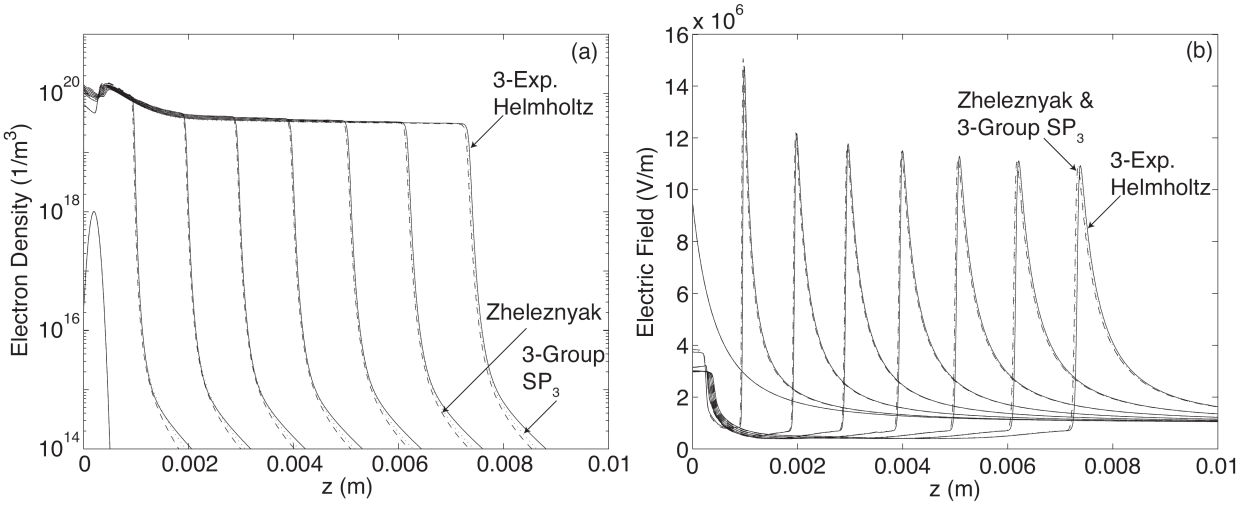

Figure III.15: Same caption as Fig. III.14 except that the results are obtained by the Scharfetter-Gummel (SG) based numerical technique. Dotted line: three-group SP_3 with boundary conditions provided by Zheleznyak integral solution. Dashed line: Zheleznyak model. Solid line: three-exponential Helmholtz model.

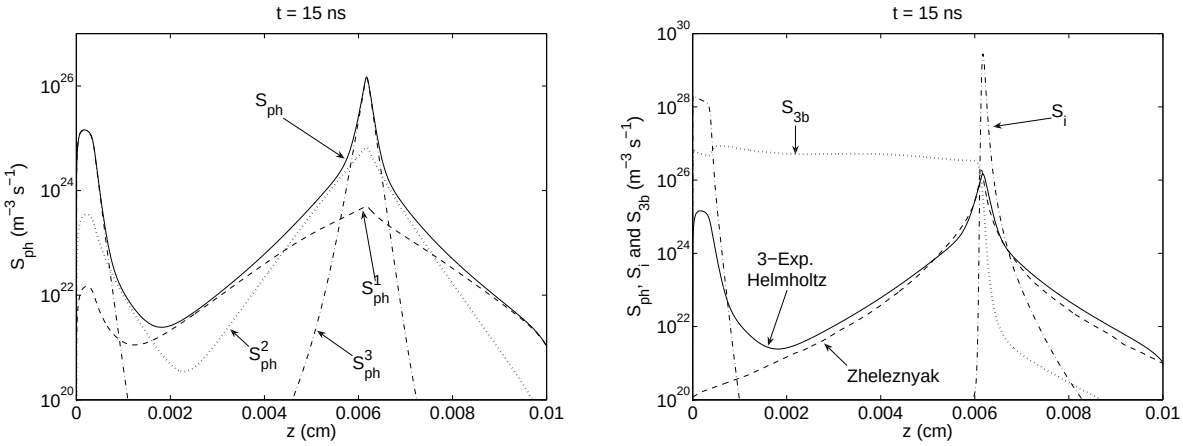

Figure III.16: Photoionization production rate $S_{\rm ph}$ at $t = 15$ ns along the symmetry axis of the computational domain. (a) $S_{\rm ph}$ and the three components $S^1_{\rm ph}$, $S^2_{\rm ph}$, and $S^3_{\rm ph}$ of the three-exponential Helmholtz model. (b) $S_{\rm ph}$ calculated using the three-exponential Helmholtz and Zheleznyak models, electron impact ionization production rate S_i, and three-body electron attachment rate $S_{\rm 3b}$.

Figure III.16(b) compares the photoionization source term calculated by the three-exponential Helmholtz model and the optimized integral Zheleznyak model, the electron impact ionization rate, and the three-body electron attachment rate. For the photoionization production rate, results from both models are in a very good agreement in the region of, and ahead of the streamer head. A significant difference is observed in the region near the spherical electrode. As already discussed for the double-headed streamer test-case, the optimized integral solution does not include contributions from the emission sources outside of the region around the streamer head, but the Helmholtz solution does. A relatively strong photoionization appears in the region near the spherical electrode implying strong photon emission source in this region. The Helmholtz model automatically accounts for this source when solving the Helmholtz differential equation. The agreement of the modeling results obtained using the two photoionization models shown by Fig. III.15 suggests that the different photoionization rates in the region near spherical electrode do not affect the dynamics of the streamer, which is mostly controlled by photons emitted by the streamer head.

Figure III.16(b) further indicates that in contrast to the high applied field case, for which electron impact ionization was a dominant process controlling production and loss of electrons in the entire simulation domain (including streamer head and streamer channel regions), the low field case is characterized by the dominance of three-body attachment in the body of the streamer, the dominance of the electron impact ionization in the streamer head, and the dominance of photoionization in the region ahead of the streamer head.

III.7 Conclusions

In this chapter, we discussed and improved several models currently proposed in the literature for calculation of the photoionization produced by plasma discharges in air. In particular, the classical Zheleznyak integral model and three photoionization models in a differential form are presented. The reported improvements of the differential models are achieved by more accurate accounting for the spectral dependence of the photoionization process. The different approaches presented in this chapter can be directly applied for photoionization calculations in model studies of the dynamics of streamers in air.

An efficient implementation of the classical Zheleznyak integral model is presented for streamer modeling in air. The three differential approaches developed are a three-exponential Helmholtz model, a three-group Eddington, and a three-group improved Eddington (SP_3) models. The Helmholtz model is based on an approximation of the absorption function of the gas in order to transform the integral expression of the photoionization term in a set of Helmholtz differential equations. The Eddington and SP_3 methods are based on the direct numerical solution of an approximation of the radiative transfer equation. It is demonstrated that the solutions involved in all three differential models require accurate definition of the boundary conditions.

We have conducted three test studies of the performance of the newly proposed photoionization models: Gaussian emission source, a double-headed streamer developing in a strong uniform electric field (greater than the conventional breakdown field) and the positive streamer propagation in weak external fields (less than the conventional breakdown field).

Our studies using the Gaussian source have demonstrated that the use of a three-exponential fit to the absorption function in air either with the Eddington, SP_3 or the Helmholtz model allows to obtain a good agreement with the Zheleznyak integral model, and that single or two-exponential fits do not allow to reproduce the Zheleznyak model accurately. We have also demonstrated that a proper setting of boundary conditions improves significantly the agreement between the Zheleznyak model and the three differential models.

Our model studies of the double-headed streamer have demonstrated that with the three-group Eddington, the three-group SP_3, or the three-exponential Helmholtz models, the calculated streamers are very similar to the one calculated using the classical Zheleznyak integral model. It is particularly interesting to note that Eddington and SP_3 models, which are in principle only very well suited to situations in which photon absorption is sufficiently high, can be used to calculate very accurately the photoionization source term using a three-group approach even if some effective absorption coefficients in the model are small. The comparison of the photoionization and ionization source terms for the studied case of strong uniform applied field indicates that photoionization only plays a role during the very early stage of the development of the streamer.

Our studies on the propagation of a positive streamer in a weak field have demonstrated that with the three-group SP_3, or the three-exponential Helmholtz models, the calculated streamers are very similar to the one calculated using the classical Zheleznyak integral model. It is important to note that in this case, the streamer dynamics is much more affected by the photoionization than in the external high-field propagation case.

In this work, we have also compared streamer modeling results obtained using different numerical techniques to solve the transport equations for charged particles: the Zalesak flux-corrected transport (FCT) method and the modified Scharfetter–Gummel (SG) algorithm. We have also utilized different techniques for solution of the Poisson's field equation: the D03EBF module of the NAG Fortran library and the SOR method, which are used in conjunction with the FCT and SG transport algorithms, respectively. Moreover, we have realized tests with the direct solver SuperLU which completely confirm the obtained results with the iterative solvers. The results of solution of the same streamer problem obtained by the FCT method based on a 3rd order QUICKEST scheme and an upwind scheme, and by the modified SG algorithm demonstrate that both numerical techniques lead to accurate and consistent solutions of the streamer problem.

The results of accurate measurement of computational time involved in calculations using different photoionization models for the considered modeled streamer are presented, which indicate, in particular, that the computational times of the differential and optimized integral models for the model case considered in the present study are of the same order. However, it is important to mention that a significant acceleration of the integral models in simple cases of single or double-headed streamers studied with these models to date has been possible due to introduction of moving meshes with variable cell sizes and employment of effective windowing and interpolation techniques. The details of related algorithms are presented in the present chapter. It is important to stress that the optimization of the integral model is rather complex and requires to be separately adapted to every new configuration studied. Conversely, the implementation of the photoionization models based on differential equation approach is straightforward and simple. Furthermore, in the optimized integral approach the photoionization source term is calculated accurately only close to the streamer heads. For example, in the double-headed test-case, we have shown that in

the optimized integral model the photoionization source term is not calculated accurately in the region between the streamer heads (see discussion of Figure III.11(b) in Section III.6.2). Conversely with the differential approaches the photoionization term is calculated accurately in the whole computation domain.

Although the different photoionization models are only used to model streamer discharges in air in this study, we expect that the models can be applied to evaluating the photoionization effects in other forms of plasma discharges in air. In addition, the extension of the photoionization models to other gases is possible if the information on all emission, absorption and photoionization coefficients of the studied gas is available.

The presented results document the range of applicability of the newly developed photoionization models and emphasize that the accurate formulation of boundary conditions represents an important task needed for a successful extension of the proposed formulations to two- and three-dimensional physical systems with obstacles of complex geometry (i.e., electrodes, dust particles, aerosols, etc.), which are opaque for the photoionizing UV photons. We have demonstrated that accurate definition of the boundary conditions can be effectively introduced with the Zheleznyak integral model. For the Eddington model we have also demonstrated performance of a set of boundary conditions consistent with the first order approximation of the radiative transfer equation, the so-called Marshak's boundary conditions (III.30). These boundary conditions are simple, fast to compute and easy to adapt to any configuration. This is also possible with the SP_3 model by using the Larsen's boundary conditions (III.31). The possibility to formulate such a consistent set of equations and boundary conditions based on radiative transfer physics is a significant advantage of the Eddington and SP_3 models in comparison with the Helmholtz model.

We emphasize that the actual advantage of differential models advanced in this chapter in comparison with the integral model lies in the simplicity of implementation of this type of models, and in unquestionable simplicity of extension of these models to complex two- and three-dimensional simulation geometries, involving, for example, propagation of multiple streamer heads in the same simulation domain, and the presence of obstacles on the streamer path (i.e., electrodes, dust particles, aerosols, etc).

Finally, it is important to note that in this work we have used only approximate solutions of the radiative transfer equation. *Capeillère et al.* [2008] have used a Finite Volume Method (FVM) on space and angular variables has been used to solve directly the radiative transfer equation. It is important to note that the FVM method is much more complex to implement than approximate differential models presented in this chapter. The FVM method was validated by comparison with the reference integral solution on a monochromatic Gaussian source. When the absorption coefficient is high enough, Eddington and SP_3 methods are as accurate and become faster than the direct method. However, when the absorption coefficient decreases, approximate methods become less accurate and more computationally expensive than the direct FVM. Therefore the direct method was applied in [*Capeillère et al.*, 2008] to the simulation of a double-headed streamer at ground pressure assuming that photoionization is monochromatic. The results obtained have been compared with those obtained with the SP_3 model and further validate the use of the SP_3 model for sufficiently high values of the absorption coefficient. In [*Capeillère et al.*, 2008], only monochromatic cases have been studied. To accurately simulate streamers propagating in air at atmospheric pressure, it is necessary to take into account the spectral dependence of the photoionization process. The three-group approach presented in this chapter could be very easily used with

the FVM to simulate streamer propagation in air in high and weak fields. The related results will be presented in a separate dedicated work.

Chapter IV

The use of a Ghost Fluid Method for Poisson's equation in complex geometries

Table of Contents

IV.1 Introduction

MANY early simulation studies on streamers have been done in the simple plane-to-plane geometry [*Dhali and Williams*, 1987; *Vitello et al.*, 1994; *Kulikovsky*, 1997b]. However, in practical situations, the electrode geometries are much more complex, often with one of the electrodes having a much smaller radius of curvature than the other (e.g., point-to-plane, wire-to-cylinder). One of the most studied configurations in the literature is the point-to-plane geometry. In Chapters II and III we studied a "sphere-to-plane" configuration, proposed by *Babaeva and Naidis* [1996], taking into account the influence of the spherical electrode on the discharge without including it in the computational domain. In this model, the computational grid is tangent to the sphere, and therefore there is only one point of contact between the spherical electrode and the computational domain. The simulation of the discharge is roughly approximated close to the sphere, in regions where the computational grid has no contact with the electrode. It is interesting to note that this approach is rather easy to implement and has been used in different works in the recent few years [*Liu and Pasko*, 2006; *Liu et al.*, 2007]. The only complexity of this model is in the implementation of the boundary conditions for Poisson's equation, where image charges in the sphere have to be taken into account (see Section II.1.2).

For more realistic electrode shapes, such as for hyperboloids [*Kulikovsky*, 1997b; *Morrow and Lowke*, 1997; *Pancheshnyi et al.*, 2001] or paraboloids [*Djermoune et al.*, 1995a, b; *Dessantes*, 2000], the electrode is usually included in the computational domain. However, as most streamer simulations are carried out using a finite volume approach and a rectilinear grid, the shape of the electrode is approximated by a staircase.

In the works of *Morrow and Lowke* [1997], *Djermoune et al.* [1995a, b], and *Dessantes* [2000], the shape of the electrode is defined as accurately as possible by defining a new axial grid point for each radial grid point, such that the position defined by the axial and radial coordinates lies on the electrode surface. This definition of the grid allows for defining the potential on the electrode surface very accurately, which serves as the boundary condition for Poisson's equation. However, the use of this approach for hyperboloids and paraboloids leads to significant variations of the cell sizes to adapt to the point electrode shape. In finite volume methods, these significant variations of cell sizes are not recommended. Furthermore, with this approach, the grid has to be adapted to each new geometry.

Another approach is to use a curvilinear grid [*Kim et al.*, 2004; *Akishev et al.*, 2002]. For example, for a hyperboloid-to-plane geometry, a quasi-orthogonal grid can be defined based on confocal hyperboloids and ellipses. In this case, the grid is orthogonal to the electrode surface, therefore the potential of the electrode is set very accurately. Furthermore, with

this approach, it is rather easy to implement boundary conditions for charged species with various secondary emission processes. However, in this case also, the grid has to be adapted to each new geometry.

Finally, some authors [*Georghiou et al.*, 1999; *Papageorghiou and Spyrou*, 2007] use finite-element methods with unstructured grids to simulate streamer propagation in wire-to-plane or point-to-plane geometries. It is clear that the use of an unstructured grid allows for an accurate local description of complex geometries with a reduced number of points in comparison to structured grids. Recently, *Ducasse et al.* [2007] have compared the results obtained with finite volume and finite element approaches with structured and unstructured grids, respectively, for a point-to-plane geometry with a 1-mm inter-electrode gap and a hyperboloid anode. Good agreement between the results obtained with both methods has been observed. However, it is important to note that the implementation of the finite element method is much more complex than the finite volume approach. *Ducasse et al.* [2007] have also shown that even with a smaller number of nodes in the grid, the computational cost of finite element method calculations appeared to be much higher than that of finite volume method calculations.

In the work reported in this chapter, we have implemented a method allowing to easily take into account electrodes of complex geometries in streamer simulations. For simplicity, we have tried to find a method based on rectilinear grids and finite volume or difference approaches. The problem of taking into account a boundary or an interface of complex geometry in a rectilinear grid has been studied in fluid mechanics. For example, to model interfaces in two-phase flows, *Fedkiw et al.* [1999] have introduced the Ghost Fluid Method (GFM). This method accurately localizes the interface, follows its time evolution with a Level Set formalism [*Liu et al.*, 2000], and gives the possibility of accurately defining boundary conditions at the interface. *Liu et al.* [2000] developed the method for the variable coefficient Poisson's equation. *Kang et al.* [2000] subsequently extended it to treat two-phase incompressible flow, including the effects of viscosity, surface tension, and gravity. *Nguyen et al.* [2001] included the reactivity of the flows. For Dirichlet boundary conditions set at the interface, the second-order-accurate symmetric discretization of Poisson's equation based on the GFM was obtained in [*Gibou et al.*, 2002]. A review of boundary condition capturing methods based on the GFM is provided in [*Hong et al.*, 2007].

Preliminary tests in applying the GFM to the simulation of a streamer discharge have been done by *Régnier* [2004]. In contrast to two-phase flows, the situation is simpler for streamer simulations since the embedded boundary (the electrode) is motionless. In this work, we will apply the GFM to the simulation of streamer discharge propagation in the classical point-to-plane and point-to-point geometries.

In Section IV.2, we present the equations needed for the numerical simulation of streamer discharges and the application of the GFM to Poisson's equation. In Section IV.3, to validate the use of the GFM for the computation of the Laplacian electric potential and of the electric field, we compare the results obtained using this approach with the analytical solution in a point-to-plane configuration. Then, in order to validate the use of the Ghost Fluid Method for streamer simulations, we compare the results obtained using the GFM with the results obtained by *Kulikovsky* [1998] for the same point-to-plane configuration. Finally, the application of the GFM to the simulation of a discharge in preheated air in a point-to-point geometry is presented and discussed.

IV.2 Model formulation

As stated in Section I.4, the starting point of our streamer simulations is the resolution of Equations (I.28)–(I.30) coupled to Poisson's equation (I.31).

It is important to note that for streamer simulations, the electric field is a key parameter. First, transport parameters and source terms in Equations (I.28)–(I.30) have a strong non-linear dependence on it. Second, the electric field is directly related to charged species densities in Equation (I.31). Therefore the simulation of streamer propagation requires an accurate calculation of the electric field in the simulation domain at each time step, especially in regions with high gradients in the field (e.g., the streamer head and the tip of the needle electrode). In the following section, we present the application of the GFM to Poisson's equation to calculate accurately the potential and the electric field in streamer simulations.

IV.2.1 The Ghost Fluid Method applied to Poisson's equation

We use the scheme presented in Section II.1.1 for the numerical resolution of Poisson's equation. In the volume of the computational domain (i.e., far from the boundaries) the second order finite difference discretization of Equation (II.1) in cylindrical coordinates gives the classical five diagonal linear system:

$$V^{\mathrm{e}}_{i,j}V_{i+1,j} + V^{\mathrm{w}}_{i,j}V_{i-1,j} + V^{\mathrm{s}}_{i,j}V_{i,j-1} + V^{\mathrm{n}}_{i,j}V_{i,j+1} + V^{\mathrm{c}}_{i,j}V_{i,j} = -\frac{\rho_{i,j}}{\epsilon_0} \tag{IV.1}$$

where the usual coefficients $V^{\mathrm{e}}_{i,j}$, $V^{\mathrm{w}}_{i,j}$, $V^{\mathrm{n}}_{i,j}$, $V^{\mathrm{s}}_{i,j}$, $V^{\mathrm{c}}_{i,j}$ of the grid node (i,j) with coordinates (x_i, r_j) in the simulation domain (i.e., far from the boundaries) are given by Equation (II.3).

As shown in Figure IV.1, the electrode is an embedded boundary in the Cartesian grid. To localize the fluid/electrode interface accurately, we use two "signed distance functions" based on the Level Set formalism (see [*Liu et al.*, 2000]): $\phi^x_{i,j}$ is defined by the distance between grid nodes and the electrode interface according to x, and $\phi^r_{i,j}$ is defined by the distance between grid nodes and the electrode interface according to r. In Figure IV.1, we define θ_j and β_i such that $|\phi^x_{i,j}| = \theta_j \Delta x_{i-1}$ and $|\phi^r_{i,j}| = \beta_i \Delta r_{j-1}$. The distance functions are readily found if one has an analytical expression of the electrode interface. Distance functions are defined as negative for nodes inside the electrode and as positive for nodes in the computational domain. For example, in Figure IV.1, the node (i,j) is outside the electrode, and therefore the distance functions (or Level Set functions) are defined as positive for this node.

Through the fluid/electrode interface, the potential is continuous, but there is a jump in the electric field. The GFM consists in setting virtual potentials (denoted by the superscript "G" for "ghost" in the following) at the nodes inside the electrode (e.g., V^{G}_{i-1} at the $i-1$ node in Figure IV.2) such that the interpolated potential at the interface between two nodes of the grid is precisely the physical potential of the electrode V_I (see Figure IV.2). For the interpolation, in this work we have used a linear interpolation both in x and r. This is a refinement of the Dirichlet boundary condition over the electrode surface which was used in *Gibou et al.* [2002].

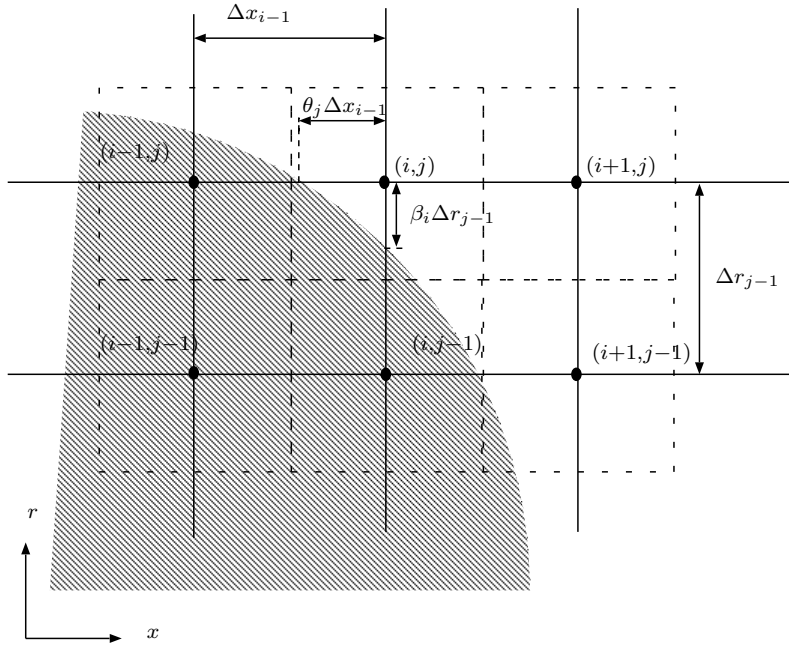

Figure IV.1: Electrode embedded in a Cartesian grid. The electric potential is fixed in the electrode (shaded) and computed in the fluid domain (not shaded). Nodes are represented on the grid and are indexed by (i, j). Dashed lines are interfaces of the grid cells.

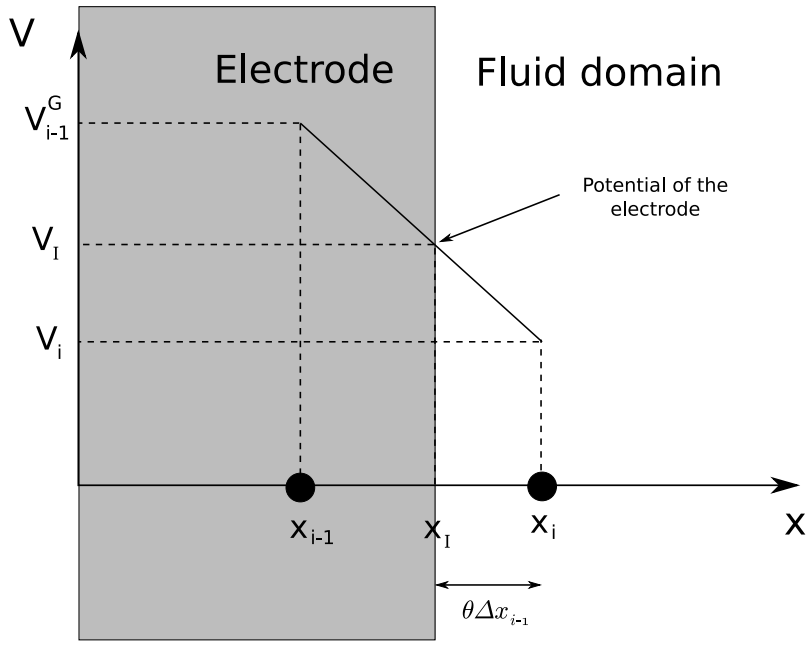

Figure IV.2: 1D description of the GFM applied to the calculation of the electrical potential. A virtual (or ghost) potential V^{G}_{i-1} is set at the node $i-1$ inside the electrode, such that the interpolated potential at the interface I between the two nodes $i-1$ and i is precisely the physical potential of the electrode V_I.

To show the new discretization of Poisson's equation around the electrode interface using the GFM, we consider as an example the case depicted by Figure IV.1 (with an interface lying between the nodes $(i-1,j)$ and (i,j) in the axial direction and $(i,j-1)$ and (i,j) in the radial direction). In this case, the nodes $(i-1,j)$ and $(i,j-1)$ are "ghost" nodes, and therefore, Equation (IV.1) becomes:

$$V^{\mathrm{e}}_{i,j}V_{i+1,j}+V^{\mathrm{w}}_{i,j}V^{\mathrm{G}}_{i-1,j}+V^{\mathrm{s}}_{i,j}V^{\mathrm{G}}_{i,j-1}+V^{\mathrm{n}}_{i,j}V_{i,j+1}-(V^{\mathrm{w}}_{i,j}+V^{\mathrm{e}}_{i,j}+V^{\mathrm{s}}_{i,j}+V^{\mathrm{n}}_{i,j})V_{i,j}=-\frac{\rho_{i,j}}{\epsilon_0} \quad \text{(IV.2)}$$

First, we consider the axial direction. Figure IV.2 shows that, using a linear extrapolation, $V^{\mathrm{G}}_{i-1,j}$ can be written as a linear function of x_{i-1}:

$$V^{\mathrm{G}}_{i-1,j}=\frac{V_{i,j}-V_I}{|\phi^x_{i,j}|}(x_{i-1}-x_I)+V_I=-\frac{|\phi^x_{i-1,j}|}{|\phi^x_{i,j}|}(V_{i,j}-V_I)+V_I \quad \text{(IV.3)}$$

where x_I is the position of the interface. By inserting Equation (IV.3) into Equation (IV.2), the terms including $V^{\mathrm{w}}_{i,j}$ become:

$$-V^{\mathrm{w}}_{i,j}V_{i,j}+V^{\mathrm{w}}_{i,j}V^{\mathrm{G}}_{i-1,j}=V^{\mathrm{w}}_{i,j}(V_I-V_{i,j})\frac{|\phi^x_{i,j}|+|\phi^x_{i-1,j}|}{|\phi^x_{i,j}|}=-\frac{V^{\mathrm{w}}_{i,j}}{\theta_j}V_{i,j}+\frac{V^{\mathrm{w}}_{i,j}}{\theta_j}V_I \quad \text{(IV.4)}$$

All other terms in Equation (IV.2) remain unchanged. A similar approach can be applied in the radial direction for the interface lying between the nodes $(i,j-1)$ and (i,j). Finally, for the 2D case of Figure IV.1, one can easily show that the discretization of Poisson's equation centered on the point (i,j) becomes

$$V^{\mathrm{e,g}}_{i,j}V_{i+1,j}+V^{\mathrm{w,g}}_{i,j}V_{i-1,j}+V^{\mathrm{s,g}}_{i,j}V_{i,j-1}+V^{\mathrm{n,g}}_{i,j}V_{i,j+1}+V^{\mathrm{c,g}}_{i,j}V_{i,j}=S^{\mathrm{g}}_{i,j} \quad \text{(IV.5)}$$

where

$$\begin{cases} V^{\mathrm{e,g}}_{i,j} &= V^{\mathrm{e}}_{i,j} \\ V^{\mathrm{w,g}}_{i,j} &= 0 \\ V^{\mathrm{n,g}}_{i,j} &= V^{\mathrm{n}}_{i,j} \\ V^{\mathrm{s,g}}_{i,j} &= 0 \\ V^{\mathrm{c,g}}_{i,j} &= -V^{\mathrm{e}}_{i,j}-\dfrac{1}{\theta_j\Delta x_{i-1}(x_{i+1/2}-x_{i-1/2})}-V^{\mathrm{n}}_{i,j}-\dfrac{2r_{j-1/2}}{\beta_j\Delta r_{j-1}(r^2_{j+1/2}-r^2_{j-1/2})} \\ S^{\mathrm{g}}_{i,j} &= -\dfrac{\rho_{i,j}}{\epsilon_0}-\dfrac{V_I}{\theta_j\Delta x_{i-1}(x_{i+1/2}-x_{i-1/2})}-\dfrac{2r_{j+1/2}V_I}{\beta_j\Delta r_j(r^2_{j+1/2}-r^2_{j-1/2})} \end{cases} \quad \text{(IV.6)}$$

and where the superscript "g" is used to define coefficients of Poisson's equation close to the interface. Different situations have to be considered, depending on how the electrode crosses the cells. This requires checking which of the five nodes required for the discretization of Poisson's equation lie in the electrode. This can be easily done by testing the signs of either ϕ^x or ϕ^r. For example, if one finds a negative value of $\phi^x_{i,j}$ at the central node (i,j), one directly sets $V_{i,j}=V_I$. In the case of an interface located between two nodes in the radial direction *only*, then $V^{\mathrm{e}}_{i,j}$ and $V^{\mathrm{w}}_{i,j}$ remain unchanged and are given by Equation (II.3), as well as $V^{\mathrm{s}}_{i,j}$, if the electrode is above the grid node (i,j), or $V^{\mathrm{n}}_{i,j}$, if the electrode is below. In the case of an interface located between two nodes in the axial direction *only*, $V^{\mathrm{n}}_{i,j}$ and

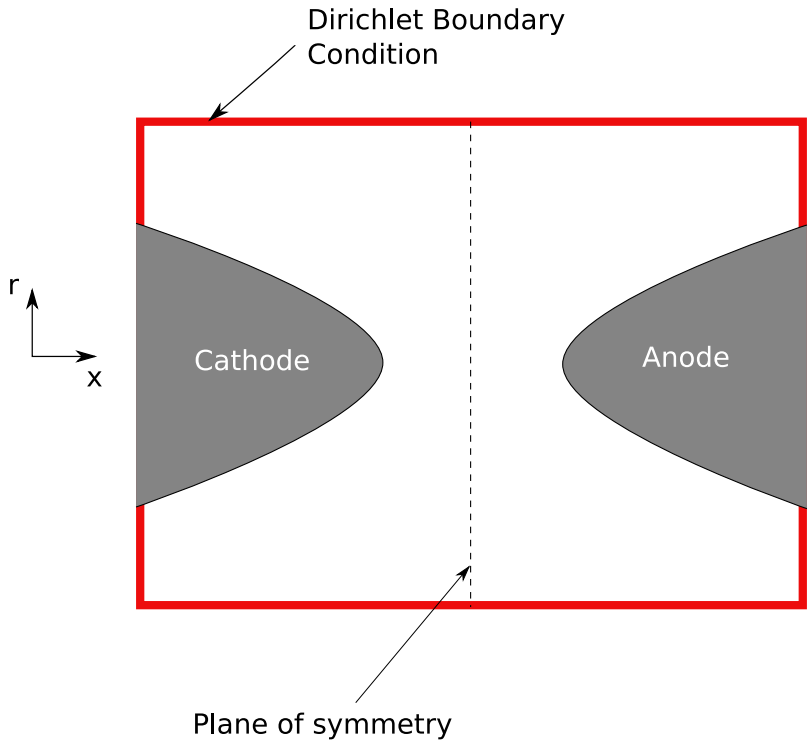

Figure IV.3: Point-to-point configuration. Boundary conditions at the electrode surface are taken into account using the GFM. The thick line shows the borders of the computational domain. The configuration is axisymmetric and also has a planar symmetry.

$V^{\mathrm{s}}_{i,j}$ remain unchanged and are given by Equation (II.3), as well as $V^{\mathrm{w}}_{i,j}$ if the electrode is to the right of the grid node (i, j), or $V^{\mathrm{e}}_{i,j}$ if the electrode is to the left.

In this work, we consider streamer simulations in point-to-plane and point-to-point geometries. The GFM is used to define the electric potential on the electrodes, but boundary conditions have to be defined on the other boundaries of the computational domain. For the point-to-point geometry, Figure IV.3 shows the two hyperboloid electrodes and the borders of the computational domain where boundary conditions have to be defined. Usually, a large computational domain is used in simulations, and the electric potential at these boundaries is specified by neglecting contributions from the charge inside the domain due to the relatively small space occupied by the charge. Two different types of boundary conditions can be used: the homogeneous Neumann boundary condition ($\vec{\nabla} V \cdot \vec{n} = 0$, where $\vec{n}$ is the unit vector normal to the surface boundary) and the Dirichlet boundary condition based on the solution of Laplace's equation (i.e., $\rho = 0$ in Equations (I.31)). For point-to-plane and point-to-point geometries, we have compared the results obtained using both boundary conditions. In order to minimize influence on the streamer propagation, it is necessary to use a much larger computational domain with the homogeneous Neumann boundary condition than with the Dirichlet boundary condition based on Laplace's equation. Thus, in this work, we have used a Dirichlet boundary condition based on the solution of Laplace's equation.

IV.2.2 Analytical solution of Laplace's equation in hyperbolic point-to-point and point-to-plane geometries

As mentioned in the previous section, the analytical solution of Laplace's equation can be used to define boundary conditions. It is also interesting to use this analytical solution to initialize the electric potential in the whole computational domain to derive the Laplacian potential at $t = 0$ if an iterative solver for Poisson's equation is to be used.

For the point-to-plane and point-to-point geometries, we consider the point electrodes to be infinite hyperboloids. In the point-to-point geometry, the electrodes are branches of the same hyperboloid. As shown in Figure IV.3, the geometrical configuration has a planar symmetry in this case. In experiments, the length of the electrodes is obviously finite. If the absolute values of the electric potential applied to the anode and to the cathode are different (e.g., a grounded cathode and the anode set to $V = V_a$), then the electric field lines starting from the anode do not necessarily converge at the cathode and can go to infinity. Thus, both electrodes are not in "total influence", and the system is no longer symmetric. The electric field in the vicinity of the anode is higher than in the vicinity of the cathode. To obtain equal electric fields, one can roughly estimate that the gap length between the two electrodes has to be less than or equal to a characteristic length of the electrodes (e.g., radius of a sphere, length of an hyperboloid, etc).

From an electrostatic point of view, the point-to-plane configuration is very close to the point-to-point configuration. Indeed, since the geometrical configuration of the two electrodes is symmetric, the plane of symmetry in the middle of the gap is an equipotential plane of the electrostatic system (see Figure IV.3). Thus, one can adjust this equipotential to any value by changing the potential at one of the electrodes.

Given the geometry of the system, it is useful to work in hyperbolic coordinates:

$$\left\{ \begin{array}{rcl} x & = & \alpha\xi(1+\eta^2)^{1/2} \\ r & = & \alpha\eta(1-\xi^2)^{1/2} \end{array} \right. \tag{IV.7}$$

where $\xi^2 < 1$ and $\alpha \neq 0$. Note that it is also possible to work in prolate spheroidal coordinates [*Durand*, 1966b, p. 177]. As shown in Figure IV.3, the needle electrodes are two branches of the same hyperboloid. The surfaces of these electrodes are defined by the Cartesian equation:

$$\frac{x^2}{a^2} - \frac{r^2}{b^2} = 1 \tag{IV.8}$$

Using Equation (IV.7), we have $a^2 = \alpha^2\xi^2$ and $b^2 = \alpha^2(1-\xi^2)$, and the squared focal length of the hyperbola is $a^2 + b^2 = \alpha^2$. In such a system of coordinates, a hyperbola with the focal length α is defined by the equation $\xi = C$, where C is a constant, and the electrode surface is defined as $\xi_0^2 = a^2/\alpha^2$. For this geometry, the electric potential has the following form [*Eyring et al.*, 1928]:

$$V(\xi) = \frac{\mathrm{A}}{2} \log \frac{1+\xi}{1-\xi} + \mathrm{B} \tag{IV.9}$$

where A and B are constants depending on the electric potentials of the electrodes and their shapes. It is interesting to note that V depends only on ξ, which means that equipotential

surfaces of the system are branches of confocal hyperbolas. In a point-to-point geometry, one can take the symmetric electrode surfaces, with $\xi = \xi_0$ for the anode of potential V_a and $\xi = -\xi_0$ for the cathode at potential V_c:

$$\begin{cases} A &= \dfrac{V_a - V_c}{\log\left(\frac{1+\xi_0}{1-\xi_0}\right)} \\ \\ B &= \dfrac{V_a + V_c}{2} \end{cases} \tag{IV.10}$$

To find A and B in the point-to-plane system, where the point is a hyperboloid and the plane is a grounded cathode, it is only necessary to set $V_c = -V_a$ in Equation (IV.10). Then, $V = 0$ represents an equipotential plane corresponding to the cathode plane defined by $\xi = 0$. Finally, to use Equation (IV.9) on a rectilinear grid, we have derived an expression for ξ in cylindrical coordinates:

$$\xi^2(x,r) = \frac{\alpha^2 + x^2 + r^2 - \left[(\alpha^2 + x^2 + r^2)^2 - 4\alpha^2 x^2\right]^{1/2}}{2\alpha^2} \tag{IV.11}$$

Note that from Equation (IV.7), $\xi < 0$ (or $\xi > 0$) corresponds to $x < 0$ (or $x > 0$).

For streamer applications, it is also interesting to derive the value of the magnitude of the electric field. Using the hyperbolic coordinates given by Equation (IV.7), we have [*Eyring et al.*, 1928]:

$$\vec{\nabla} V = \frac{1}{\Xi}\frac{\partial V}{\partial \xi}\vec{u_\xi} \tag{IV.12}$$

where $\vec{u_\xi} = \dfrac{\vec{\nabla}\xi}{\|\vec{\nabla}\xi\|}$ and

$$\Xi(\eta,\xi) = \alpha\left(\frac{\eta^2 - \xi^2 + 1}{1 - \xi^2}\right)^{1/2} \tag{IV.13}$$

Using Equations (IV.7) and (IV.11), one can easily derive $\Xi(x,r)$. Finally, the magnitude of the electric field can be derived from Equation (IV.9) as:

$$|\vec{E}(x,r)| = \frac{1}{\Xi(x,r)}\frac{A}{1 - \xi^2(x,r)} \tag{IV.14}$$

IV.2.3 Numerical methods for Poisson's equation and drift-diffusion equations

In order to compare our results in a point-to-plane geometry with those obtained by *Kulikovsky* [1998], we have used the same numerical scheme (i.e., the modified Scharfetter-Gummel algorithm [*Kulikovsky*, 1995a], see Section II.2.2) to solve the charged species transport equations. This numerical scheme has also been used for streamer simulations in point-to-point geometries in Section IV.3.3. For both geometries, there has been no special numerical treatment close to the needle electrodes to take into account the exact shape of the electrodes in setting up the boundary conditions for the drift-diffusion equations of

charged species. The boundary conditions are computed in both directions simply assuming that the interface has a "staircase" shape. In this work, as in [*Kulikovsky*, 1997a], we have taken into account simplified boundary conditions: near the anode and cathode surfaces, gradients of electron density are assumed to be equal to zero.

In [*Kulikovsky*, 1998], the finite difference form of Poisson's equation is solved using the symmetrical successive overrelaxation (SOR) method. This method is simple and robust, and has been widely used for streamer simulations. However, the SOR method is well-known to converge rather slowly. To reduce computation times, we used two numerical methods for the resolution of Poisson's equation described in Section II.1.3, namely the D03EBF iterative module of the NAG Fortran library and the direct SuperLU solver. Then, as part of the preparatory work for the studies presented in this chapter, we conducted several test runs to compare the results obtained using the iterative NAG module and the direct SuperLU solver. It turned out that there are only minor changes in the streamer dynamics computed using these two solvers. Direct solvers are inherently very accurate and robust. Furthermore, for the case of a fixed grid, the most time-consuming step in the calculation of the solution (i.e., the factorization) needs to be done only once, at the beginning of the discharge simulation. As a result, at each time step of the discharge simulation, the calculation of the solution for different source terms (i.e., term in the right hand side of Equation (IV.1)) is very fast. Thus, SuperLU solver was adopted for all simulation studies presented in this chapter.

To calculate the photoionization source term in the streamer model, we use the three-group SP_3 model presented in Chapter III with the Larsen's boundary conditions (Section III.5).

IV.3 Results and Discussion

IV.3.1 Laplacian field in a point-to-plane geometry

In this section, a point-to-plane configuration is used to compare the electric potential calculated in the whole computational domain using the GFM presented in Section IV.2.1 and the analytical solution presented in Section IV.2.2. We have considered the same configuration as in [*Kulikovsky*, 1998]: a hyperboloid anode (V_a = 13 kV) is located at x = 1 cm and a plane grounded-cathode (i.e., V = 0) is located at x = 0. Parameters of the shape of the hyperboloid anode are the same as in [*Kulikovsky*, 1998]: a = 1 cm and b = 0.18 cm, which correspond to a radius of curvature at the tip of the electrode of b^2/a = 324 μm. The computational domain dimension is 2×1 cm^2 and is discretized on a Cartesian grid in both the radial and axial directions. The total number of cells is $n_x \times n_r = 1000 \times 500$, where n_x and n_r represent the number of cells in the axial and radial directions, respectively. This corresponds to cell sizes of 20 μm both in the axial and radial directions. For streamer simulations, the typical cell size is much smaller and is on the order of 5 μm or less. In this section, we use a large grid size to demonstrate the efficiency of the GFM clearly.

Figure IV.4 compares the isocontours of the electric potential calculated using the GFM and the analytical solution given by Equation (IV.9). Very good agreement between both results is observed. Small variations in the electric potential can lead to significant changes in the

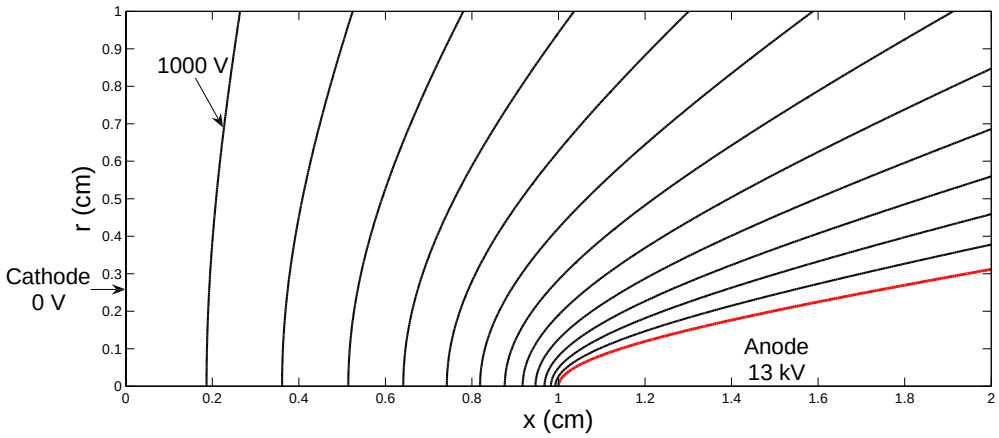

Figure IV.4: Isocontours of the electric potential in a point-to-plane configuration. The isocontours are shown from 0 V (cathode) to 13000 V (anode), with a step of 1000 V. In this figure, the isocontours of the analytical solution overlap those from the numerical simulation with GFM, demonstrating a good agreement between the two solutions.

electric field. Figure IV.5 compares the analytical solution of the electric field (Equation (IV.14)) with the electric field computed with the GFM, for the same condition as Figure IV.4. For the scale used in Figure IV.5, very good agreement is observed between the electric field computed using the GFM and the analytical solution. To show clearly the quantitative improvement due to the use of the GFM close to the electrode, we compare the magnitude of the electric field in Figures IV.6 and IV.7, computed on the same grid with the GFM and without any specific treatment to take into account the real shape of the electrode (i.e., "the staircase approach").

On the axis of symmetry, Figure IV.6 shows that the electric field calculated using the GFM is in very good agreement with the analytical solution close to the electrode. The results obtained with the staircase approach on the same grid overestimates the electric field in the vicinity of the electrode. We have checked that the discrepancy between the two numerical approaches increases as the grid becomes coarser.

Figure IV.7 shows the magnitude of the electric field obtained with and without the GFM in the whole computational domain. We note that the results obtained without the GFM exhibit oscillations in the electric field along the electrode interface due to the random crossing of the electrode over the cells. Furthermore, it is important to mention that the maximum of the electric field with this grid is not located at the electrode tip on the symmetry axis but a few cells below (see Figure IV.7). We have carried out simulations of streamer propagation with both Laplacian electric fields, and we have observed that the oscillations in the electric field calculated without using the GFM may lead to streamer branching close to the electrode. Using the GFM on the same grid, no streamer branching has been observed.

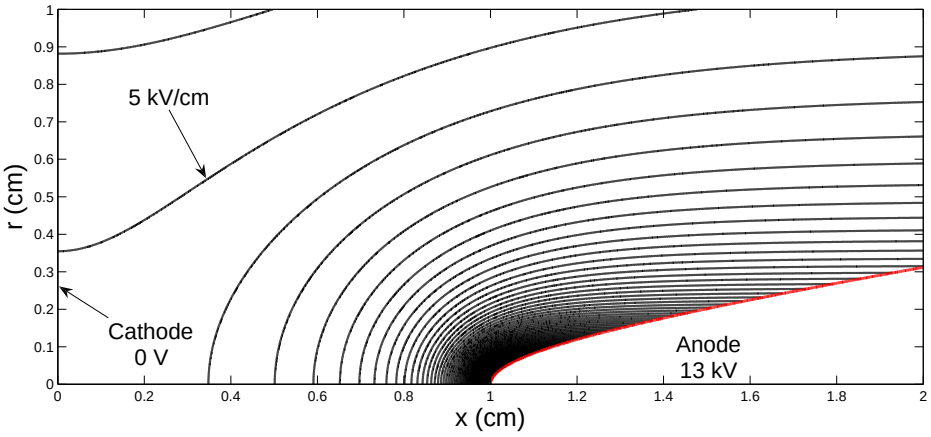

Figure IV.5: Isocontours of the magnitude of the electric field for the same conditions as in Figure IV.4. The isocontours are shown from 1 kV/cm to 160 kV/cm, with a step of 1 kV/cm. In this figure, the isocontours of the analytical solution overlap those of the electric field computed using the GFM, demonstrating a good agreement between the two solutions.

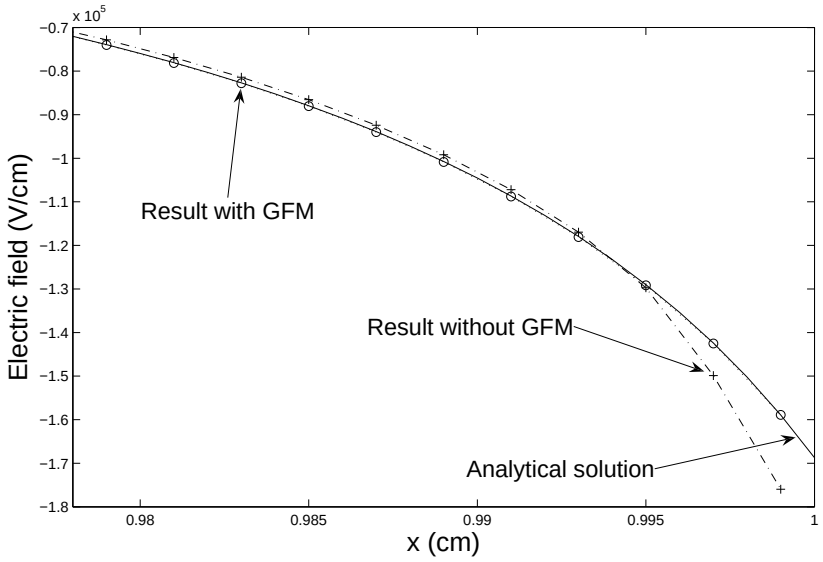

Figure IV.6: Magnitude of the electric field along the symmetry axis in the vicinity of the anode tip. Solid line: analytical solution (Equation (IV.14)). Dotted line with circles: numerical results using the GFM. Dot-dashed line with crosses: numerical results without the GFM (i.e., "staircase" approach). The symbols for the numerical results correspond to the grid nodes.

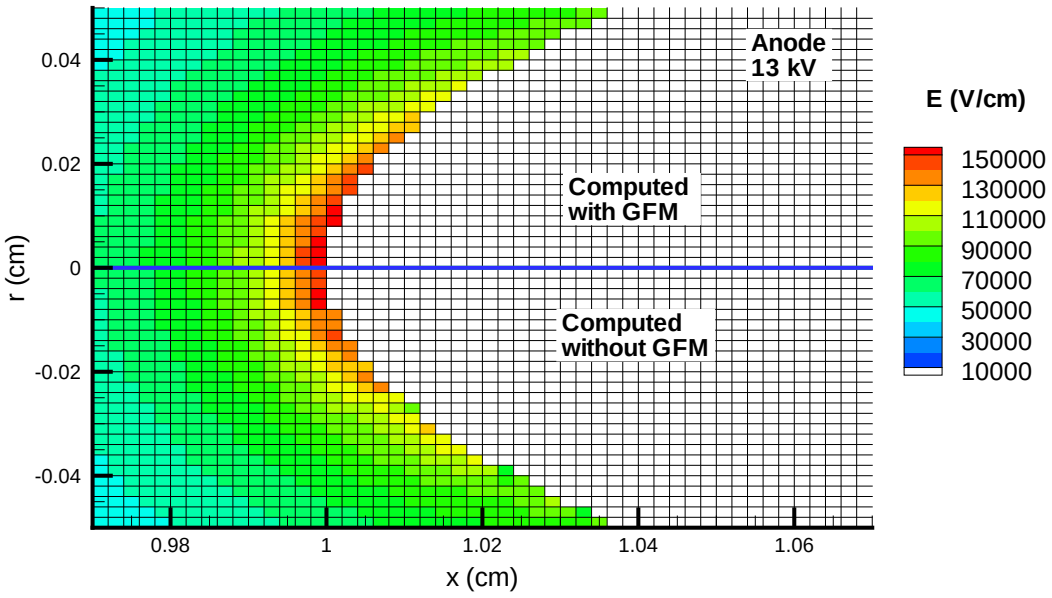

Figure IV.7: Comparison between the magnitude of the electric field computed with and without the GFM in the same point-to-plane configuration as in Figure IV.4. The white region of the color scale corresponds to the hyperboloid anode. In the case without the GFM, all the potentials $V_{i,j}$ are set equal to V_a if the point (i, j) is inside the electrode. In the case with GFM, the nodes inside the electrode are also set to V_a, except for the points close to the interface.

IV.3.2 Positive streamer propagation in a point-to-plane geometry

In order to validate the use of the Ghost Fluid Method for streamer simulations, in this section we compare the results obtained using this approach with the results obtained by *Kulikovsky* [1998] for the same point-to-plane configuration. The parameters of the shape of the hyperboloid anode, the location of the electrodes and the applied voltage are the same as in Section IV.3.1. We have used the same transport parameters and reaction rates as in [*Kulikovsky*, 1998]. In the work of *Kulikovsky* [1998], the photoionization source term in air is calculated using an optimized integral approach based on the model proposed by *Zheleznyak et al.* [1982]. In our work, this model is also used, but we have implemented it using the differential three-group SP_3 model [*Bourdon et al.*, 2007]. If the integral model is used without any geometric limitations on the emitting volume of the discharge, we have shown in [*Bourdon et al.*, 2007] that the results of both approaches are in very good agreement. In [*Kulikovsky*, 1998], the computational domain dimension is 6×1.1 cm^2 and is discretized on a grid with $n_x \times n_r = 134 \times 640$ points. The streamer head is covered by a moving window with an uniform fine grid (of $\simeq 400$ cells) with a cell size of 6.3 μm $\times$ 8 μm. In this chapter, to validate the use of the GFM, we have first used a fixed grid. We have also carried out different tests on the grid to reduce the size of the computational domain and to limit the number of grid points. Finally, in this chapter we have also used a 2×0.5 cm^2 computational domain discretized on a fixed rectilinear grid with $n_x \times n_r = 2254 \times 344$ cells. The grid is Cartesian, with a fixed cell size of 5 μm in the region where the streamer propagates. Beyond this region (i.e., $x \in [1.1, 2]$ cm and $r \in [0.15, 0.5]$ cm), the grid expands according to a geometric progression. As in [*Kulikovsky*, 1998], a neutral plasma spot is

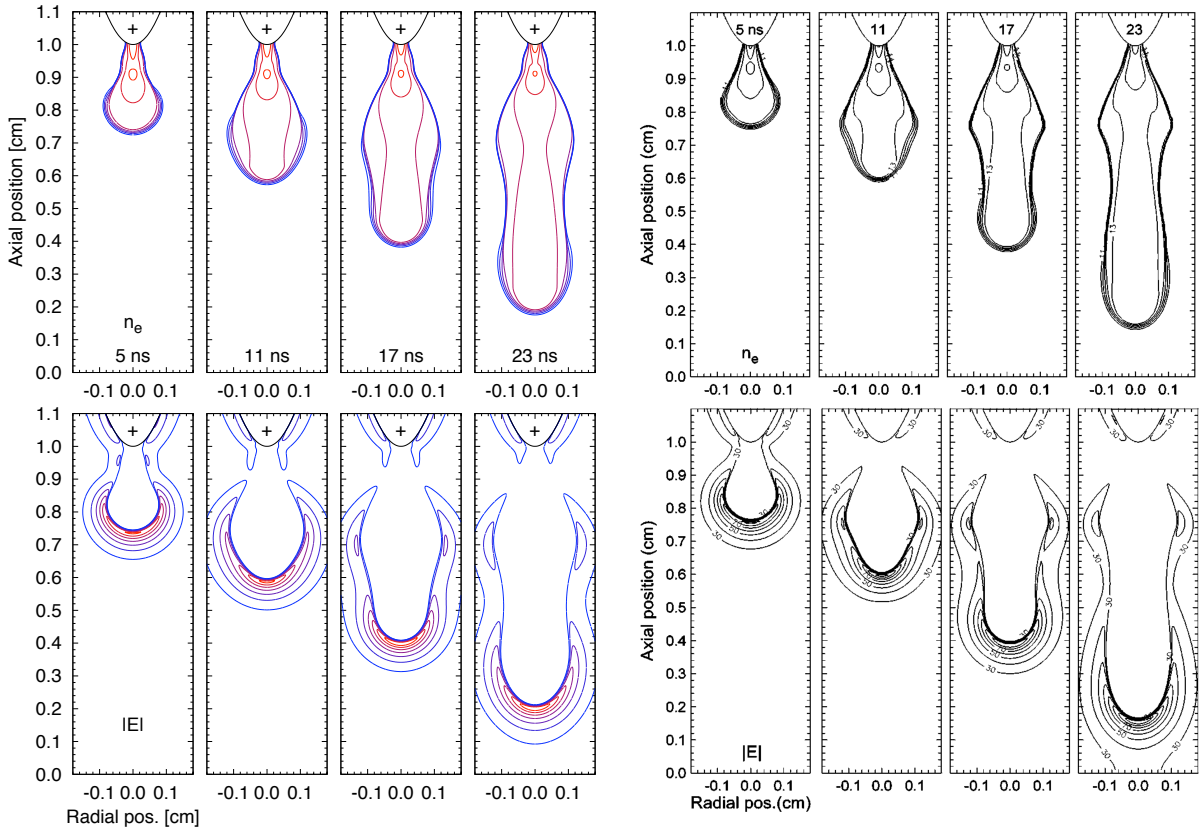

Figure IV.8: Two-dimensional isocontours of the electron density and the magnitude of the electric field at $t = 5$, 11, 17, and 23 ns. For the electron density, the isocontours go from 10^{11} to 10^{14} cm^{-3}, with a multiplier step of $10^{0.5}$ cm^{-3}. For the electric field, the isocontours go from 30 to 90 kV/cm, with a step of 10 kV/cm. The left panel presents results from our code. The right panel is taken from [*Kulikovsky*, 1998, Figure 2].

placed at the anode tip to initiate streamer formation:

$$n_{\mathrm{p}}(x,r)|_{t=0} = n_{\mathrm{e}}(x,r)|_{t=0} = n_0 \exp\left[-\frac{r^2}{\sigma_r^2} - \frac{(x-x_0)^2}{\sigma_x^2}\right] \tag{IV.15}$$

where $x_0 = a - \sigma_x$, $\sigma_x = 0.025$ cm, and $\sigma_r = 0.01$ cm. At $t = 0$ there are no negative ions. The initial maximum density is $n_0 = 10^{14}$ cm^{-3}.

The left panels of Figures IV.8 and IV.9 show the same results as Figures 2 and 3 in [*Kulikovsky*, 1998]. Results from [*Kulikovsky*, 1998] are included for reference in the right panels of Figures IV.8 and IV.9. Figure IV.8 shows the contour lines of the electron density and the magnitude of the electric field during the positive streamer propagation towards the cathode. Figure IV.9 shows the evolution of axial profiles of the electron density and electric field. For both figures, we have good agreement with the results of [*Kulikovsky*, 1998]. Slight differences are observed on the contour lines. From Figure IV.8, we note that in our results the contour line for 30 kV/cm is slightly larger in the radial direction and slightly shorter in the axial direction than in the results of [*Kulikovsky*, 1998]. Direct inspection of the contour lines of the electron density indicates that the variation of the thickness of the streamer channel is smoother in our results than in the results from [*Kulikovsky*, 1998]. These small differences may come from the different grid used and the different

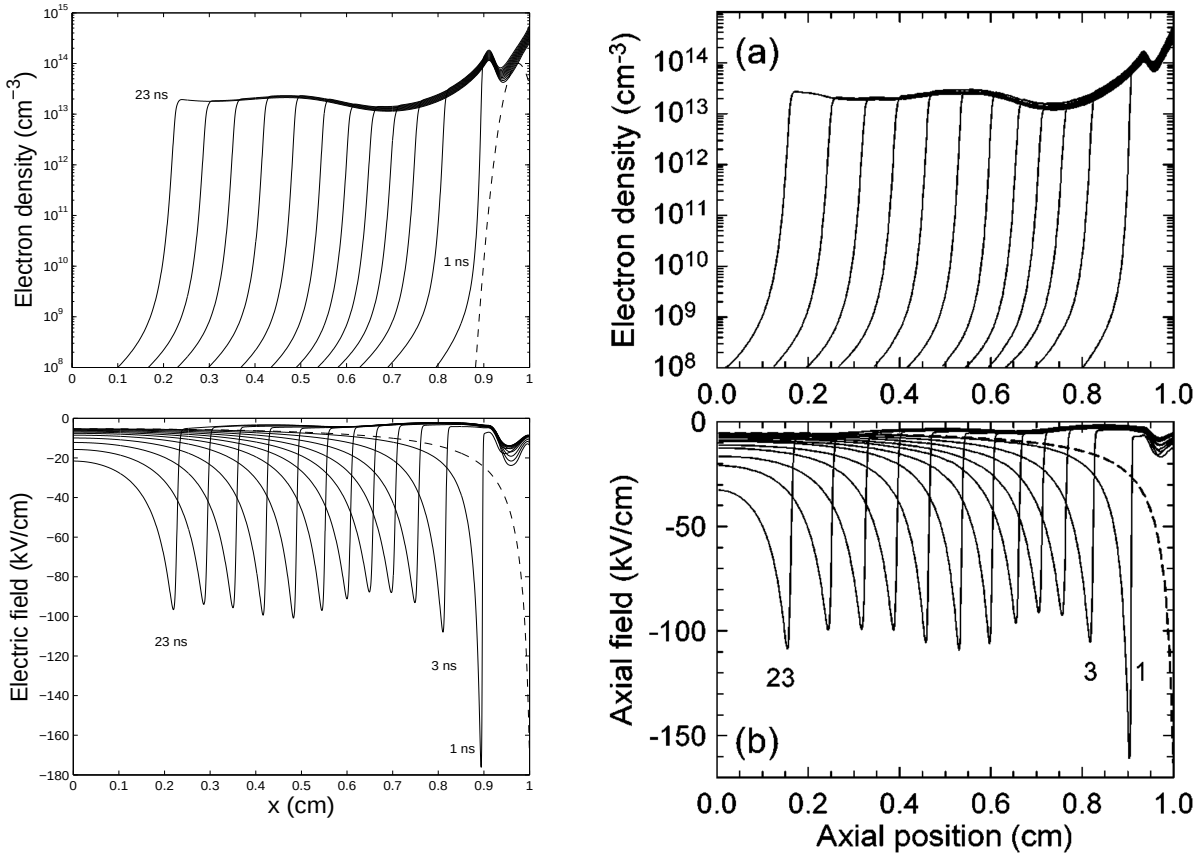

Figure IV.9: Electron density and electric field on the axis of symmetry at $t = 1$ ns to 23 ns with a timestep of 2 ns. Dashed line: electron density and electric field at $t = 0$. The left panel presents results from our code. The right panel is taken from [*Kulikovsky*, 1998, Figure 3].

treatment of the photoinization source term in our work and from that in [*Kulikovsky*, 1998]. At time $t = 1$ ns the field in the streamer head is higher in our results than in the results of *Kulikovsky* [1998]. This is possibly due to the fact that the GFM is not used in [*Kulikovsky*, 1998]. In Figures IV.8 and IV.9, the two phases of the streamer propagation can be clearly observed. The first one lasts about 5 ns and corresponds to the positive streamer formation close to the point anode and to its propagation in the high field region close to the electrode tip. We note that during the first phase, the streamer radius increases as the streamer propagates towards the cathode. For $t > 5$ ns, the streamer propagates with the velocity almost constant, the radius of the plasma channel and the maximum electric field in the streamer head. In [*Kulikovsky*, 1998], this phase is called the stationary propagation phase of the streamer.

The results obtained in this section clearly validate the use of the GFM for the simulation of streamer propagation.

IV.3.3 Streamer propagation in point-to-point geometry

In this section, we apply the GFM to simulate a discharge in air at atmospheric pressure between two point electrodes. This discharge has been studied experimentally in [*Pai et al.*, 2008; *Pai*, 2008]. These authors use a nanosecond repetitively pulsed voltage ($5 - 10$ kV) with a repetition rate of 10 kHz to generate a discharge in a preheated air flow between two pin electrodes separated by 5 mm. *Pai et al.* [2008] showed that for a temperature $T = 1000$ K, three different regimes are observed. At low voltages, corona discharges are observed. This is called the "C" regime. For voltages higher than 7 kV, a "F" regime is observed. This regime is reminiscent of a spark discharge, with intense emission and a high conduction current. Finally, for voltages in a narrow range between 6 kV and 7 kV, a regime with an emission which fills the gap in a diffuse manner is observed; this is the "D" regime.

To take a first step towards understanding the different discharge regimes, we simulated a point-to-point configuration for different temperatures and voltages. In the following we present results obtained for three different temperatures. The temperature $T = 1000$ K has been extensively studied in [*Pai*, 2008], and therefore we use this temperature as a reference point. We also study discharges at ambient temperature $T = 300$ K, which are of great interest for applications. Furthermore, results at $T \leq 2000$ K were obtained by *Packan* [2003] for discharges in air at atmospheric pressure using a point-to-point configuration, and therefore we also show here results for the temperature $T = 1800$ K. For all the cases studied in the present work, we found that the study of the dynamics of the streamers could give interesting information on the final discharge structure.

In the experimental study of *Pai* [2008], the exact shape of the electrodes is not known accurately. Nevertheless, the radius of curvature of both needle electrodes is roughly estimated to be close to 200 μm. As a first approximation, we have considered that both electrodes are hyperboloids with a radius of curvature of 324 μm as in Sections IV.3.1 and IV.3.2.

The simulation of successive discharges due to nanosecond voltage pulses applied at high repetition rate is beyond the scope of this thesis. In this work, we apply the GFM to simulate a single discharge in air generated by a single 10 ns-long voltage pulse. As many discharges have occurred before the one we simulate in this work, it is necessary to estimate

the density of seed charge in the inter-electrode gap. Based on the work of *Pancheshnyi* [2005], we have assumed the density of the initial charges before each new pulse to be in the $10^9 - 10^{10}$ cm^{-3} range at ambient temperature, forming a neutral and homogeneous background. Furthermore, the pre-ionized background is not expected to change sharply with the gas density [see *Pancheshnyi*, 2005]. As a first approximation, a value of 10^9 cm^{-3} has been used as a uniform pre-ionized background for the calculations presented in this section. We have checked that photoionization has no influence on the results presented in this section.

In the experiments, the velocity of the air flow is on the order of 1 m/s, and thus we have assumed that the air is static during one discharge pulse and is uniformly preheated. To take into account the fact that the discharge occurs at different temperatures, we have simply changed the value of the total density $N = N_0 T_0/T$ where $N_0 = 2.45 \times 10^{25}$ m^{-3} is the air neutral density at ground pressure and ambient temperature ($T_0 = 300$ K). This decrease of the total density by a factor T/T_0, increases the local reduced electric field E/N by the same factor, and thus has a direct impact on transport parameters and reaction rates in air, which are assumed to be functions of E/N. In this section the transport parameters and source terms are the same as in Section IV.3.2.

Note that the results obtained in this work cannot be understood solely by considering of similarity laws. Indeed, in the present simulations the radius of curvature of the electrodes as well as the initial densities are not scaled along with the neutral gas density [see *Liu and Pasko*, 2006, for further details on similarity laws]. For the different temperatures studied in this section, we do not attempt to scale the Laplacian electric field by the same factor as the gas density. Instead, we used typical values of experimental studies.

In this work, we have used a 2×0.5 cm^2 computational domain discretized on a fixed rectilinear grid with $n_x \times n_r = 1510 \times 347$ cells. The grid is Cartesian, with a fixed cell size of 5 μm in the region of the streamers propagation. Beyond this region, the grid expands according to a geometric progression. The tip of the anode is located at $x = 1.25$ cm, and the tip of the grounded cathode is located at $x = 0.75$ cm.

Discharge at 1000 K

Figure IV.10 shows the evolution of the contour lines of the electron density and of the absolute values of the electric field for $V_a = 7$ kV. Figures IV.11 and IV.12 shows the evolution of axial profiles of the electric field and of the electron density, respectively.

Two phases of the discharge evolution can be clearly distinguished. The first lasts about 5 ns. During this time period, two discharges are initiated at both electrode tips where the Laplacian electric field is highest (i.e., 70 kV/cm), and these discharges propagate in the gap. On the anode side, the conditions for positive streamer propagation are fulfilled in the first nanosecond, and a positive streamer propagates towards the grounded cathode. The electron density in the streamer channel is about 1.5×10^{13} cm^{-3}, and the maximum electric field on the streamer axis is 50 kV/cm. It is interesting to note that these values are less than those obtained for the positive streamer simulated in Section IV.3.2. In fact, due to the pre-ionization in the gap and the lower total density, the conditions are much more favorable for positive streamer propagation than in Section IV.3.2 and therefore the streamer propagates with a lower electric field and lower electron density in its head. It is

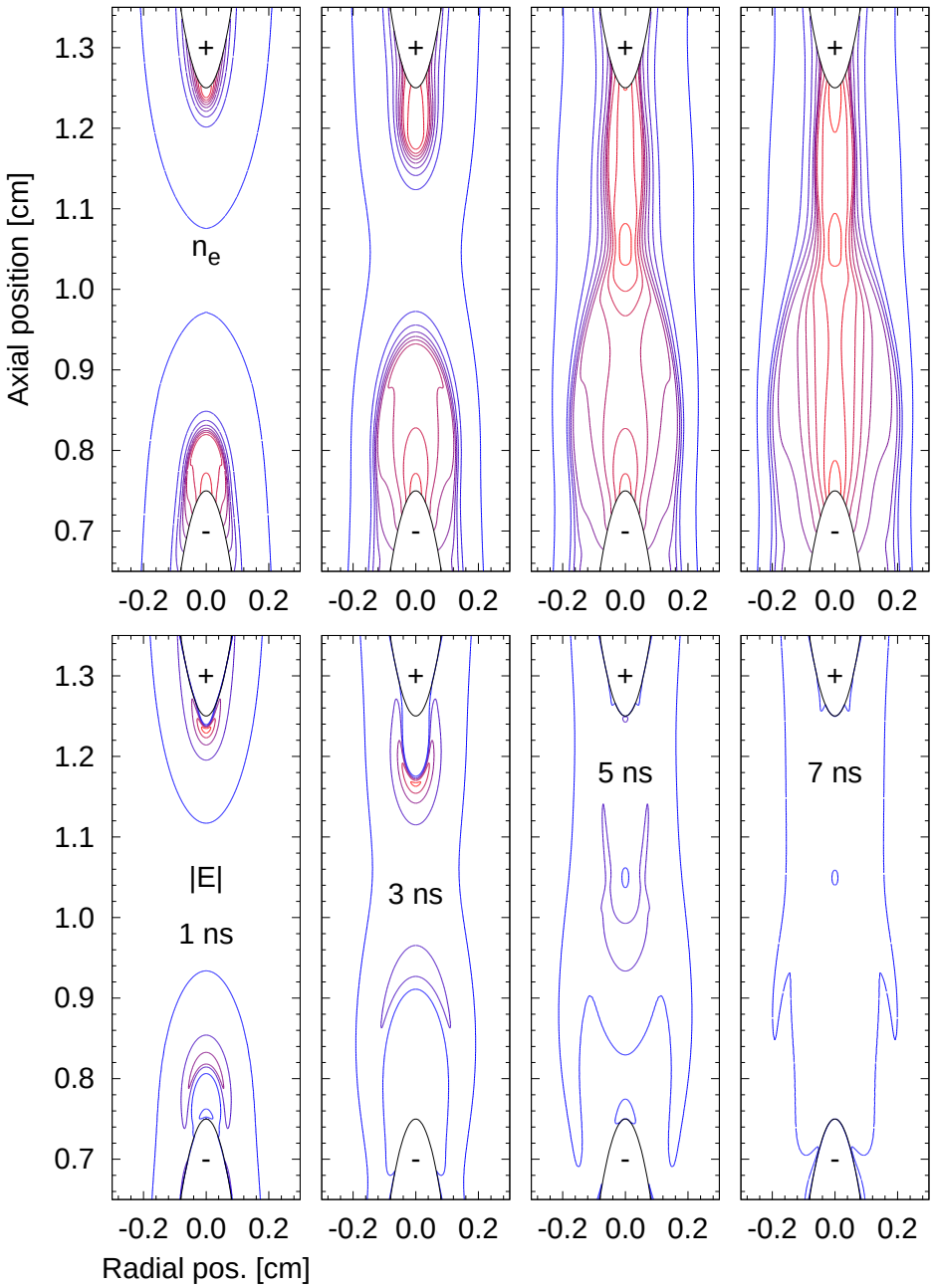

Figure IV.10: Point-to-point geometry: Two-dimensional isocontours of the electron density and the magnitude of the electric field for $t = 1$, 3, 5, and 7 ns. For the electron density, the isocontours vary from 10^9 to $10^{13.5}$ cm^{-3}, with a multiplier step of $10^{0.5}$ cm^{-3}. For the electric field the isocontours vary from 10 to 50 kV/cm, with a step of 10 kV/cm. In this case $T = 1000$ K and $V_a = 7$ kV.

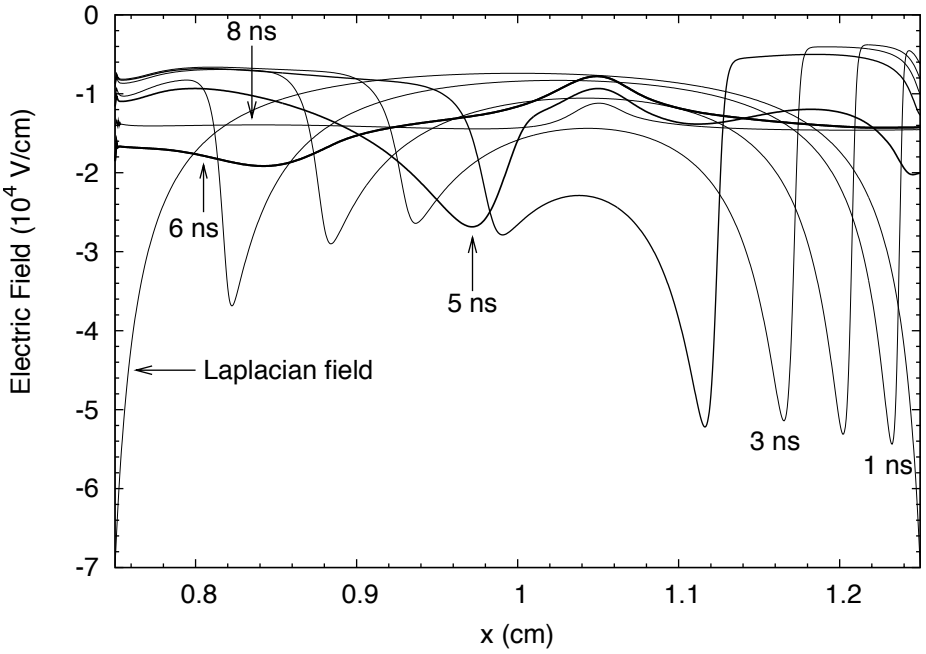

Figure IV.11: Point-to-point geometry: Electric field along the axis of symmetry for $t = 0$ ns to 8 ns.

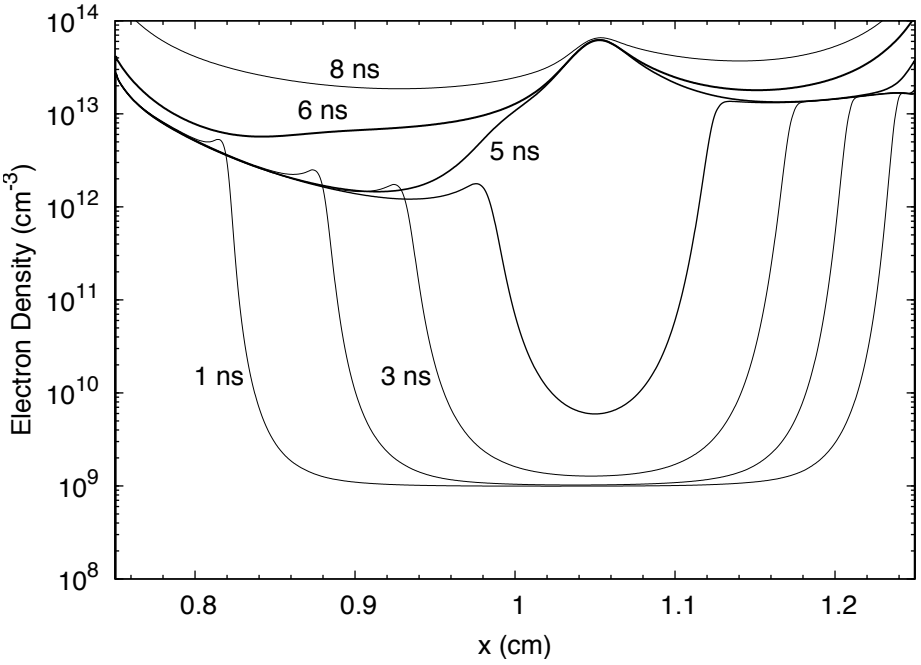

Figure IV.12: Point-to-point geometry: Electron density along the axis of symmetry for $t = 1$ ns to 8 ns.

interesting to note that *Liu and Pasko* [2006] have compared streamer propagation at 300 K at atmospheric pressure to that at lower pressures. These authors indicated that at low pressures, the maximum electric field and electron density are less than that at atmospheric pressure. In their work, the change of pressure has a direct impact on the quenching of the radiative molecular states responsible for photoionization, and thus the photoionization source term decreases as the pressure increases. We note that our results obtained at 1000 K with pre-ionization in the gap are close to the results of *Liu and Pasko* [2006] at low pressure. However, we note again that in our case the Laplacian electric field and the pre-ionization level are not defined following the similarity laws.

On the cathode side, in the first few nanoseconds we observe the expansion of a discharge towards the anode. The maximum electric field in the discharge decreases as the discharge propagates towards the anode and is on the order of 30 kV/cm. The electron density in the discharge front is on the order of 10^{12} cm^{-3}. Due to the pre-ionization in the inter-electrode gap, these values are less than those usually obtained for negative streamers [e.g., *Bourdon et al.*, 2007], and we can quantify that the discharge which propagates from the cathode as a "weak" negative streamer. We also carried out simulations without a continuous ionized background, and initializing the streamer by a neutral plasma cloud in the vicinity of the anode (as in Section IV.3.2). In this case we found that the weak negative streamer is ignited from the cathode as well, but in this situation the ignition is only due to the photoionization of the positive streamer instead of the uniform background density.

In Figure IV.10 both discharges have very different radial expansions. At $t \simeq 5$ ns, both discharges interact at $z \simeq 1.05$ cm, and Figures IV.11 and IV.12 clearly show that the positive streamer propagates very rapidly towards the cathode in the volume pre-ionized by the "weak" negative streamer. Then at $t = 7$ ns the positive streamer reaches the grounded electrode, and Figure IV.11 shows the rapid redistribution of the potential in the interelectrode gap. In Figure IV.12, we note that the interaction between the two discharges creates an enhancement in the electron density at $z \simeq 1.05$ cm and this enhancement remains nearly unchanged for $t > 5$ ns. We also note that for $t > 5$ ns the electron number density increases on the discharge axis.

All these results indicate that a positive streamer could propagate between the two point electrodes in less than 7 ns, which is in qualitative agreement with the experimental results. In this case an electrical connection between two electrodes is realized with quite a high electron density. This junction is created after the positive streamer reaches the cathode. Depending on the temperatures and voltages studied, this connection can form during the applied-voltage pulse (10 ns long for the experiment considered). As a result, the current in the conducting junction increases and the plasma filament develops into a spark discharge.

In Figure IV.13, the conditions are the same as in Figure IV.10, except that the applied voltage at the anode is $V_a = 5$ kV. As for Figure IV.10, we observe that two discharges are ignited in the vicinity of the electrodes, which are of opposit polarity. The results obtained are similar to the case with $V_a = 7$ kV, but in this case the propagation time scale of negative and positive streamers is much longer. The positive streamer contacts the region ionized by the weak negative streamer only after 13.5 ns and finally reaches the cathode after 20 ns. The electrical connection is not realized during the 10 ns long voltage pulse, and therefore one expects to obtain only corona discharges on such a time scale.

In the experimental results at 1000 K, corona discharges are present up to $V_a = 6$ kV, and

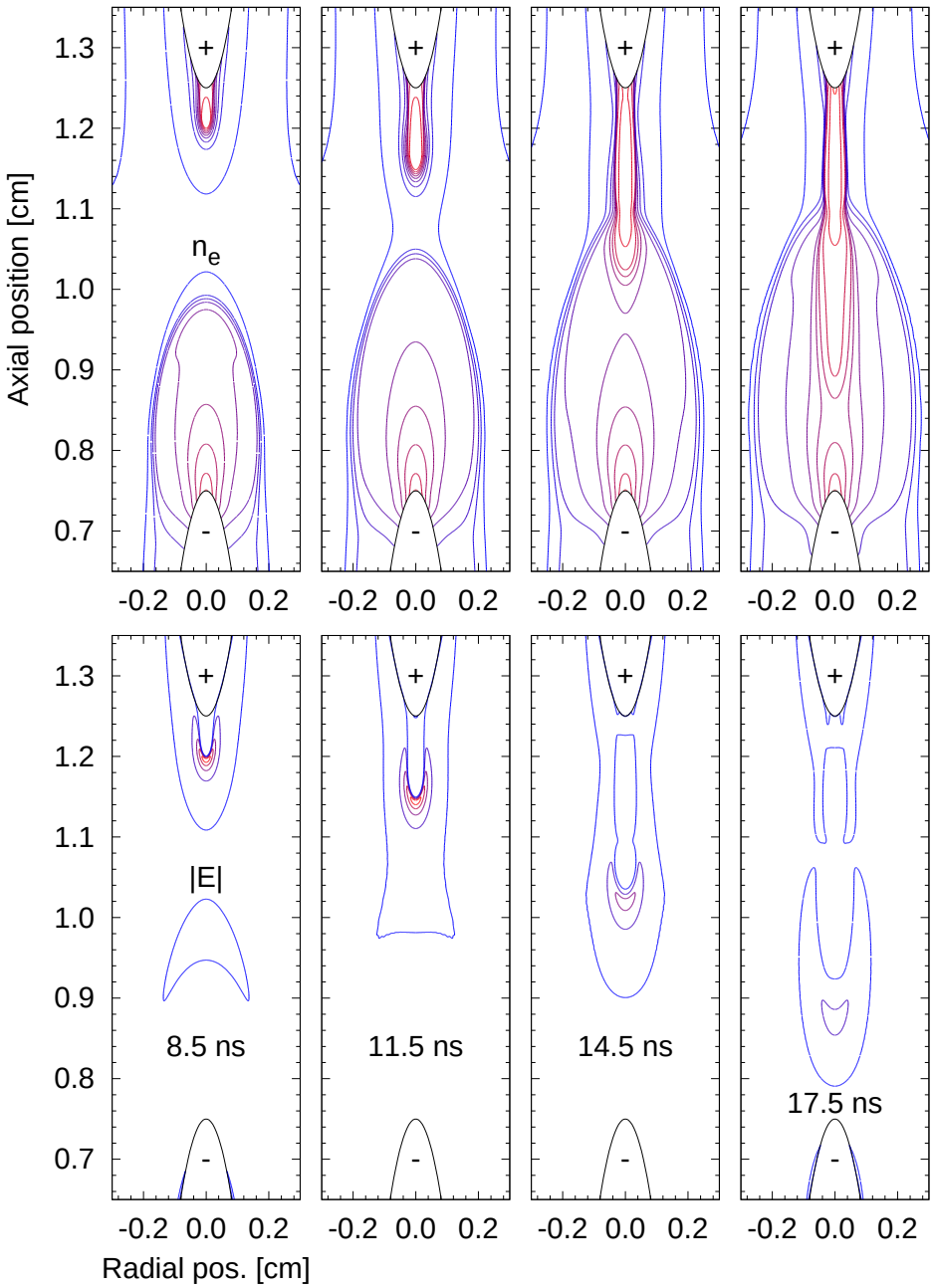

Figure IV.13: Point-to-point geometry: Two-dimensional isocontours of the electron density and the magnitude of the electric field at $t = 8.5$, 11.5, 14.5, and 17.5 ns. For the electron density the isocontours vary from 10^9 to $10^{13.5}$ cm^{-3}, with a multiplier step of $10^{0.5}$ cm^{-3}. For the electric field, the isocontour vary from 10 to 50 kV/cm, with a step of 10 kV/cm. In this case $T = 1000$ K and $V_a = 5$ kV.

for voltages higher than 7 kV spark discharges occur. In this respect, the simulation results are considered to be in good agreement with the experimental results. We presume that the very strong impact of the applied voltage on the time required to create the electrical connection is related to the narrowness of the voltage range allowing for the diffuse regime. Note also that for the case of $V_a = 5$ kV in [*Pai*, 2008], only anode corona discharges are visible. We stated at the beginning of Section IV.2.2 that as the electrode points are spatially finite in the experiments, a grounded cathode and a high-potential anode do not necessarily give symmetric distribution of the Laplcian fields magnitude at the tips of the electrodes. The field lines starting from the anode can diverge to the grounded objects around the exprerimental device, therefore electrodes are not in total influence. However, the Laplacian field is perfectly symmetric in the simulations. Note that recent experimental work[1] of *David Pai* with a cathode set at -5 kV and the anode at 5 kV results in corona discharges on both electrodes.

Discharge at 300 K

In this section, we present simulation results for $T = 300$ K. In this model case, for voltages below 7 kV, we did not observe any positive streamer propagation. Figure IV.14 shows the results obtained for $V_a = 10$ kV. We note that the time scale for positive and negative discharge propagation is much longer than that of the cases studied at 1000 K. For example, the positive and negative streamers contact each other at $t = 16.5$ ns. However, one notes that the positive streamer eventually reaches the cathode after $t = 20$ ns. But for 10 ns long voltage pulses, this appears to be insufficient to produce a spark discharge.

Figure IV.15 shows the results obtained for $V_a = 13$ kV. The positive streamer enters the ionized zone created by the negative streamer at 6.5 ns and reaches the cathode at $t = 8.5$ ns. That is only 2 ns after the two streamers touch each other. Therefore, for the considered pulse durations (10 ns), these results indicate that the electrical connection could be realized before the end of the pulse and these conditions may produce a spark discharge. As already observed at $T = 1000$ K, we note that at $T = 300$ K a small increase in the voltage has a significant impact on streamer propagation time scales.

Discharge at 1800 K

The experimental results for a point-to-point case at 2000 K in a 1-cm gap have been reported in [*Packan*, 2003]. The exact shape and radius of curvature of the electrodes were not known accurately. In [*Packan*, 2003] the pulse repetition rate was 100 kHz with a voltage pulse duration of 10 ns. For $V_a = 6$ kV, *Packan* [2003] observed the propagation of two discharges starting at the same time from both electrodes and contacting each other in the middle of the gap after about 10 ns and then producing a diffuse discharge.

As previously noted, the detailed study of the nanosecond repetively pulsed discharge at 2000 K is beyond the scope of this thesis. In this section, we have kept the same geometry as in the previous section, and we have studied the influence of a higher tempertaure ($T = 1800$ K) on the discharge dynamics.

[1] Private communication with David Pai.

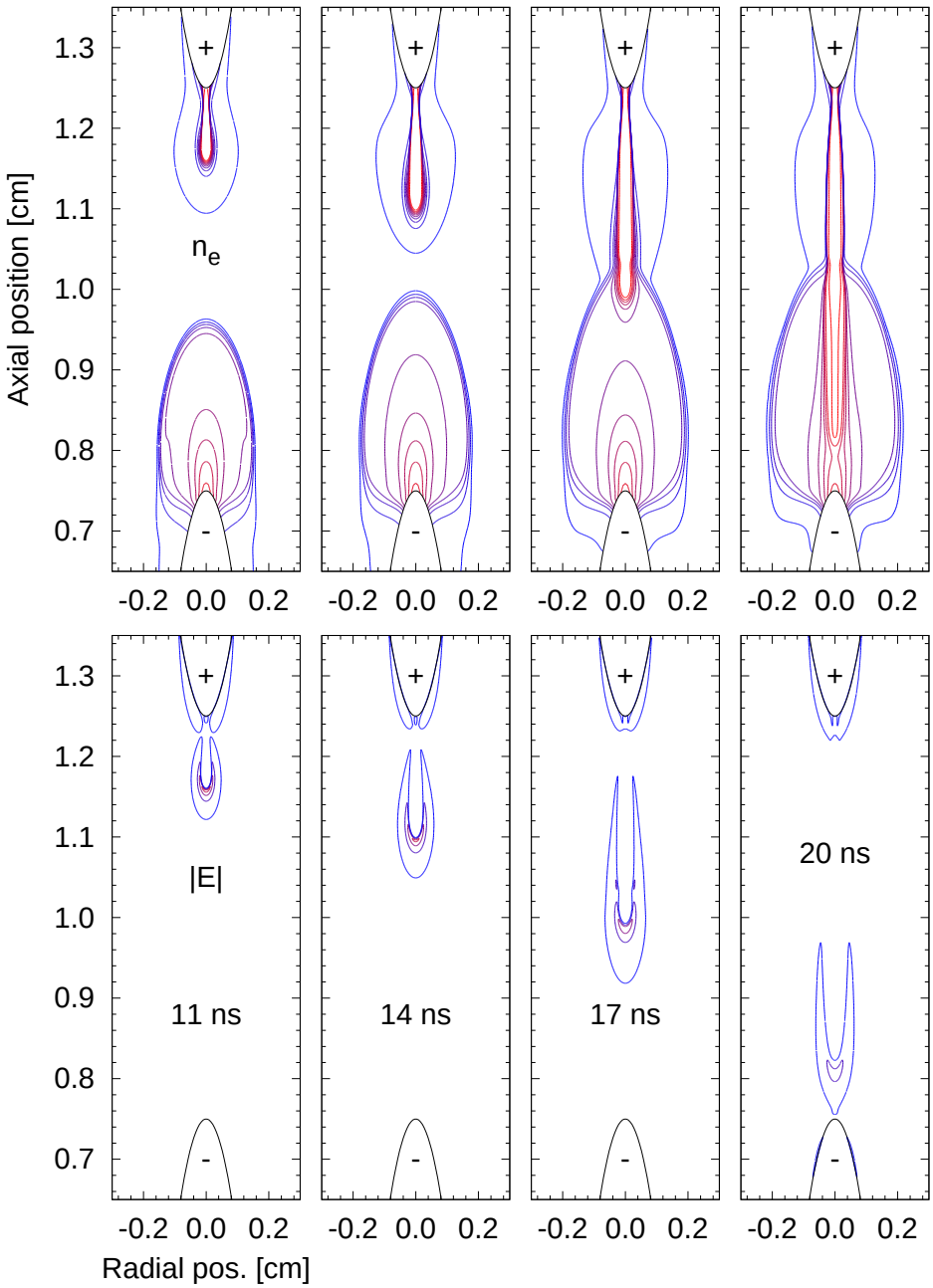

Figure IV.14: Point-to-point geometry: Two-dimensional isocontours of the electron density and the magnitude of the electric field at $t = 11$, 14, 17, and 20 ns. For the electron density, the isocontours vary from 10^9 to $10^{13.5}$ cm^{-3}, with a multiplier step of $10^{0.5}$ cm^{-3}. For the electric field the isocontours vary from 30 to 150 kV/cm, with a step of 30 kV/cm. In this case $T = 300$ K and $V_a = 10$ kV.

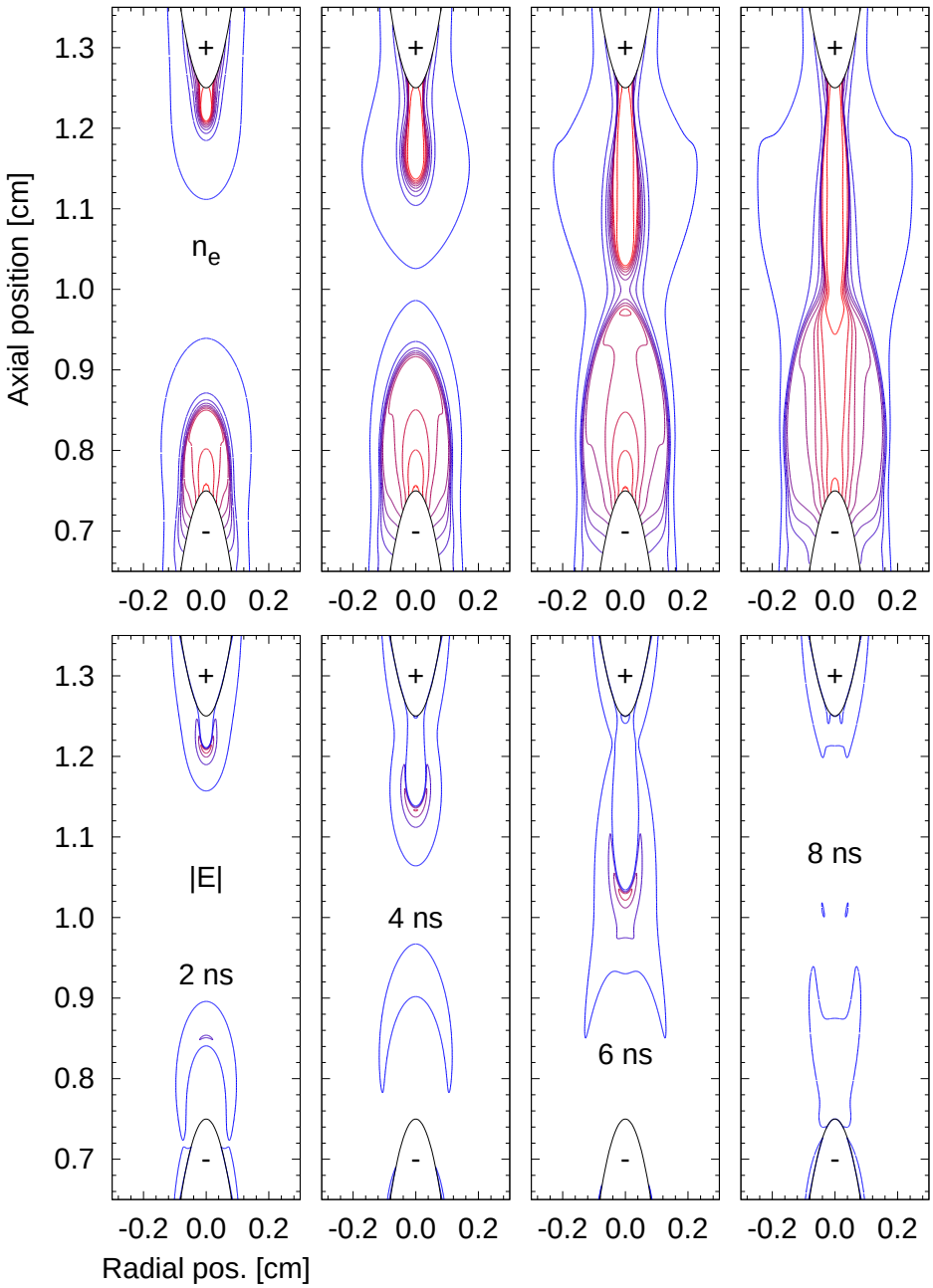

Figure IV.15: Point-to-point geometry: Two-dimensional isocontours of the electron density and the magnitude of the electric field at $t = 2$, 4, 6, and 8 ns. For the electron density the isocontours vary from 10^9 to $10^{13.5}$ cm^{-3}, with a multiplier step of $10^{0.5}$ cm^{-3}. For the electric field the isocontours vary from 30 to 150 kV/cm, with a step of 30 kV/cm. In this case $T = 300$ K and $V_a = 13$ kV.

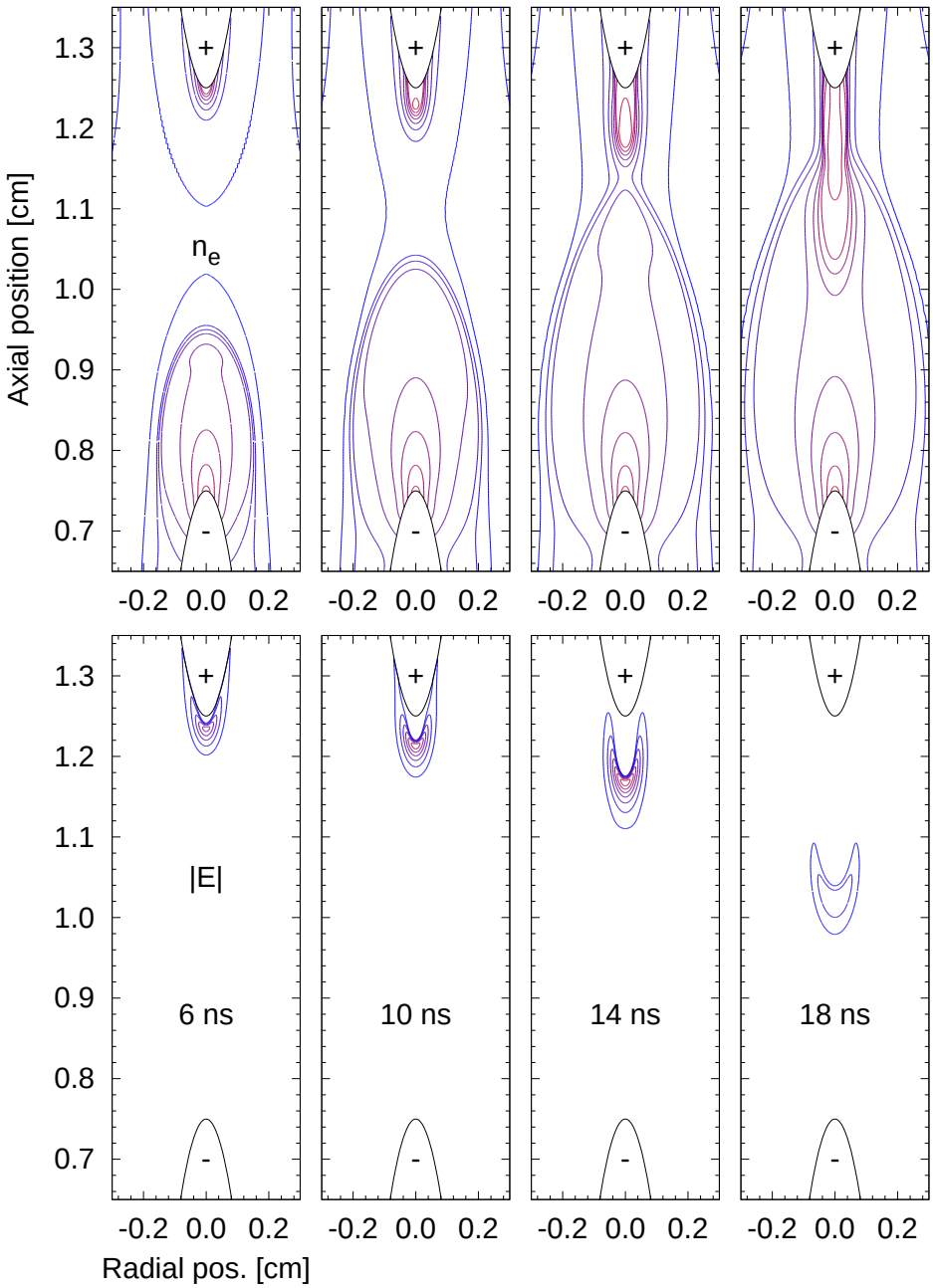

Figure IV.16: Point-to-point geometry: Two-dimensional isocontours of the electron density and the magnitude of the electric field at $t = 6$, 10, 14, and 18 ns. For the electron density the isocontours vary from 10^9 to $10^{13.5}$ cm^{-3}, with a multiplier step of $10^{0.5}$ cm^{-3}. For the electric field the isocontours vary from 10 to 30 kV/cm, with a step of 2.5 kV/cm. In this case $T = 1800$ K and $V_a = 3$ kV.

Figure IV.16 shows the results obtained at $T = 1800$ K and $V_a = 3$ kV. This figure presents a characteristic case where the positive streamer never reaches the cathode, even after contact with the negative discharge. That is, both the electron enhancement due to the discharge starting from the cathode and the electric field in the positive streamer head are insufficient to produce an electrical connection with significant enhancement in electron density. It is interesting to note that the negative discharge is broader than for cases at higher voltages.

Figure IV.17 shows the results at $T = 1800$ K and $V_a = 5$ kV. In this figure the junction is formed in less than 4 ns. Figure IV.17 also clearly shows the increase in the electron density in the discharge channel between 4.5 and 5.5 ns. Thus, this discharge will possibly turn into spark discharge during the applied voltage pulse.

Figure IV.18 shows the results at $T = 1800$ K and $V_a = 7$ kV. In this figure, the positive and negative streamers are clearly visible. They propagate toward each other and collide at $t = 1.7$ ns. This collision develops on a very short time scale compared to the previously studied cases. Furthermore, a high electron density is produced in both streamers. Given the remaining time of the voltage pulse, these conditions will likely produce a high-current spark discharge.

Similarly to the other temperature cases studied, one sees that the applied voltage has a significant impact on the propagation time scales of positive and negative streamers.

IV.4 Conclusions

In this chapter, we presented the application of the Ghost Fluid Method (GFM) with the simulation of streamer discharges between electrodes of complex geometries. In streamer simulations, it is particularly important to calculate the electric field accurately because, it is directly related to charged species densities in Poisson's equation, and because, transport parameters and source terms have a strong non-linear dependence on the electric field. Thus in this work, we have used the GFM for solving Poisson's equation in order to calculate the potential and electric field accurately close to the electrode. This method takes into account the influence of the exact shape of the electrodes in a rectilinear grid, no matter how the electrode surfaces cross the grid.

Two numerical solvers for Poisson's equation have been tested in this work: the iterative NAG module and the direct SuperLU solver. Only minor discrepancies have been observed in the streamer dynamics computed using these two solvers. In fact, direct solvers are inherently very accurate and robust. Furthermore for the case of a fixed grid, the most time-consuming step in calculating the solution (i.e., the factorization) needs to be done only once, at the beginning the discharge simulation. Thus, the direct SuperLU solver was adopted for all studies presented in this chapter.

We have conducted two validation studies to test the performance of the GFM in solving Poisson's equation for streamer simulations. In a point-to-plane geometry, we have compared the analytical solution for the potential and the Laplacian electric field with the results calculated with the GFM. Very good agreement has been observed. To show the improvement due to the use of the GFM close to the electrode, we have also compared the magnitude of the electric field computed on the same grid, with the GFM and without any special treatment for taking into account the real shape of the electrode (i.e., "the staircase

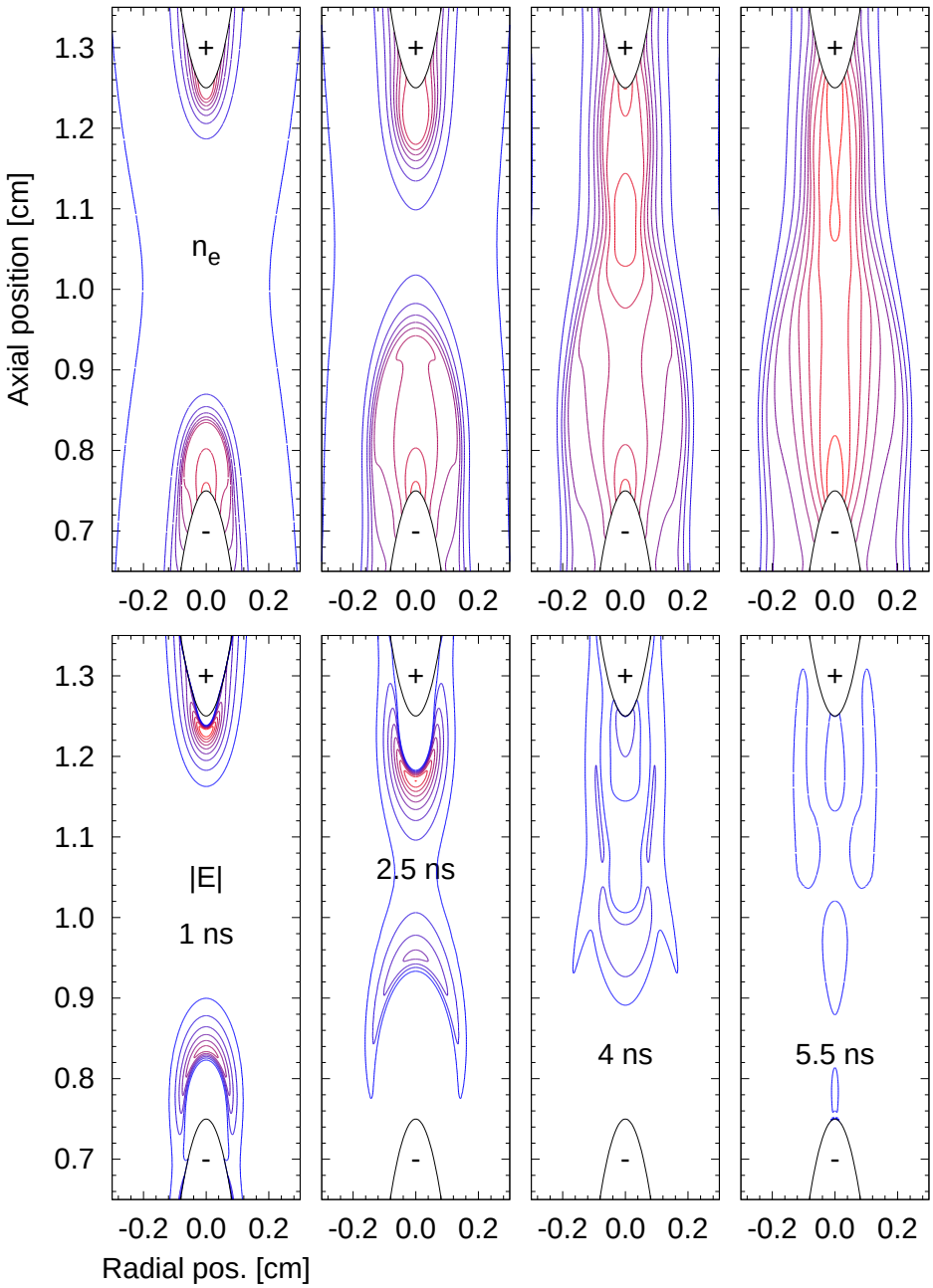

Figure IV.17: Point-to-point geometry: Two-dimensional isocontours of the electron density and the magnitude of the electric field at $t = 1$, 2.5, 4, and 5.5 ns. For the electron density the isocontours vary from 10^9 to $10^{13.5}$ cm^{-3}, with a multiplier step of $10^{0.5}$ cm^{-3}. For the electric field the isocontours vary from 10 to 30 kV/cm, with a step of 2.5 kV/cm. In this case $V_a = 5$ kV.

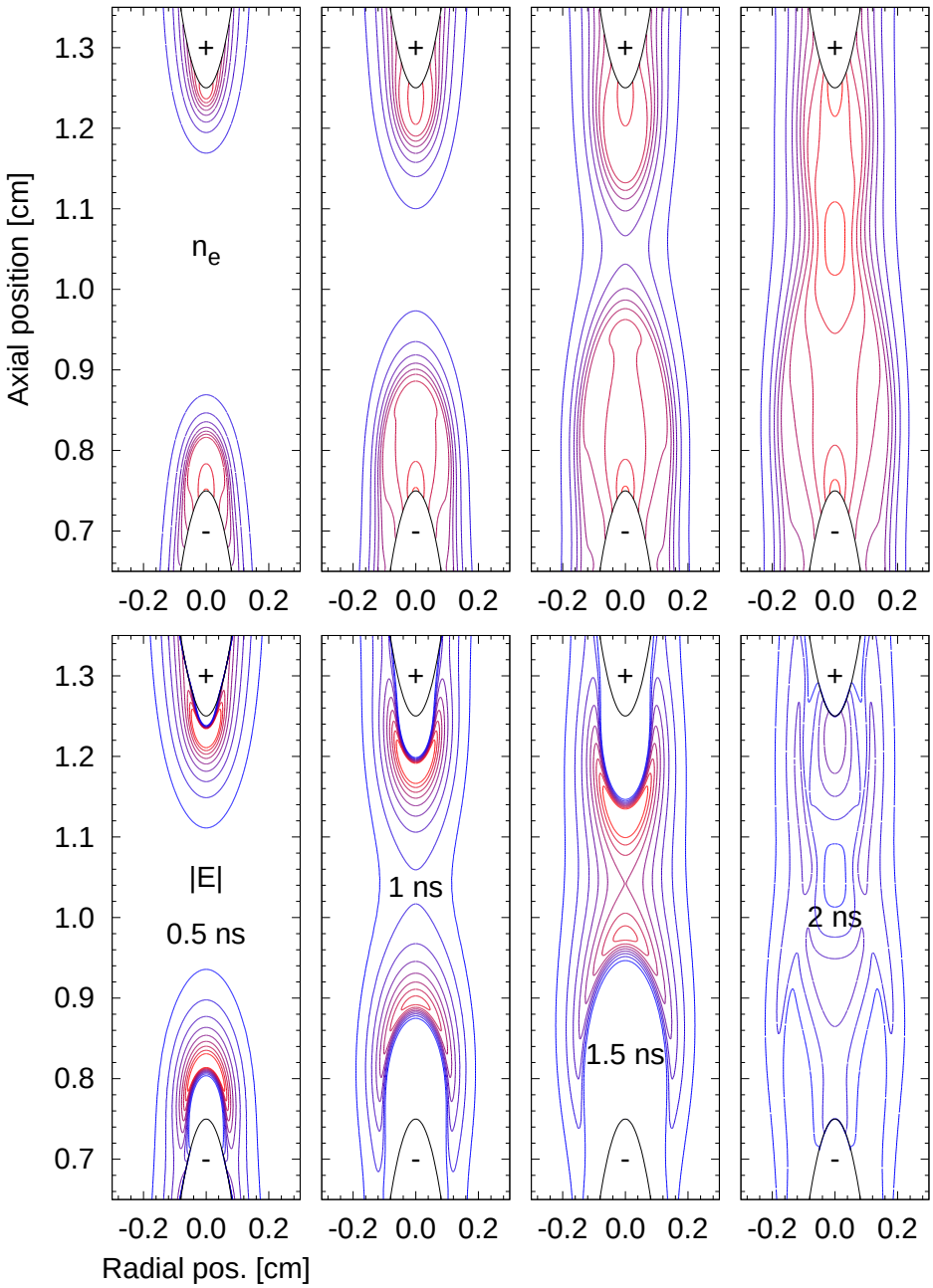

Figure IV.18: Point-to-point geometry: Two-dimensional isocontours of the electron density and the magnitude of the electric field at $t = 0.5$, 1, 1.5, and 2 ns. For the electron density the isocontours vary from 10^9 to $10^{13.5}$ cm^{-3}, with a multiplier step of $10^{0.5}$ cm^{-3}. For the electric field the isocontours vary from 10 to 30 kV/cm, with a step of 2.5 kV/cm. In this case $V_a = 7$ kV.

approach"). As expected, the discrepancy between the two numerical approaches increases as the grid becomes coarser. We have also shown that without the GFM, the electric field along the electrode surface may present unphysical oscillations due to the random crossing of the electrode surface with the grid. Second, we have compared results obtained using the GFM with results obtained by *Kulikovsky* [1998] for the simulation of the positive streamer propagation in a hyperboloid-to-plane configuration. Good agreement has been obtained on all positive streamer characteristics during its propagation in the interelectrode gap. Finally, we have applied the GFM to simulate the discharge in preheated air (at 1000 K) at atmospheric pressure in point-to-point geometry (with a 5 mm interelectrode gap). This discharge has been studied experimentally in [*Pai et al.*, 2008; *Pai*, 2008]. For a constant applied voltage of 7 kV, we have shown that positive and negative streamers start to propagate in the gap from the anode and cathode, respectively. After the streamer interact in the gap, we have observed a very rapid propagation of the positive streamer towards the cathode in the volume pre-ionized by the negative streamer. This structure of the discharge is in qualitative agreement with the experiments.

To take a first step towards understanding of the structure of discharges in point-to-point geometry in preheated air, we have carried out a short comparison study for several temperatures and applied voltages. Considering propagation time scale of the positive streamer make possible to draw conclusions about the final discharge structure (i.e., spark discharges or corona discharges) that are in good agreement with the experiments. This also indicates that the streamer modeling at short time scales can be of a great help for the understanding of nano-pulsed discharges at atmospheric pressure. In particular, it could indicate on the key physical mechanisms leading to the diffuse regime ("D" regime) and the ranges of parameters needed for generating this regime at atmospheric pressure. However, this study is only a first step towards a more thorough comparison study between experiment and simulation.

In this work, we have shown that the GFM is a simple method which can be readily implemented in existing discharge codes. In this chapter, we have studied discharges propagating between metallic electrodes, but the GFM can be easily extended to simulate dielectric barrier discharges in complex two- and three-dimensional geometries, or to study the influence of obstacles (i.e., dust particles, droplets, etc) on the streamer propagation.

In this work, no special numerical treatment has been done close to the needle electrodes to take into account the exact shape of the electrode in setting up boundary conditions for drift-diffusion equations of charged species. The boundary conditions are computed in both directions on the grid assuming that the interface has a "staircase" shape. In this chapter, as in [*Kulikovsky*, 1997a], we have used simplified boundary conditions: near the anode and cathode surfaces, the gradient of the electron density is taken to be equal to zero. More realistic boundary conditions for electrodes with complex geometries (i.e., secondary emission processes due to ion bombardment, photoemission, etc), require modeling the real shape of the electrode for setting up boundary conditions of drift-diffusion equations of charged species. For flows in complex geometries, *Tseng and Ferziger* [2003] have developed the ghost-cell immersed boundary method (GCIBM). This method handles Dirichlet and Neumann boundary conditions while preserving the overall second-order accuracy of the solver that they use in the flow far from boundaries. In [*Zeghondy et al.*, 2007], we have applied the GCIBM to implement Neumann boundary conditions on a hyperboloid anode in a point-to-plane geometry.

Chapter V

Experimental study of the impact of a dielectric material on the filamentary discharges

Table of Contents

As a clear example of the strong influence a dielectric material on the filamentary discharges, we experimentally studied a specific Dielectric Barrier Discharge (DBD) configuration. Some results of this chapter have been published in [*Celestin et al.*, 2008b].

V.1 Introduction

DIELECTRIC barrier discharges (DBDs), also known as barrier discharges or silent discharges, have been studied since the invention of the ozonizer by Siemens in 1857. Nowadays DBDs are widely used for industrial applications [*Eliasson and Kogelschatz*, 1991a], such as gas depollution, surface treatment, excimer lamps, ozone generation and plasma display panels. At atmospheric pressure (for gaseous gaps on the order of a few millimeters), DBDs are mainly constituted of unstably triggered non-equilibrium transient plasma filaments (also called microdischarges) [*Eliasson and Kogelschatz*, 1991a]. The short duration (a few tens of nanoseconds) and unpredictable triggering of these filaments make them difficult to study experimentally. During the last decade, a few authors have succeeded in following the propagation of a single filament (the streamer phase) with high resolution in time and space in a double dielectric barrier configuration, and thus have determined the electron density and electric field inside using spectroscopic diagnostics [*Kozlov et al.*, 2001].

Guikema et al. [2000] observed self-organized patterns in a one-dimensional symmetric DBD system with He/Ar mixtures and associated the patterns with characteristics for charge transfer during one cycle of the applied voltage (for frequencies on the order of a few kilohertz). They concluded that the patterns resulted from the presence of surface charge deposits; that is, related to the intrinsic so-called memory effect of DBDs [e.g., *Eliasson and Kogelschatz*, 1991a; *Golubovskii et al.*, 2002]. *Klein et al.* [2001] progressed further in this study by improving the time resolution of the imaging technique and observed that the patterns obtained in [*Guikema et al.*, 2000] were in fact constituted of several filaments ignited at different times, which were spatially and temporally controlled by the residual surface charges on the dielectric. It is also interesting to note that *Chirokov et al.* [2004] also demonstrated a behavior of self-organization in a plane-to-plane DBD in air at atmospheric pressure driven by high-frequency sinusoidal voltage (kHz) through a comparison of experimental results with a numerical model.

Recently, *Guaitella et al.* [2006] described the bimodal behavior of the statistical distribution of current peaks in a cylindrical DBD, and they concluded that the high-current group was due to the self-triggering of several filaments, presumably correlated by a radiative effect called the collective effect. They also studied the impact of this collective effect on the injected energy in the discharge, which directly controls the chemistry. Collective behavior of microdischarges has also been recently observed by imaging with a CCD camera on

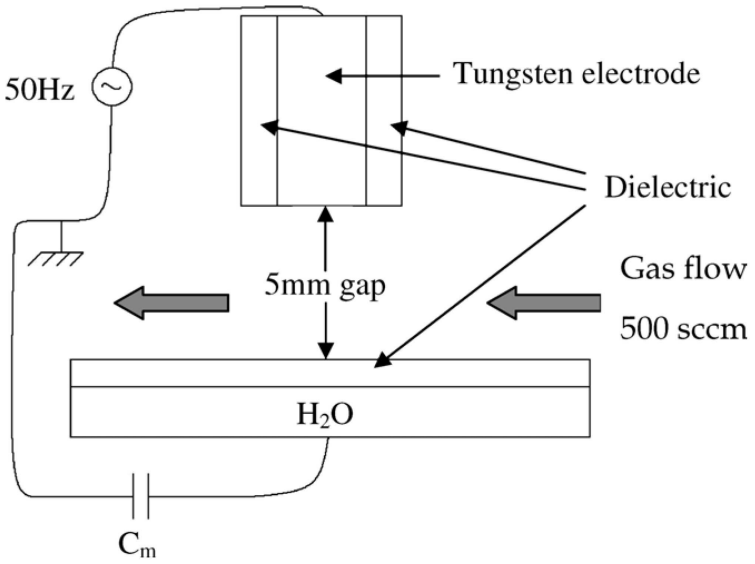

Figure V.1: Scheme of the reactor.

asymmetric surface dielectric barrier discharges (ASDBD) in [*Allegraud et al.*, 2007].

This Chapter seeks to demonstrate the strong influence of the dielectric material and the charges deposited on it on the filamentary discharges in air at atmospheric pressure at low frequency (50 Hz) using a new experimental device coupled with an imaging method.

Firstly, we describe the experimental setup and the diagnostics in Section V.2. In Section V.3 we show the characteristic regimes of the DBD by a statistical study. To show a clear correlation between discharges corresponding to different peaks and the collective behaviors of the microdischarges we present CCD imaging results of individual current peaks during the positive half-cycle in Section V.4. Then we support the argument that the deposited charges on the dielectric plate are responsible for the spatial and temporal organization of the discharges in Sections V.5 and V.6.

V.2 Experimental setup

V.2.1 DBD reactor

The discharges are produced in a Pyrex cell (see Figure V.1). The upper electrode is a cylinder in tungsten (diameter 2 mm) coated with a 1 mm layer of dielectric except on its tip, and it is linked to a 50 Hz sine wave high-voltage power supply. The lower electrode is salt water to allow for imaging. The discharge was not influenced by the salt concentration or the resulting change in the resistance of the water. In the following the conductivity of the water is ~ 800 μS/cm.

The dielectric is a cylindrical Pyrex plate of 2.2 cm diameter and 2 mm thickness (Figures V.1 and V.2) and placed above the water. Dry synthetic air flows at 500 SCCM (Standard Cubic Centimeter) through the 5 mm gap at atmospheric pressure is used for the purpose of pollution control. A gauge controls the pressure downstream of the reactor.

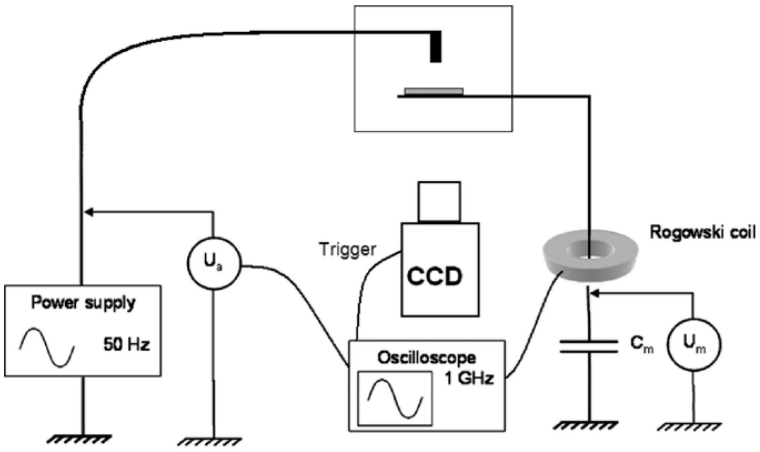

Figure V.2: Experimental set-up scheme.

V.2.2 Electrical diagnostics

At atmospheric pressure in air, breakdown occurs at about 13 kV in this reactor. This study was performed for three applied voltage amplitudes V_a of 15, 18 and 20 kV.

CCD imaging is performed by an Andor iStar 734 camera, via a B7838-UV Pentax objective which is efficient in the spectral range $230 - 800$ nm. The Lecroy LT584M 1 GHz 4 Gs/s oscilloscope, which can output an electric signal upon detecting a rising front, is used to trigger the camera. The camera can be positioned either underneath the reactor (as sketched in Figure V.2) to image the plasma zone through the water or beside the reactor to image the gap. Current peaks are measured with a Fischer F33-5 Rogowski coil with a bandwidth from 1 to 100 MHz. A capacitor C_m=1.11 nF is connected in series with the reactor to measure injected energy and charge transfer. Both V_a and V_m are measured with Lecroy PPE20kV probes (see Figure V.2). The DBD generates a small number of very short current peaks, measured as voltage steps across the capacitor as shown in Figure V.3, due to the ignition of microdischarges between the electrodes that are extinguished by the screening from the charge deposited on the dielectric plate (this process occurs over a few tens of nanoseconds) [*Eliasson and Kogelschatz*, 1991a]. The first and second current peaks correspond to the first and second voltage steps, respectively. Although DBDs generally exhibit a great number of current peaks, in this configuration only a few current peaks are observed (up to 4).

Note that in such an experimental configuration, the electrical signal of the capacitor voltage possesses a jitter of about 1 ms because of the usual unpredictability of AC DBDs at atmospheric pressure and low frequency without specific preparation of the high-field electrode [*Eliasson and Kogelschatz*, 1991b]. Moreover, one or several current peaks occur during the positive half-cycle. The total number of current peaks in one positive half-cycle depends on the applied voltage.

Figure V.4 shows an example of a characteristic current peak as a single-shot record, corresponding to the first step on the measurement capacitor voltage, measured with the Rogowski coil. We can see that its total duration is about 100 ns and its maximum is about 2 A. After $\sim$ 100 ns the current becomes slightly negative (~ -0.1 A). We have

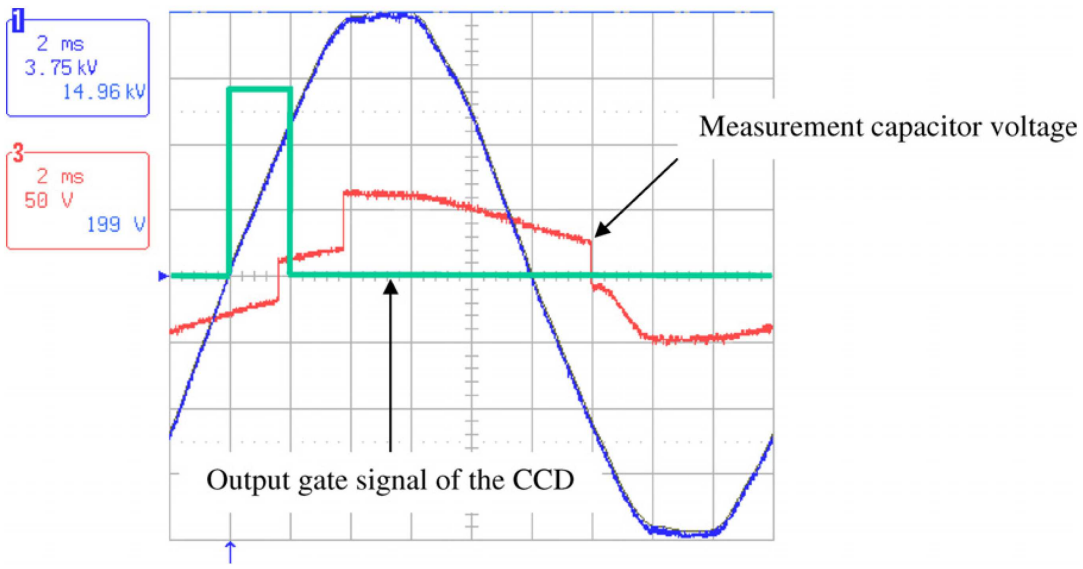

Figure V.3: Screenshot of the oscilloscope. Sinusoidal curve: power supply voltage, 3.75 kV·div^{-1}. Measurement capacitor voltage: 50 V·div^{-1}. Output gate signal of the CCD: arbitrary units. Timebase: 2 ms·div^{-1}.

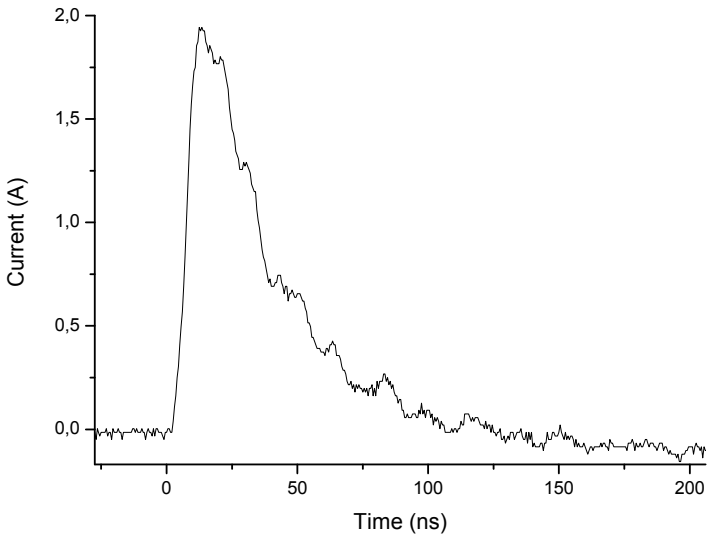

Figure V.4: Current peak measured by the Rogowski coil.

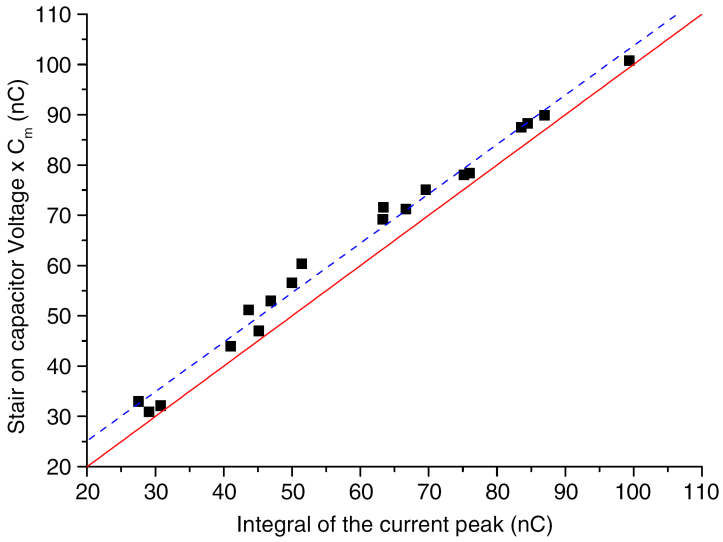

Figure V.5: Closed squares: measured integration of current peak versus the capacitor charge. Dashed line: the linear regression. Solid line: representation of the function $y = x$.

assumed that this was due to perturbations in the electrical circuit.

Figure V.3 also shows the output gate signal of the CCD camera. The CCD array is opened when the signal is non-zero. When the power supply changes polarity, the CCD switches on for 2 ms in order to overlap with the first positive step of the measured capacitor voltage. The aim of this work is to detect an event corresponding to an individual current peak (one step in the capacitor voltage) and to record the current peak and the corresponding image. Given that few current peaks occur during the positive half-cycle, a CCD gate of 2 ms results in the detection of only a single current peak. Sometimes, two current peaks can appear during the opening of the CCD, but such images are then discarded.

V.2.3 Current measurement and charge transfer

The transferred charge is estimated in two ways:

1. The voltage increase at the measurement capacitor, using $Q = \mathrm{C_m} \cdot \Delta \mathrm{U_m}$,

2. The integration of the current peak, using $Q = \int i(t)\mathrm{d}t$ from $t = 0$ to $t(i = 0)$, for a current peak recorded in single-shot.

Figure V.5 shows that the two measurement methods give close results.

We can see that the charge measured using the integral of the current peak is generally less than the charge measured with the capacitor. This is due to the sampling of the current peak (recorded in single-shot) by the oscilloscope; the integral of the current peak (2) is then slightly underestimated.

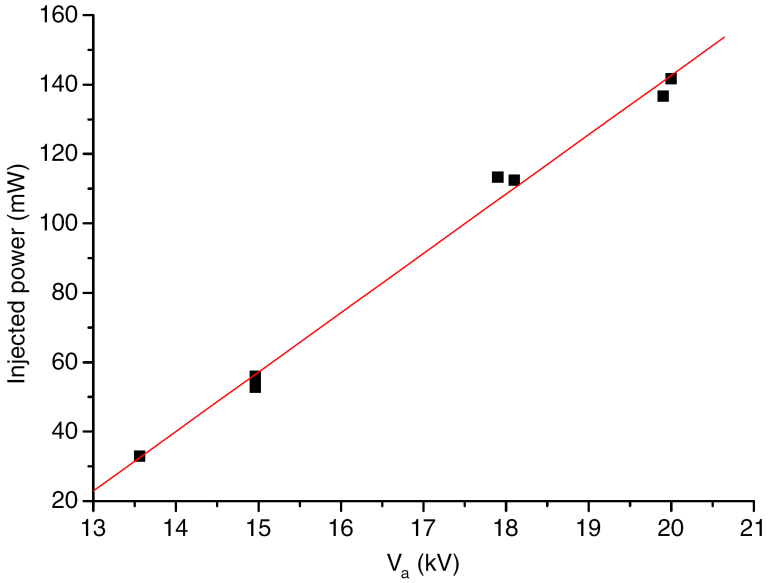

Figure V.6: Mean injected power measured using the Manley method versus the applied voltage amplitude V_a.

V.2.4 Injected power

We measured the mean power injected in the gas by the discharge for a given applied voltage amplitude using the Manley method [*Manley*, 1943] (or Lissajous method) as described in [e.g., *Allegraud et al.*, 2007; *Guaitella et al.*, 2006]. Figure V.6 shows that the mean injected power is a linear function of the maximum voltage. The injected power increases by about 17 mW per kilovolt. Compared with the results obtained in [*Guaitella et al.*, 2006], the mean injected power we obtained here is less by a factor of ten. This is related to the difference in the reactor geometries used; for example, it is interesting to note that the zone where the plasma takes place in the reactor used in [*Guaitella et al.*, 2006] is about ten times larger than the one used for this study.

V.3 Current peak statistics

V.3.1 Temporal occurrence of current peaks

In order to characterize the DBD, a statistical study over ignition times of current peaks was carried out for different applied voltage amplitudes V_a. Figures V.7(a) and V.7(b) present the mean number of peaks averaged over 100 periods of applied voltage, during each millisecond increment of the period, starting from $t = 0$ up to 20 ms (the period of the power supply voltage), for applied voltage amplitudes of 15 and 18 kV; $t = 0$ refers to the voltage zero value, increasing voltage.

Figure V.7(a) shows that at $t = 2.5 \pm 0.5$ ms, there is a 96% chance of measuring a current peak and the corresponding discharge. Figure V.7(a) also shows the fluctuation in the moment of appearance of the current peaks. We notice two time intervals for their appearance

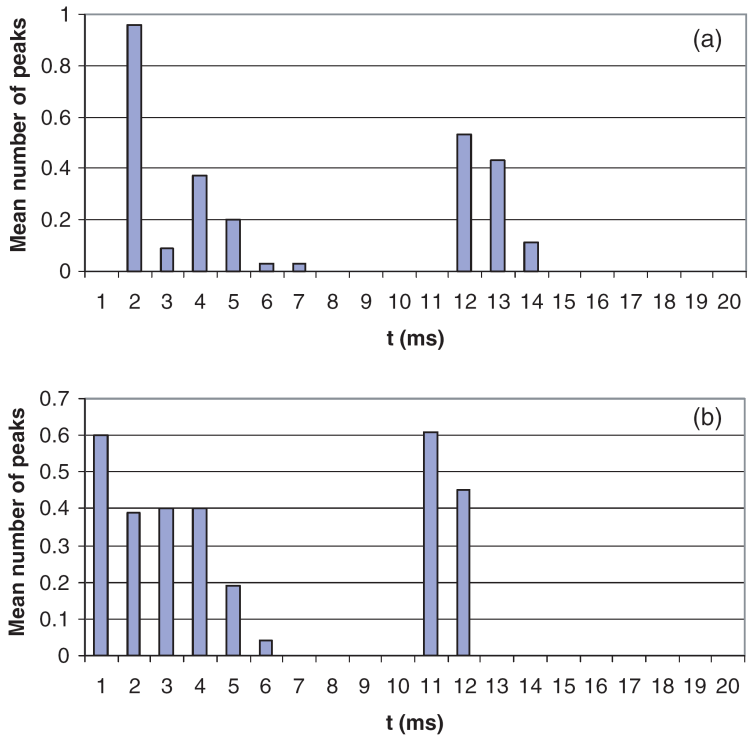

Figure V.7: Mean number of current peaks per millisecond from $t = 0$ ms to $t = 20$ ms. Between 10 and 20 ms, the current peaks are negative. (a) $V_a = 15$ kV and (b) $V_a = 18$ kV.

in the positive half-cycle ($t \in [0, 10]$ ms). Current peaks appear more consistently in time during the positive half-cycle in Figure V.7(b), which shows the measurements for the case of $V_a = 18$ kV. But Figures V.7(a) and V.7(b) cannot detail the probability of the total number of current peaks in the overall half-cycle nor the influence of the applied voltage on this probability.

V.3.2 Number of current peaks per half-cycle

The relative number of current peaks occurring in the positive half-cycle is shown in Figure V.8 for power supply voltage amplitudes of 15, 18 and 20 kV. Figure V.8 was obtained by counting the total number of events (1, 2, 3 or 4 current peaks during the positive half-cycle) over 100 complete positive half-cycles of the applied voltage, unlike the incremental method used to obtain Figures V.7(a) and V.7(b).

For 15 kV, Figure V.8 shows that two situations are observed in this regime: either only one or two current peaks occur during the positive half-cycle, with the latter in the majority of cases. For the two current peaks case, there are about 2 ms between peaks (see Figure V.3). Similar results for 18 and 20 kV are presented in Figure V.8.

The maximum of occurrences obtained for every V_a is two current peaks; the cases of 3 and 4 total current peaks only occur when the amplitude is 18 or 20 kV. There was only one current peak during the negative half-cycle for all the studied applied voltages.

From the results presented in Figure V.8, we can estimate an average number of current

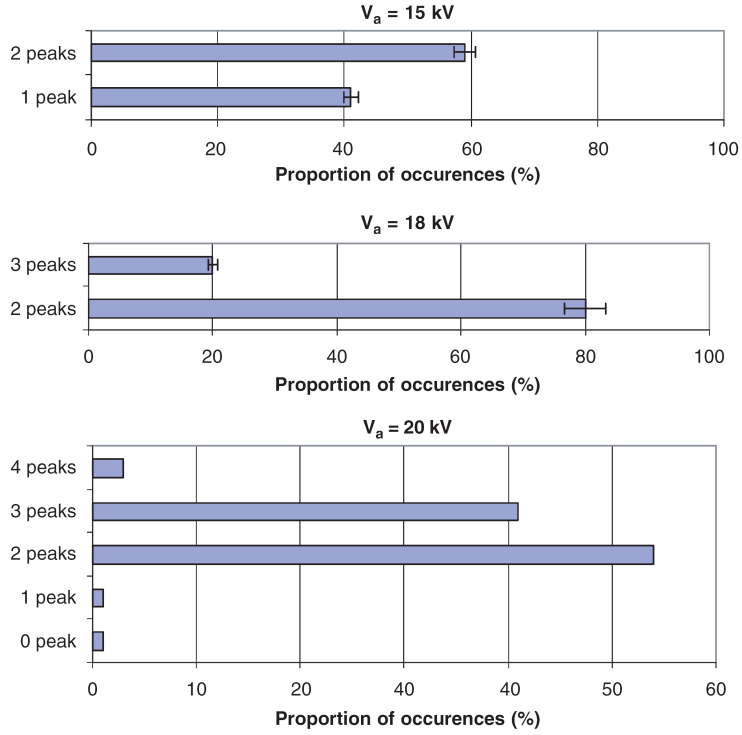

Figure V.8: Number of observed total current peaks by percentage during the positive half-cycle for a power supply voltage amplitudes of 15, 18 and 20 kV.

Table V.1: Average total number of current peaks during the positive half-cycle.

V_a(kV)	15	18	20
$\langle N \rangle$	1.6	2.2	2.4

peaks during the positive half-cycle for each applied voltage amplitude (see Table V.1). The data are consistent although insufficient to evaluate a real tendency. Indeed, as expected for a DBD, the number of events increases with the applied voltage amplitude. One can estimate a "statistical error" by summing the probabilities obtained in Figures V.7(a) and V.7(b) and dividing by the average total number of peaks. For 15 and 18 kV the error bars are shown in Figure V.8. These error bars are small (less than 10%) and show the consistency of the statistical approach used in Figures V.7 and V.8.

V.3.3 Influence of first event on subsequent events

The measured current amplitude of first current peaks during the positive half-cycle when V_a is 18 kV is plotted as a function of V_{peak}, the ignition voltage of a first current peak, in Figure V.9. The accuracy of the maximum of a current peak depends on the sampling rate of the current peak by the oscilloscope. Error bars are then evaluated according to the sampling rate. Higher sampling rates result in smaller error, but lower sampling rates permit a larger time range.

One can clearly see from Figure V.9 that the maximum of first current peak increases with

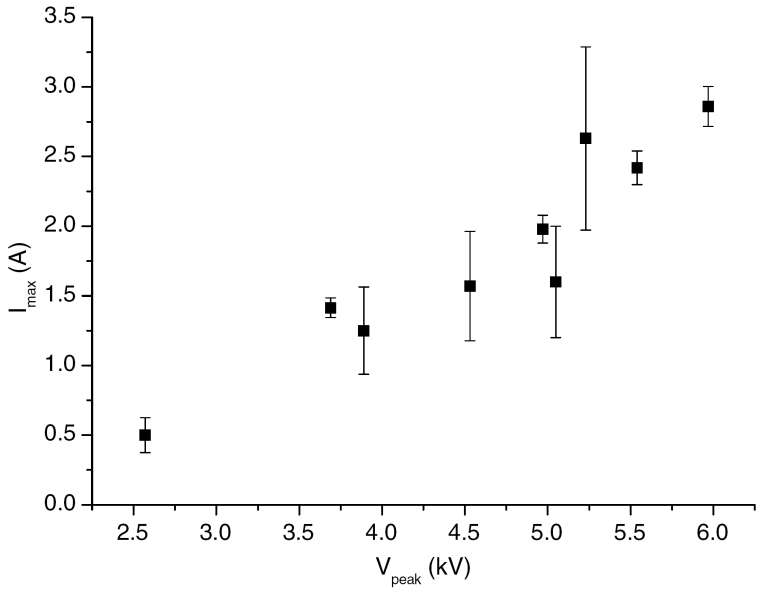

Figure V.9: Measured current amplitude of first current peaks as a function of the applied voltage at which they occur (V_{peak}). Applied voltage amplitude: $V_{\text{a}} = 18$ kV.

ignition voltage, and the same trend is observed for the transferred charge corresponding to the first current peaks. This is not clearly observed for the subsequent peaks. This is explained further in Section V.6.

To exhibit the influence of the first current peak on the subsequent ones for each positive half period we plot in Figure V.10 the number of peaks per positive half period as a function of the ignition voltage of the first one.

Figure V.10 shows that the subsequent peaks (second, third and fourth) are strongly influenced by the first one. On average, if the first current peak is ignited at small applied voltages, the subsequent events can be numerous; it becomes possible to have two, three or four peaks in total. Furthermore, according to Figure V.9, the total number of current peaks is inversely related to the intensity of the first. Figures V.9 and V.10 show that the higher the ignition voltage of the first peak, the higher its corresponding maximum current and charges transferred and the smaller the number of following peaks during this positive half-cycle. This result is explained further in Section V.6.

The spatial behavior of the microdischarges is described in the following section using CCD images corresponding to individual current peaks (first, second, etc).

V.4 CCD imaging of individual current peaks during the positive half-cycle

V.4.1 Methodology

In the previous section, we showed that depending on the AC voltage, a statistical number of peaks appear during the positive half-cycle. Here, we do not monitor the propagation of the

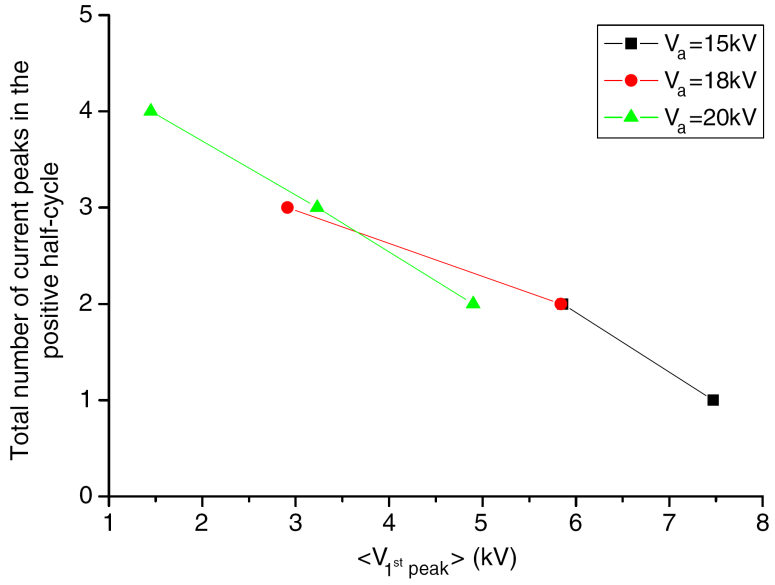

Figure V.10: Total number of current peaks in the positive half-cycle for three applied voltage amplitudes as a function of the mean ignition voltage of the first current peak.

plasma filaments. CCD imaging has been used to take pictures of individual current peaks (first, second, etc) to study the influence of their ranks (i.e., of their order of appearance in the positive half-cycle).

The total transmission time of the trigger signal from the oscilloscope to the CCD was estimated accurately to be 200 ns.

A CCD gate of 1 ms captures microdischarges emission corresponding to an individual current peak. The CCD gate is synchronized to a reference of zero applied voltage by triggering the CCD with the oscilloscope and can be shifted in time by introducing a delay, in order to picture the current peaks of different ranks.

Events pictured can be preceded or followed by other events. They always correspond to an individual current peak and are not accumulated.

Triggering the CCD with the rising current peak, as opposed to the zero voltage reference, always results in a blank picture for gate times ranging from 10 ns up to the time at which a subsequent current peak is measured. Thus no luminous events occur 200 ns after the rising current peak trigger time, thereby eliminating the possibility that microdischarges go undetected by the current probe.

V.4.2 Imaging results

As mentioned previously, only a few current peaks occur during the positive half-cycle (up to four for the 20 kV amplitude case). In the comparisons of plasma filament behavior that follow, it will be seen that the order of occurrence (i.e., rank) of the current peak is very important.

Colour scale of Figures V.11 and V.12 are represented in arbitrary units (the red being more intense than the violet).

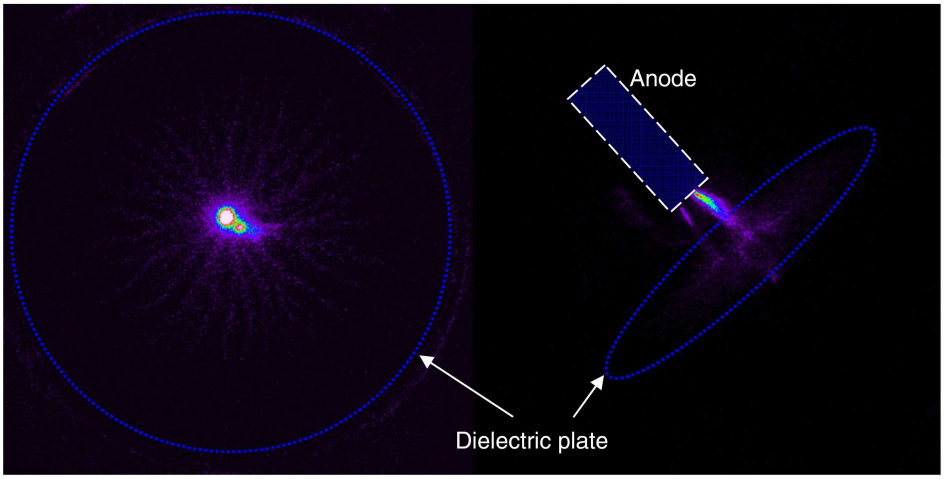

Figure V.11: CCD images of the event corresponding to a first current peak when the camera is set up underneath the reactor (left image) and in perspective from an angle (right image).

Images of a 'first current peak'

Figure V.11 shows the luminous event corresponding to a first current peak in the positive half-cycle when $V_a = 18$ kV. In this case, three current peaks can take place in total during the positive half-cycle (two discharges follow the presented one). The picture on the left of Figure V.11 corresponds to a current peak of 0.35 A, which involves a charge transfer of 10 nC; the picture on the right corresponds to a current peak of 0.9 A, which involves a charge transfer of 45 nC.

Figure V.11 is representative of discharges corresponding to a first current peak. They are localized around the center of the dielectric for the underneath visualization and most of the time corresponding to one or two filaments close to the central axis. We can also see on the left image of Figure V.11 that thin luminous filaments emanate on the dielectric surface from the 'footprint' of the filament crossing the gas gap [see also *Celestin et al.*, 2008a]. The figure obtained is close to the typical Lichtenberg figure for a positive charge deposition [*Bertein*, 1973; *Zhu et al.*, 1996; *Murooka et al.*, 2001, and references therein]. The area of this Lichtenberg figure is considerably larger than the luminous channel diameter as mentioned in [*Kogelschatz*, 2002].

Images of a 'second current peak'

Images of a second current peak in the positive half-cycle were obtained in the same manner as for the first current peak. Figure V.12 shows the features of such an event, for $V_a = 18$ kV and for three current peaks in total in the positive half-cycle. The picture on the left of Figure V.12 corresponds to a current peak of 2.25 A, which involves a charge transfer of 90 nC; the picture on the right corresponds to a current peak of 1.5 A, which involves a charge transfer of 76 nC.

One can see that the thick filaments from the left-hand image of Figure V.12 correspond to the filaments in the gaseous gap from the right-hand image. The ends of the thick

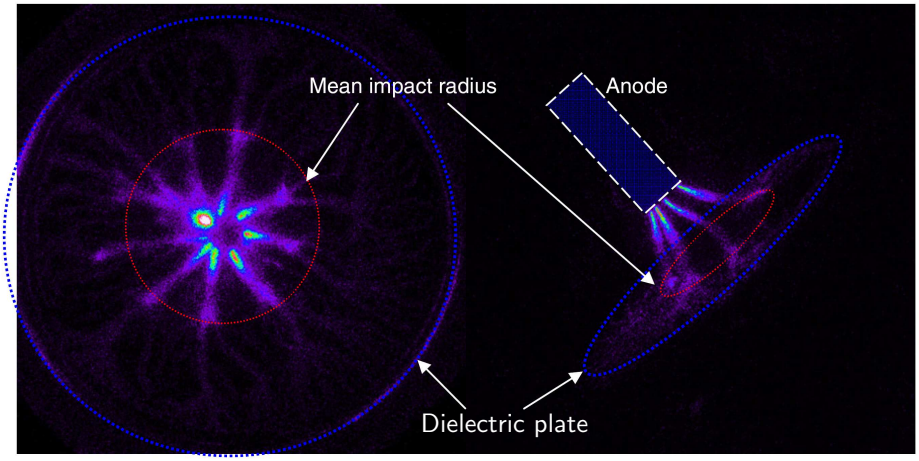

Figure V.12: CCD images of the event corresponding to a second current peak when the camera is set up underneath the reactor (left image) and in perspective from an angle (right image).

filaments on the left-hand image are in fact the 'footprints' of filaments. Hence, one can define the 'mean impact radius' from the center of the dielectric to the filaments footprints as sketched in Figure V.12. If the picture contrast is increased, one sees that yet more filaments emanate on the surface from the footprints up to the dielectric edge, forming a Lichtenberg figure for each filament in the volume.

For each V_a studied, Figure V.12 is representative of microdischarges corresponding to a second current peak. The third and fourth current peaks also have this typical multifilament and organized structure, which is quite different from the first current peaks. This behavior of microdischarges is discussed in Section V.6.

V.4.3 Spatial and temporal self-organization relation between filament length and ignition voltage of a current peak

It is possible to analyze the relation between the layout of the filaments and the electrical measurements by comparing the CCD camera pictures and the current peaks measured by the capacitor C_m or the Rogowski coil.

Mean impact radii were calculated for several current peaks and were related to the applied voltage at which the current peaks occur (V_{peak}). We realized these measurements for three applied voltage amplitudes: $V_a = 15$, 18 and 20 kV.

Increasing the applied voltage amplitude V_a, reduces the average time of the first peak appearance. This is a well-known effect in DBDs, which is due to the fact that the total amount of transferred charge in cycles of the applied voltage increases with applied voltage. This results in greater residual surface charge on the dielectric surface, causing the first peak to ignite sooner. To avoid this shift and make an overall comparison for different V_a, $\langle V_{peak} \rangle$ the average voltage at which the first peak occurs for one V_a, was estimated and subtracted from each V_{peak} [*Allegraud et al.*, 2007].

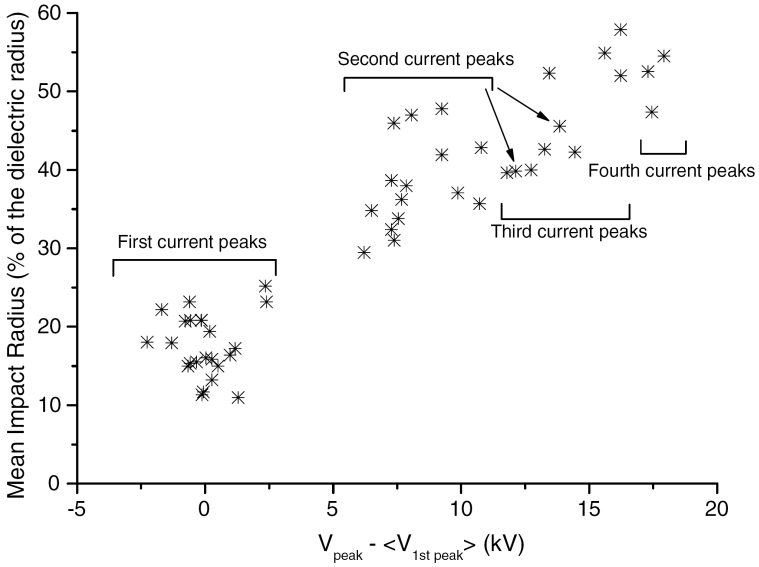

Figure V.13: Mean impact radius length versus the corrected voltage.

The graph from Figure V.13 clearly shows an increasing linear relation of the envelope of the points. It must be noticed as well that data for the three applied voltage amplitudes 15, 18 and 20 kV match. Finally, one can see that filaments corresponding to peaks of different ranks are in different voltage ranges of V_{peak} and different length ranges of the mean impact radius. Beyond the fourth peak, we observed that the dielectric plate is not large enough for continuing the tendency shown in Figure V.13. Filaments which cannot reach the dielectric plate anymore may reach the side of the reactor (also made of Pyrex).

The increase in the mean impact radius in one positive half-cycle with the rank of the current peak is due to the deposition of charges by the previous discharges in the same positive half-cycle; this is confirmed by a simple electrostatic model in Section V.5 and also discussed in Section V.6.

V.5 Electrostatic modeling

A numerical 2D-axisymmetric electrostatic model simulation of the reactor has been performed using COMSOL Multiphysics® to validate the measured transferred charge by a microdischarge and to understand the physical impact of the charges deposited on the dielectric plate on the transient filamentary discharges (see Figure V.14).

Breakdown occurs when the metallic electrode is at about 13 kV. As seen previously, the breakdown voltage decreases for the subsequent microdischarges due to the deposition of charges on the dielectric. Assuming a quasi-uniform distribution of the negative charge over the dielectric during the negative cycle, the potential difference between the metallic electrode and the water electrode then has to be on the order of 13 kV for a first current peak. Under this assumption, we fixed the metallic electrode at 13 kV and placed no charge upon the dielectric surface. Having defined the boundary conditions for the simulation domain, we can obtain the Laplacian electric field in the gaseous gap (see Figure V.14), and we

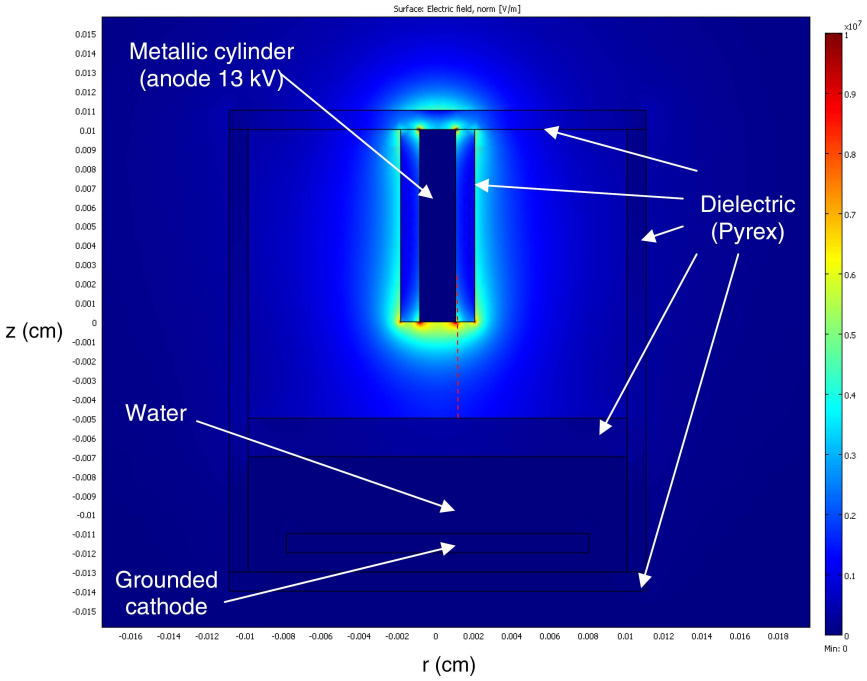

Figure V.14: Electric field ($V \cdot m^{-1}$) given by the electrostatic model without surface charge on the dielectric plate. Red dashed line: line along which we take the norm of the electric field in Figure V.15.

can also define a positive surface charge density upon the dielectric to model the screening of the electrostatic field by the transferred positive charges of a first current peak. This surface charge density is not homogeneous [*Kozlov et al.*, 2001; *Yurgelenas and Wagner*, 2006] and is assumed to be Gaussian:

$$\sigma_s(r) = \frac{Q}{2\pi\sigma^2} \exp\left(-\frac{r^2}{\sigma^2}\right) \tag{V.1}$$

where σ is the characteristic length of the charge deposit (which can be chosen according to the experimental results) and Q is the total amount of charge (integration of (V.1) from $r = 0$ to infinity). From the measured mean impact radius of the first peaks from Figure V.13, we can take $\sigma = 0.2$ cm and look for the results with different Q. By running this simulation, we found that Q must be $\sim 10 - 100$ nC to obtain an electric field comparable to the electric field applied. This corresponds well to the values we obtained experimentally. In Figure V.15 we plot the results of the simulation for the electric field along the red dashed line of Figure V.14 (called arc-length) from the place of the maximum Laplacian electric field (at the edge of the metallic cylinder electrode) to the dielectric plate, for different Q.

We can see in Figure V.15 that the value of Q for which the maximum field (at the metallic edge) is the most shielded is 40 nC. The electric field increases at this point for lower or higher Q, with the latter case corresponding to an inversion of the field. This fits well with the experimental results, as indeed $Q = 40$ nC is the average charge transferred by a first current peak.

One also can see in Figure V.15 that the electric field on the dielectric surface increases significantly with Q and can exceed the breakdown voltage. The physics is then no longer

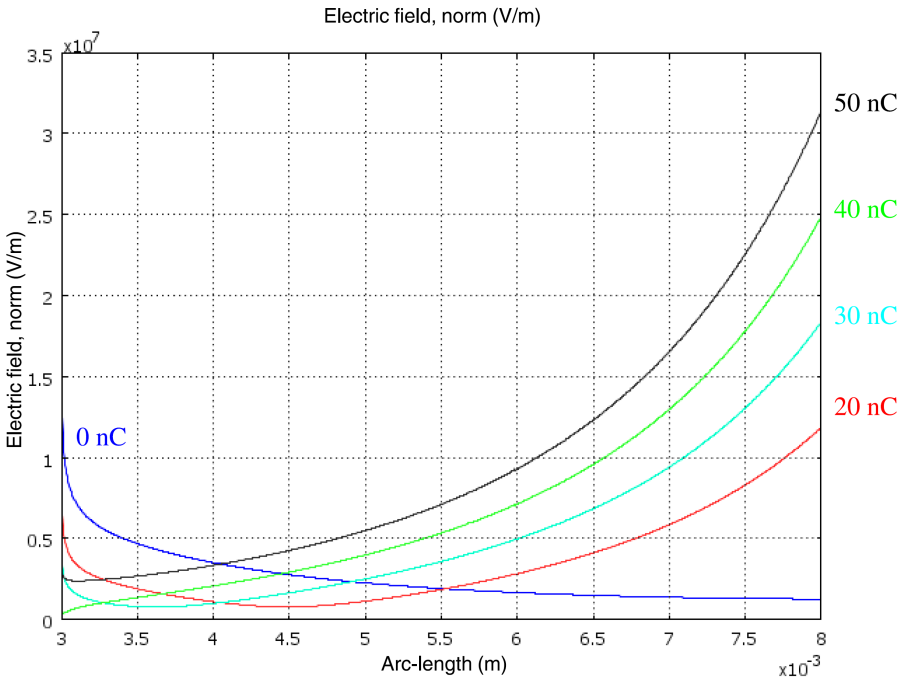

Figure V.15: Norm of the electric field for several total amounts of charge upon the dielectric. Arc-length= 3 mm corresponds to the edge of the metallic electrode and Arc-length= 8 mm corresponds to the dielectric plate with a Gaussian surface charge distribution (V.1), with $\sigma = 2 \cdot 10^{-3}$ m.

static and involves the triggering of surface discharges. Of course, a dynamic simulation would be necessary to completely model this behavior and we make a first step to realize it in the chapter VI.

V.6 Discussion

From this study, it follows that for discharges generated in air at atmospheric pressure using this particular reactor driven by a 50 Hz sine wave power supply, only a few current peaks appear in the positive half-cycle of the applied voltage (similar to the results of [*Guikema et al.*, 2000] for another DBD configuration). The electrical measurements combined with the imaging diagnostics revealed that the first current peak in the positive half-cycle corresponds mostly to a single centred filament in the gaseous gap (see Figure V.11). All of the subsequent peaks always correspond to a bunch of filaments in the gaseous gap (see Figure V.12). This reveals the generation of several transient discharges in a time window smaller than 50 ns, according to the current peak measurements (i.e., Figure V.4), which is a time scale effectively instantaneous compared with the characteristic rising time of the applied voltage ($\sim$ 1 ms for the results presented herein). Photon radiation coupling may explain the correlation between so many filaments over such a time scale. *Guaitella et al.* [2006] explained that an initial filament triggers the others by irradiating the dielectric plate, but we can also suggest that additional radiative processes by a first streamer play a role, such as photoionization in the high-field region.

Furthermore, we see in Figure V.12 that the subsequent discharges following a first peak do not reach the center of the dielectric anymore. More precisely, the mean impact radius was measured as an increasing function of V_{peak} (see Figure V.13). This effect on the layout of the plasma filaments is due to the charges deposited on the dielectric. It must be noted that the behavior of the transient filaments and the measurements of the charge transferred by a first current peak are in good agreement with a simple electrostatic model discussed in Section V.5. This model also confirms that the screening mechanism of a DBD, namely the deposition of charges on a dielectric, changes the entire field configuration in the gaseous gap as well as the propagation of subsequent streamers. As stated in [*Kogelschatz*, 2002], in a typical discharge situation there is a competition between individual microdischarges for the available surface area. In the situation we encountered in this chapter, this competition is dominated by the residual charges already deposited on the dielectric by the previous discharges, and this effect makes the filaments of successive current peaks extend farther and farther from the center of the dielectric to deposit their charge. It has to be noted that in this study we did not observe a single sequence of current peaks in the same positive half-cycle of the applied voltage. It was impossible because the readout time of the CCD was too long.

Moreover, Figure V.9 shows that, for the first peak in the positive half-cycle, the maximum current increases with V_{peak}, the applied voltage at which the current peak appears. Therefore, because the charge transferred is related to the screened field, in this experimental configuration, the discharge does not occur for a constant voltage in the gaseous gap (meaning the gap above the deposits of charge). Equivalently, the discharge does not occur at a constant field, presumably the breakdown field, in the high-field region near the metal cylinder edge. Indeed, if the microdischarge occurred at a constant voltage in the gaseous gap (presumably the breakdown voltage in the considered geometry), it would generate always the same current necessary to transfer sufficient charge to screen the electric field. We propose that the ignition time of the first current peak (of which current-voltage relationship is shown in Figure V.9) corresponds to the efficiency and the stochasticity of the initiation of the 'pre-breakdown phase' described in [*Kozlov et al.*, 2001; *Yurgelenas and Wagner*, 2006] or the 'Townsend phase' described in [*Braun et al.*, 1992]. In the configuration used in this chapter, the pre-breakdown phase activity occurs at the edge of the metallic cylinder electrode, where the radius of curvature is smallest and hence where the electric field is strongest. The moment of the beginning of the Townsend phase is suspected here to be influenced by the charge deposited on the dielectric, as surface charge can affect the secondary emission from the dielectric. The current of this microdischarge is then determined by the electric field at the metallic electrode when the microdischarge finally occurs.

The impact of the amount of charge deposited on the dielectric plate on (1) the multifilament behavior and (2) the intensity of the discharges cannot be resolved solely by using a static model; a dynamic model of streamer propagation toward a charged dielectric plate is required.

V.7 Conclusions

The electrical measurements combined with the imaging diagnostics revealed that the first current peak in the positive half-cycle corresponds mostly to a single centred filament in the gaseous gap, but all of the subsequent peaks always correspond to organized multi-filamentary discharges in the gaseous gap. Both kinds of discharges are strongly branching over the dielectric material.

The spatial organization of plasma filaments is strongly affected by the deposited charges on the dielectric material. A first discharge in the positive half-cycle deposits charges close to the center of the dielectric plate. Subsequent discharges are affected by these surface charges and plasma filaments then impact the dielectric farther and farther from the center of the dielectric plate.

The first current peak ignition time corresponds to the efficiency and the stochasticity of the initiation of the 'pre-breakdown phase' and consequently the amount of transferred charges in the positive half-cycle is correlated with the voltage at the metallic electrode when a first current peak occurs. This has an impact on the temporal organization of discharges in one positive half-cycle.

A model of the streamers dynamics in such an experimental configuration is required to better understand the impact of a dielectric material, and the charges deposited upon it, on the streamers dynamics. Such a study is presented in Chapter VI.

Chapter VI

Simulation of streamer propagation in a point-to-plane DBD configuration

Table of Contents

VI.1 Introduction

As stated in Chapter V, in order to further advance in the understanding of the discharge, it is necessary to study streamer dynamics in Dielectric Barrier Discharges. However, the experimental setup used in this Chapter has a complex geometry, especially with a dielectric around the tip anode. Therefore, three-dimensional computations would be necessary to simulate this discharge.

In this chapter, we consider a simplified axisymmetric configuration using a hyperboloid point-to-plane geometry with a dielectric material on the plane cathode. We study the streamer dynamics in this configuration, and we show that the results obtained are in good agreement with the experimental results obtained in Chapter V.

The point-to-plane configuration studied is depicted in Figure VI.1 and is similar to the one presented in Chapter IV, with the addition of a dielectric material on the plane cathode. The configuration is axisymmetric, with a needle anode that is assumed to be an infinite hyperboloid body of revolution about the axis of symmetry. The cathode is the plane perpendicular to the axis of symmetry and coinciding with the origin of x coordinate.

Near the needle electrode, the electric potential is calculated by solving the discretized Poisson's equation (II.2) using the Ghost Fluid Method (see Chapter IV). As for the case with no dielectric material, the analytical Dirichlet boundary condition is used in order to reduce the time consumption of the simulation. Indeed, as stated at the end of Section IV.2.1, solving Poisson's equation accurately using the homogeneous Neumann boundary condition ($\vec{\nabla}V \cdot \vec{n} = 0$, where $\vec{n}$ is the unit vector normal to the surface boundary) would be more time-consuming as it requires expanding the computational domain and thus significantly increasing the computation time of the simulation.

In Figure VI.1, we have divided the electrode gap into two domains Ω_1 and Ω_2. The domain Ω_1 is constituted of air at $t = 0$, therefore the dielectric permittivity in this domain is $\epsilon = \epsilon_0$; this is the domain in which the discharges propagate. The domain Ω_2 is the dielectric material with permittivity $\epsilon = \epsilon_2$.

To take into account several domains with different dielectric permittivities, the governing equation for the electric field is:

$$\vec{\nabla} \cdot \vec{D} = \rho \tag{VI.1}$$

where $\vec{D} = \epsilon_0 \vec{E} + \vec{P}$ is the electric displacement field, and $\vec{P}$ the polarization density of the material. For linear and isotropic media, $\vec{D} = \epsilon \vec{E} \equiv \epsilon_r \epsilon_0 \vec{E}$, where ϵ and ϵ_r are scalars. Thus, as $\vec{E} = -\vec{\nabla}V$, the equation governing the electric potential is Poisson's equation

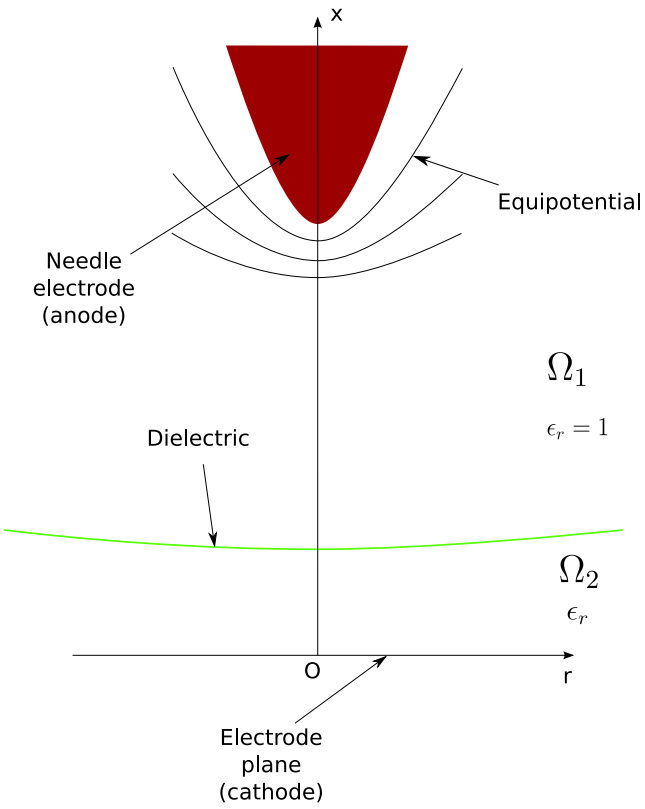

Figure VI.1: Illustration of the hyperboloid needle-to-plane system with a dielectric material layer above the plane cathode. The potential at the needle is V_a. The electric potential at the cathode plane is 0 V. The domain Ω_1 is in air, and therefore has a dielectric permittivity ϵ_0. The domain Ω_2 is the dielectric with a dielectric permittivity ϵ_2.

(I.31) with variable coefficients:

$$\vec{\nabla} \cdot (\epsilon \vec{\nabla} V) = -\rho \tag{VI.2}$$

where the charge density ρ is generally a function in space at a given time. The dielectric of the reactor described in Chapter V is made of Pyrex, hence its relative permittivity ranges between 4.6 and 5. In the following, we take ϵ_r=5 for the relative permittivity of the dielectric material. Its thickness is $d = 1$ mm.

In Section VI.2 we will present the discretization of Equation (VI.2) on a numerical grid. In Section VI.3 we will find the analytical solution of (VI.2) in a configuration similar to the one we will simulate. This analytical solution will be used in the simulations as boundary conditions for Poisson's equation. The streamer simulations in the point-to-plane configuration with a dielectric plane will be presented in Section VI.4. The obtained results will then be compared to experimental measurements presented in Chapter V.

VI.2 Discretization of a Poisson's equation with variable coefficients

To take the plane dielectric layer positioned above the cathode into account, one can discretize Equation (VI.2) using the same method as for Poisson's equation with constant coefficients (II.1). The coefficients of the discretized Poisson's equation (II.2) become:

$$\begin{cases} V^{\mathrm{n}}_{i,j} &= \dfrac{2r_{j+1/2}\epsilon_{i,j}\epsilon_{i,j+1}}{(r^2_{j+1/2}-r^2_{j-1/2})(\epsilon_{i,j}(r_{j+1}-r_{j+1/2})+\epsilon_{i,j+1}(r_{j+1/2}-r_j))} \\ V^{\mathrm{s}}_{i,j} &= \dfrac{2r_{j-1/2}\epsilon_{i,j}\epsilon_{i,j-1}}{(r^2_{j+1/2}-r^2_{j-1/2})(\epsilon_{i,j-1}(r_j-r_{j-1/2})+\epsilon_{i,j}(r_{j-1/2}-r_{j-1}))} \\ V^{\mathrm{e}}_{i,j} &= \dfrac{\epsilon_{i,j}\epsilon_{i+1,j}}{(x_{i+1/2}-x_{i-1/2})(\epsilon_{i,j}(x_{i+1}-x_{i+1/2})+\epsilon_{i+1,j}(x_{i+1/2}-x_i))} \\ V^{\mathrm{w}}_{i,j} &= \dfrac{\epsilon_{i,j}\epsilon_{i-1,j}}{(x_{i+1/2}-x_{i-1/2})(\epsilon_{i-1,j}(x_i-x_{i-1/2})+\epsilon_{i,j}(x_{i-1/2}-x_{i-1}))} \\ V^{\mathrm{c}}_{i,j} &= -(V^{\mathrm{w}}_{i,j}+V^{\mathrm{e}}_{i,j}+V^{\mathrm{s}}_{i,j}+V^{\mathrm{n}}_{i,j}) \end{cases} \tag{VI.3}$$

where $\epsilon_{i,j}$ is the dielectric permittivity at grid node (i,j). We also have to take into account the surface charge density on the dielectric σ_s, which causes an additional jump in the normal component of the electric field. As we consider here a plane dielectric, σ_s is only a function of the radial position, and we define $\sigma_{sj} \equiv \sigma_s(r_j)$. Considering the numerical grid, as depicted in Figure VI.2, we assume that the dielectric surface lies on the interface between the nodes (i^*,j) and (i^*+1,j); i.e., on the edge of cell $(i^*+1/2,j)$. Thus, the source term $\rho_{i,j}$ of (II.2) has to be replaced with $\rho'_{i,j}$ only at the points $(i=i^*,j)$ and $(i=i^*+1,j)$, such that:

$$\begin{cases} \rho'_{i^*+1,j} = \rho_{i^*+1,j} - \dfrac{\sigma_{sj}(x_{i^*+1/2}-x_{i^*})}{(x_{i^*+3/2}-x_{i^*+1/2})(\epsilon_{i^*+1,j}(x_{i^*+1/2}-x_{i^*})+\epsilon_{i^*,j}(x_{i^*+1}-x_{i^*+1/2}))} \\ \rho'_{i^*,j} = \rho_{i^*,j} - \dfrac{\epsilon_{i^*,j}\sigma_{sj}(x_{i^*+1}-x_{i^*+1/2})}{\epsilon_{i^*+1,j}(x_{i^*+1/2}-x_{i^*-1/2})(\epsilon_{i^*,j}(x_{i^*+1}-x_{i^*+1/2})+\epsilon_{i^*+1,j}(x_{i^*+1/2}-x_{i^*}))} \end{cases} \tag{VI.4}$$

In the considered configuration, $\epsilon_{i^*+1,j}=\epsilon_0$ and $\epsilon_{i^*,j}=\epsilon_2$. The surface charge density on the dielectric material is caused by the fluxes of charged species to the dielectric surface, and thus we define the surface charge at time t^{k+1} as:

$$\begin{cases} \sigma^{k+1}_{sj} = \sigma^k_{sj} + qF^{x,k}_{p,i^*+1/2}\dfrac{\Delta t}{\Sigma_{i^*+1/2,j}} & \text{if } E^x_{i^*+1/2}>0 \\ \sigma^{k+1}_{sj} = \sigma^k_{sj} - qF^{x,k}_{e,i^*+1/2}\dfrac{\Delta t}{\Sigma_{i^*+1/2,j}} & \text{if } E^x_{i^*+1/2}<0 \end{cases} \tag{VI.5}$$

where subscripts "p" and "e" refer to positive ions and electrons, respectively, $\Sigma_{i^*+1/2,j}$ is the surface of the interface of the cell in contact with the dielectric, and $F^{x,k}_{i^*+1/2}$ refers to the fluxes defined in Chapter II accounting for drift fluxes and diffusion fluxes (depending

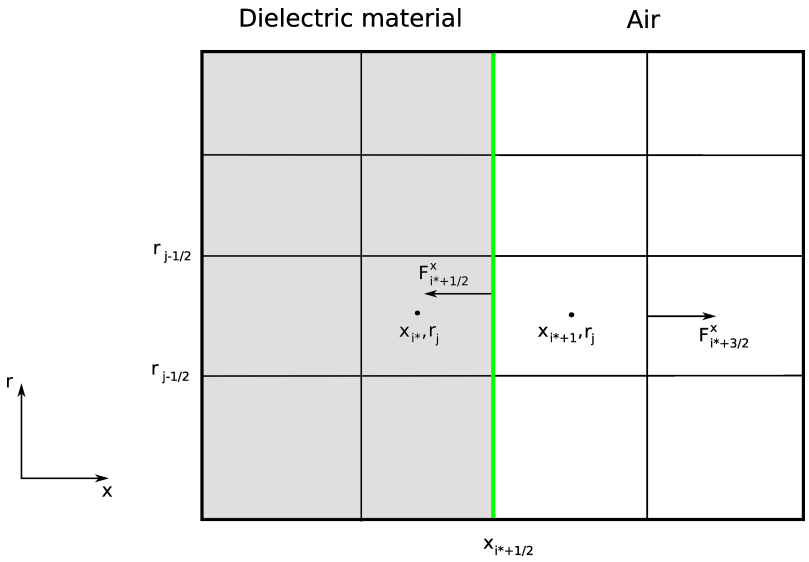

Figure VI.2: Representation of the numerical grid in the presence of a plane dielectric. The shaded domain represents the region Ω_2. The gas/dielectric interface lies at $x_{i^*+1/2}$.

on the chosen boundary conditions). Relation (VI.5) means that charged species can be deposited on the dielectric, but we do not consider that they can leave the dielectric surface on the time scale studied in this work.

VI.3 Analytical electrostatic study of the point-to-plane configuration with dielectric

In Section IV.2.2 we solved Laplace's equation with constant coefficients in hyperbolic geometries. Equation VI.2 (with $\rho = 0$) can be solved in similar fashion, that is through the use of the symmetry of the electrostatic system. In Section IV.2.2, we showed that this problem is clearly simplified by the use of hyperbolic coordinates, since equipotential surfaces and electric field lines are confocal hyperboloids of revolution and their corresponding orthogonal ellipsoids, respectively. Ideally, we would simulate a planar dielectric material, since it is planar in the experimental study. Using a plane also simplifies the definition of boundary conditions for the fluxes in a rectilinear mesh. However, in this hyperbolic configuration a plane dielectric breaks the symmetry of the system. Indeed, the planar dielectric surface cannot be defined as an equipotential surface, and the polarizing effect of the dielectric may distort the layout of electric potential in a very complex way.

The analytical solution of Poisson's equation (VI.2) with $\rho = 0$ is needed for defining the boundary conditions (see Figure IV.3). It can also be used to initialize an iterative solver for Poisson's equation in the whole simulation domain. To derive this analytical solution, we have assumed that the dielectric interface is not exactly a plane but instead follows an equipotential surface of the point-to-plane system without dielectric. That is, we have assumed that the dielectric interface is a hyperboloid confocal to the anode (see Figure VI.1). It is interesting to note that the hyperbolic equipotential surfaces in the case without dielectric material remain so in the case with dielectric because of the system symmetry.

We recall the transformation from Cartesian to hyperbolic coordinates (IV.7):

$$\begin{cases} x &= \alpha\xi(1+\eta^2)^{1/2} \\ r &= \alpha\eta(1-\xi^2)^{1/2} \end{cases} \tag{VI.6}$$

where $\xi^2 < 1$ and $\alpha \neq 0$. The equipotential surfaces of the problem are defined by $\xi(x,r) = C$, where C is a constant. We note that $\xi = \xi_0$ defines the anode surface, $\xi = 0$ defines the cathode plane, and $\xi = \xi_1$ defines the dielectric interface.

To define the dielectric interface, we consider a hyperboloid equipotential surface $\xi = \xi_1$ close enough to the cathode to be considered a good approximation of a plane dielectric.

VI.3.1 Electric potential

The relative dielectric permittivity ϵ_r is a constant in each domain Ω_1 and Ω_2. Thus it is possible to solve for the electric potential in each domain separately. Given the symmetries of the system, the solution in each domain follows from the electric potential given in Section IV.2.2 (i.e., Equation (IV.9)):

$$\begin{cases} V_1 = \dfrac{A}{2}\log\dfrac{1+\xi}{1-\xi} + B & \text{in } \Omega_1 \\ \\ V_2 = \dfrac{A'}{2}\log\dfrac{1+\xi}{1-\xi} + B' & \text{in } \Omega_2 \end{cases} \tag{VI.7}$$

where A, B, A', and B' are the four unknowns determined according to the four boundary condition equations:

$$V_1(\xi_0) = \frac{A}{2}\log\frac{1+\xi_0}{1-\xi_0} + B = V_\mathrm{a} \tag{VI.8}$$

$$V_2(\xi = 0) = B' = 0 \tag{VI.9}$$

$$V_1(\xi_1) = V_2(\xi_1) \tag{VI.10}$$

$$\epsilon_0(\vec{n}\cdot\vec{E}|_{\xi>\xi_1,\xi\to\xi_1}) - \epsilon_2(\vec{n}\cdot\vec{E}|_{\xi<\xi_1,\xi\to\xi_1}) = \sigma_s = 0 \tag{VI.11}$$

where $\vec{n}$ is the unit vector normal to the dielectric interface, and σ_s is the surface charge density upon the dielectric material, which is considered to be zero in this analytical study. Equation (VI.8) defines the potential value V_a at the anode. Equation (VI.9) sets the zero-potential value at the cathode. Equation (VI.10) is the condition for the electric potential continuity across the dielectric interface. Finally, Equation (VI.11) defines the discontinuity of the normal component of the electric field through the dielectric interface [e.g., *Durand*, 1966a, c].

From the formulation of gradient in this coordinates system (IV.12), one has:

$$\vec{E} = -\vec{\nabla}V = -\frac{1}{\Xi}\frac{\partial V}{\partial \xi}\vec{u_\eta} \tag{VI.12}$$

Then, from (VI.11) one gets:

$$\epsilon_0 \left.\frac{\partial V_1}{\partial \xi}\right|_{\xi_1} (\vec{n}.\vec{u_\eta}) = \epsilon_2 \left.\frac{\partial V_2}{\partial \xi}\right|_{\xi_1} (\vec{n}.\vec{u_\eta}) \Rightarrow A\epsilon_0 = A'\epsilon_2$$

Thus, the coefficients of (VI.7) are given by:

$$\begin{aligned} A &= \frac{2V_a}{\left(\frac{1}{\epsilon_r}-1\right)\log\left(\frac{1+\xi_1}{1-\xi_1}\right)+\log\left(\frac{1+\xi_0}{1-\xi_0}\right)} \\ B &= \frac{A}{2}\left(\frac{1}{\epsilon_r}-1\right)\log\left(\frac{1+\xi_1}{1-\xi_1}\right) \\ A' &= A/\epsilon_r \\ B' &= 0 \end{aligned} \tag{VI.13}$$

The electric potential is fully determined by (VI.7) and (VI.13). To transform these relations into cylindrical coordinates, Equation (IV.11) is used.

VI.3.2 Electric field

The electric field in each domain is derived from Equations (VI.12), (VI.7) and (VI.13) as:

$$\begin{cases} E_1 = \dfrac{A}{2\Xi}\left(\dfrac{1}{1+\xi}+\dfrac{1}{1-\xi}\right) & \text{in } \Omega_1 \\ E_2 = \dfrac{A}{2\Xi\epsilon_r}\left(\dfrac{1}{1+\xi}+\dfrac{1}{1-\xi}\right) & \text{in } \Omega_2 \end{cases} \tag{VI.14}$$

and $\vec{E} = E_i\vec{u}_\eta$ in the domain Ω_i. Note that $\epsilon_r = 1$ equalizes the electric potential in both domains and gives the results obtained in Section IV.2.2. As noted previously, in the following, we take ϵ_r=5 to be the relative permittivity of the dielectric material. Its thickness is taken to be $d = 1$ mm.

VI.3.3 Approximation of the analytical model

In this chapter we use a simulation domain dimension of 1×0.5 cm^2 and a thickness of 1 mm for the dielectric layer. The parameters a and b (see (IV.8)) of the hyperboloid anode are defined by $a = 0.5$ and $b = 0.18$, giving a radius of curvature of 648 μm, which is on the same order of magnitude as the radius of the edge of the metallic cylinder in Chapter V. The cathode is the plane defined by $x = 0$, and the anode is set to 13 kV, which corresponds to the experimental breakdown voltage of a very first discharge ignition (see Section V.5).

In the previous section, the analytical solution was found using a hyperbolic dielectric interface. However, the dielectric layer upon the cathode is planar in the simulated configuration. Since the analytical solution of the electric potential is used as the boundary condition at the radial boundary $r = R_d$ of the simulation domain, we have chosen to define

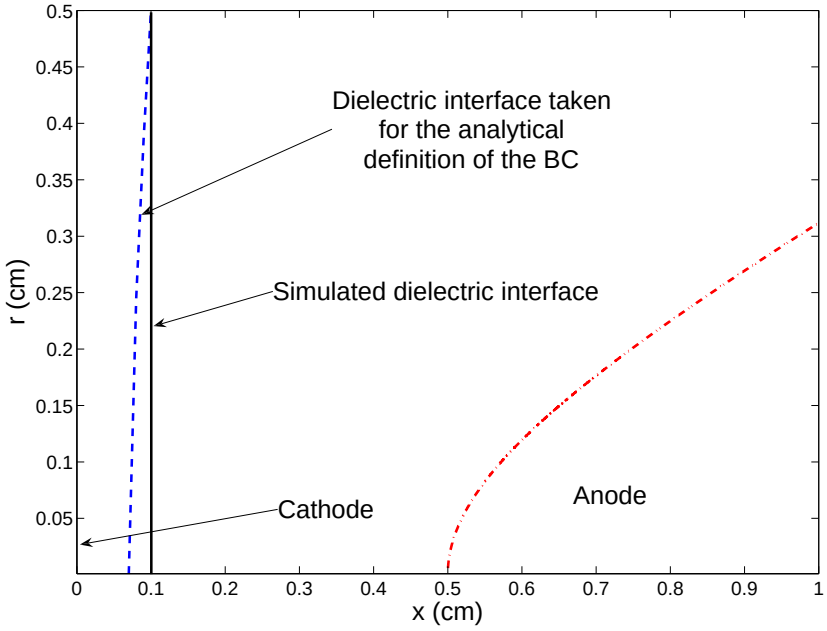

Figure VI.3: Solid line: shape of the simulated dielectric interface in the streamer code. Dotted line: dielectric interface taken in the analytical model for the calculation of the boundary conditions for Poisson's equation. Dot-dashed line: surface of the anode.

the dielectric interface as the confocal hyperboloid which crosses the plane dielectric at the radial boundary. The geometry is illustrated in Figure VI.3.

Figure VI.4 shows that for such a simulation domain and dielectric layer, this method gives accurate results. Indeed, Figure VI.4 demonstrates that the results from analytical and numerical models are close, especially in the vicinity of the tip of the anode. We note that discrepancies are visible close to the dielectric interface. Determining the exact solution for the problem with a plane dielectric is not straightforward and it is difficult to quantify the accuracy of our approach better than by the range given by the difference between the solutions represented in Figure VI.4. However, the error in the Laplacian field close to the dielectric is clearly negligible compared to the space charge electric field of the streamer head when the streamer reaches the dielectric. Moreover, from a numerical point of view, the number of iterations required of the NAG solver is heavily reduced by these new boundary conditions, indicating that the obtained numerical solution is very close to the real solution of this system.

VI.4 Simulation of streamer dynamics

As preliminary work, we have carried out the same electrostatic study as in Section V.5. We found that for a distribution of surface charge defined by Equation V.1 with a characteristic size $\sigma = 0.2$ cm, the electric field at the anode tip falls to zero for a total charge $Q \simeq 40$ nC. This is equal to the charge we found in Section V.5 for the electrostatic modeling of the experimental reactor. For the same shape of charge distribution, the total surface charge

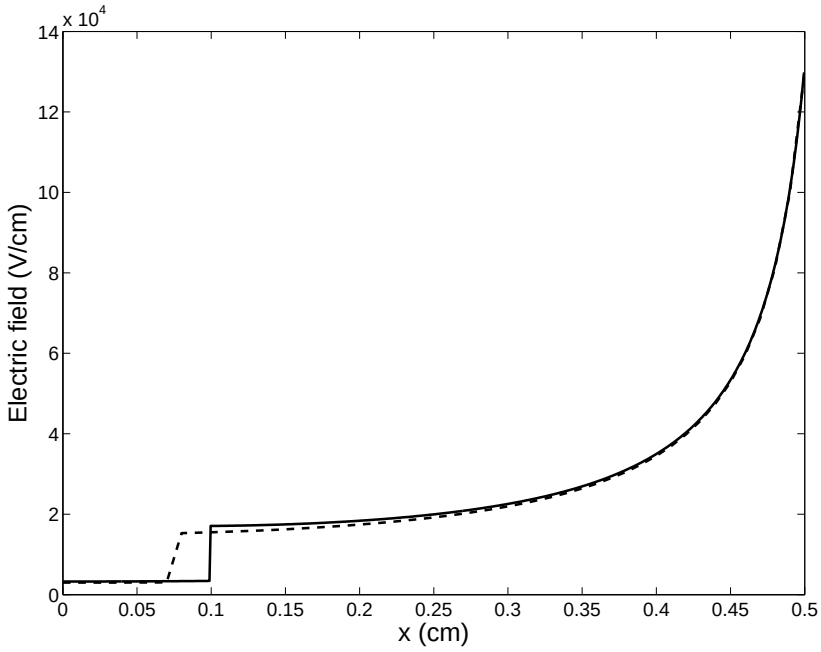

Figure VI.4: Magnitude of the electric field along the axis of symmetry, calculated for setting the Dirichlet boundary conditions. Solid line: numerical solution of Laplace's equation computed on a 1000×500 Cartesian grid. Dashed line: analytical solution used for setting the Dirichlet boundary condition.

$Q \simeq 35$ nC is required to decrease the electric field to the breakdown field $E_k \simeq 30$ kV/cm. Considering Section V.5, this indicates that the simplified configuration considered in this chapter can be used to obtain the order of magnitude for the main electrical characteristics related to a first current peak in the positive half-cycle of the experimental work discussed in Chapter V.

In the following, we study streamer dynamics in the above defined configuration. As for the point-to-plane configuration without dielectric studied in Section IV.3.2, we initiate the positive streamer by placing a Gaussian spot of neutral plasma close to the anode tip:

$$n_{\mathrm{p}}(x,r)|_{t=0} = n_{\mathrm{e}}(x,r)|_{t=0} = n_0 \exp\left[-\frac{r^2}{\sigma_r^2} - \frac{(x-x_0)^2}{\sigma_x^2}\right] \tag{VI.15}$$

where $x_0 = 0.5 - \sigma_x$, $\sigma_x = 0.01$ cm, and $\sigma_r = 0.01$ cm. At $t = 0$, there are no negative ions. The initial maximum density is $n_0 = 10^{14}$ cm^{-3}.

In this study we have used the same transport parameters and reaction rates as in [*Kulikovsky*, 1998], and we have used the positive ion mobility from [*Morrow and Lowke*, 1997]. Given the complexity of the simulated problem, the results shown in the present work are computed using the upwind scheme. We mentioned in Chapter II that the upwind scheme is able to provide essential information on streamer dynamics, although it overestimates the electron density and the electric field.

The simulation domain is 1×0.5 cm^2, discretized on a 1597×344 grid. In the axial direction, the grid is:

- uniform with a cell size of $\Delta x = 5$ μm from $x = 0$ to 0.75 cm

- refined around the dielectric interface with $\Delta x = 1$ μm from $x = 0.75$ cm to 0.125 cm
- non-uniform from $x = 0.125$ cm to 0.15 cm with a geometric expansion $\Delta x_i = 1.1\Delta x_{i-1}$ up to $\Delta x = 5$ μm at $x = 0.15$ cm
- uniform with $\Delta x = 5$ μm until $x = 0.55$ cm
- non-uniform, following a geometric progression with a ratio of 1.1 up to $x = 1$ cm

In the radial direction we have used a grid that is:

- uniform with $\Delta r = 5$ μm up to $r = 0.15$ cm
- non-uniform, following a geometric progression with a ratio of 1.1 up to $r = 0.5$ cm

The photoionization source term has been computed using the three-group SP_3 approach with Larsen's boundary conditions (see Chapter III).

The boundary conditions for fluxes at the dielectric surface have been observed to play a significant role after the streamer contacts the dielectric material. In the following, the boundary conditions are zero for the diffusion and drift fluxes. We model the secondary emission due to ion bombardment by the second Townsend coefficient γ defined as the average number of electrons produced by one ion as it impacts the dielectric material. At the end of this chapter we also show some results obtained with the dielectric acting as a perfectly emitting boundary, that is with a zero-gradient condition on the electron density $\frac{\partial n_e}{\partial x}\Big|_{x=0.1} = 0$.

VI.4.1 Streamer propagation in the gas gap

At the beginning of the simulation, the positive streamer is initiated close to the anode tip and then propagates towards the grounded plane. As an example of the results obtained, Figures VI.5 and VI.6 show cross-sectional views of the electron density and the magnitude of the electric field, respectively, at $t = 3$ ns.

We found that the secondary emission via ion bombardment at the dielectric interface does not play any role during streamer propagation in the gas gap. Conversely, the role of secondary emission becomes significant when the streamer reaches the dielectric surface. This will be discussed in the next section.

The propagation of the streamer from the anode to the dielectric surface lasts ∼4.5 ns. During this phase, the ions and electrons near the dielectric surface are produced only by the photoionization. Figure VI.7 shows that the increase of the surface charge density due to the ion drift towards the dielectric is slow. During the streamer propagation, the surface charge density does not increase sufficiently to distort the Laplacian electric field. Figure VI.7 also illustrates the modification of the surface charge variation at $t = 4.5$ ns, indicating the interaction of the streamer with the dielectric surface.

To compare our results with experiments, we have also calculated the electric current collected by the cathode. The cathode plane is under the dielectric material and therefore the collected current at the cathode is the displacement current:

$$I = \int_S \frac{\partial \vec{D}}{\partial t} \cdot \mathrm{d}\vec{S} = \epsilon_2 \int_S \frac{\partial \vec{E}}{\partial t} \cdot \mathrm{d}\vec{S} \tag{VI.16}$$

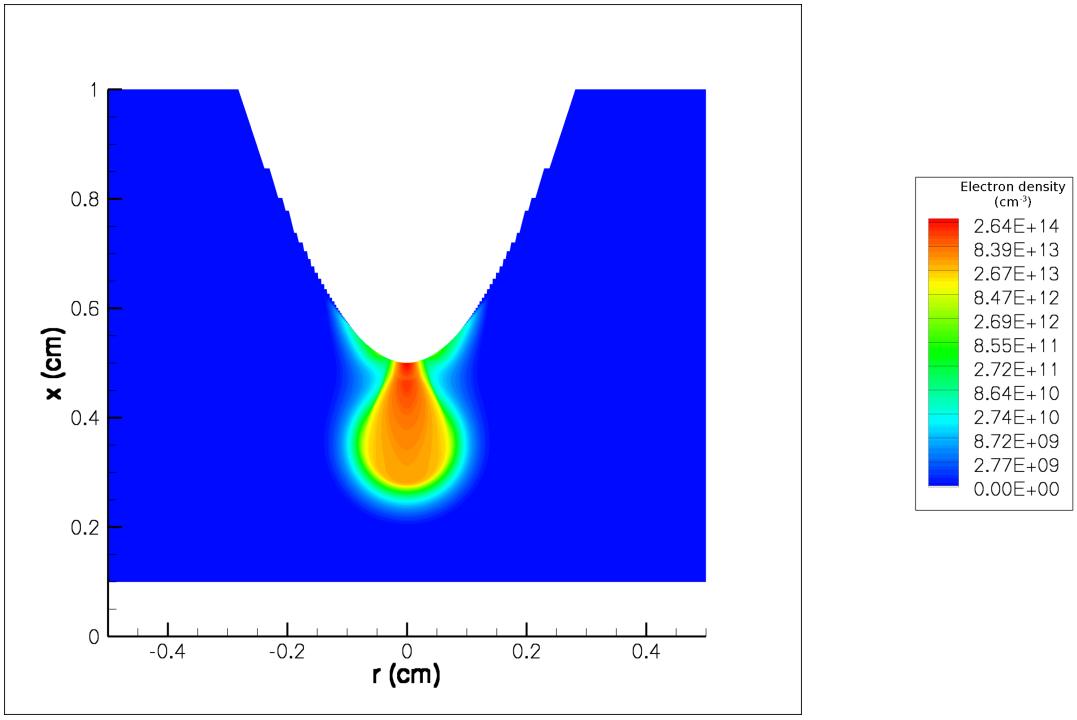

Figure VI.5: Cross-sectional view of the distribution of the electron density at $t = 3$ ns. The white areas represent the anode and the dielectric material.

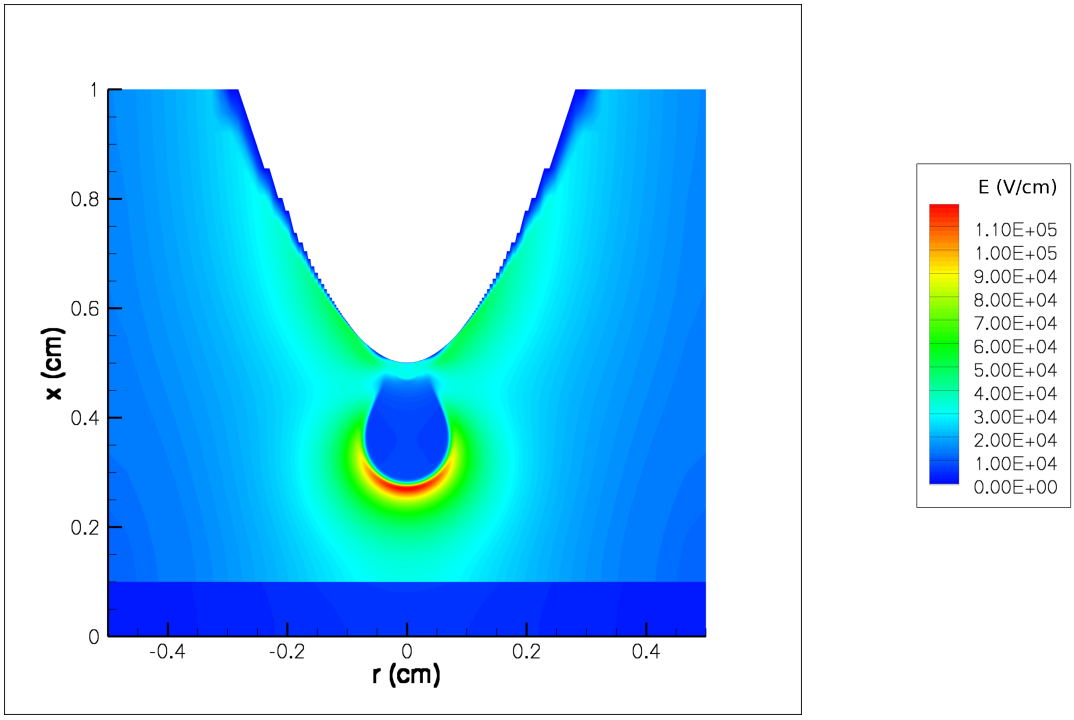

Figure VI.6: Cross-sectional view of the distribution of the magnitude of the electric field at $t = 3$ ns. The white area represents the anode.

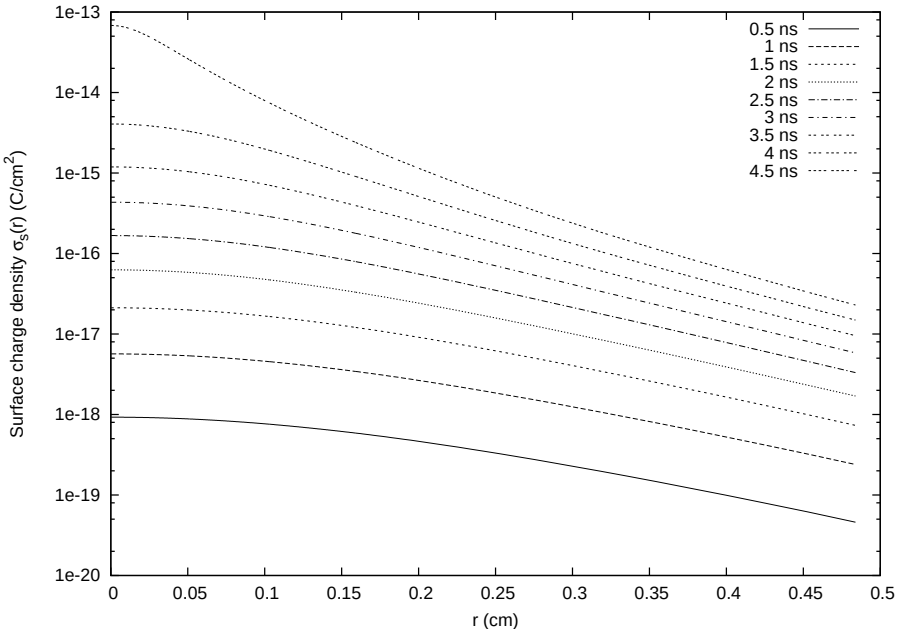

Figure VI.7: Radial distribution of the surface charge density upon the dielectric before the streamer reaches the dielectric surface, from $t = 0$ to $t = 4.5$ ns.

where S is the surface of the cathode. This calculation is not representative of the total current of the discharge but gives an estimation of the current measured by a current probe linked to the cathode, as performed in the experiments described in Chapter V. Figure VI.8 shows the current collected by the cathode during streamer propagation.

Figure VI.8 shows a clear increase of the current as the streamer head gets closer to the cathode. A maximum of 0.76 A is reached at $t = 4.6$ ns when the streamer impacts the dielectric surface. In the current measurements, such as those shown in Figure V.4, one cannot accurately resolve the short time scale of streamer propagation, although we can estimate that streamer propagates on the same order of time. The maximum current is in good agreement with typical measurements in the experiments. As mentioned previously, the γ parameter has not been found to play a significant role during streamer propagation in the gas gap, and thus the current is not modified by the value of γ until the impact of the streamer head on the dielectric.

Figures VI.9 and VI.10 show the cross-sectional structure of the discharge at the moment of the impact on dielectric (i.e., $t = 4.5$ ns).

Because of the zero boundary condition for fluxes, except for the secondary electron flux due to ion bombardment, a small region of about 20 μm close to the dielectric surface has a low electron concentration, and thus the streamer stops when it reaches this region until secondary processes such as photionization, photoelectric effect, or ion bombardment can compensate for the lack of electrons. Then, a sufficient number of electrons is created to neutralize the streamer head partially. As for the secondary processes, some preliminary studies showed that the photoelectric effect becomes very important, or even predominant, when the streamer reaches the dielectric. This provides enough electrons to neutralize the streamer head. In the present study, we did not take into account the photoelectric effect in order to save computation time. However, to compensate for the lack of electrons and to model streamer dynamics after contact with the dielectric surface, we artificially increase

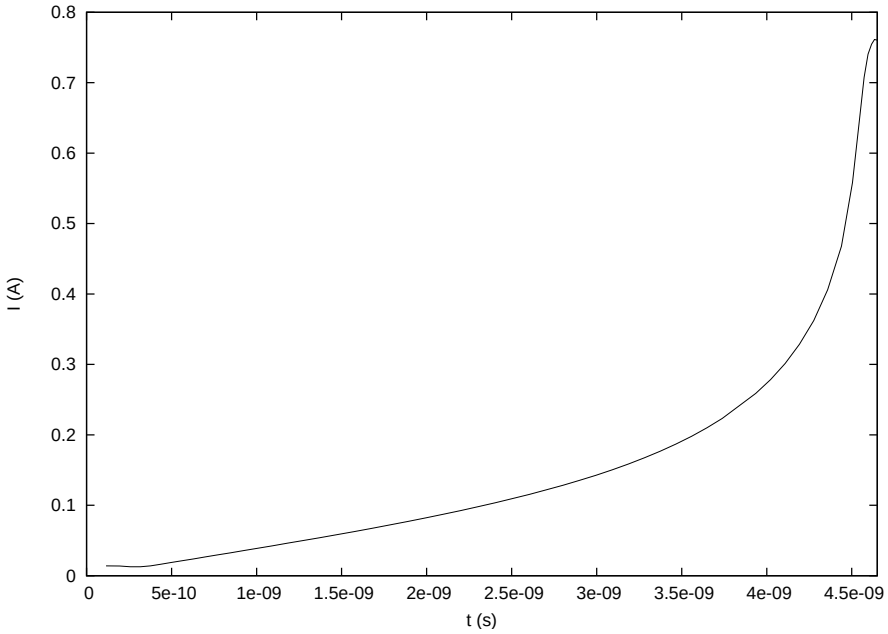

Figure VI.8: Current collected by the cathode as a function of time during streamer propagation.

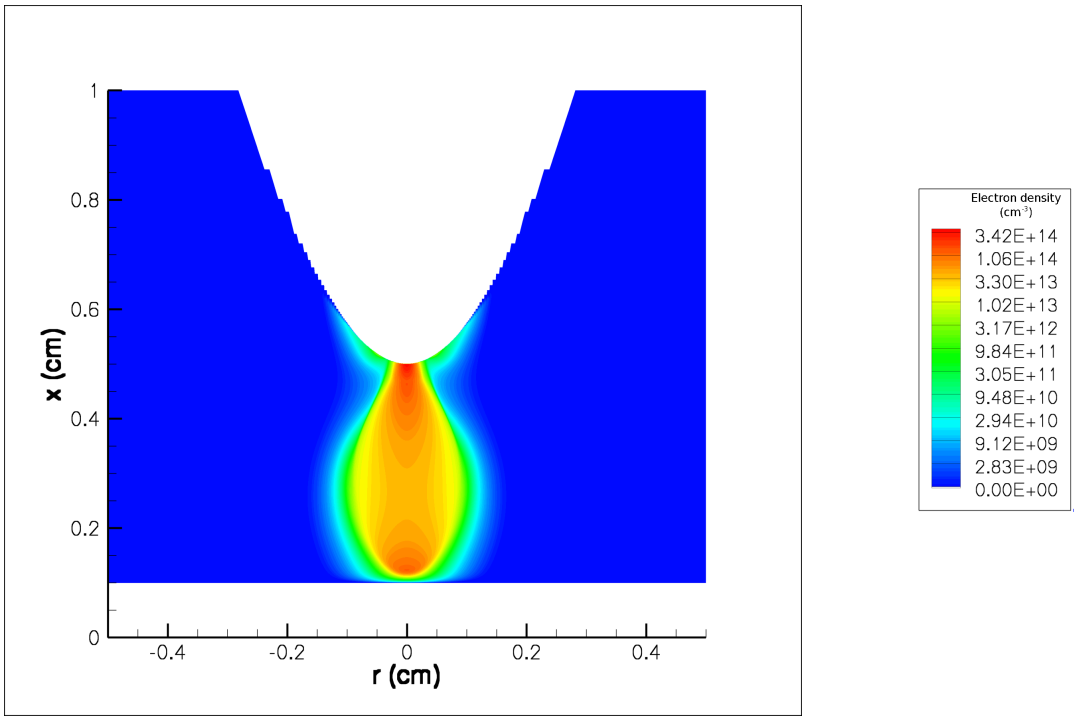

Figure VI.9: Cross-sectional view of the distribution of the electron density at $t = 4.5$ ns. The white areas represent the anode and the dielectric material. In this simulation $\gamma = 0.1$.

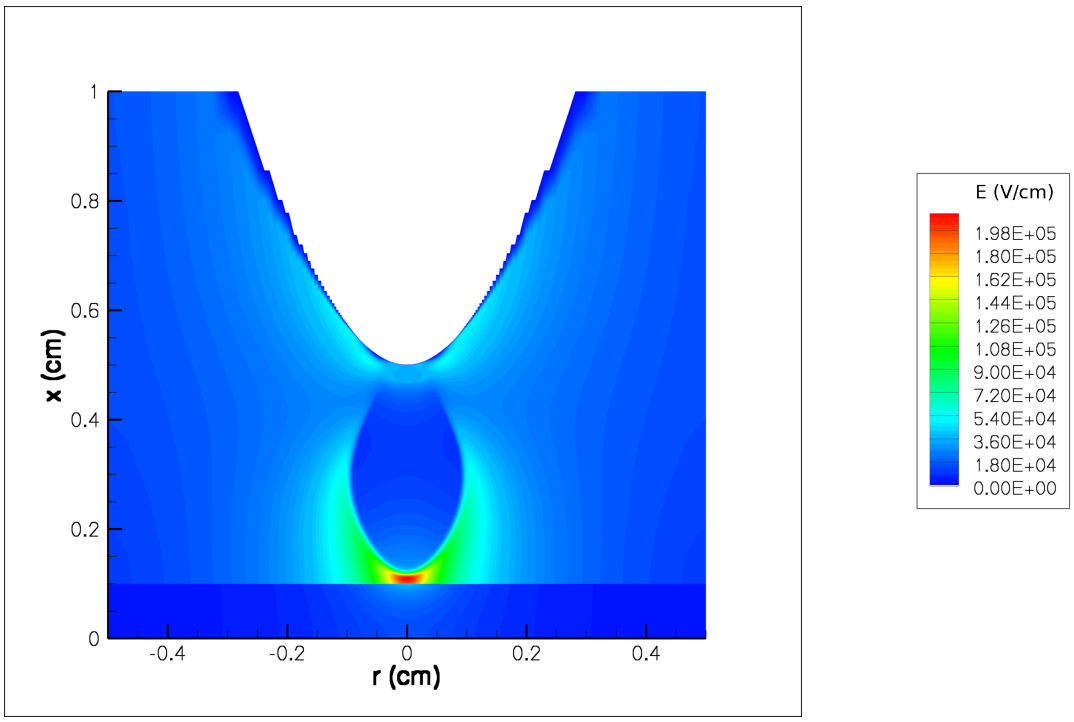

Figure VI.10: Cross-sectional view of the distribution of the magnitude of the electric field at $t = 4.5$ ns. The white area represents the anode. In this simulation $\gamma = 0.1$.

the γ coefficient. Note that the variation of γ has no impact on the propagation phase of the streamer (from $t = 0$ to $t = 4.5$ ns) nor on the current shown in Figure VI.8. The typical value for *gamma* found in the literature for dielectrics such as Pyrex is $\gamma \simeq 0.01$ [e.g., *Golubovskii et al.*, 2002]. In this work, we use γ as a parameter and study the results obtained for values of γ between 0.01 and 1.

VI.4.2 Interaction between the streamer and the dielectric

Because of electron emission from the dielectric surface, the streamer head is partially neutralized. However, the neutralization of the streamer head is not complete, and the streamer eventually branches on the dielectric surface. Surface discharges then spread out on the dielectric. Figures VI.11 and VI.12 show cross sectional views of the electron density and the magnitude of the electric field, respectively, at $t = 8.5$ ns and for $\gamma = 0.1$. Figure VI.12 clearly shows that during this phase the electric field is screened, except at two visible spots, which are the surface streamer heads (as the simulation is axisymmetric this discharge has a ring shape).

Figure VI.13 shows the radial profile of surface charge deposited upon the dielectric during the propagation of the surface discharge. There is clearly a peak in the profile of the surface charge, just before a sharp decrease. This corresponds to the position of the surface streamer head propagating along the dielectric surface. Furthermore, the surface charge density at $r = 0$ decreases for $t > 6.5$ ns. In this simulation, the only way for the surface charge to decrease is through the deposition of electrons on the dielectric surface (see Equation (VI.5)). Hence, as the surface streamer propagates, the high field in its head increases the surface charge by ion deposition, and after the streamer head passes, the electron flux

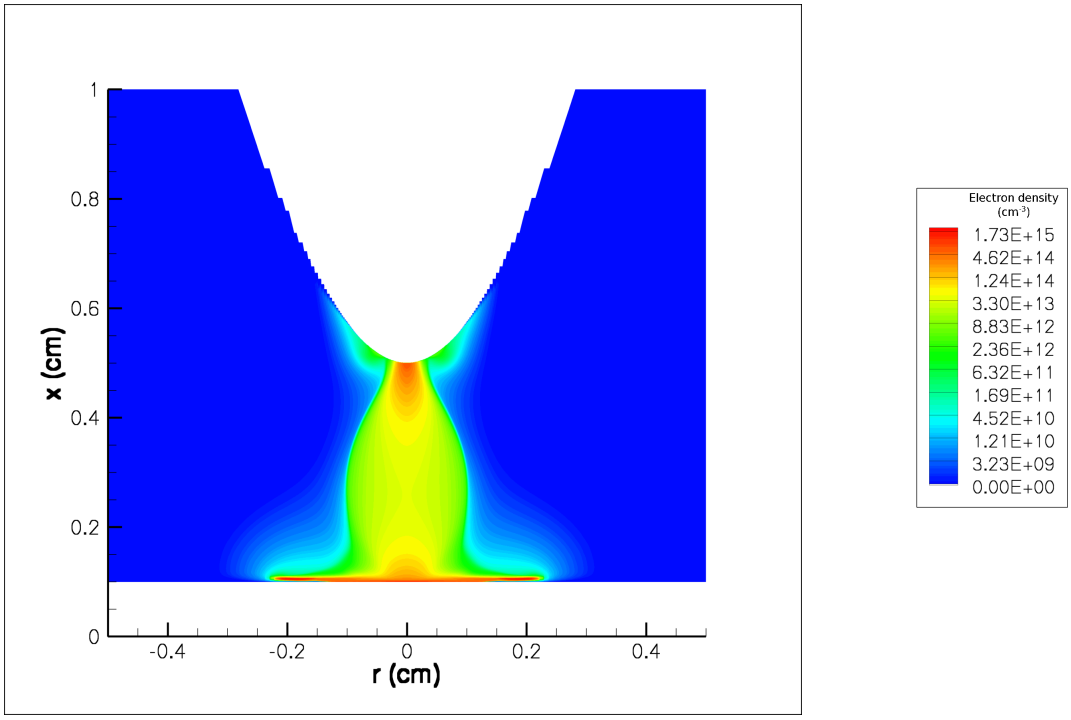

Figure VI.11: Cross-sectional view of the distribution of the electron density at $t = 8.5$ ns. White areas represent the anode and the dielectric material. In this simulation $\gamma = 0.1$.

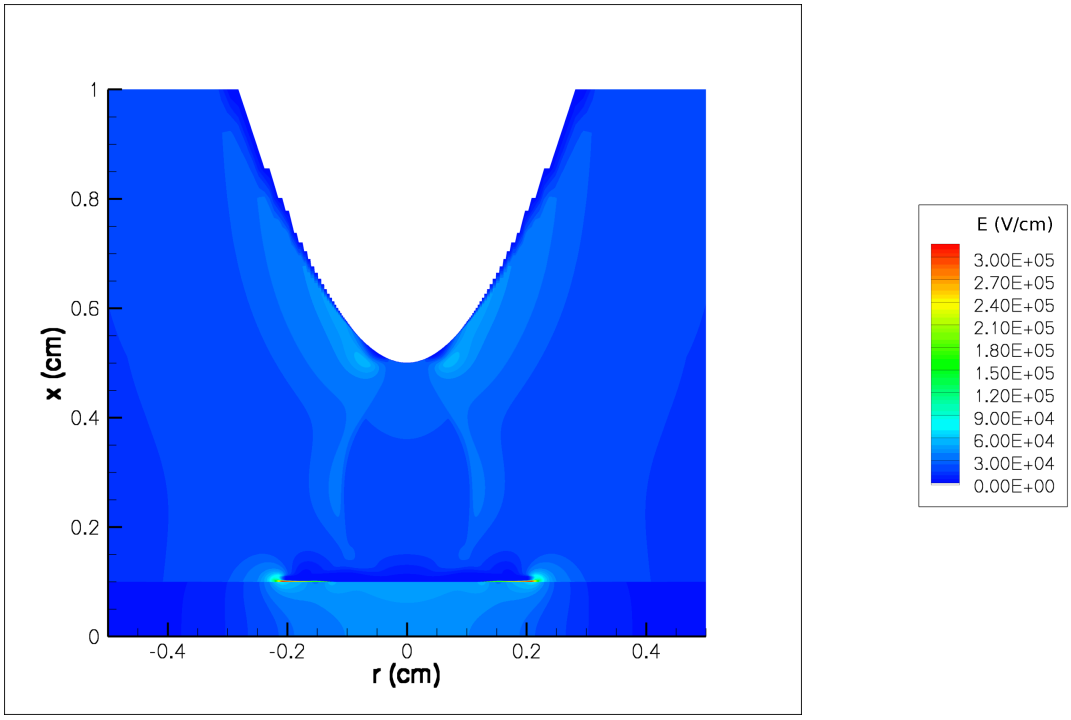

Figure VI.12: Cross-sectional view of the distribution of the magnitude of the electric field at $t = 8.5$ ns. White area represents the anode. In this simulation $\gamma = 0.1$.

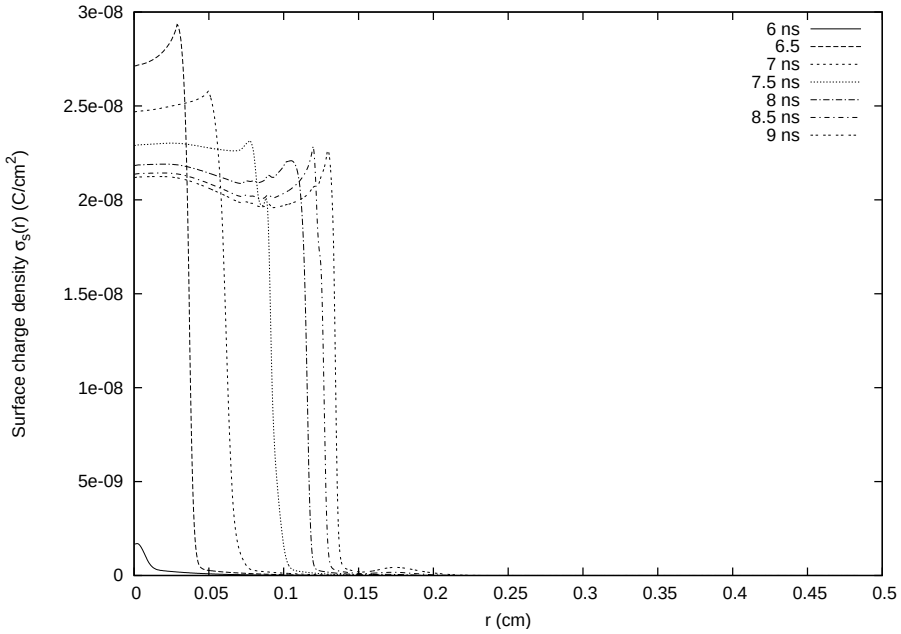

Figure VI.13: Surface charge density upon the dielectric. Results are computed using a fine grid ($\Delta x = 1$ μm close to the dielectric surface) and with $\gamma = 0.1$.

decreases the surface charge density until the electric field is screened.

It is interesting to note that, for all values of γ studied in this work, the surface charge affects the propagation of the surface discharge only after 6.5 ns. That is, the surface charge field becomes greater than E_k only after 6.5 ns (this is verified by keeping σ_s constant for a given moment of time, and by solving (VI.2) with $\rho = 0$) i.e., after the ignition of the surface discharge. This means that the breakdown field required for the surface discharge to be ignited is not exceeded through surface charge accumulation, but instead by the space charge density in a volume close the dielectric surface. This is the case even when the streamer head is easily neutralized, that is for high γ values or for a perfectly emitting dielectric surface.

From the results presented in Figure VI.13, one finds that the total surface charge at time $t = 9$ ns is 1.2 nC, which is 40 times less than the total surface charge to screen the Laplacian electric field (see the beginning of Section VI.4). This means that the screening of the electric field is mostly due to the space charge. To compare the different contributions of surface charge and space charge in the screening of the electric fields, we computed the surface charge and/or the space charge electric fields, from the results obtained at $t = 9$ ns. The results are shown on Figure VI.14. We note that the total electric field in the plasma channel between the anode and the dielectric is roughly constant and on the order of the breakdown field. This means that there is no significant electron multiplication in this channel, but instead just electron drift towards the dielectric. Note that this behavior was also observed for different configurations in [e.g., *Braun et al.*, 1992; *Gibalov and Pietsch*, 2000]. Moreover, one sees that both surface and space charge have to be taken into account to understand the screening of the electric field. The main effect of the space charge field is the screening of the high field region close to the anode tip, while the main effect of the surface charge is the screening of the electric field close to the dielectric surface.

Figure VI.15 compares the surface charge computed using a coarse grid with $\Delta x = 5$ μm in

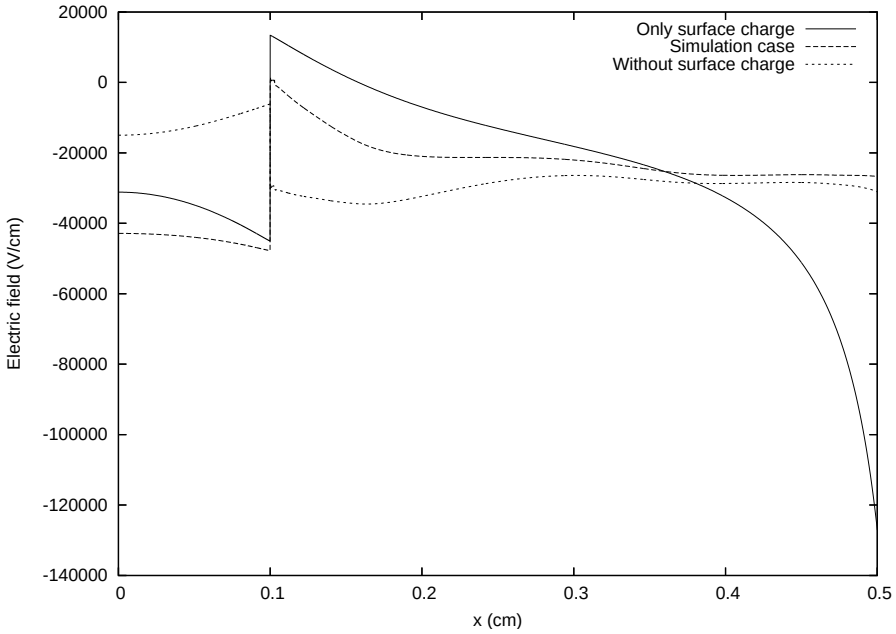

Figure VI.14: Axial electric field at time $t = 9$ ns along with the individual contributions from space charge and surface charge. Solid line: only the surface charge given by the streamer simulation is taken into account (no space charge). Dashed line: electric field given by the streamer simulation. Dotted line: results without taking into account the surface charge.

the vicinity of the dielectric to that using the reference refined grid at $t = 6$ ns. This figure shows that at $t = 6$ ns the surface charge obtained with the coarse grid is much higher than that obtained with the fine grid (see Figure VI.13). Furthermore, the refinement of the grid close to the dielectric surface has a significant impact on the simulation results. In general, it delays surface discharge ignition and slows down its propagation. As shown by Figure VI.15 these discrepancies are much larger than the effect of varying the γ parameter.

VI.4.3 Perfectly emitting dielectric surface and electron density in the vicinity of the anode tip

We have performed simulations considering a surface that could provide as many electrons as required by the electric field (boundary condition: $\frac{\partial n_e}{\partial x}\Big|_{x=0.1} = 0$, instead of zero flux). This corresponds to a dielectric surface that completely neutralizes the streamer head. In this case, we have observed no propagation of the surface discharge on the dielectric.

In this situation, instead of taking photionization processes into account, which partly counterbalance the lack of electrons due to the zero-flux boundary condition, one can use a neutral background of 10^9 cm^{-3} (see Appendix C). For a case without dielectric, we have demonstrated that this reproduces the main features of streamer dynamics (see Section II.3). In the present configuration, we observe the propagation of a primary streamer and its screening by surface charge deposition on the dielectric, as in the case with photoionization. However the continuous background provides enough electrons close to the tip of the anode to trigger streamers outside the screened channel.

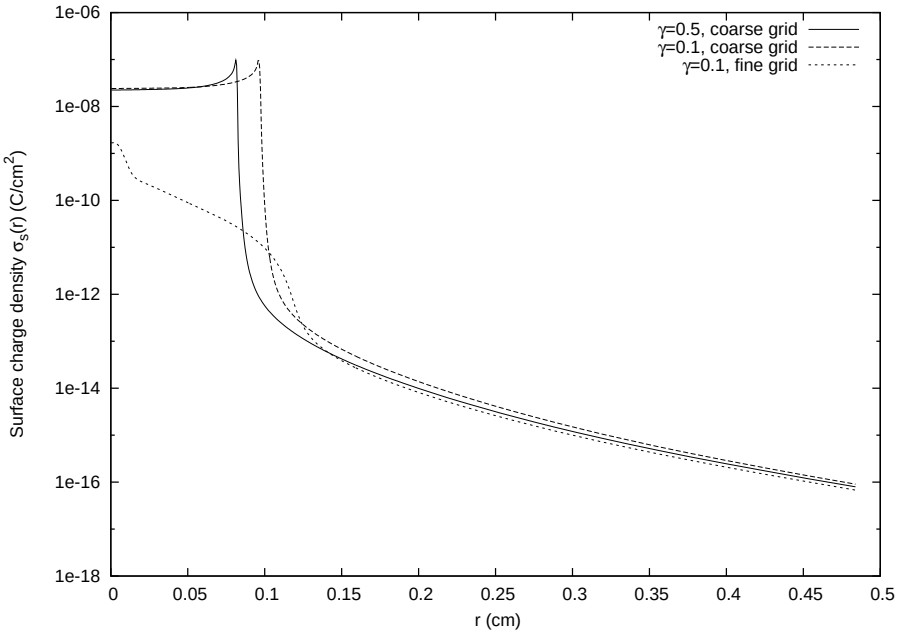

Figure VI.15: Surface charge density upon the dielectric at $t = 6$ ns.

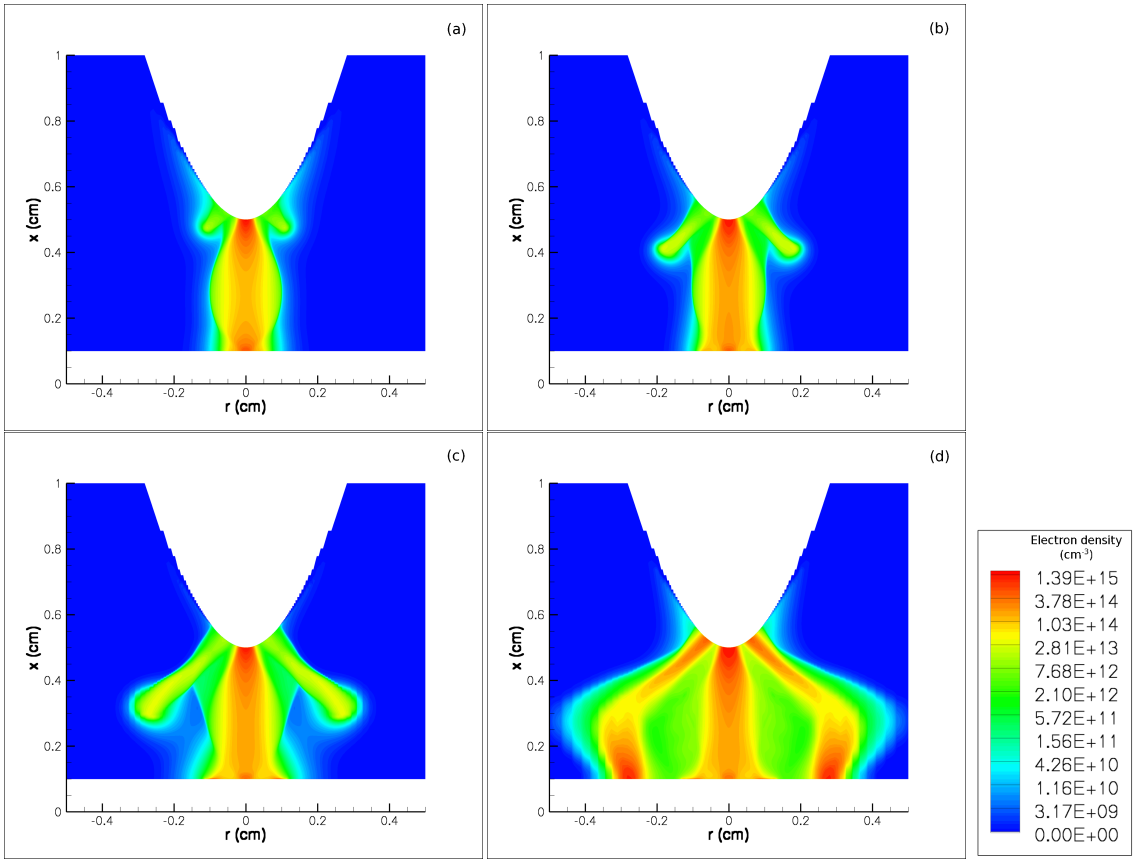

Figure VI.16: Cross-sectional view of the distribution of the electron density at different times. (a): 9.5 ns. (b): 14.5 ns. (c): 19.5 ns. (d): 24.5 ns. The white areas represent the anode and the dielectric material. Simulations are done assuming a perfectly emitting dielectric surface and with a neutral background of 10^9 cm^{-3}.

Figure VI.16 clearly shows the triggering of the subsequent discharge. Note that the simulated discharge is not fully physical, since we use a 2D axisymmetric approach to describe a 3D phenomenon. We note that during these simulations the second streamer reaches the expanding region of the numerical grid, which is the reason for the presence of the small squares visible in Figures VI.16(c) and VI.16(d). We presume that this is also the reason for the non-physical swelling of the discharge zone visible in Figure VI.16(d). In a full 3D simulation, one could expect this secondary discharge to split into several independant streamers. Moreover, as stated previously, the screening of the electric field on such a short time scale (∼10 ns) results from both surface charge and space charge. Conversely, the screening of the central part of the electric field in the experiment, which determines the particular shape of filaments corresponding to second current peaks (see Section V.4.2), can only come from the surface charge trapped on the dielectric. Indeed, the characteristic time between two discharges (∼1 ms) is longer than the volume recombination time. However, the surface charge is known to remain for a very long time (see [*Golubovskii et al.*, 2002] for a detailed study of processes related to surface charge upon a dielectric surface). Nevertheless, these results show how a second streamer could start from the anode following the screening of the electric field by the primary central discharge of a similar radius. This characteristic feature resembles the secondary discharge in the positive half-cycle presented in Section V.4.2.

VI.5 Conclusions

In this chapter we have simulated a Dielectric Barrier Discharge in a point-to-plane configuration. Even without space charge in the simulation domain, this configuration is rather complex. To define Dirichlet boundary conditions for Poisson's equation based on an analytical solution, we used a slightly modified geometry with a hyperbolic dielectric interface instead of a plane. We demonstrated that this approximation is accurate, and we successfully applied it in the framework of streamer modeling via using of the Ghost Fluid Method.

The dynamics of dielectric barrier discharges has been studied, including the initiation of a surface discharge after the propagation of the streamer in the gas gap. We also studied the importance of the second Townsend coefficient γ, which has been observed to work as an acceleration parameter for the initiation and propagation of the surface discharge. In these simulations, we found that the surface discharge initiated by the main streamer starts from the space charge close to the dielectric surface and not from an accumulation of surface charge. The surface charge plays an important role in the screening of the Laplacian electric field close to the dielectric, and the space charge contributes significantly to the screening of the electric field in the vicinity of the anode tip on the considered time scale (∼10 ns). This is why the total charge accumulated on the dielectric surface found in simulations (∼1 nC) is less than the surface charge required to screen the electric field (∼40 nC) (see the beginning of Section VI.4). We assume that the total charge of 40 nC found in the experiments (and in our electrostatic studies) corresponds to a surface charge accumulated over a much longer time.

In this work we have carried out axisymmetric 2D simulations, although a three-dimensional simulation would be necessary to simulate the experiment accurately. However, we have

shown that the screening of the electric field in the channel produced by the initial central streamer can influence the subsequent streamers by deflecting them from their expected trajectories, as observed in the experiments. In the simulations, the impact radius and the spatial distribution of the discharge are comparable to the experimental results from Section V.4.2.

General Conclusion

In this Ph.D. thesis we contribute to several aspects of research on streamer physics in air at atmospheric pressure through both experimental and numerical studies. We show that studying transient phenomena such as streamer discharges, whose timescales are very short compared to the operating times in applications, results in useful informations concerning their underlying physical mechanisms.

In this work we have studied streamer dynamics based on the most common and effective model, using drift-diffusion equations for charged species coupled with Poisson's equation. The numerical resolution of this set of equations requires careful attention to the efficiency of the numerical schemes used. In fact, it requires making a strict selection of numerical solvers for the different components of the resolution. The computation of the electric field is a key point in streamer modeling. First, transport parameters and source terms of the drift-diffusion equations have a strongly non-linear dependence on the reduced electric field. Second, the electric potential itself is directly related to charged species densities via Poisson's equation. Thus, to obtain a reliable calculation of the electric field, we have used two different solvers for Poisson's equation. The first one is an iterative solver based on a NAG library routine. And the second one called SuperLU is a direct solver. Both provide very accurate solutions in all the configurations we tested. Moreover, these solvers are also used in the computation of the photoionization processes using the differential approaches. As Poisson's equation is elliptic, we have carefully defined the boundary conditions for each case studied in this work. Numerical methods and schemes used to solve the drift-diffusion equations for charged species have been also described. In this work, we have mainly used three different schemes: the simple first-order upwind scheme, the FCT method based on the the upwind and QUICKEST3 schemes and Zalesak's limiter, and the modified Scharfetter-Gummel scheme. We showed that the upwind scheme can give the main physical parameters of streamer dynamics. However, it is unable to attain the accuracy of high-order schemes on the considered numerical grids. Thus, to accurately resolve streamer propagation, higher order schemes such as the FCT method and the modified Scharfetter-Gummel scheme are required.

A considerable effort has been to calculate the photoionization process. Indeed, photoionization is considered to be of great importance in streamer dynamics in air. The classical Zheleznyak approach, as an integral model, is very time consuming. As a consequence, several differential approaches have been proposed in the literature to reduce the computation time of numerical models for plasma discharges in air. In this work we have developed three differential approaches: a three-exponential Helmholtz model, a three-group Eddington model, and a three-group improved Eddington (SP_3) model. The Helmholtz model is based on approximating of the absorption function of the gas in order to transform the integral expression of the photoionization term in a set of Helmholtz differential equations.

The Eddington and SP_3 methods are based on the direct numerical solution of an approximation of the radiative transfer equation. Finally, we have demonstrated that the solutions involved in all three differential models require accurate definitions of boundary conditions, and we have derived these boundary conditions.

We have carried out comparative studies of these models using mainly two different configurations for streamer propagation. The homogeneous electric field configuration was used for igniting streamers of both polarities propagating in a strong electric field ($E>E_k$, where E_k is the conventional breakdown field). In this case ionization by electron impact dominates over photoionization, where the latter is a second order process. Thus, the choice of the differential model for calulating the photoionization source term has a small impact on the streamer dynamics. In the other configuration studied, a sphere with high electric potential lies in an initially weak homogeneous electric field. In this case we studied the propagation of a streamer in the weak electric field ($E<E_k$). In this configuration the streamer dynamics is heavily influenced by the photoionization processes. In this case, we found that the best agreement with the reference Zheleznyak integral model is obtained using the three-group SP_3 model. Furthermore, we have shown that the advantage of the three-group SP_3 approach over the three-exponential Helmholtz method is that it provides a purely physical and consistent set of closed equations with the boundary conditions. The actual advantage of differential models derived in this work over the integral model lies in the simplicity of the implementation of this type of models, and in the unquestionable simplicity of extending these models to complex two- and three-dimensional simulation geometries. For example, this could involve the propagation of multiple streamer heads in the same simulation domain and the presence of obstacles in the streamer path (e.g., electrodes, dust particles, aerosols, etc).

In the experiments, electrodes with small radii of curvature are often used in order to localize streamer ignition. To take the electrode shapes into account in the simulations, we have adapted the Ghost Fluid Method to solve Poisson's equation in order to calculate the electric potential and field close to the electrode accurately. This method allows us to take the influence of the exact shape of the electrodes into account in the framework of finite volume methods using a regular grid, no matter how the electrode surfaces cross the grid.

After having validated the method with classical numerical results of the literature in a point-to-plane geometry, we carried out simulations in a point-to-point geometry closely linked with recent experimental results in pre-heated air discharges generated by Nanosecond Repetitively Pulsed (NRP) plasmas. We found out that by considering the propagation timescales of streamers in this configuration, it is possible to draw some conclusions about the final discharge structure (i.e., spark or coronas discharges) which are in good agreement with the experiments. This also indicates that streamer modeling on short time scales can be of a great help towards the understanding of nano-pulsed discharges at atmospheric pressure. In particular, this work points out the potential of such a study for finding the ranges of parameters allowing for a diffuse regime at atmospheric pressure and ambient temperature.

Dielectric Barrier Discharges (DBDs) are widely used for industrial applications. At atmospheric pressure and low frequency (50 Hz), they are mainly constituted of unstably triggered non-equilibrium transient plasma filaments produced by streamer propagation. In the experimental part of this work, we have studied a particular behavior of plasma filaments in a DBD during the positive half-cycle of the applied voltage. In the experimen-

tal device close to the point-to-plane configuration studied, the dynamics of discharges has been found to be greatly affected by the surface charge deposited upon the dielectric material. We have studied the impact of this behavior on the organization of plasma filaments. In such a device, the trapping on long time scales of the charges on the dielectric surface is responsible for the coupling between subsequent discharges (leading to a substantial current in the gap during about a hundred nanoseconds) that follows after several milliseconds.

Having gathered the models and methods presented in this Ph.D. thesis, we performed simulations in a point-to-plane configuration with a dielectric upon the plane cathode in order to improve the understanding of the behavior experimentally observed in the DBD device. In this work we were able to simulate the propagation of the streamer from its ignition point at the anode to the dielectric material, as well as its splitting into surface discharges upon reaching the dielectric. We found that the obtained surface discharges are not ignited by an over-accumulation of charges on the dielectric surface, but rather by a residual space charge of the streamer head in a thin layer close to the dielectric. We also found that the Laplacian electric field quenches on a very short timescale (<10 ns) because of both the contribution of the accumulated surface charge and the residual space charge in the streamer channel. On such time scales the surface charge contributes mainly to the screening of the electric field close to the dielectric, while the space charge contributes mainly to the screening of the field close to the anode. From the perspective to this study, it would be interesting to analyze the decrease of the current along with the related transport of charges and to study several amplitudes of the applied voltage.

Considering the time scales of the applied voltage at low frequency, the space charge necessarily disappears in the during the time between two subsequent discharges observed experimentally. Furthermore the surface charge found in simulations for time scales of about 10 ns is not sufficient to screen the electric field by itself. Thus, we assumed that the major part of the surface charge is accumulated on a much longer timescale, corresponding to the decrease of the current peak found in the measurements ($\sim$100 ns). We also observed that the increased population of electrons in the vicinity of the anode allows for the ignition of subsequent streamers. The propagation of these streamers is deflected because of the screening of the electric field, which is in agreement with experimental observations.

Suggestions for future research

It has been demonstrated in this work that fluid simulations of streamers in complex electric fields configurations represents a very interesting potential concerning the prediction of the different regimes in NRPs. From this perspective, it is important to check the influence of initial and external conditions on the simulation results. For example, studying the effects of the radius of curvature and the pre-ionized background on the discharge dynamics would allow us to verify the consistency of simulation results[1]. To determine the spatial distribution of pre-ionized background just before a new discharge more accurately, it would be very interesting to simulate the spatio-temporal distribution of charged species in the post-discharge. Furthermore, it would be interesting to obtain additional results on the voltage ranges of the diffuse regime (as a function of the temperature) and to analyze them carefully to differentiate this regime from the corona and spark regimes. It would be also interesting to take the increase of the neutral gas temperature into account in the simulations, especially for determining the range of applied voltages for obtaining spark discharges accurately. As an extensive experimental work has been done on the spectroscopy of the discharge at 1000 K, it would be of great interest to compute (at least as a post-treatment of simulation results) the excited states densities and to compare them with the experimental results, especially the observation of wave propagation in the diffuse regime. Finally, it would be interesting to simulate successive discharges to study synergy effects at high frequency. In the future, the challenge is to couple these simulations with Navier-Stokes flow codes to study the plasma/flow interaction which is of great importance for applications such as plasma-assisted combustion or flow control.

Considering the DBD studies, experimental studies (not shown in this thesis) have shown that negative discharges occurring in the considered experimental device are much more diffuse than the positive ones. In the future, it would be interesting to simulate this behavior and to obtain the shape of the surface charge produced by such a discharge. In this work, we have considered simplified boundary conditions with a global γ coefficient at the dielectric plane. It would be interesting to model surface processes in the simulations by taking into account photoemission, recharging of ions, thermal influence, etc. Furthermore, in this work we have simulated only one discharge assuming a constant applied voltage. It would be interesting to simulate the discharge during several cycles of the applied voltage to understand the role of surface charges on long timescales better.

Concerning the theoretical approach on streamer dynamics, many questions remain open. Some of them have been summarized in [*Pasko*, 2006]. For example, stability and branching

[1] At the time of publishing this thesis, one parametric study on the radius of curvature [Blackmond *et al.*, NSF EE REU Penn State Annual Research Journal, Vol. VII, 2009] and one study about the pre-ionized background [Bourdon *et al.*, accepted for publication in PSST, 2009] have been already carried out in the same configuration.

of streamers remain unsolved problems. It is obvious that a better theoretical understanding of the streamer dynamics would lead to great improvements in the conception of new reactors, as well as in the understanding of natural phenomenon involving streamers.

Appendix A

Accuracy of different photoionization models for different simulation domain dimensions and boundary conditions

Figure A.1 presents the same information as Figure III.5, only for the domain dimension 2×2 cm^2 with σ=0.1 cm.

Figures A.1(a) and A.1(b) show the axial and radial profiles of the photoionization source term S_{ph} calculated by the Zheleznyak model in comparison with the Helmholtz solutions obtained using the two and three-exponential fits. As in Figure III.5, the ionization term S_i is also shown for reference. The results obtained with the three-exponential fit appear to match better with the Zheleznyak integral solution in the region where $S_{\text{ph}}>S_i$ and, in particular, close to the boundaries. The two-exponential Helmholtz model fails to provide an accurate solution in this case. This result directly relates to a poor two-exponential fit at large $p_{O_2}R$>60 Torr cm values (i.e., R>0.5 cm at ground pressure considered here), as can be seen in Figure III.2. The better performance of the three-exponential Helmholtz model directly relates to a better three-exponential fit at large $p_{O_2}R$ values (i.e., R>0.5 cm at ground pressure), as also can be seen in Figure III.2.

Figures A.1(c) and A.1(d) compare the 3-group Eddington approximation and the 3-group SP_3 with the Zheleznyak model for the same domain dimension 2×2 cm^2. We note that the use of the SP_3 allows to improve the agreement with the Zheleznyak model, in particular, close to the boundaries.

Finally, Figures A.1(e) and A.1(f) compare the 3-group SP_3 and the 3-exponential Helmholtz model with the Zheleznyak model. In this case, both models give very similar results in the axial direction and are very close to the Zheleznyak model. In the radial direction, the results obtained with the SP_3 model appear to be slightly more accurate than the three-exponential Helmholtz model in the region where $S_{\text{ph}}>S_i$.

As we emphasized at the beginning Section III.6.1, for the domain with L_d=R_d the effective distance from the source at the center of the simulation domain to the boundary is two times longer in the radial direction than in the axial direction (i.e., 2 cm versus 1 cm in Figure A.1). Therefore the radial distances exceeding 1 cm allow to observe the behavior

of different models in the region beyond applicability of the model fits obtained for the range $1<p_{O_2}R<150$ Torr cm for the three-exponential Helmholtz model (Figure III.2) and for $0.1<p_{O_2}R<150$ Torr cm for the three-group Eddington and SP_3 models (Figure III.3) (i.e., for $R<1$ cm at atmospheric pressure $p_{O_2}=150$ Torr). All models shown in Figures A.1(e) and A.1(f) show outstanding performance in both axial and radial directions at distances <1 cm from the source, as expected from the range of validity of related fits in Figures III.2 and III.3. In the same vein we note that a special caution should be used when models described in the present work are applied in large simulation domains for which $p_{O_2}R$ product exceeds 150 Torr cm.

Figure A.2 is presented in the same format as Figures III.5 and A.1, only for the domain dimension 0.02×0.02 cm^2 with $\sigma=0.001$ cm.

Figures A.2(a) and A.2(b) show the axial and radial profiles of the photoionization source term $S_{\rm ph}$ calculated by the Zheleznyak model and the Helmholtz solution using two and three-exponential fits. As expected from the fits shown in Figure III.2 for small distances, the results obtained with both solutions are poor, but we note that in the region of interest for streamer simulations (where $S_{\rm ph}>S_i$), the three-exponential Helmhotz model appears to be in a relatively good agreement with the Zheleznyak model.

In Figures A.2(c) and A.2(d), we compare the three-group Eddington approximation and the three-group SP_3 with the Zheleznyak model. We note that the use of the SP_3 allows to improve the agreement with the Zheleznyak model, in particular, in the region where $S_{\rm ph}>S_i$.

In Figures A.2(e) and A.2(f), we compare the three-group SP_3 and the three-exponential Helmholtz model with the Zheleznyak model. In this case, in the region where $S_{\rm ph}>S_i$ both models give very similar results in the axial direction and are very close to the Zheleznyak model. In the radial direction, the results obtained with the SP_3 model appear to be slightly more accurate than the three-exponential Helmholtz model in the region where $S_{\rm ph}>S_i$.

Figures A.3(a) and A.3(b) demonstrate comparative performance of the boundary conditions specified by equations (III.29) or (III.31) using the three-group SP_3 approximation for domain dimensions 2×2 cm^2 and $\sigma=0.1$ cm. The results are in very good agreement with the results of the Zheleznyak model. Nevertheless, one can note that the use of equation (III.31) slightly overestimates the exact value of the photoionization source term at the boundaries in the radial direction, but the agreement is good in the axial direction. In Figures A.3(c) and A.3(d) which present computations for a domain dimension 0.02×0.02 cm^2 and $\sigma=0.001$ cm, the use of equation (III.31) for defining boundary conditions slightly overestimates the exact value of the photoionization source term at the boundaries in both the axial and radial directions.

Figures A.4(a) and A.4(b) correspond to the domain dimension 0.02×0.02 cm^2 with $\sigma=0.001$ cm. In this case, the use of equation (III.30) slightly overestimates the exact value of the photoionization source term at the boundaries in both the axial and radial directions, although for the domain dimension 2×2 cm^2 with $\sigma=0.1$ cm (Figures A.4(e) and A.4(f)) the photoionization source term at the boundaries in both the axial and radial directions is underestimated.

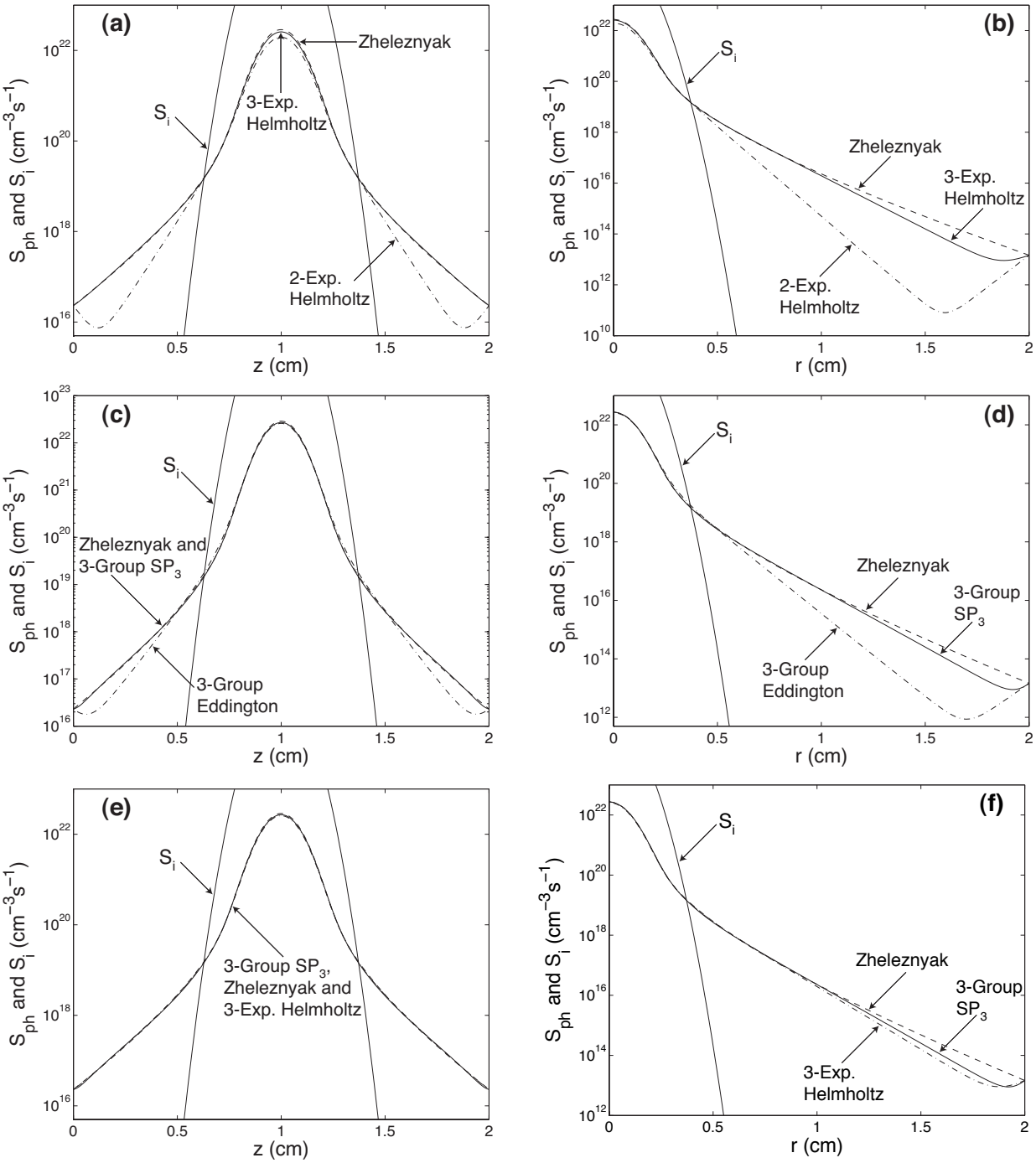

Figure A.1: Same caption as Figure III.5 only for domain dimension 2×2 cm^2 and σ=0.1 cm.

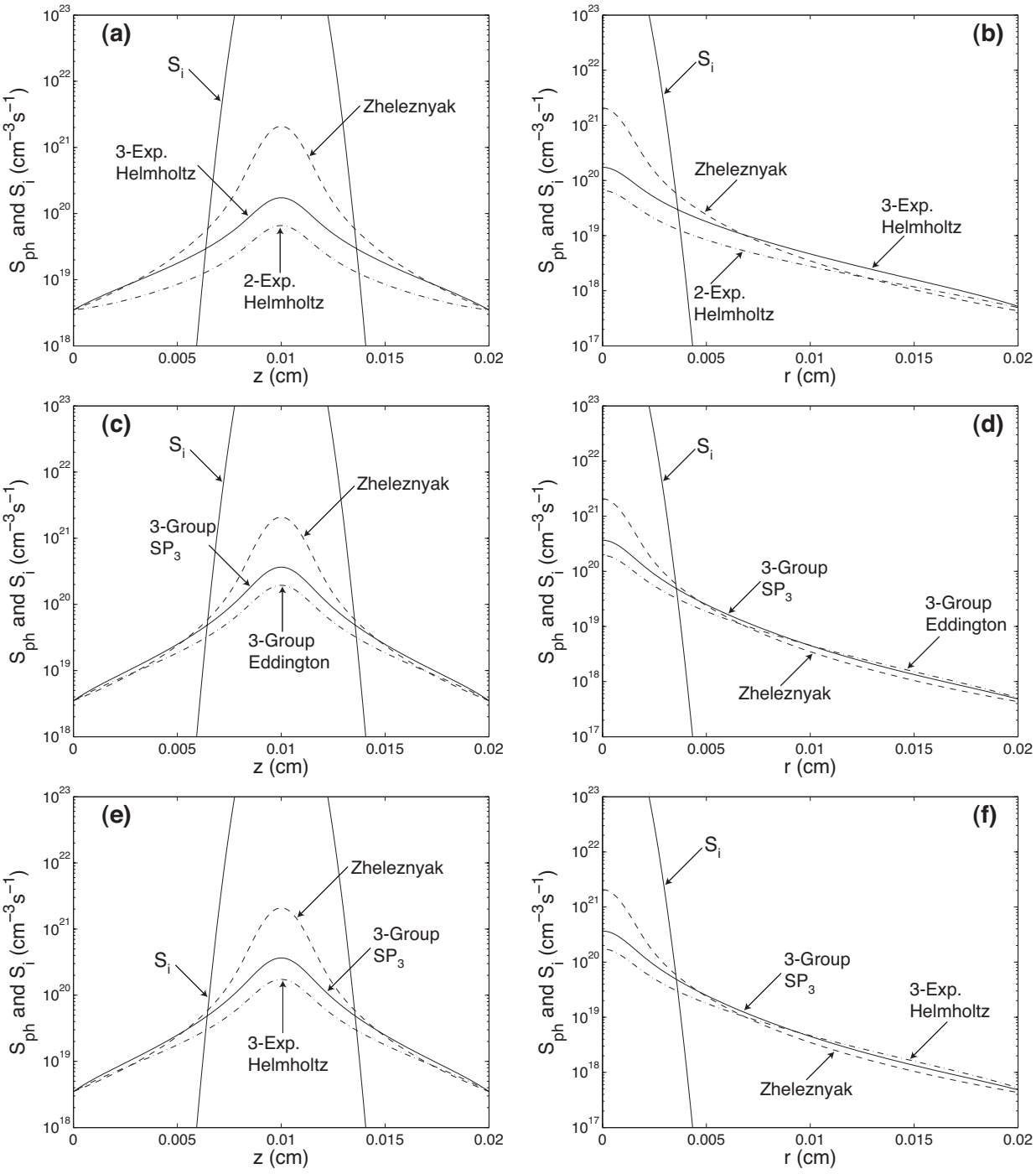

Figure A.2: Same caption as Figure III.5 only for domain dimension 0.02×0.02 cm^2 and σ=0.001 cm.

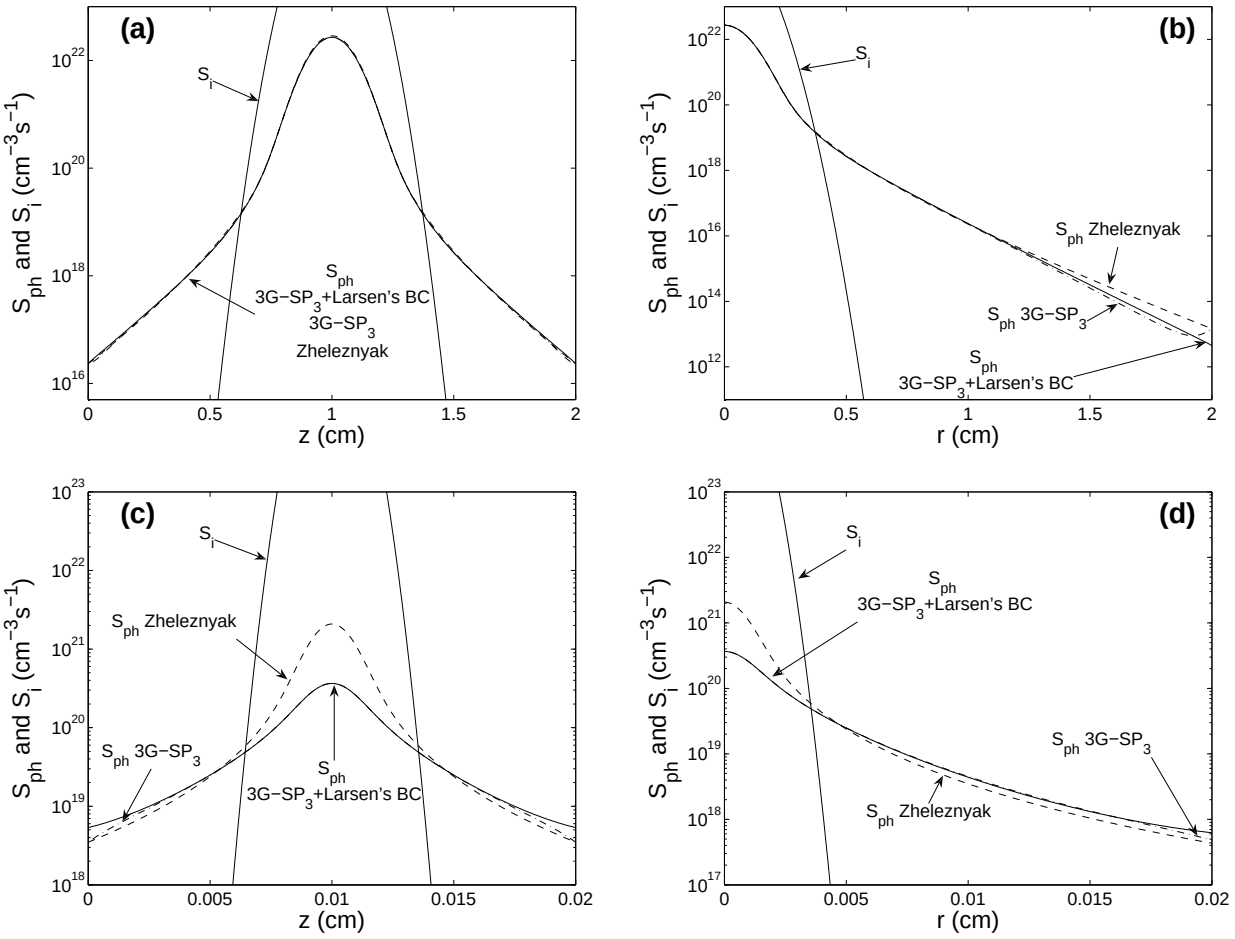

Figure A.3: Same caption as Figure III.6(a) and III.6(b) for domain dimensions 2×2 cm^2 and σ=0.1 cm ((a) and (b)), and for domain dimensions 0.02×0.02 cm^2 and σ=0.001 cm ((c) and (d)).

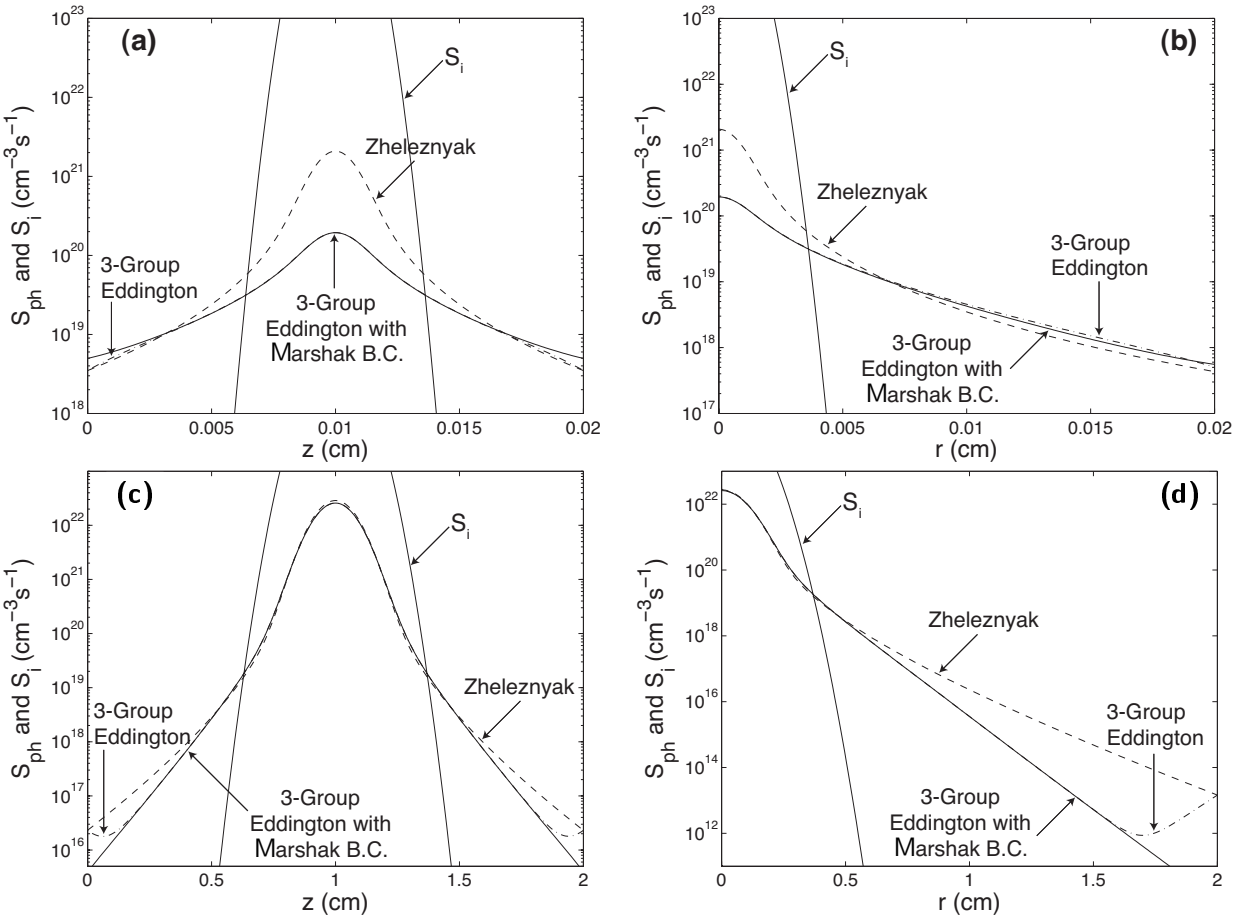

Figure A.4: Same caption as Figure III.6(c) and III.6(d) for domain dimensions 2×2 cm^2 and σ=0.1 cm ((a) and (b)), and for domain dimensions 0.02×0.02 cm^2 and σ=0.001 cm ((c) and (d)).

Appendix B

Mathematical relationships between the Eddington, SP_3 and Helmholtz models

Some results of this appendix have been published in [*Bourdon et al.*, 2007].

The three-group Eddington and SP_3 models presented in Chapter III have been derived on physical grounds from the general radiative transfer equation. These physics based models have certain advantages in comparison with the Helmholtz model, allowing in particular to formulate a consistent and computationally efficient set of equations and boundary conditions based on a radiative transfer theory (see Section III.4). It is useful, however, to bring to attention of the readers that the equation (III.20) of the Eddington model and equations (III.21) and (III.22) of the SP_3 model are Helmholtz equations. Therefore, as demonstrated below in this Appendix, for these equations it is possible to derive effective representations of the $g(R)/p_{O_2}$ function of the type specified by equation (III.9) of the Helmholtz model described in Section III.3. The establishment of these mathematical relationships between Eddington, SP_3 and Helmholtz models is very useful for interpretation of results presented in Section III.6.1, and evaluation of performance of the Eddington and SP_3 models in the general context of the quality of the fit of the $g(R)/p_{O_2}$ function given by equation (III.9) in comparison with the original $g(R)/p_{O_2}$ function of the Zheleznyak photoionization model specified by equation (III.3).

Each of the Helmholtz differential equations (III.8) is similar to equations for wave potentials commonly encountered in antenna theory in electromagnetics [*Harrington*, 2001; *Landau and Lifshitz*, 1971, Chapter VIII, § 64]. On a conceptual level the electromagnetic problem corresponds to a case of purely imaginary λ_j values for which the equation (III.7) would represent outgoing waves [*Harrington*, 2001, p. 80]. In the photoionization problem the λ_j values are real, reflecting exponential spatial damping of the solutions due to the absorption of the photoionizing radiation. The appearance of the similar Helmholtz equations (III.20), (III.21) and (III.22) in the Eddington and improved Eddington approximations to the radiative transfer equation is also consistent with the above physical interpretation. In this Appendix we demonstrate that the solutions of the Helmholtz, Eddington and SP_3 models can be represented in a mathematically equivalent form, however, all represent approximate solutions of the same problem, rely on different numerical values of the model coefficients, and therefore generally do not lead to identical results.

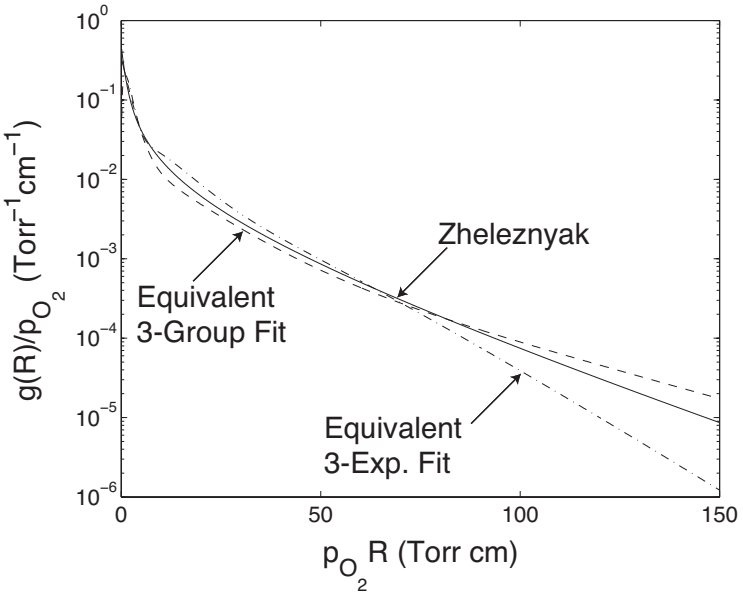

Figure B.1: Solid line: The $g(R)/p_{O_2}$ function given by equation (III.3) from the model of *Zheleznyak et al.* [1982]. Dot-dashed line: Equivalent three-exponential fit for the Helmholtz model obtained from the three-group Eddington approximation. Dashed line: Equivalent three-group fit for the Eddington approximation based on three-exponential Helmholtz model.

In this context it is useful to recall that the Eddington and the Helmholtz models are simply based on different forms of approximation of the integral specified by equation (III.1). The original integral contains a difference of two exponents divided by R^3, the three-group Eddington model approximates the function under integral by a sum of three exponents divided by R^2 (Section III.4), and the three-exponential Helmholtz model approximates the same function by three exponents divided by R (Section III.3). If the problem is solved correctly all approximations should lead to solutions consistent with $S_{\rm ph}$ (III.1).

In this Appendix in order to distinguish between the coefficients involved in the Helmholtz (Table III.2) and the Eddington (Table III.3) models, we will use notations A_j^* [cm^{-2} Torr $^{-2}$], λ_j^* [cm^{-1} Torr $^{-1}$], and A_j [cm^{-1} Torr $^{-1}$], λ_j [cm^{-1} Torr $^{-1}$], for the Helmholtz, and the Eddington models, respectively.

We observe that the Helmholtz equations (III.20) appearing as part of the development of the Eddington approximation are similar in structure to (III.8) and therefore have formal solutions of the type specified by (III.7). On these grounds, after simple algebraic manipulations, we can write solution for the photoionization production rate satisfying equations (III.20) in the form:

$$S_{\rm ph}(\vec{r}) = \iiint_{V'} \frac{I(\vec{r}\,')p_{O_2}}{4\pi R^2}(p_{O_2}R)\sum_j 3A_j\lambda_j e^{-\sqrt{3}\lambda_j p_{O_2}R}{\rm d}V' \tag{B.1}$$

Alternatively, the equation (III.13), representing the same $S_{\rm ph}(\vec{r})$ before the approximation based in the isotropic part of the photon distribution function is applied (see Section III.4),

can be written as:

$$S_{\mathrm{ph}}(\vec{r}) = \iiint_{V'} \frac{I(\vec{r}\,')p_{O_2}}{4\pi R^2} \sum_j A_j e^{-\lambda_j p_{O_2} R} \mathrm{d}V' \tag{B.2}$$

Having introduced $A_j^*{=}3A_j\lambda_j$ and $\lambda_j^*{=}\sqrt{3}\lambda_j$, and remembering that in accordance with (III.9) and (III.14):

$$\frac{g(R)}{p_{O_2}} = (p_{O_2}R) \sum_j A_j^* e^{-\lambda_j^* p_{O_2} R} = \sum_j A_j e^{-\lambda_j p_{O_2} R} \tag{B.3}$$

it can be easily seen that the equation (B.1) employs exactly the same form of approximation to the $g(R)/p_{O_2}$ function as is used in the Helmholtz model. These relationships demonstrate mathematical equivalence between the three-exponential Helmholtz model based on equations (III.8) and the three-group Eddington approximation based on equations (III.20).

We note that taking the three-group Eddington parameters from Table III.3 and calculating the three-exponential Helmholtz model parameters using the above derived relationships $A_j^*{=}3A_j\lambda_j$ and $\lambda_j^*{=}\sqrt{3}\lambda_j$ leads to $g(R)/p_{O_2}{=}(p_{O_2}R)\sum_j A_j^* e^{-\lambda_j^* p_{O_2} R}$ function shown in Figure B.1 by the dot-dashed line, which does not agree with similar function shown in Figure III.2. Thus obtained A_j^* and λ_j^* are different from those given in Table III.2.

Alternatively, taking A_j^* and λ_j^* from Table III.2 and calculating $\lambda_j{=}\lambda_j^*/\sqrt{3}$ and $A_j{=}A_j^*/(3\lambda_j)$ leads to $g(R)/p_{O_2}{=}\sum_j A_j e^{-\lambda_j p_{O_2} R}$ shown in Figure B.1 by the dashed line, which significantly deviates from similar function shown in Figure III.3. Similarly to the previous case we note that thus obtained A_j and λ_j are different from those given in Table III.3.

These results demonstrate that although the two model formulations can be represented in mathematically equivalent form, additional approximations involved on previous steps of the derivation of the Eddington model (i.e., related to the spherical harmonic expansion of the photon distribution function) lead to different numerical values of model coefficients and explain why results obtained from these two model are not identical.

It is interesting to note that since the three-group Eddington model is based on solutions of the Helmholtz equations (III.20) of the form (B.1) with $g(R)/p_{O_2}$ effectively given by dot-dashed line in Figure B.1, the discrepancies observed between the three-group Eddington approximation and the Zheleznyak model in Figures A.1(c) and A.1(d) of Section III.6.1 can be directly linked to the discrepancies between the $g(R)/p_{O_2}$ and the Zheleznyak model at large $p_{O_2}R$ values in Figure B.1. The establishment of these relationships is therefore useful for evaluation of the performance of the Eddington model.

In view of the above mentioned mathematical relationships between the two models it might be tempting to replace the parameters of the Eddington model with the ones from the Helmholtz model providing a better fit. However, this step is not justified in the context of the rigorous development of the Eddington and the improved Eddington (SP_3) models, and as discussed in Section III.6.1 and further reiterated below in this Appendix the SP_3 model takes full advantage of the original accurate fit specified by parameters given in Table III.3 and leads to significantly improved solutions in comparison with the Eddington model.

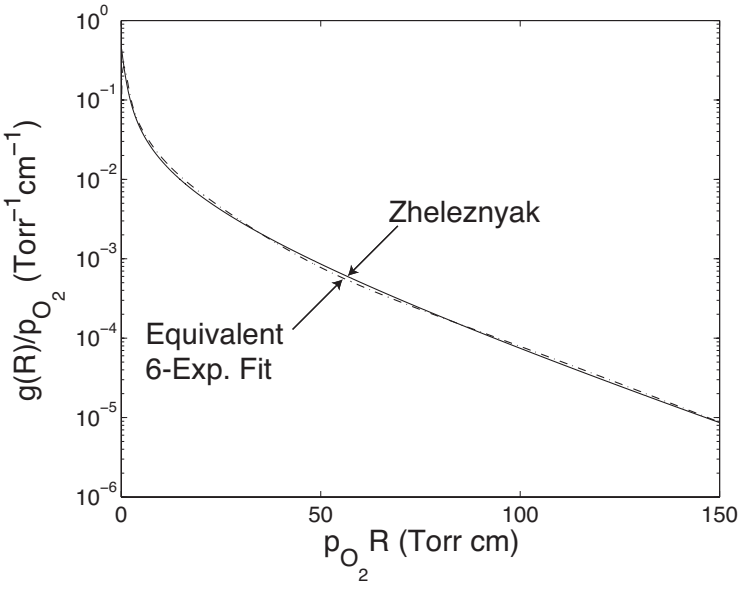

Figure B.2: Solid line: The $g(R)/p_{O_2}$ function given by equation (III.3) from the model of *Zheleznyak et al.* [1982]. Dot-dashed line: Equivalent six-exponential fit for the Helmholtz model obtained from the three-group SP_3 model.

We note that the Helmholtz equations (III.21) and (III.22) appearing as a part of the SP_3 model are similar in structure to (III.8) and have formal solutions of the type (III.7). By summing these solutions using equation (III.23), the corresponding photoionization rate (III.25) can be expressed in the form

$$S_{\rm ph}(\vec{r}) = \iiint_{V'} \frac{I(\vec{r}\,')p_{O_2}}{4\pi R^2}(p_{O_2}R)\sum_j A_j^* e^{-\lambda_j^* p_{O_2}R}{\rm d}V' \tag{B.4}$$

with the corresponding six pairs of $(A_j^*,\ \lambda_j^*)$ of the equivalent six-exponential Helmholtz model defined by: $\lambda_1^*{=}\lambda_1/\kappa_1$, $\lambda_2^*{=}\lambda_2/\kappa_1$, $\lambda_3^*{=}\lambda_3/\kappa_1$, $\lambda_4^*{=}\lambda_1/\kappa_2$, $\lambda_5^*{=}\lambda_2/\kappa_2$, $\lambda_6^*{=}\lambda_3/\kappa_2$; $A_1^*{=}\frac{\gamma_2}{\gamma_2-\gamma_1}\frac{\lambda_1 A_1}{\kappa_1^2}$, $A_2^*{=}\frac{\gamma_2}{\gamma_2-\gamma_1}\frac{\lambda_2 A_2}{\kappa_1^2}$, $A_3^*{=}\frac{\gamma_2}{\gamma_2-\gamma_1}\frac{\lambda_3 A_3}{\kappa_1^2}$, $A_4^*{=}{-}\frac{\gamma_1}{\gamma_2-\gamma_1}\frac{\lambda_1 A_1}{\kappa_2^2}$, $A_5^*{=}{-}\frac{\gamma_1}{\gamma_2-\gamma_1}\frac{\lambda_2 A_2}{\kappa_2^2}$, $A_6^*{=}{-}\frac{\gamma_1}{\gamma_2-\gamma_1}\frac{\lambda_3 A_3}{\kappa_2^2}$.

Having taken the three-group Eddington parameters $(A_j,\ \lambda_j)$ from Table III.3 and calculated the six-exponential Helmholtz model parameters using the above derived relationships leads to the $g(R)/p_{O_2}{=}(p_{O_2}R)\sum_j A_j^* e^{-\lambda_j^* p_{O_2}R}$ function shown in Figure B.2 by the dot-dashed line, which is in a substantially better agreement with the original Zheleznyak function in comparison to the similar equivalent three-exponential fit, obtained for the three-group Eddington model, shown by dot-dashed line in Figure B.1. The good performance of the three-group SP_3 model in Figures A.1(c) and A.1(d) of Section III.6.1 can be directly linked to the better agreement between the six-exponential $g(R)/p_{O_2}$ fit with the original Zheleznyak function in Figure B.2.

In summary, in this appendix we have demonstrated the mathematical equivalence of the Eddington, SP_3 and Helmholtz models. All solutions of these models can be written in essentially same mathematical form, with differences between these models only arising from different numerical values of the model coefficients. The presented analysis demonstrates that the three-exponential Helmholtz model presented in Section III.3 is more accurate than the three-group Eddington model presented in Section III.4, in agreement with re-

sults presented in Section III.6.1. The presented analysis also demonstrates that the SP_3 model can be effectively represented in a mathematical form equivalent to six-exponential Helmholtz model. This approach allows a simple interpretation of better performance of the three-group SP_3 model in comparison with the three-group Eddington model introduced in Section III.4, and in comparison with the three-exponential Helmholtz model presented in Section III.4, in agreement with the results presented in Section III.6.1.

Appendix C

Determination of the pre-ionization level for streamer propagation in weak field at ground pressure in air

Using an initial continuous neutral pre-ionization level instead of the full model for photoionization is a simple way to save computation time. Obviously, the important point is then the determination of the pre-ionization level. In this appendix, we develop an approach to determine this pre-ionization level.

Pancheshnyi et al. [2001] have mentioned that it is possible to attain the coincidence of some characteristics (but not for all the characteristics simultaneously) of streamer discharges, by varying the level of pre-ionization background. To avoid doing systematic parametric studies with different pre-ionization levels, in this appendix, we determine the level of pre-ionization based on the dynamics of the streamer head. This analysis is based on the simulation results obtained with the full model for photoionization. Figure C.1 shows the direct ionization by electron impact rate, the photoionization rate, and the electron density at time $t = 17.5$ ns in the simulation case of streamer propagation in a weak field depicted in Section III.6.2 and computed using the FCT+QUICKEST3 scheme (see Chapter II).

As mentioned in Chapter III, the ionization rate is higher than the photoionization rate in the narrow region of the streamer head. Behind this region, in the streamer channel, the photoionization rate is higher than the ionization rate. In front of the streamer head, where the gas is still mainly neutral, the creation of electrons and ions mainly results from the photoionization process beyond the intersection point of the ionization and photoionization rates. In Figure C.1 at time $t = 17.5$ ns one can say that the creation of seed electrons is mainly governed by photoionization in the region $x \gtrsim 0.77$ cm.

Moreover, the electron density which corresponds to the location of equal ionization and photoionization rates, is quite constant during stable streamer propagation. We concluded that this value of the electron density, which is negligible compared to the density inside the streamer channel, can be interpreted as the electron density mainly produced by photoionization at this location. Considering the impact of photoionization on the local dynamics of the head, this value could replace the seed electrons due to photoionization in front of the streamer head. In the case of Figure C.1 this value is $\sim 10^9$ cm^{-3}.

We have checked this method in different configurations and we observed that it is efficient

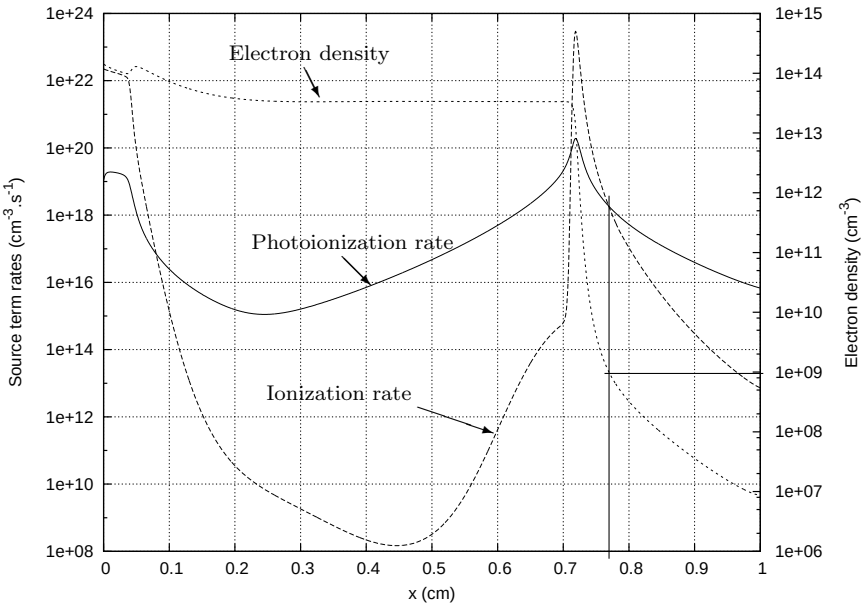

Figure C.1: Photoionization and direct ionization rates, and electron density at time $t = 17.5$ ns for the streamer propagation in a weak field presented in Section III.6.2.

to find a good approximation of the pre-ionization level.

Figures C.2 and C.3 show the comparison of the electron densities and axial electric field, respectively, between the simulations using either a pre-ionization background or the computation of the photoionization source term. In the cases without photoionization we considered the pre-ionization levels of 10^9 cm^{-3} and 10^{10} cm^{-3}. For a pre-ionization level of 10^8 cm^{-3}, we have not observed any streamer propagation.

Figure C.2 shows that the pre-ionization level of 10^9 cm^{-3} gives a good agreement with the computation of the photoionization source term. The electron density in the channel is in very good agreement, as well as the electric field in the streamer channel showed by Figure C.3. The electric field in the streamer head is also well described. The main difference between the case with the pre-ionization level at 10^9 cm^{-3} and the case with the computation of the photoionization source term is the propagation velocity, which is a slightly higher when the photoionization source term is calculated.

One can also note that with a pre-ionization level of 10^{10} cm^{-3}, the propagation of the streamer is slower in spite of relation (I.13). This means that increasing the pre-ionized background does not have a simple impact on the streamer dynamics and leads, for example, to a non-negligible change of the electric field (see Figure C.3). To argue in this direction, we also noted that, at the beginning of the propagation, for the pre-ionized case at 10^{10} cm^{-3} the streamer is faster than for the other cases, but streamers calculated using photoionization model and 10^9 cm^{-3} pre-ionization pass it at about 12 ns.

In conclusion, we have shown that to reproduce the streamer propagation in the weak field case presented in Section III.6.2, a pre-ionization level of 10^9 cm^{-3} gives a good agreement

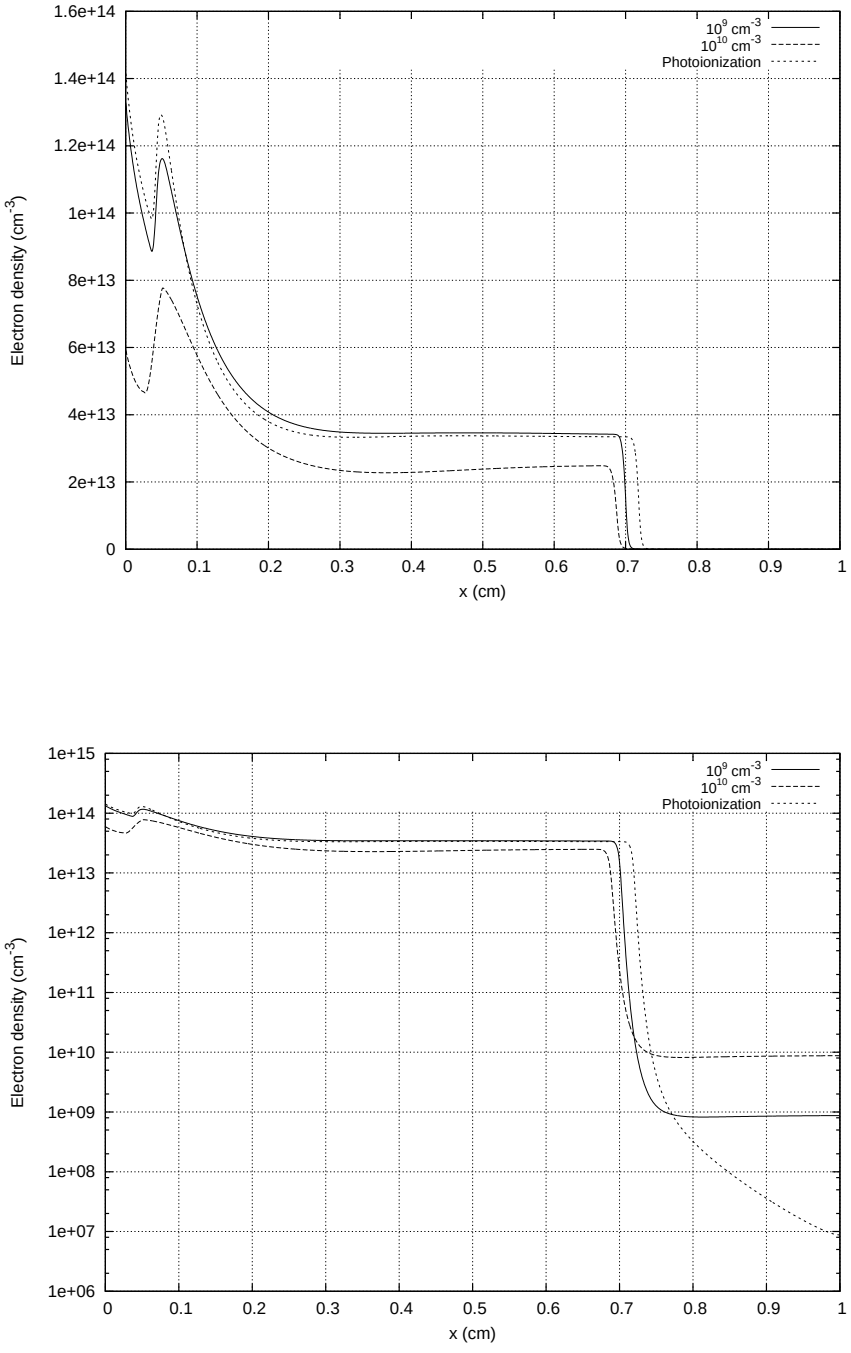

Figure C.2: Electron density. Upper image: linear scale. Lower image: logscale. Solid line: pre-ionization level of 10^9 cm^{-3}. Dashed-line: pre-ionization level of 10^{10} cm^{-3}. Dotted-line: computation taking into account the photoionization. Time $t = 17.5$ ns.

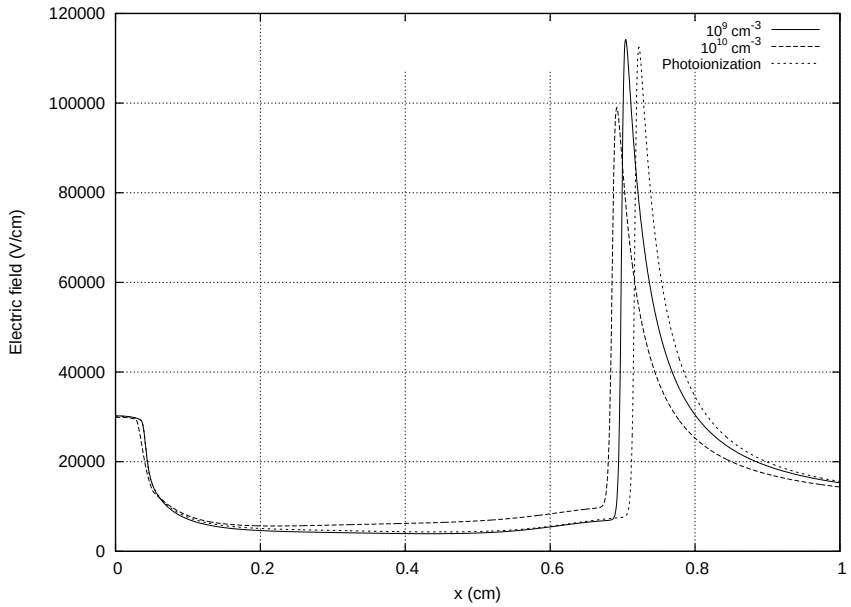

Figure C.3: Electric field along the axis of symmetry. Solid line: pre-ionization level of 10^9 cm^{-3}. Dashed-line: pre-ionization level of 10^{10} cm^{-3}. Dotted-line: computation taking into account the photoionization. Time $t = 17.5$ ns.

with the results of computations using the photoionization source term.

Bibliography

Aints, M., A. Haljaste, T. Plank, and L. Roots (2008), Absorption of photo-ionizing radiation of corona discharges in air, *Plasma Process. and Polym.*, *5*(7), 672–680, doi: 10.1002/ppap.200800031.

Akishev, Y., I. Kochetov, A. Loboiko, and A. Napartovich (2002), 3-dimensional model for trichel pulses: results of numerical studies for air, in *Proc. 8th Int. Symp. on High Pressure Low Temperature Plasma Chemistry (Puhajarve, Estonia)*, pp. 1–5.

Aleksandrov, N. L., and I. V. Kochetov (1996), Electron rate coefficients in gases under non-uniform field and electron density conditions, *J. Phys. D: Applied Physics*, *29*(6), 1476–1483.

Allegraud, K., O. Guaitella, and A. Rousseau (2007), Spatio-temporal breakdown in surface DBDs: evidence of collective effect, *J. Phys. D: Applied Physics*, *40*(24), 7698–7706.

Amestoy, P. R., I. S. Duff, and J.-Y. L'Excellent (2000), Multifrontal parallel distributed symmetricand unsymmetric solvers, *Comput. Methods Appl. Mech. Eng.*, *184*, 501–520.

Amestoy, P. R., I. S. Duff, J. Koster, and J.-Y. L'Excellent (2001), A fully asynchronous multifrontal solver using distributed dynamic scheduling, *SIAM J. Matrix Anal. Appl.*, *23*(1), 15–41.

Amestoy, P. R., A. Guermouche, J.-Y. L'Excellent, and S. Pralet (2006), Hybrid scheduling for the parallel solution of linear systems, *Parallel Computing*, *32*(2), 136–156.

Arrayás, M., U. Ebert, and W. Hundsdorfer (2002), Spontaneous branching of anode-directed streamers between planar electrodes, *Phys. Rev. Lett.*, *88*, 174502(R), doi:10.1103/PhysRevLett.88.174502.

Babaeva, N. Y., and G. V. Naidis (1996), Two-dimensional modelling of positive streamer dynamics in non-uniform electric fields in air, *J. Phys. D: Applied Physics*, *29*, 2423–2431, doi:10.1088/0022-3727/29/9/029.

Babaeva, N. Y., and G. V. Naidis (1997), Dynamics of positive and negative streamers in air in weak uniform electric fields, *IEEE Trans. Plasma Sci.*, *25*, 375–379.

Babaeva, N. Y., A. N. Bhoj, and M. J. Kushner (2006), Streamer dynamics in gases containing dust particles, *Plasma Sources Sci. Technol.*, *15*, 591–602.

Bazelyan, E., and Y. Raizer (1998), *Spark discharge*, CRC Press, ISBN: 978-0849328688.

Bertein, H. (1973), Charges on insulators generated by breakdown of gas, *J. Phys. D: Applied Physics*, *6*(16), 1910–1916.

Bessières, D. (2006), Modélisation des décharges électriques filamentaires, Ph.D. thesis, University of Pau et des Pays de l'Adour, France.

Bessières, D., J. Paillol, A. Bourdon, P. Ségur, and E. Marode (2007), A new one-dimensional moving mesh method applied to the simulation of streamer discharges, *J. Phys. D: Applied Physics*, *40*(21), 6559–6570.

Boeuf, J.-P., and L. Pitchford (1991), Pseudospark discharges via computer simulation, *IEEE Trans. Plasma Sci.*, *19*(2), 286–296, doi:10.1109/27.106826.

Boris, J. P., and D. L. Book (1973), Flux-Corrected Transport. I. SHASTA, A Fluid Transport Algorithm That Works, *J. Comput. Phys.*, *11*, 38–69.

Boris, J. P., and D. L. Book (1976), Flux-Corrected Transport. III. Minimal-Error FCT Algorithms, *J. Comput. Phys.*, *20*, 397–431.

Bourdon, A., V. P. Pasko, N. Y. Liu, S. Célestin, P. Ségur, and E. Marode (2007), Efficient models for photoionization produced by non-thermal gas discharges in air based on radiative transfer and the Helmholtz equations, *Plasma Sources Sci. Technol.*, *16*(3), 656–678, doi:10.1088/0963-0252/16/3/026.

Braun, D., V. Gibalov, and G. Pietsch (1992), Two-dimensional modelling of the dielectric barrier discharge in air, *Plasma Sources Sci. Technol.*, *1*(3), 166–174.

Briels, T. M. P., J. Kos, E. M. van Veldhuizen, and U. Ebert (2006), Circuit dependence of the diameter of pulsed positive streamers in air, *J. Phys. D: Applied Physics*, *39*, 5201–5210.

Capeillère, J., P. Ségur, A. Bourdon, S. Célestin, and S. Pancheshnyi (2008), The finite volume method solution of the radiative transfer equation for photon transport in non-thermal gas discharges: application to the calculation of photoionization in streamer discharges, *J. Phys. D: Applied Physics*, *41*, 234018, doi:10.1088/0022-3727/41/23/234018.

Carlson, B. C. (1977), Elliptic integrals of the first kind, *SIAM J. Math. Anal.*, *8*(2), 231–242, doi:10.1137/0508016.

Celestin, S., K. Allegraud, G. Canes-Boussard, N. Leick, O. Guaitella, and A. Rousseau (2008a), Patterns of plasma filaments propagating on a dielectric surface, *IEEE Trans. Plasma Sci.*, *36*(4), 1326–1327, doi:10.1109/TPS.2008.924519.

Celestin, S., G. Canes-Boussard, O. Guaitella, A. Bourdon, and A. Rousseau (2008b), Influence of the charges deposition on the spatio-temporal self-organization of streamers in a DBD, *J. Phys. D: Applied Physics*, *41*(20), 205214 (10pp), doi:10.1088/0022-3727/41/20/205214.

Chanrion, O., and T. Neubert (2008), A pic-mcc code for simulation of streamer propagation in air, *J. Comput. Phys.*, *227*(15), 7222–7245, doi:10.1016/j.jcp.2008.04.016.

Chirokov, A., A. Gutsol, A. Fridman, K. D. Sieber, J. M. Grace, and K. S. Robinson (2004), Analysis of two-dimensional microdischarge distribution in dielectric-barrier discharges, *Plasma Sources Sci. Technol.*, *13*(4), 623–635.

Demmel, J. W., S. C. Eisenstat, J. R. Gilbert, X. S. Li, and J. W. H. Liu (1999a), A supernodal approach to sparse partial pivoting, *SIAM J. Matrix Anal. Appl.*, *20*(3), 720–755.

Demmel, J. W., J. R. Gilbert, and X. S. Li (1999b), An asynchronous parallel supernodal algorithm for sparse gaussian elimination, *SIAM J. Matrix Anal. Appl.*, *20*(4), 915–952.

Dessantes, P. (2000), Modélisation de décharges électriques de type streamer dans l'air à haute pression sous géométrie fortement non uniforme, Ph.D. thesis, University of Paris XI, Orsay, France.

DeVore, C. R. (1998), An improved limiter for multidimensional flux-corrected transport, *Naval Research Report*, *NRL/MR/6440–98-8330*, 1–19.

Dhali, S. K., and P. F. Williams (1987), Two-dimensional studies of streamers in gases, *J. Appl. Phys.*, *62*, 4696–4707.

Djakov, A. F., Y. K. Bobrov, and Y. V. Yourguelenas (1998), Modeling of a positive streamer in air in a non-uniform external field, in *Physics and Technology of Electric Power Transmission*, vol. Book 1, edited by A. F. Djakov, pp. 161–200, MPEI Publishers, Moscow.

Djermoune, D., E. Marode, and P. Ségur (1995a), Two dimensional modelling of a streamer induced discharge, in *Proc. 22th Int. Conf. on Phenomena in Ionized Gases (Hoboken, USA)*, pp. 33–34.

Djermoune, D., S. Samson, E. Marode, and P. Ségur (1995b), A time resolved two dimensional modelling of the electrical behaviour and the chemical yield of the streamer induced discharge, in *Proc. 11th Int. Conf. on Gas Discharges and Their Applications (Chuo University, Tokyo, Japan)*, pp. 484–487.

Ducasse, O., L. Papageorghiou, O. Eichwald, N. Spyrou, and M. Yousfi (2007), Critical analysis on two-dimensional point-to-plane streamer simulations using the finite element and finite volume methods, *IEEE Trans. Plasma Sci.*, *35*(5, Part 1), 1287–1300.

Durand, E. (1966a), *Electrostatique I. Les distributions.*, vol. 1, Masson et C^{ie}.

Durand, E. (1966b), *Electrostatique II. Problèmes généraux. Conducteurs.*, vol. 2, Masson et C^{ie}.

Durand, E. (1966c), *Electrostatique III. Méthodes de Calcul. Diélectriques.*, vol. 3, Masson et C^{ie}.

Dyakonov, M. I., and V. Y. Kachorovskii (1988), Theory of streamer discharge in semiconductors, *Soviet Physics JETP, Engl. Transl*, *67*, 1049–1054.

Dyakonov, M. I., and V. Y. Kachorovskii (1989), Streamer discharge in a homogeneous field, *Soviet Physics JETP, Engl. Transl*, *68*, 1070–1074.

Eliasson, B., and U. Kogelschatz (1991a), Modeling and applications of silent discharge plasmas, *IEEE Trans. Plasma Sci.*, *19*(2), 309–323, doi:10.1109/27.106829.

Eliasson, B., and U. Kogelschatz (1991b), Nonequilibrium volume plasma chemical processing, *IEEE Trans. Plasma Sci.*, *19*(6), 1063–1077, doi:10.1109/27.125031.

Eyring, C. F., S. S. MacKeown, and R. A. Millikan (1928), Fields Currents from Points, *Phys. Rev.*, *31*, 900–909.

Fedkiw, R. P., T. Aslam, B. Merriman, and S. Osher (1999), A Non-oscillatory Eulerian Approach to Interfaces in Multimaterial Flows (the Ghost Fluid Method), *J. Comput. Phys.*, *152*, 457–492.

Ferziger, J., and M. Peric (2002), *Computational Methods for Fluid Dynamics*, 3rd ed., Springer-Verlag, ISBN: 3-540-42074-6.

Fiala, A., L. C. Pitchford, and J. P. Boeuf (1994), Two-dimensional, hybrid model of low-pressure glow discharges, *Phys. Rev. E*, *49*(6), 5607–5622, doi:10.1103/PhysRevE.49.5607.

Franz, R. C., R. J. Nemzek, and J. R. Winckler (1990), Television image of a large upward electric discharge above a thunderstorm system, *Science*, *249*, 48.

Georghiou, G. E., R. Morrow, and A. C. Metaxas (1999), The theory of short-gap breakdown of needle point-plane gaps in air using finite-difference and finite-element methods, *J. Phys. D: Applied Physics*, *32*(12), 1370–1385.

Gibalov, V. I., and G. J. Pietsch (2000), The development of dielectric barrier discharges in gas gaps and on surfaces, *J. Phys. D: Applied Physics*, *33*(20), 2618–2636.

Gibou, F., R. P. Fedkiw, L.-T. Cheng, and M. Kang (2002), A Second-Order-Accurate Symmetric Discretization of the Poisson Equation on Irregular Domains, *J. Comput. Phys.*, *176*, 205–227.

Godunov, S. (1959), A finite difference method for the numerical computation and discontinuous solutions of the equations of fluid dynamics, *Matematicheskii Sbornik*, *47*, 271–306, (in Russian) Translated US Joint Publ. Res. Service, JPRS 7226 (1969).

Golubovskii, Y. B., V. A. Maiorov, J. Behnke, and J. F. Behnke (2002), Influence of interaction between charged particles and dielectric surface over a homogeneous barrier discharge in nitrogen, *J. Phys. D: Applied Physics*, *35*(8), 751–761.

Guaitella, O., F. Thevenet, C. Guillard, and A. Rousseau (2006), Dynamic of the plasma current amplitude in a barrier discharge: influence of photocatalytic material, *J. Phys. D: Applied Physics*, *39*(14), 2964–2972.

Guikema, J., N. Miller, J. Niehof, M. Klein, and M. Walhout (2000), Spontaneous pattern formation in an effectively one-dimensional dielectric-barrier discharge system, *Phys. Rev. Lett.*, *85*(18), 3817–3820, doi:10.1103/PhysRevLett.85.3817.

Guo, J.-M., and C.-H. J. Wu (1993), Two-dimensional nonequilibrium fluid models for streamers, *IEEE Trans. Plasma Sci.*, *21*(6), 684–695, doi:10.1109/27.256788.

Hallac, A., G. E. Georghiou, and A. C. Metaxas (2003), Secondary emission effects on streamer branching in transient non-uniform short-gap discharges, *J. Phys. D: Applied Physics*, *36*, 2498–2509, doi:10.1088/0022-3727/36/20/011.

Harrington, R. F. (2001), *Time-harmonic electromagnetic fields*, IEEE Press, John Wiley and Sons, Inc., New York.

Hassouni, K., F. Massines, and J.-M. Pouvesle (2004), *Plasmas Froids. Génération, caractérisation et technologies*, chap. Plasmas hors-équilibre à des pressions atmosphériques, pp. 49–108, Publications de l'Université de Saint-Etienne, ISBN: 2-86272-339-8.

Hong, J.-M., T. Shinar, M. Kang, and R. Fedkiw (2007), On boundary condition capturing for multiphase interfaces, *J. Sci. Comput.*, *31*(1-2), 99–125.

Kang, M., R. P. Fedkiw, and X. dong Liu (2000), A boundary condition capturing method for multiphase incompressible flow, *J. Sci. Comput.*, *15*, 323–360.

Kim, Y., J. Park, and S. Hong (2004), Geometrical effects of the discharge system on the corona discharge and chemically active species generated in wire-cylinder and wire-plate reactors, *Journal of the Korean Physical Society*, *44*(6), 1458–1467.

Klein, M., N. Miller, and M. Walhout (2001), Time-resolved imaging of spatiotemporal patterns in a one-dimensional dielectric-barrier discharge system, *Phys. Rev. E*, *64*(2), 026,402, doi:10.1103/PhysRevE.64.026402.

Kogelschatz, U. (2002), Filamentary, patterned, and diffuse barrier discharges, *IEEE Trans. Plasma Sci.*, *30*(4), 1400–1408, doi:10.1109/TPS.2002.804201.

Kogelschatz, U. (2004), Atmospheric-pressure plasma technology, *Plasma Phys. Control. Fusion*, *46*(12B), B63–B75.

Kozlov, K. V., H.-E. Wagner, R. Brandenburg, and P. Michel (2001), Spatio-temporally resolved spectroscopic diagnostics of the barrier discharge in air at atmospheric pressure, *J. Phys. D: Applied Physics*, *34*(21), 3164–3176.

Kulikovsky, A. A. (1995a), A more accurate Scharfetter-Gummel algorithm of electron transport for semiconductor and gas discharge simulation, *J. Comput. Phys.*, *119*, 149–155.

Kulikovsky, A. A. (1995b), Two-dimensional simulation of the positive streamer in N_2 between parallel-plate electrodes, *J. Phys. D: Applied Physics*, *28*(12), 2483–2493.

Kulikovsky, A. A. (1997a), Production of chemically active species in the air by a single positive streamer in a nonuniform field, *IEEE Trans. Plasma Sci.*, *25*(3), 439–446, doi: 10.1109/27.597258.

Kulikovsky, A. A. (1997b), Positive streamer between parallel plate electrodes in atmospheric pressure air, *J. Phys. D: Applied Physics*, *30*, 441–450.

Kulikovsky, A. A. (1998), Positive streamer in a weak field in air: A moving avalanche-to-streamer transition, *Phys. Rev. E*, *57*, 7066–7074, doi:10.1103/PhysRevE.57.7066.

Kulikovsky, A. A. (2000a), The role of photoionization in positive streamer dynamics, *J. Phys. D: Applied Physics*, *33*, 1514–1524.

Kulikovsky, A. A. (2000b), The role of the absorption length of photoionizing radiation in streamer dynamics in weak fields: a characteristic scale of ionization domain, *J. Phys. D: Applied Physics*, *33*(1), L5–L7.

Kulikovsky, A. A. (2001), The efficiency of radicals production by positive streamer in air: the role of laplacian field, *IEEE Trans. Plasma Sci.*, *29*(2), 313–317, doi:10.1109/27.922740.

Kunhardt, E. E., and Y. Tzeng (1988), Development of an electron avalanche and its transition into streamers, *Phys. Rev. A*, *38*, 1410–1421.

Kunhardt, E. E., J. Wu, and B. Penetrante (1988), Nonequilibrium macroscopic descriptions of electrons in weakly ionized gases, *Phys. Rev. A*, *37*, 1654–1662, doi:10.1103/PhysRevA.37.1654.

Landau, L. D., and E. M. Lifshitz (1971), *The classical theory of fields*, Course of theoretical physics - Pergamon International Library of Science, Technology, Engineering and Social Studies, Oxford: Pergamon Press, 1971, 3rd rev. engl. edition.

Larsen, E. W., G. Thömmes, A. Klar, M. Seaïd, and T. Götz (2002), Simplified P_N Approximations to the Equations of Radiative Heat Transfer and Applications, *J. Comput. Phys.*, *183*, 652–675.

Leonard, B., A. Lock, and M. MacVean (1995), *Extended Numerical Integration for Genuinely Multidimensional Advective Transport Insuring Conservation*, vol. 9, 1–12 pp., Pineridge Press.

Leonard, B. P. (1979), A stable and accurate convective modelling procedure based on quadratic upstream interpolation, *Comput. Meth. Appl. Mech. Engrg.*, *19*, 59–98.

Leonard, B. P. (1991), The ULTIMATE conservative difference scheme applied to unsteady one-dimensional advection, *Comput. Methods Appl. Mech. Eng.*, *88*, 17–74.

Li, C., W. J. M. Brok, U. Ebert, and J. J. A. M. van der Mullen (2007), Deviations from the local field approximation in negative streamer heads, *J. Phys. D: Applied Physics*, *101*(12), 123305, doi:10.1063/1.2748673.

Liu, N. (2006), Dynamics of positive and negative streamers in sprites, Ph.D. thesis, The Pennsylvania State University, USA.

Liu, N., S. Célestin, A. Bourdon, V. P. Pasko, P. Ségur, and E. Marode (2007), Application of photoionization models based on radiative transfer and the Helmholtz equations to studies of streamers in weak electric fields, *Appl. Phys. Lett.*, *91*(21), 211501, doi:10.1063/1.2816906.

Liu, N. Y., and V. P. Pasko (2004), Effects of photoionization on propagation and branching of positive and negative streamers in sprites, *J. Geophys. Res.*, *109*, A04301, doi:10.1029/2003JA010064.

Liu, N. Y., and V. P. Pasko (2006), Effects of photoionization on similarity properties of streamers at various pressures in air, *J. Phys. D: Applied Physics*, *39*, 327–334, doi:10.1088/0022-3727/39/2/013.

Liu, X.-D., R. P. Fedkiw, and M. Kang (2000), A Boundary Condition Capturing Method for Poisson's Equation on Irregular Domains, *J. Comput. Phys.*, *160*, 151–178.

Loeb, L. B. (1965), Ionizing Waves of Potential Gradient, *Science*, *148*, 1417–1426.

Loeb, L. B., and J. M. Meek (1940a), The Mechanism of Spark Discharge in Air at Atmospheric Pressure. I, *J. Appl. Phys.*, *11*, 438–447.

Loeb, L. B., and J. M. Meek (1940b), The Mechanism of Spark Discharge in Air at Atmospheric Pressure. II, *J. Appl. Phys.*, *11*, 459–474.

Luque, A., U. Ebert, C. Montijn, and W. Hundsdorfer (2007), Photoionization in negative streamers: Fast computations and two propagation modes, *Appl. Phys. Lett.*, *90*, 081501, doi:10.1063/1.2435934.

Lyons, W. A. (2006), The meteorology of transient luminous events - An introduction and overview, in *Sprites, Elves and Intense Lightning Discharges*, *NATO Science Series II: Mathematics, Physics and Chemistry*, vol. 225, edited by M. Füllekrug and E. A. Mareev and M. J. Rycroft, pp. 19–56, Springer, Heidleberg, Germany.

Manley, T. C. (1943), The electric characteristics of the ozonator discharges, *Trans. Electrochem. Soc.*, *84*, 83–96.

Meek, J. M. (1940), A theory of spark discharge, *Phys. Rev.*, *57*(8), 722–728, doi:10.1103/PhysRev.57.722.

Montijn, C., and U. Ebert (2006), Diffusion correction to the raether–meek criterion for the avalanche-to-streamer transition, *J. Phys. D: Applied Physics*, *39*(14), 2979–2992.

Moreau, E. (2007), Airflow control by non-thermal plasma actuators, *J. Phys. D: Applied Physics*, *40*(3), 605–636.

Morrow, R. (1981), Numerical Solution of Hyperbolic Equations for Electron Drift in Strongly Non-Uniform Electric Fields, *J. Comput. Phys.*, *43*, 1–15.

Morrow, R., and J. J. Lowke (1997), Streamer propagation in air, *J. Phys. D: Applied Physics*, *30*, 614–627.

Murooka, Y., T. Takada, and K. Hiddaka (2001), Nanosecond surface discharge and charge density evaluation, Part I: review and experiments, *17*(2), 6–16, doi:10.1109/57.917527.

Naidis, G. V. (1997), Effects of nonlocality on the dynamics of streamers in positive corona discharges, *Tech. Phys. Lett.*, *23*, 493–494.

Naidis, G. V. (2006), On photoionization produced by discharges in air, *Plasma Sources Sci. Technol.*, *15*, 253–255.

Nguyen, D. Q., R. P. Fedkiw, and M. Kang (2001), A Boundary Condition Capturing Method for Incompressible Flame Discontinuities, *J. Comput. Phys.*, *172*, 71–98.

Packan, D. (2003), Repetitive nanosecond glow discharge in atmospheric pressure air, Ph.D. thesis, Stanford University, USA.

Pai, D. (2008), Nanosecond repetitively pulsed plasmas in preheated air at atmsopheric pressuregeneration of diffuse nonthermal plasmas in air at atmospheric pressure, Ph.D. thesis, Ecole Centrale Paris, France.

Pai, D., D. Lacoste, and C. Laux (2008), Images of nanosecond repetitively pulsed plasmas in preheated air at atmospheric pressure, *IEEE Trans. Plasma Sci.*, *36*(4), 974–975, doi:10.1109/TPS.2008.924484.

Pancheshnyi, S. (2005), Role of electronegative gas admixtures in streamer start, propagation and branching phenomena, *Plasma Sources Sci. Technol.*, *14*(4), 645–653.

Pancheshnyi, S., M. Nudnova, and A. Starikovskii (2005), Development of a cathode-directed streamer discharge in air at different pressures: Experiment and comparison with direct numerical simulation, *Phys. Rev. E*, *71*(1), 016407, doi:10.1103/PhysRevE.71.016407.

Pancheshnyi, S. V., S. M. Starikovskaia, and A. Y. Starikovskii (2001), Role of photoionization processes in propagation of cathode-directed streamer, *J. Phys. D: Applied Physics*, *34*, 105–115.

Papageorghiou, L., and N. Spyrou (2007), Formation and propagation of ionization potential waves in various pressures, in *Proc. 28th Int. Conf. on Phenomena in Ionized Gases (Prague, Czech Republic)*, pp. 1–4.

Parker, J. H., and J. J. Lowke (1969), Theory of electron diffusion parallel to electric fields. I. Theory, *Phys. Rev.*, *181*(1), 290–301, doi:10.1103/PhysRev.181.290.

Pasko, V. P. (2006), *NATO Science Series II: Mathematics, Physics and Chemistry Vol. 225*, chap. Theoretical modeling of sprites and jets, in Sprites, Elves and Intense Lightning Discharges, pp. 253–293, Heidleberg: Springer.

Pasko, V. P. (2007), Red sprite discharges in the atmosphere at high altitude: the molecular physics and the similarity with laboratory discharges, *Plasma Sources Sci. Technol.*, *16*, S13–S29, doi:10.1088/0963-0252/16/1/S02.

Pasko, V. P., U. S. Inan, and T. F. Bell (1998), Spatial structure of sprites, *Geophys. Res. Lett.*, *25*, 2123–2126.

Penney, G. W., and G. T. Hummert (1970), Photoionization measurements in Air, Oxygen, and Nitrogen, *J. Appl. Phys.*, *41*, 572–577.

Pilla, G., D. Galley, D. A. Lacoste, F. Lacas, D. Veynante, and C. O. Laux (2006), Stabilization of a turbulent premixed flame using a nanosecond repetitively pulsed plasma, *IEEE Trans. Plasma Sci.*, *34*(6), 2471–2477, doi:10.1109/TPS.2006.886081.

Pomraning, G. (1973), *The equations of radiation hydrodynamics*, Pergamon Press, New York.

Potin, J. (2001), Modélisation numérique d'une décharge filamentaire controlée par barrière diélectrique dans l'azote à la pression atmosphérique, Ph.D. thesis, Université Paul Sabatier de Toulouse, France.

Press, W. H., S. A. Teukolski, W. T. Vetterling, and B. P. Flannery (1992), *Numerical Recipes in FORTRAN - The Art of Scientific Computing - Third Edition*, University Press, Cambridge.

Raizer, Y. P. (1991), *Gas Discharge Physics*, Springer-Verlag, New York, NY.

Rax, J.-M. (2005), *Physique des Plasmas*, Dunod, Paris.

Régnier, P. (2004), Modélisation de décharges filamentaires. Applications à la combustion et au traitement d'effluents gazeux, Ph.D. thesis, University of Rouen, France.

Scharfetter, D., and H. Gummel (1969), Large-signal analysis of a silicon read diode oscillator, *IEEE Trans. Electron Devices*, *16*(1), 64–77.

Ségur, P., A. Bourdon, E. Marode, D. Bessières, and J. H. Paillol (2006), The use of an improved Eddington approximation to facilitate the calculation of photoionization in streamer discharges, *Plasma Sources Sci. Technol.*, *15*, 648–660.

Sentman, D. D., E. M. Wescott, D. L. Osborne, D. L. Hampton, and M. J. Heavner (1995), Preliminary results from the Sprites94 campaign: Red sprites, *Geophys. Res. Lett.*, *22*, 1205–1208.

Stanley, M., P. Krehbiel, M. Brook, C. Moore, W. Rison, and B. Abrahams (1999), High speed video of initial sprite development, *Geophys. Res. Lett.*, *26*, 3201–3204.

Starikovskaia, S. M. (2006), Plasma assisted ignition and combustion, *J. Phys. D: Applied Physics*, *39*(16), R265–R299.

Stone, H. L. (1968), Iterative solution of implicit approximations of multidimensional partial differential equations, *SIAM J. Numer. Anal.*, *5*(3), 530–558.

Taine, J., and A. Soufiani (1999), Gas IR radiative properties: from spectroscopic data to approximate models, in *Advances in Heat Transfer*, vol. 33, edited by J. Hartnett and T. Irvine, pp. 295–414, Academic Press, San Diego, California.

Teich, T. H. (1967), Emission gasionisierender strahlung aus electronenlawinen I. Meßanordnung und Meßverfahren. Messungen in Sauerstoff, *Z. Phys.*, *199*, 378–394.

Tseng, Y.-H., and J. H. Ferziger (2003), A ghost-cell immersed boundary method for flow in complex geometry, *J. Comput. Phys.*, *192*(2), 593–623.

Vitello, P. A., B. M. Penetrante, and J. N. Bardsley (1994), Simulation of negative-streamer dynamics in nitrogen, *Phys. Rev. E*, *49*, 5574–5598.

Wu, C., and E. E. Kunhardt (1988), Formation and propagation of streamers in N_2 and $N_2 - SF_6$ mixtures, *Phys. Rev. A*, *37*, 4396–4406.

Yurgelenas, Y. V., and H.-E. Wagner (2006), A computational model of a barrier discharge in air at atmospheric pressure: the role of residual surface charges in microdischarge formation, *J. Phys. D: Applied Physics*, *39*(18), 4031–4043.

Zalesak, S. T. (1979), Fully multidimensional flux-corrected transport algorithms for fluids, *J. Comput. Phys.*, *31*, 335–362.

Zalesak, S. T. (1979), Fully multidimensional flux-corrected transport algorithms for fluids, *J. Comput. Phys.*, *31*, 335–362.

Zeghondy, B., S. Célestin, A. Bourdon, P. Ségur, D. Bessières, and J. Paillol (2007), An immersed boundary method to simulate positive streamer propagation in point-to-plane geometry in air, in *Proc. 28th Int. Conf. on Phenomena in Ionized Gases (Prague, Czech Republic)*, pp. 1–4.

Zheleznyak, M. B., A. K. Mnatsakanyan, and S. V. Sizykh (1982), Photoionization of nitrogen and oxygen mixtures by radiation from a gas discharge, *High Temp.*, *20*, 357–362.

Zhu, Y., T. Takada, K. Sakai, and D. Tu (1996), The dynamic measurement of surface charge distribution deposited from partial discharge in air by pockels effect technique, *J. Phys. D: Applied Physics*, *29*(11), 2892–2900.